The Casimir energy and radiative heat transfer between nanostructured surfaces

Lussange A. Johann

THESE DE DOCTORAT DE
L'UNIVERSITE PIERRE ET MARIE CURIE

Spécialité : Physique

Ecole doctorale ED 107

Réalisée au
Laboratoire Kastler Brossel (UPMC-ENS-CNRS)

Présentée par
Johann LUSSANGE

Pour obtenir le grade de :
DOCTEUR de l'UNIVERSITÉ PIERRE ET MARIE CURIE

Sujet de la thèse :

The Casimir energy and radiative heat transfer between nanostructured surfaces

Soutenue le 10 Septembre 2012 devant le jury composé de :

Mme. Astrid LAMBRECHT : Directrice de thèse

M. Karl JOULAIN : Rapporteur

M. George PALASANTZAS : Rapporteur

M. Mauro ANTEZZA : Examinateur

M. Daniel BLOCH : Examinateur

M. Jean-Marc FRIGERIO : Examinateur

M. Cyriaque GENET : Examinateur

M. Serge REYNAUD : Invité

Contents

I. BREF RÉSUMÉ EN FRANÇAIS

Le sujet de cette thèse porte sur les calculs numériques de deux observables quantiques influents à l'échelle submicrométrique : le premier étant la force de Casimir et le second étant le transfert thermique radiatif. En champ proche, ces deux grandeurs physiques sont à l'origine de nombreuses applications potentielles dans le domaine de la nano-ingénierie.

Elles sont théoriquement et expérimentalement bien évaluées dans le cas de géométries simples, comme des cavités de Fabry-Pérot formées par deux miroirs plans parallèles. Mais dans le cas des géométries complexes invariablement rencontrées dans les applications nanotechnologiques réelles, les modes électromagnétiques sur lesquels elles sont construites sont assujettis à des processus de diffractions, rendant leur évaluation considérablement plus complexe.

Ceci est le cas par exemple des NEMS ou MEMS, dont l'architecture est souvent non-triviale et hautement dépendante de la force de Casimir et du flux thermique, avec par exemple le problème de malfonctionnement courant dû à l'adhérence des sous-composants de ces systèmes venant de ces forces ou flux. Dans cette thèse, je m'intéresse principalement à des profils périodiques de forme corruguée —c'est-à-dire en forme de créneaux— qui posent d'importantes contraintes sur la simplicité de calcul de ces observables.

Après une revue fondamentale et théorique jetant les bases mathématiques d'une méthode exacte d'évaluation de la force de Casimir et du flux thermique en champ proche centrée sur la théorie de diffusion, la seconde et principale partie de ma thèse consiste en une présentation des estimations numériques de ces grandeurs pour des profils corrugués de paramètres géométriques et de matériaux diverses. En particulier, j'obtiens les tous premiers résultats exacts de la force de Casimir hors-équilibre-thermique et du flux thermique radiatif entre des surfaces corruguées. Je conclus par une proposition de conception d'un modulateur thermique pour nanosystèmes basée sur mes résultats.

II. SHORT SUMMARY IN ENGLISH

The subject of this thesis is about the numerical computations of two influent quantum observables at the nanoscale: the Casimir force and the radiative heat transfer. In near field, these two physical quantities are at the origin of numerous potential applications in the field of nano-engineering.

They are theoretically and experimentally well evaluated in the case of simple geometries such as Fabry-Pérot cavities, which consist in two parallel plane mirrors separated by vacuum. But in the case of the more complex geometries which are unavoidably encountered in practical nanotechnological applications, the electromagnetic modes from which they are derived are subject to scattering processes which make their evaluation considerably more complex.

This is for instance the case of NEMS and MEMS, whose general architecture is often non-trivial and highly dependent on the Casimir force and radiative heat flux, with for example the often encountered problem of stiction in these nano-devices. In this thesis I mainly focus on corrugated periodic profiles, which bring important constraints on the simplicity of the computations associated with these observables.

After a fundamental review of the mathematical foundations of an exact method of computation of the Casimir force and of the heat flux based on scattering theory, I present in the second part of this thesis the results of the numerical calculations of these quantities for corrugated profiles of various geometrical parameters and for different materials. In particular, I obtain the very first exact results of the out-of-thermal equilibrium Casimir force and of the radiative heat flux between corrugated surfaces. I conclude with a proposal for the design of a thermal modulator device for nanosystems based on my results.

III. ACKNOWLEDGMENTS

Je voudrais tout d'abord remercier chaleureusement Romain, sans qui la plus grande partie de ce travail n'aurait pas pu être fait. Un grand merci également à Astrid, qui m'a guidé pendant ces trois années de thèse et qui a toujours su m'encourager dans les différents sujets de recherche, ainsi qu'à Serge pour tous ses conseils et son aide. Merci également à Diego Dalvit, Jean-Jacques Greffet, Felipe Rosa, et Jean-Paul Hugonin pour tout leur travail, et pour leur fructueuse collaboration.

Je remercie aussi Antoine Canaguier-Durand, Antoine Gérardin, Alexandre Brieussel, Etienne Brion, Francesco Intravaia, Ricardo Messina, Ricardo Decca, Umar Mohideen, Ho Bun Chan, Peter van Zwol pour toutes nos discussions. Merci au travail des équipes du LKB : Monique Granon, Laetitia Morel, Corinne Poisson, avec un remerciement tout spécial à Serge Begon pour son aide informatique à toute épreuve.

Un grand merci aux membres du jury qui ont fait le déplacement depuis l'étranger ou depuis la province pour assister à ma soutenance de thèse : George Palasantzas, Karl Joulain, Cyriaque Genet, Mauro Antezza, Daniel Bloch, et Jean-Marc Frigerio, et qui ont pris le temps de lire et d'étudier mon manuscrit. Merci enfin à Marianne Peuch pour sa précieuse aide administrative reliée à l'ED-107, ainsi qu'à Roland Combescot et Vladimir Dotsenko.

IV. INTRODUCTION

Shortly after the war, a young Dutchman named Hendrik Casimir was working at Philips Research Laboratories in the Netherlands on the topic of *colloidal solutions*. These are viscous solutions, either gaseous or liquid, containing micron-sized particles in suspension —such as clay mixed in water, milk, ink, and smoke. Theodor Overbeek, a colleague of Casimir, realized that the theory that was used to describe the *van der Waals forces* between these particles in colloids was in contradiction with observations. The van der Waals interaction between molecules was simply considered as the sum of the attractive and repulsive forces between these molecules (or their subcomponents), apart from the electrostatic contribution due to ions, and apart from the force arising from covalent bonds.

Overbeek asked Casimir to study this problem. Working together with Dirk Polder, and after some suggestions by Niels Bohr, Casimir had the intuition that the van der Waals interaction between neutral molecules had to be interpreted in terms of *vacuum fluctuations*. From then on, he shifted his focus from the study of this interaction in the case of two particles to the case of two parallel plane mirrors. In 1948 he thus predicted the quantum mechanical attraction between conducting plates now known as the *Casimir force* [1]. This force has since then been well studied in its domain of validity by both experimental precision measurements [2–13] and theoretical calculations [14–40].

The Casimir force arises from a quantum mechanical understanding of vacuum [41, 42]. In the classical picture, vacuum could be understood by a cubic box emptied of all its particles, and kept at zero temperature. However in the quantum mechanical description, the electromagnetic fields present in vacuum are subject to *vacuum fluctuations*. This is because quantum field theory requires all fields, and hence the electromagnetic fields present in vacuum, to be uniformly quantized at every point in space. At each spatial point, these quantized fluctuations can be described by a local harmonic quantum oscillator.

At any given moment, the energy of the fields present in vacuum varies around a constant mean value corresponding to the vacuum expectation value of the energy, or *vacuum energy*. It is given by the quantization of a simple harmonic oscillator requiring the lowest possible energy of that oscillator to be equal to half the energy of the photon:

$$E = \frac{1}{2}\hbar\omega$$

A consequence of this vacuum energy can be observed in different physical phenomena such as *spontaneous emission*, the *Lamb shift*, and of course the Casimir effect and van der Waals interaction. It also has influence on the cosmological constant and hence at the macroscale.

All electromagnetic fields have a specific spectrum made out of different ranges of wavelengths. In free space, the

wavelengths of the spectra of the fields in vacuum all have the same equal importance. But in a cavity formed by the two parallel planes mirrors that Casimir thought about, the field's vacuum fluctuations are amplified at *cavity resonance*, which is when the length of the cavity separating the two plates equals half of the field's wavelengths multiplied by an integer. Conversely, the field is suppressed at all the other wavelengths. This is due to multiple interference processes inside the cavity.

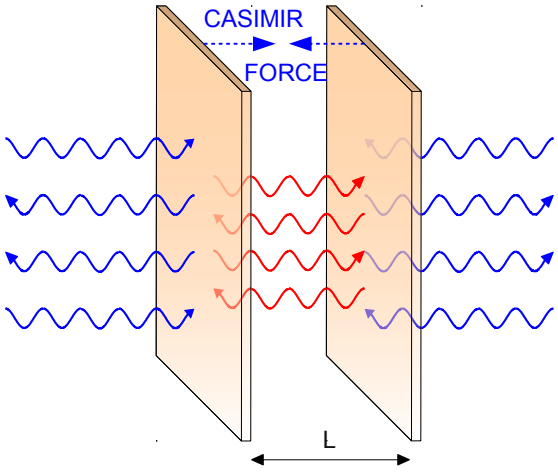

FIG. 1: Fabry-Pérot cavity formed by two parallel plates of area $\mathcal{A}$ separated by a distance L in vacuum.

Furthermore the vacuum energy associated with these extra- and intra-cavity fields brings a *field radiation pressure*, which increases with the fields' frequency. At cavity-resonance, the radiation pressure inside the cavity is larger than the one outside and hence the mirrors are pushed apart. However out of cavity-resonance, the radiation pressure inside the cavity is smaller than the one outside and the mirrors are pushed towards one another.

What leads to the Casimir force being in general attractive is that on average the attractive components outweigh the repulsive ones. However in some specific cases (distinct temperatures for each mirror, distinct materials for each mirrors with specific impedances, role of permeability), the Casimir force can be repulsive [43–51]. Notice that the Casimir force can also exist if the vacuum gap is replaced by another medium [52, 53]. Between two plates of area $\mathcal{A}$ separated by a distance L, it can be approximated by :

$$F \sim \mathcal{A}/L^4$$

On FIG. 1, we show such a cavity (named a *Fabry-Pérot* cavity) formed by two parallel plates separated by vacuum.

One can see from the equation above that the Casimir force is given by an inverse power law with the separation distance between the plates. This is the reason why the Casimir force becomes large at very short distances, in general below a few microns. At 100 nm, the Casimir force at zero temperature is approximatively equal to 1 $\mathrm{N.m^{-2}}$ for two plates of silicon carbide SiC, and about 3 $\mathrm{N.m^{-2}}$ for two plates of gold Au. At 1μm, the Casimir force has decreased to about 230 $\mu\mathrm{N.m^{-2}}$ and 900 $\mu\mathrm{N.m^{-2}}$ for these two cases, respectively.

This issue of extreme near-field dependence together with the proportionally large magnitude of the Casimir force could have many practical nanotechnological applications [54–58]. But it also has several consequences at the nanoscale, such as the problem of *stiction* in nanoelectromechanical systems (NEMS) and microelectromechanical systems (MEMS), causing their malfunctioning [59]. For this reason, the accurate calculation and understanding of the Casimir force is an ongoing challenge and topic of fundamental research.

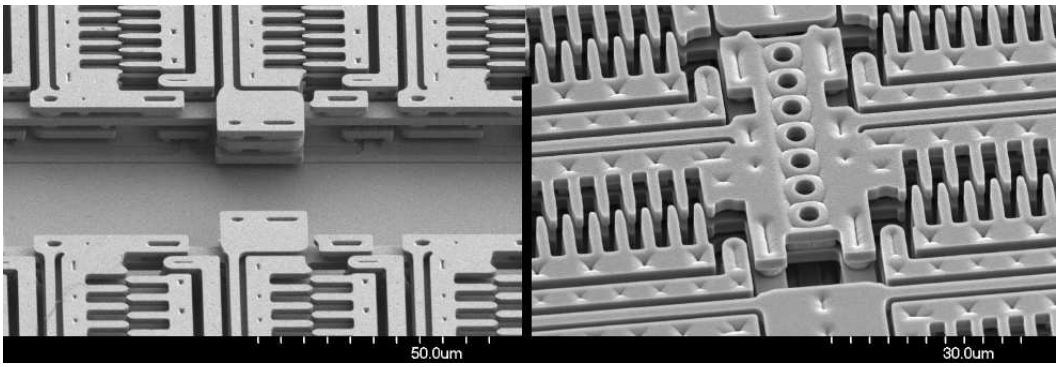

FIG. 2: Large force electrostatic MEMS comb drive (left), and electrostatic actuator (right).

Another important physical observable which is distinct from the Casimir force [60, 61] but also affects nanosystems in various ways is the *radiative heat transfer* between two bodies of different temperatures that are separated by a gap of vacuum below a few microns. However contrary to the Casimir force, the radiative heat transfer plays a major role at the macroscale as well—a perfect example being the heat conveyed to earth by sunlight.

The fluctuating electromagnetic field in the vacuum of the Fabry-Pérot cavity contains not only propagating but evanescent modes, which enhance the radiative heat transfer at short separations. Furthermore, if the surface of the body contains localized surface modes such as surface polaritons (dielectrics) or surface plasmons (for metals), the heat flux is greatly enhanced. This makes the magnitude of the radiative heat transfer at the nanoscale subject to a quantum contribution practically seen in the flux greatly exceeding the black body limit predicted by the classical picture [62–81].

At 100 nm, the radiative heat transfer between two planes of silicon dioxide SiO_2 at temperatures 290 K and 310 K is approximatively equal to 300 $\mathrm{W.m^{-2}.K^{-1}}$, and about 70 $\mathrm{W.m^{-2}.K^{-1}}$ for two planes of gold Au. At 1μm, the

heat flux has decreased to about 13 $\mathrm{W.m^{-2}.K^{-1}}$ and 0.2 $\mathrm{W.m^{-2}.K^{-1}}$ for these same cases, respectively.

The real electromechanical systems encountered in nanoengineering are far from being as architecturally simple in their design as the Fabry-Pérot cavity made out of the two planar surfaces shown in FIG. 1. As an example, one can readily check the potential complexity of the geometrical structures of the MEMS displayed on FIG. 2.

Just as for the Casimir force equations, the heat flux equations between two parallel planes have a simple analytical form and are well understood, but such a simple geometrical configuration is rarely seen in nanoengineering. It is therefore crucial to establish a theoretical description with numerical computations of the Casimir force and heat flux for nanostructured profiles describing real materials.

A basic type of nanostructured profile that we will study throughout this text is made out of periodic *corrugations*, as shown on FIG. 3. The reflection of a mode at a planar surface follows the simple Snell–Descartes law of refraction, but here the modes present in the cavity are diffracted at incidence according to a complex scattering from the corrugations. Corrugated surfaces are a special case of the more general surface roughness considerations impacting the magnitude of the Casimir force [82–84].

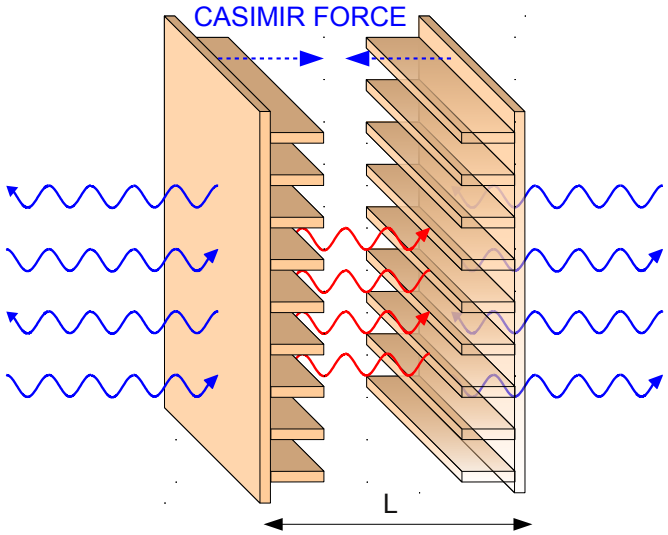

FIG. 3: Fabry-Pérot cavity formed by two parallel corrugated gratings separated by a distance L in vacuum.

The outcome of the numerical calculations of both the Casimir force and the radiative heat transfer between such

corrugated profiles lies in the determination of the scattering matrix associated with each profile. These scattering matrices contain the sets of Fresnel-Stokes amplitudes for reflection and transmission of the modes at the media interfaces. The two sets of parameters fully characterizing a given grating will be found in its associated scattering matrix : those specifying its geometry, and those specifying the material it is made of. Therefore one can say that the scattering matrix is used to define both a given nanostructured profile, and the way the cavity modes are diffracted by it.

The backbone of the mathematical formalism that we will use to compute the scattering matrices associated with corrugated surfaces is the *Rigorous Coupled-Wave Analysis* (RCWA) method from scattering theory [85]. The main aim of section V will first be to lay down the foundations of quantum field theory and the thermodynamics used in Casimir physics and nanoscale heat transfer, and in section VI we will derive the expressions of the Casimir force and of the heat flux between corrugated surfaces in the framework of scattering theory.

The results of our numerical computations for the Casimir force between gratings with various geometrical parameters and materials are then presented in section VII —for corrugated profiles and several arbitrary periodic profiles. In section VIII we will discuss the Casimir energy as a function of an overall non-zero temperature, and the Casimir force when the two profiles have distinct non-zero temperatures. In section IX, we will conclude with a study of radiative heat transfer between corrugated profiles, and propose a thermal modulator device for nanosystems based on such a study.

V. THEORY : QUANTUM FIELDS AND THE VACUUM STATE

A. Quantum theory and radiative heat transfer in the classical description

1. *Quantization of light : Planck's law, and Einstein's generalization to photons*

By the beginning of the 1900's, what is now known as classical physics was facing challenging issues. One of these issues concerned its understanding of *thermal radiation*, which is the electromagnetic radiation of an object due to its temperature. This led to the study of a perfect thermal emitter called the *black body*. By definition, a black body is an object perfectly absorbing all electromagnetic radiation at all frequencies —and thus 'black', emitting only the thermal part of its electromagnetic radiation. In this terminology, a real object, which will never perfectly absorb all electromagnetic radiation, is called a grey body.

It was well-known to 19th century physicists that when a metal is heated to increasingly large temperatures, its glow colour changes from red, to yellow, to blue, and eventually to white. The peak wavelength of a black body thermal radiation was already known since 1893 as a direct consequence of the so-called *Wien's displacement law* :

$$\lambda_{max} = \sigma_w / T \tag{1}$$

with $\sigma_w = 2.897 \times 10^{-3}$ m.K the Wien's displacement constant, and T the absolute temperature of the black body. Furthermore, its overall energy radiated per unit surface area was known since the 1880's through the *Stefan-Boltzmann law* :

$$W = \epsilon \sigma T^4 \tag{2}$$

with $\sigma = \frac{2\pi^5 {k_B}^4}{15c^2h^3} = 5.670 \times 10^{-8}$ J.s^{-1}.m^{-2}.K^{-4} being the *Stefan-Boltzmann constant*, $k_B = 1.381 \times 10^{-23}$ J.K^{-1} the *Boltzmann constant*, $h = 6.626 \times 10^{-34}$ J.s the *Planck constant*, and c the speed of light in vacuum. The dimensionless *emissivity* ϵ is equal to 1 for a black body, but again any real object has $\epsilon < 1$.

A direct consequence of Wien's displacement law was that the wavelength at which the thermal radiation of a heated object is the strongest increases with its temperature. However, after shifting from the red, yellow, blue, and white parts of the visible spectrum, and furthermore into the ultra-violet, the object increasingly continues to glow in the visible spectrum. In other words, as the temperature increases, the object never becomes invisible but the radiation of visible light increases continually.

Classical physics explained this peculiar phenomena by the Rayleigh–Jeans law, or alternatively by the Wien approximation. But the former agreed with experiment for long wavelengths only, and the latter for short wavelengths

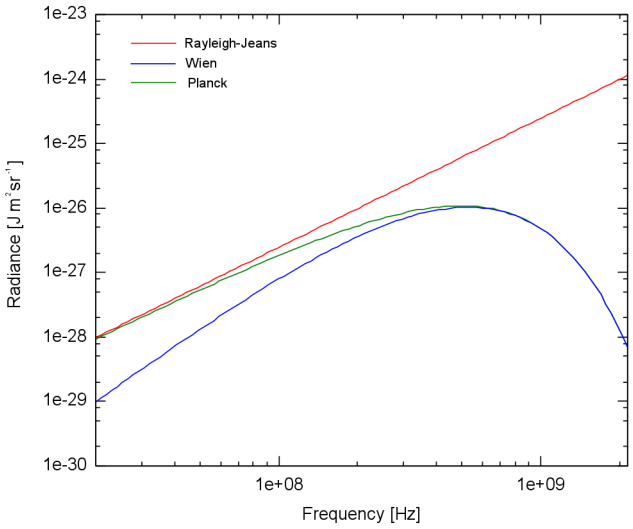

FIG. 4: Comparison between Wien's approximation, the Rayleigh–Jeans's law, and Planck's law, for a body at $T = 0.008K$.

only. In 1911, Paul Ehrenfest retrospectively called this unsolvable puzzle the 'ultraviolet catastrophe' : it inferred to the fact that at small wavelengths, objects with high temperatures will emit energy at an infinite rate.

However in 1900, Max Planck established a model [86] that faithfully took into account the full spectrum of thermal radiation (FIG. 4), thereby involuntarily laying the first foundation of the quantum theory. He proposed to model the thermal radiation as being in equilibrium by using a set of harmonic oscillators. He assumed that energy can only be absorbed or emitted in small, discrete packets by means of these oscillators. By this simple mathematical trick, he thus proposed that each of these individual harmonic oscillators should not give an arbitrary amount of energy, but instead an integral number of units of energy —*quanta* of energy— where each should be proportional to the oscillator's own frequency. This proportionality is now known as the Planck constant h, already encountered in equation (2). Thus in this model, the energy E of an harmonic oscillator of frequency ν (or angular frequency $\omega = 2\pi\nu$) is given by :

$$E = nh\nu = n\hbar\omega \tag{3}$$

for $n = 1, 2, 3, ...$ and $\hbar = h/2\pi$ being the so-called *reduced Planck constant*. In this approach, Planck's law leads to the following spectral radiance of a black body, that is, the amount of radiative energy for a given frequency ω :

$$I_\omega(T) = \frac{\hbar\omega^3}{4\pi^3 c^2} \frac{1}{e^{\frac{\hbar\omega}{k_B T}} - 1} \tag{4}$$

Planck's law is thus a distribution of thermodynamic equilibrium (like Bose–Einstein, Fermi–Dirac, or Maxwell–Boltzmann distributions). One should notice the second term on the r.h.s, which is related to the so-called *partition function* of the individual harmonic oscillators. This term contains the *Boltzmann factor*, which is a factor determining the probability of an oscillator to be in a specific state out of the total many-states system which is at thermodynamic equilibrium.

Just as a material body is specified by a given temperature and energy distribution at thermal equilibrium (like for example the Boltzmann distribution), the electromagnetic field may be considered as a photon 'gas' of given temperature and energy distribution at thermal equilibrium —in which case, it is explained by Planck's law.

In 1905 Albert Einstein took a step further [87], adding to Planck's concept of quanta of energy and applying it to light. The issue of light being of a wave-like or a particle-like nature was a major question of Physics. By the early 1900's, it was commonly accepted that light was more of a wave-like nature, partly because it was able to explain the experimental results on the polarization of light, as well as the optical phenomena of refraction and diffraction. Yet daringly, Einstein took on a more particle-like approach and proposed following Planck's idea, that light's energy was divided into quanta of energies —today called *photons* :

$$E = h\nu \tag{5}$$

Over time Einstein's view came to be respected, partly due to its ability to accurately describe the photoelectric effect —the fact that under high-frequency electromagnetic radiation, matter can emit electrons as a consequence of energy absorption.

2. Laws of thermodynamics and Onsager's reciprocal relations

By thermodynamics, one refers to the macroscopic description of energy as *work* or *heat* exchange between physical systems. If for example a system is at *thermodynamic equilibrium*, it implies that over time no macroscopic change can be detected in the system. As a tool to give a macroscopic description of the universe, thermodynamics implicitly postulates that over an infinite amount of time, all systems confined within a fixed volume will eventually reach thermodynamic equilibrium. It is basically constructed around three postulates :

- The *first law of thermodynamics* [88] states that any transformation or internal energy variation δU from one equilibrium state to another is equal to the energy transfer exiting the system subtracted from the energy transfer entering the system. This exchange of energy can appear as work W and as heat transfer Q :

$$\delta U = \delta Q - \delta W \tag{6}$$

  An illustration of this law is the conservation of energy under any transformation : energy can be exchanged or transformed, but not created nor annihilated. It calls upon the concept of internal energy of a system, and

can be extrapolated to the whole universe, saying that the sum of the energies represented by all the existing particles within it should be a constant over time.

- The *second law of thermodynamics* [89] states that any thermodynamical transfer in a system is such that there is a net increase in the global entropy ΔS_{global}, which is the sum of the entropy of the system ΔS_{sys} and the entropy of the outside environment ΔS_{env} :

$$\Delta S_{\text{global}} = \Delta S_{\text{sys}} + \Delta S_{\text{env}} \geqslant 0 \tag{7}$$

Entropy can be seen as a way to express randomness or disorder, and the equation above implies that physical transformations are irreversible —if they were reversible, no entropy would be created and ΔS_{global} would be zero. As a consequence, an isolated system's entropy will always increase or stay constant, since there is no heat transfer with the outside environment. In practice, irreversibility is caused by many factors, among which the inhomogeneity of diffusion processes (such as temperature and pressure), or dissipative phenomena (such as dry or fluid friction processes), and chemical reactions.

- The *third law of thermodynamics* was established by Walther Nernst in 1904 [90] and states that the entropy of a system tends to zero *if possible*, as the temperature of that system tends to zero. Notably, this limit to a zero entropy can be expected for perfect crystals with a unique ground state. But degenerate states such as fermions cannot display this zero entropy limit at zero temperature.

This is an important law because it provides a reference frame for the determination of absolute entropy. Since it concerns perfect crystals, a consequence of the third law of thermodynamics is that it is impossible to cool down a system to the absolute zero temperature. With the expansion of statistical physics, the third law is now seen as a consequence of the definition of entropy from the statistical mechanics viewpoint, defined for macroscopic systems composed of a given number Ω of microstates as :

$$S = k_B \log \Omega \tag{8}$$

One can link this law to the quantum mechanical principle of integer-spin particles being in the same quantum state, which has become a recent topic of interest, with the study of the properties of Bose–Einstein condensates.

Over the years many other important results of thermodynamics and statistical mechanics have been raised more or less successfully to the status of 'law of thermodynamics', but we shall especially retain what has sometimes been called :

- The *zeroth law of thermodynamics*, which states that two systems at equilibrium with a third system are at equilibrium with each other. Hence thermal equilibrium between systems is an equivalence relation. According to Max Planck, a consequence of this is that it provides the definition of temperature as a measurable quantity —practically, by the approximation of the absolute zero through the study of gases at low temperatures.

- The *fourth law of thermodynamics*, generalized by the so-called *Onsager reciprocal relations* [91, 92], expresses the equality of ratios of forces and flows for systems out of thermodynamical equilibrium, albeit for which there still exist a certain notion of local equilibrium. More specifically, let us consider the internal energy density u of a fluid system, which is related to the entropy density s and matter density ρ according to :

$$ds = \frac{1}{T}du - \frac{\mu}{T}d\rho. \tag{9}$$

where T is the temperature and μ a combination of chemical potential and pressure. Equation (9) comes from (6), and is in this sense a derivation from the first law of thermodynamics. If written in terms of du, one can identify Tds with the heat transfer within the system, and $\mu d\rho$ with the chemical and mechanical work. In the case of non-fluid systems, this latter work term will be described by different variables, but for now the general idea remains the same.

The energy density u and the matter density ρ are conserved so that their flows verify the following continuity equations :

$$\partial_t u + \nabla \cdot \mathbf{J}_u = 0 \tag{10}$$

$$\partial_t \rho + \nabla \cdot \mathbf{J}_\rho = 0 \tag{11}$$

for t the local time-rate of change, and for $\mathbf{J}_u$ and $\mathbf{J}_\rho$ the energy and matter density flows, respectively. These are related to the notion of flux and force, respectively. The terms $\frac{1}{T}$ and $-\frac{\mu}{T}$ in equation (9) are the respective conjugate variables of u and ρ, and are similar to potential energies. Therefore their gradients are seen as thermodynamic forces, which bring flows associated with energy and matter densities.

In the absence of matter flows, the following is a consequence of Fourier's law of heat conduction :

$$\mathbf{J}_u = k\,\nabla\frac{1}{T} \tag{12}$$

In the absence of heat flows, the following is a consequence of Fick's first law of diffusion :

$$\mathbf{J}_\rho = -D\,\nabla\frac{\mu}{T} \tag{13}$$

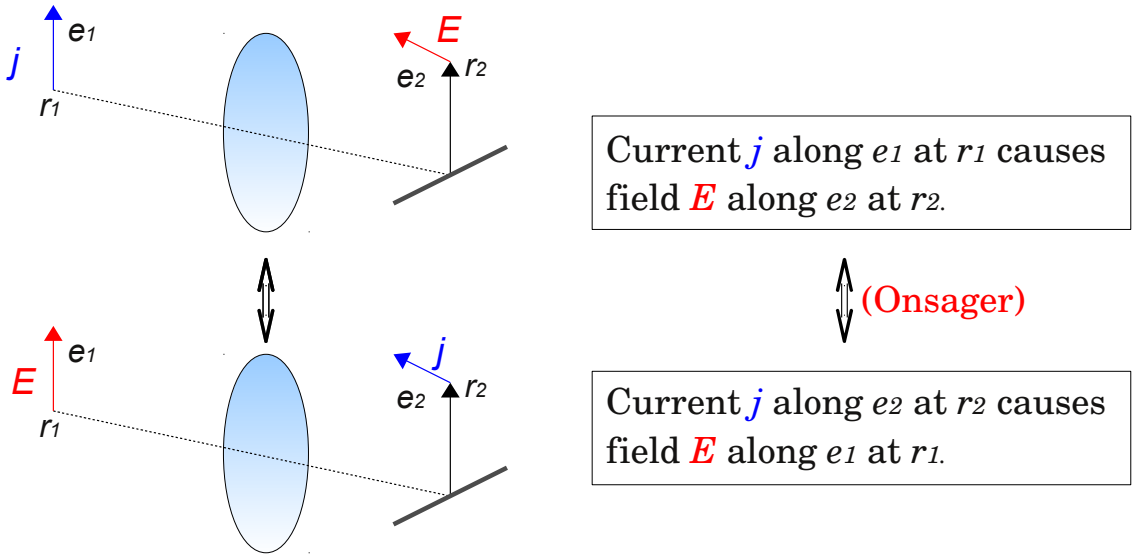

FIG. 5: Equivalence shown by the Onsager reciprocity relations based on [93].

where k and D are related to the thermal conductivity and mass diffusivity, respectively. Therefore, when both heat and matter flows are present, one can establish proportionality cross-term coefficients describing the overlapping effects between the flows and forces $L_{u\rho}$ and $L_{\rho u}$, and direct transport coefficients L_{uu} and $L_{\rho\rho}$ through the equations :

$$\mathbf{J}_u = L_{uu}\,\nabla\frac{1}{T} - L_{u\rho}\,\nabla\frac{\mu}{T} \tag{14}$$

$$\mathbf{J}_\rho = L_{\rho u}\,\nabla\frac{1}{T} - L_{\rho\rho}\,\nabla\frac{\mu}{T} \tag{15}$$

These equations finally give the Onsager reciprocity relations :

$$L_{u\rho} = L_{\rho u} \tag{16}$$

These are valid only when the flows and forces are linearly dependent so that the considered system is not too far from equilibrium, and the concept of microscopic reversibility or local equilibrium takes effect. Hence generally the Onsager theory is a *macroscopic* theory of linear coupling of irreversible events, such as thermal conductivity and mass diffusivity. The general geometrical implications of the Onsager reciprocity relations are shown in FIG. 5.

3. Properties of radiative heat transfer

Even though classical thermodynamics comprise the study of energy of a system through both work and heat, we will now restrain ourselves to the description of heat transfer, as defined by the transfer of energy in a system through any other means than work —mechanical work, electrical work, chemical work, etc. There are different ways by which heat may be transferred :

- *Conduction* or *diffusion* can produce heat transfer between systems in physical contact, such as for example cold air cooling down the human body.
- *Convection* can cause heat transfer in fluids or viscous materials by means of collective molecular movements within it. So convection is a consequence of the local variations of density within the fluid due to the variations of temperature. A good example is the heating of water in a pot, where flows and movements from the bottom to the surface of the water start to appear before boiling.
- *Radiation* can cause heat transfer to or from a system by emission or absorption of electromagnetic radiation. The best example of radiative heat transfer is the heat felt on earth from the sun through sunlight. According to the kinetic theory, heat in a macroscopic system can be understood as a constant random motion of the microscopic particles constituting it. The greater the temperature, the greater the speed of the particles' random motion. When approaching the absolute zero temperature, this thermal motion is expected to decrease proportionally and to vanish at absolute zero.

This said, one can define thermal radiation more precisely as the electromagnetic radiation generated by the thermal motion of the *charged particles* within the atoms —such as protons and electrons— composing the system. This thermal energy is thus a collective mean kinetic energy of the charged particles of the body due to their own individual oscillations, which generates coupled electric and magnetic fields, eventually producing photons [94]. These photons are thus emitted and carry away a part of the body's energy as thermal electromagnetic radiation. Therefore all matter with a non-zero temperature emits a given amount of thermal radiation.

As we saw in section V A 1, this thermal emission may be in the form of visible light, such as for the tungsten wire of a light bulb, or not, such as the infrared radiation emitted by hot-blooded animals, or microwave radiation such as the cosmic microwave background radiation. For a given body, the rate of electromagnetic radiation emitted at a given frequency is proportional to its level of electromagnetic absorption from the source. Therefore a given body which would absorb a larger amount of frequencies in the UV regime will radiate thermally more in the UV also. As a matter of fact this important property of thermal radiation does not only concern the frequency and hence color

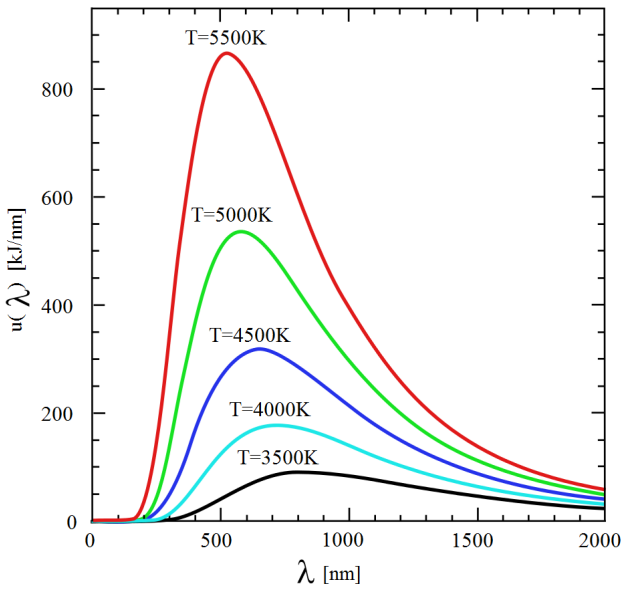

FIG. 6: Radiance as a function of wavelength for different temperatures at $3500K$ in black, $4000K$ in cyan, 4500 in blue, $5000K$ in green, and $5500K$ in red, as an illustration of radiative heat transfer. The wavelength associated with the intensity maximum decrease with larger temperatures. The thermal emission contains a factor $1/\lambda^2$ numbering the Fourier modes of wavelength λ, and another dimensional regularization factor to convert frequencies to wavelengths.

of the electromagnetic wave involved, but also its polarization, direction, and even coherence. It is thus possible to obtain in laboratory conditions a thermal radiation of selected polarization, coherence, direction, etc.

As a reminder, if the system is considered a black body, one can study its most probable wavelength of thermal radiation through Wien's displacement law (1), its intensity through the Stefan-Boltzmann law (2), and its radiation spectrum through Planck's law (4). This is represented in FIG. 6, which shows the thermal emission intensity of the black body as a function of the wavelength at temperatures $T = 3500$ K, 4000 K, 4500 K, 5000 K, and 5500 K, and where one can see that the wavelength associated with the intensity maximum decrease with larger temperatures.

If a random body receives a thermal radiation from another one and thereby emits back only specific frequencies and is transparent to the others, only these emitted frequencies will add to its thermal equilibrium. But in the specific case of a black body, which will absorb by definition all incoming electromagnetic radiations, all the different frequencies will add to its thermal equilibrium.

The energy radiated by a given body divided by the energy radiated by a black body at the same temperature defines this body's emissivity $\epsilon(\nu)$ at a given frequency ν. A black body has an emissivity $\epsilon = 1$. The emissivity of a given material thus decreases with increasing reflectivity : for example polished silver has an emissivity of $0,02$.

Absorptivity, reflectivity, and emissivity of all systems depend on the radiation frequency ν and are comprised between 0 and 1. The ratio of the radiation $I_{\text{reflected}}(\nu)$ reflected by a body over its incident radiation $I(\nu)$ is its

spectral reflectivity :

$$r(\nu) = \frac{I_{\text{reflected}}(\nu)}{I(\nu)} \tag{17}$$

One can also define the spectral transmissivity $t(\nu)$ as the ratio of intensity of the radiation coming out of the body for a particular frequency $I_{\text{transmitted}}(\nu)$ by the intensity of the incident radiation :

$$t(\nu) = \frac{I_{\text{transmitted}}(\nu)}{I(\nu)} \tag{18}$$

Then one can define the spectral absorptivity $a(\nu)$ as the ratio of the light intensity at a given frequency after having been absorbed by the body $I_{\text{absorbed}}(\nu)$, over the intensity $I(\nu)$ before being absorbed :

$$a(\nu) = \frac{I_{\text{absorbed}}(\nu)}{I(\nu)} \tag{19}$$

In addition the properties of thermal radiation of a given object depend on its surface characteristics —such as its absorptivity, emissivity, or temperature— and we will have, as a consequence of the first law of thermodynamics :

$$a(\nu) + t(\nu) + r(\nu) = 1 \tag{20}$$

For completely opaque surfaces, we will have $t(\nu) = 0$ and hence $a(\nu) + r(\nu) = 1$.

It is possible to define the spectral absorptivity, reflectivity, and transmissivity in terms of a given solid angle and hence chosen direction [95]. The definitions above are for total hemispherical properties, since $I(\nu)$ represents the spectral light intensity coming from all directions over the hemispherical space, and as thus equations (17), (18), and (19) represent the *average* absorptivity, reflectivity, and transmissivity in all directions.

An important property is that the spectral absorption $a(\nu)$ is equal to the emissivity $\epsilon(\nu)$. This is known as as *Kirchhoff's law* of thermal radiation [96] :

$$a(\nu) = \epsilon(\nu) \tag{21}$$

We are now in a position to define the radiative heat transfer $W_{a\to b}$ between two grey body surfaces a and b of respective temperatures T_a and T_b, as the radiation from a arriving at b, minus the radiation leaving b. Furthermore we consider these two surfaces to be diffuse and opaque, with respective surface areas A_a and A_b, and to form an enclosure so that the *net rate* of radiative heat transfer $\partial W_{a\to b}/\partial t$ from a to b is equal to the net rate $\partial W_a/\partial t$ *from* a, and to the net rate $-\partial W_b/\partial t$ *to* b.

$$\frac{\partial W_{a\to b}}{\partial t} = \frac{\sigma(T_a^4 - T_b^4)}{\dfrac{1-\epsilon_a}{A_a\epsilon_a} + \dfrac{1}{A_a F_{a\to b}} + \dfrac{1-\epsilon_b}{A_b\epsilon_b}} = \frac{\partial W_a}{\partial t} = -\frac{\partial W_b}{\partial t} \tag{22}$$

One should notice that the numerator in equation (22) corresponds to the Stefan-Boltzmann law as the overall energy radiated per unit surface area from equation (2). The denominator is composed of three terms, each respectively corresponding to the radiation emitted by a, transmitted from a to b, and received by b.

$F_{a\to b}$ is the *view factor*, which is a coefficient describing the proportion of the radiative flux leaving a and arriving at b, and with the property that the sum of all view factors from a given surface is equal to 1. The view factor is subject to the *reciprocity theorem* :

$$A_a F_{a\to b} = A_b F_{b\to a} \tag{23}$$

The view factor is dependent on the geometry of the two bodies, so that in the case of two infinitely large identical parallel plates a and b —forming a Fabry-Pérot cavity, as we will see later when studying the Casimir effect—, we have $F_{a\to b} = 1$ and $A_a = A_b = A$. Applying these to equation (22), we find the following important result for radiative heat transfer in the classical description [95] :

$$\dot{W}_{a\to b} = \frac{\partial W_{a\to b}}{\partial t} = \frac{A\epsilon_a\epsilon_b\sigma(T_a^4 - T_b^4)}{\epsilon_a + \epsilon_b - \epsilon_a\epsilon_b} \tag{24}$$

4. Thermal radiation through a medium

One can take a step further and set a plane thermal shield or coating s, at equal distance in between the two flat planes of the example above in order to attenuate the radiative heat transfer, as shown in FIG. 7. This configuration is often met in aerospace and cryogenic technologies, and will also be encountered in our discussion on near-field radiative heat transfer. We thus define the emissivity of the shield facing plane a as ϵ_{sa}, and the emissivity of the shield facing plane b as ϵ_{sb}. We set $A_a = A_b = A_s = A$, and since $F_{a\to s} = F_{b\to s} = 1$ we can write :

$$\dot{W}_{a\to s\to b} = \frac{A\sigma(T_a^4 - T_b^4)}{(\frac{1-\epsilon_a}{A_a\epsilon_a} + \frac{1}{A_a F_{a\to b}} + \frac{1-\epsilon_{sa}}{A_s\epsilon_{sa}}) + (\frac{1-\epsilon_b}{A_b\epsilon_b} + \frac{1}{A_s F_{s\to b}} + \frac{1-\epsilon_{sb}}{A_s\epsilon_{sb}})} = \frac{A\sigma(T_a^4 - T_b^4)}{(\frac{1}{\epsilon_a} + \frac{1}{\epsilon_b} - 1) + (\frac{1}{\epsilon_{sa}} + \frac{1}{\epsilon_{sb}} - 1)} \tag{25}$$

where the second term in the denominator of the r.h.s equality describes the attenuation of the radiative heat transfer between the planes a and b induced by the thermal shield s set in between. The different terms in the denominator correspond to the different spatial segments along the radiation's path, as seen in FIG. 7.

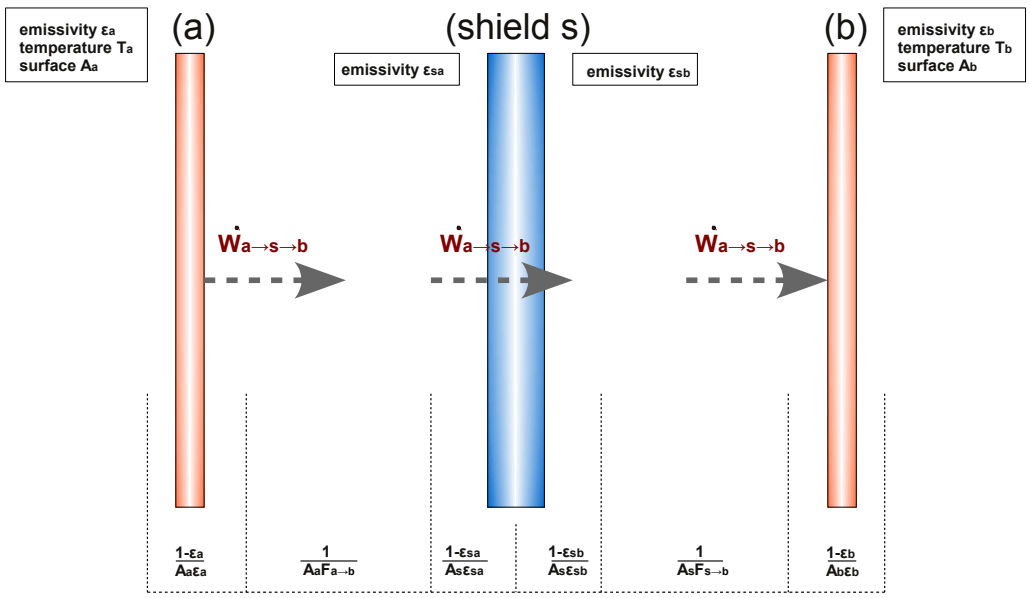

FIG. 7: Radiative heat transfer rate between two parallel planes a and b separated by a thermal shielding plate s. The different terms in the denominator of equation (25) are outlined along the thermal radiation's path between the two planes.

Equation (25) above can intuitively be generalized to an arbitrary number n of shields $s_1, s_2, ..., s_n$, of respective emissivities $\epsilon_{s_1 a}, \epsilon_{s_2 a}, ..., \epsilon_{s_n a}$ and $\epsilon_{s_1 b}, \epsilon_{s_2 b}, ..., \epsilon_{s_n b}$ such that :

$$\dot{W}_{a \to s_1 \to ... \to s_n \to b} = \frac{A\sigma(T_a^4 - T_b^4)}{(\frac{1}{\epsilon_a} + \frac{1}{\epsilon_b} - 1) + (\frac{1}{\epsilon_{s_1 a}} + \frac{1}{\epsilon_{s_1 b}} - 1) + ... + (\frac{1}{\epsilon_{s_n a}} + \frac{1}{\epsilon_{s_n b}} - 1)} \tag{26}$$

In the case where all the emissivities are equal to ϵ, this reduces to $\dot{W}_{a \to b}/(n+1)$, where $\dot{W}_{a \to b}$ is the heat transfer rate without shield, given by equation (24). This means that when all emissivities are equal, one shield will reduce the rate of radiative heat transfer by a factor two, and 9 shields will reduce it by a factor 10.

Notice also that this computation can be performed for other geometries than parallel planes, provided the view factor is changed accordingly in order to correctly describe the desired configuration.

Now let's consider a different case, where we have a medium of thickness L subject to a radiative heat transfer with an incident radiation of spectral intensity $I(\nu, x = 0)$ on the medium, as seen in FIG. 8. This radiation intensity will decrease, by effect of dissipation through the medium, over its length L. If we now consider the medium to be built up of an infinite number of layers, each of thickness dx for an x-axis defined as parallel to the propagation of

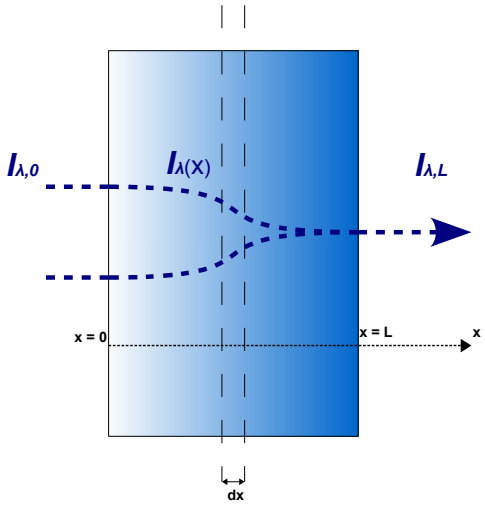

FIG. 8: Dissipation of radiative heat transfer through a medium of thickness L.

the radiation, we can derive the so-called *Beer's law* :

$$\frac{dI(\nu,x)}{dx} = -\kappa_\nu I(\nu,x) \tag{27}$$

where the proportionality factor κ_ν is called the medium's *spectral absorption coefficient*, with units in m^{-1}. It is important to notice that this proportionality factor gives a measure of the dissipation, and will be encountered again in a different form in our later discussion based on scattering theory.

Beer's law basically says that the radiation intensity will decay exponentially as the thermal radiation travels within the medium along the x-axis. This is readily seen by integrating from 0 to L each term of equation (27) after a variable separation, so that based on the assumption that the medium has an isotropic absorptivity, we obtain :

$$\frac{I(\nu,L)}{I(\nu,0)} = e^{-\kappa_\nu L} = t(\nu) \tag{28}$$

Now this ratio of the spectral intensity leaving a given medium over the incident spectral intensity is none other that the transmissivity $t(\nu)$ from equation (18), albeit now for a dissipative medium of spectral absorption coefficient κ_ν. For a non-reflective body, $r(\nu) = 0$ and one can thus re-derive the Kirchoff's law of equation (20) as :

$$a(\nu) = \epsilon(\nu) = 1 - t(\nu) = 1 - e^{-\kappa_\nu L} \tag{29}$$

One can insert the result above in equations (24) or (26) for instance and recover the net rate of radiative heat transfer for dissipative materials of a given thickness. Another consequence is that an optically thick surface, with a large $\kappa_\nu L$, will approach the black body description for a given frequency, and hence for a given specific temperature.

5. Conclusion

We have seen how a simple mathematical trick used by Max Planck in 1900 to explain the black body radiation led to the discovery of quanta of energy, soon generalized by Einstein to photons in 1905.

We have seen how the core foundations of thermodynamics rely on the works of Clausius in 1850, Carnot in 1824, and Nernst in 1904, establishing the fundamental first, second, and third laws of thermodynamics. The first law of thermodynamics, calling on the fundamental concept of internal energy, led to the famous conclusion that all energy is exchanged or transformed, never created nor annihilated. The second law of thermodynamics implies the increase of global entropy for any thermodynamical transfer in a system, and thereby bringing about the famous result of the universe's irreversible nature. The third law of thermodynamics finally framed the notion of absolute entropy and absolute temperature as normally unreachable. In the case when a system out of thermal equilibrium is yet not too far from equilibrium, we also discussed the important result of Onsager's reciprocal relations of equality between ratios of flows and forces.

Then we described the main mechanicsm of general heat transfer apart from mechanical work as being through conduction, convection, and radiation, and went on to discuss the properties of radiative heat transfer. Radiative heat transfer happens through a wide range of frequencies, described in the ideal black body picture by Planck's law (4). There is a peak in the black body radiation at high frequencies, described by Wien's displacement law (1). The total radiative intensity increases sharply with temperature, and in the case of a black body, it rises as the fourth power of the absolute temperature, as expressed by the Stefan–Boltzmann law from equation (2).

Finally we have described how the properties of the thermal radiation emitted by a given body —such as its frequency, polarization, direction, coherence— are directly related to those absorbed by that same body, and how by Kirchoff's law of equation (21), absorptivity and emissivity are equal. We eventually derived the net rate of radiative heat heat transfer between two arbitrary grey bodies in equation (22), between two planes in equation (24), and between two planes separated by a given number of thermal shields in equation (26), The expression of spectral emissivity through a dissipative medium of specific thickness has also been given in equation (29).

B. Quantum fields and electrodynamics

1. *From quantum particles to relativistic fields*

In 1925, Werner Heisenberg, Max Born, and Pascual Jordan developed the first field theory by deriving the internal degrees of freedom of a given field as an infinite set of harmonic oscillators, with their own individual canonical quantization. This was a free field theory in the sense that no charges nor current were assumed in it. Then by 1927, Paul Dirac was trying to construct a quantum mechanical description of the electromagnetic field. This led to a *quantum theory of fields*.

The first important aspect of the early quantum field theory developed by Dirac as applied to electromagnetism, was that it could encompass quantum processes in which the total number of particle changes —for instance as in the case of an atom emitting a photon, with the atom's electron losing a quantum of energy. The second important feature was that a consistent quantum field theory had to be relativistic.

The mathematical formalism of quantum mechanics implies operators acting on a Hilbert space which represent observables, i.e real physical quantities, and where the eigenspace contains the probable states of the quantum system. In this picture, the observables and their associated physical quantities are linked to the system's *degrees of freedom* —for example the observables of a quantum system's motion are its position and momentum, the three-dimensional coordinates of which represent its degrees of freedom. The set of all degrees of freedom of a given quantum system defines the *phase space*.

The formal definition of a quantum field is a quantum system possessing a large or even infinite number of degrees of freedom. In general these are denoted by a discrete index. In the classical picture, a field was described by a set of degrees of freedom for each set of spatial coordinates —such as the electric field taking on specific values as a function of position in space. But in the quantum definition, the field as a whole is now described as quantum system whose observables form an infinite set of degrees of freedom, because of the continuity of the fields' spatial set of coordinates.

The fundamental quantity of classical mechanics is the action S, which is the time integral of the Lagrangian L, itself locally described as the spatial integral of the Lagrangian density $\mathcal{L}$ as a function of fields $\psi(x)$ and their derivatives $\partial_\mu \psi(x)$ such that :

$$S = \int L dt = \int d^4x \mathcal{L}(\psi, \partial_\mu \psi) \tag{30}$$

We are in the Minkowski space-time metric with diagonal elements of its tensor $(+1, -1, -1, -1)$, and this is for coordinates μ running over $0, 1, 2, 3$ (or t, x, y, z), and hence such that $x^\mu = (x^0, x^1, x^2, x^3)$ has partial derivatives

$\partial_\mu = \partial/\partial x^\mu$. We will now work in *natural units* $\hbar = c = 1$. According to the *principle of least action*, a quantum system evolves from one configuration to the another in a given time interval along the path in configuration space for which the action is a usually a minimum. By configuration space, we understand the set of all possible space-time positions that the quantum system can potentially have. This leads to the Euler-Lagrange equation of motion for each and every field within the Lagrangian density $\mathcal{L}$:

$$\partial_\mu \left(\frac{\partial \mathcal{L}}{\partial(\partial_\mu \psi)} \right) = \frac{\partial \mathcal{L}}{\partial \psi} \tag{31}$$

All these expressions are Lorentz-invariant, and have thus been used in a straightforward way to formulate a field theory abiding by the laws of special relativity. However, staying close to a more systematic quantum formulation for now, one can derive the Hamiltonian H and its density $\mathcal{H}$ as :

$$H = \int \left(\frac{\partial \mathcal{L}}{\partial \dot{\psi}(x)} \dot{\psi}(x) - \mathcal{L} \right) d^3x = \int d^3x \mathcal{H} \tag{32}$$

where the integrand gives the expression of the Hamiltonian density $\mathcal{H}$.

From this early field theory formalism, two important equations were derived. The first is the Klein-Gordon equation, which accounts for special relativistic effects of spinless particles but still considers fields in the classical sense, so that it cannot be fully considered a type of Schrödinger equation :

$$(\partial_\mu \partial^\mu + m^2)\psi = (\Box + m^2)\psi = 0 \tag{33}$$

where we have defined the mass m, and the Lapalacian in Minkowski space $\Box = \partial_\mu \partial^\mu$ as the product of the covariant and contravariant derivatives.

The second is the Dirac equation, which is a special relativistic quantum equation describing half-spin particles through fields :

$$(i\gamma^\mu \partial_\mu - m)\psi(x) = 0 \tag{34}$$

For a *Weyl* or *chiral* representation built on identity matrices I_2 of dimension 2 :

$$\gamma^0 = \begin{pmatrix} 0 & I_2 \\ I_2 & 0 \end{pmatrix}, \qquad \gamma^i = \begin{pmatrix} 0 & \sigma^i \\ -\sigma^i & 0 \end{pmatrix}, \tag{35}$$

with $i = 1, 2, 3$ and *Pauli matrices* :

$$\sigma^1 = \begin{pmatrix} 0 & 1 \\ 1 & 0 \end{pmatrix}, \qquad \sigma^2 = \begin{pmatrix} 0 & -i \\ i & 0 \end{pmatrix}, \qquad \sigma^3 = \begin{pmatrix} 1 & 0 \\ 0 & -1 \end{pmatrix}. \tag{36}$$

Therefore the Lorentz-invariant Dirac-Lagrangian associated to it [97] is given by :

$$\mathcal{L}_D = \overline{\psi}(i\gamma^\mu \partial_\mu - m)\psi \tag{37}$$

For the adjoint spinor $\overline{\psi} \equiv \psi^\dagger \gamma^0$, with $\psi^\dagger$ the Hermitian-conjugate associated to ψ. Then one can show that $\overline{\psi}\gamma^\mu\psi$ is a 4-vector, and use the Euler-Lagrange equation of motion (31) for $\psi^\dagger$ to recover Dirac equation (34) for ψ, and likewise for ψ to recover the Hermitian-conjugate form of Dirac equation for $\overline{\psi}$:

$$-i\partial_\mu \overline{\psi}\gamma^\mu - m\overline{\psi} = 0 \tag{38}$$

Now our original intent was to derive a *quantum* theory of relativistic fields. In order to do this we must place certain conditions on the fields ψ themselves so that they obey the laws of quantum mechanics. Let's first consider the free Dirac field Lagrangian :

$$\mathcal{L} = \overline{\psi}(i\partial\!\!\!/ - m)\psi = \overline{\psi}(i\gamma^\mu \partial_\mu - m)\psi \tag{39}$$

with a Dirac Hamiltonian density :

$$\mathcal{H}_D = -i\gamma^0\gamma^i.\nabla + m\gamma^0 \tag{40}$$

Then let $u^s(\mathbf{p})e^{i\mathbf{p}.x}$ be the eigenfunctions of $\mathcal{H}_D$ with eigenvalues $E_\mathbf{p}$, and likewise $v^s(\mathbf{p})e^{-i\mathbf{p}.x}$ the eigenfunctions of $\mathcal{H}_D$ with eigenvalues $-E_\mathbf{p}$, both forming a complete set of eigenfunctions such that for any given $\mathbf{p}$ there are two eigenvectors u and two eigenvectors v corresponding to the four-dimensional square matrix $\mathcal{H}_D$. Then one can define the fields for spin polarization s such that :

$$\psi(x) = \int \frac{d^3p}{8\pi^3\sqrt{2E_\mathbf{p}}} \sum_s \left(a^s_\mathbf{p} u^s(p)e^{-ip.x} + b^{s\dagger}_\mathbf{p} v^s(p)e^{ip.x}\right) \tag{41}$$

$$\overline{\psi}(x) = \int \frac{d^3p}{8\pi^3\sqrt{2E_\mathbf{p}}} \sum_s \left(b^s_\mathbf{p} \overline{v}^s(p)e^{-ip.x} + a^{s\dagger}_\mathbf{p} \overline{u}^s(p)e^{ip.x}\right) \tag{42}$$

where $a^s_\mathbf{p}$ and $b^s_\mathbf{p}$, which respectively increase and lower the energy of a state, are called the *creation* and *annihilation* operators. Therefore one can quantize the fields $\psi(x)$ and $\overline{\psi}(x)$ above by requiring these operators to obey the following anticommutation laws :

$$\{a^r_\mathbf{p} a^{s\dagger}_\mathbf{q}\} = \{b^r_\mathbf{p} b^{s\dagger}_\mathbf{q}\} = 8\pi^3\delta^{(3)}(\mathbf{p}-\mathbf{q})\delta^{rs} \tag{43}$$

where all the other anticommutators vanish. We used the notation $\delta^{(3)}$ for the Dirac delta function in three dimensions, and δ^{rs} as the Kronecker symbol. Now we are in a measure to obtain a fully quantized picture, having performed the so-called *second quantization* by writing the equal-time anticommutation relations for the fields themselves :

$$\{\psi_a(x), \psi_b^\dagger(y)\} = \delta^{(3)}(x-y)\delta_{ab} \tag{44}$$

$$\{\psi_a(x), \psi_b(y)\} = \{\psi_a^\dagger(x), \psi_b^\dagger(y)\} = 0 \tag{45}$$

with a vacuum state $|0\rangle$ defined in such a way that $a_{\mathbf{p}}^s |0\rangle = b_{\mathbf{p}}^s |0\rangle = 0$ and a Hamiltonian given by :

$$H = \int \frac{d^3p}{8\pi^3} \sum_s E_{\mathbf{p}} \left(a_{\mathbf{p}}^{s\dagger} a_{\mathbf{p}}^s + b_{\mathbf{p}}^{s\dagger} b_{\mathbf{p}}^s \right) \tag{46}$$

As we saw with the free Klein-Gordon field, the classical equations of motion of a field are identical to the equation of the wave-equation describing its quanta. Therefore, historically this process is called *second quantization*, as a reference to the fact that quantizing fields may seem like quantizing a theory which is already quantized.

The Dirac equation (34) is fundamental to the quantum theory of fields. As we saw, it is Lorentz-invariant and hence special relativistic, and also fully quantized through the anticommutation expressions (45) above.

As both $a_{\mathbf{p}}^{s\dagger}$ and $b_{\mathbf{p}}^{s\dagger}$ create particles of energy $E_{\mathbf{p}}$ and momentum $\mathbf{p}$, we refer to them respectively as fermions and antifermions. Historically this is important, as the Dirac equation in the quantized field description above was the first prediction of the existence of antimatter. One can predict the half-spin value of the particle fields in the Dirac equation using the *Noether's theorem*, which we will now see. A given solution to the Dirac equation is also a solution to the Klein–Gordon equation, albeit the converse is not true.

2. Noether's theorem and the stress-energy tensor

The Lagrangian of equation (30) under any symmetry that is continuous will give rise to a *conserved current* $j^\mu(x)$ such that the equations of motion give :

$$\partial_\mu j^\mu(x) = \frac{\partial j^0}{\partial t} + \nabla \cdot \mathbf{j} = 0 \tag{47}$$

This is called the *Noether's theorem* and implies in turn a *local conservation of charge* Q such that :

$$Q = \int_{\mathbb{R}^3} d^3x j^0 \tag{48}$$

By saying that the charge conservation is a *local* property, one says that by taking a given volume V as a subset of $\mathbb{R}^3$, it is possible to show after integration that any charge leaving the volume V implies a flow of the current $\mathbf{j}$ out of the volume. This is a general property of local conservation of charge that applies to any local field theory [97].

To really understand this property of local charge conservation, let's consider an infinitesimal continuous transformation of the field ψ :

$$\psi(x) \to \psi'(x) = \psi(x) + \epsilon\Delta\psi(x) \tag{49}$$

for an infinitesimal parameter ϵ and a given deformation of the field $\Delta\psi(x)$. Of course such a transformation is symmetric if it leaves the equation of motion (31) invariant. This implies that the action is invariant to this transformation, and hence also the Lagrangian, up to a 4-divergence $\mathcal{J}^\mu$:

$$\mathcal{L}(x) \to \mathcal{L}(x) + \epsilon\partial_\mu\mathcal{J}^\mu(x) \tag{50}$$

We can use this together with equation (31) in order to compute $\Delta\mathcal{L}$ and obtain Noether's theorem from equation (47), with $j^\mu(x)$ now given by :

$$j^\mu(x) = \frac{\partial\mathcal{L}}{\partial(\partial_\mu\psi)}\Delta\psi - \mathcal{J}^\mu \tag{51}$$

This said, let's take an important application example of Noether's theorem, which we will see is at the foundation of the equation describing the Casimir force as a pressure and of the near-field radiative heat transfer as a flux. First let's recall the fact that conservation of momentum and energy comes in classical mechanics from the invariance properties of spatial and time translations respectively. Now in field theory, let's consider the respective infinitesimal translation of the fields and Lagrangian such that :

$$x^\mu \to x^\mu - \epsilon^\mu \qquad \Rightarrow \qquad \psi(x) \to \psi(x+\epsilon) = \psi(x) + \epsilon^\mu\partial_\mu\psi(x) \tag{52}$$

$$\tag{53}$$

and

$$\mathcal{L} \to \mathcal{L} + \epsilon^\mu\partial_\mu\mathcal{L} = \mathcal{L} + \epsilon^\nu\partial_\mu(\delta^\mu_\nu\mathcal{L}) \tag{54}$$

Now if compare equation (50) with (54) above, we can readily check that $\mathcal{J}^\mu$ does not vanish and by applying Noether's theorem (47), we eventually find four separately conserved currents called the *stress-energy tensor* or *energy-momentum tensor* of the field ψ :

$$T^\mu_\nu \equiv \frac{\partial\mathcal{L}}{\partial(\partial_\mu\psi)}\partial_\nu\psi - \mathcal{L}\delta^\mu_\nu = (j^\mu_\nu) \tag{55}$$

Hence the stress-energy tensor satisfies the conservation law $\delta_\mu T^\mu_\nu$. From this is derived another quantity that will be crucial to our future mathematical construction of the Casimir force as a pressure : the conserved charge in this regime associated with time translation is no other than the Hamiltonian, and its related Hamiltonian density gives the zeroth components of the stress-energy tensor T^{00} through the total energy E of the field configuration :

$$E = \int T^{00} d^3x \tag{56}$$

Also, the total momentum of the field configuration is given by the conserved charges under spatial translation :

$$P^i = \int T^{0i} d^3x = -\int \pi \partial_i \psi d^3x \tag{57}$$

Together, equations (56) and (57) are the four conserved quantities mentioned above that fully define the stress-energy tensor.

3. Green's functions and field interactions

When working with quantum fields, we often use a type of functions drawn from many-body theory called *Green's functions*, which can give us an idea of the way quantum field operators are related to one another. For this reason, Green's functions are also often called *correlators* or *correlation functions*. Most notably, they give us in quantum field theory the possibility to estimate the correlation between the annihilation and creation operators of equation (43).

Green's functions used in field theory are originally related to those used in mathematics, which are used to solve inhomogeneous differential equations —albeit technically only the two-points Green's functions from physics are related to the latter.

Following [98], let's consider a given differential equation applied to a function F with variable z, with boundary conditions such as :

$$\hat{L}(z)F(z) = S(z) \quad \text{for} \quad \hat{L}(z) \equiv A_n \frac{d^n}{dz^n} + A_{n-1}\frac{d^{n-1}}{dz^{n-1}} + \ldots + A_0 \tag{58}$$

for a *source term* $S(z)$. We can then define a Green's function $G(z, z')$ for that differential equation by replacing the source term by $\delta(z - z')$, so that :

$$\hat{L}(z)G(z, z') = \delta(z - z') \tag{59}$$

If we can solve this equation for that Green's function, then we can derive the solution of equation (58) from :

$$f(z) = \int dz' G(z, z') S(z') \tag{60}$$

This can be seen by putting equations (58) and (59) together :

$$\hat{L}(z) f(z) = \int dz' \hat{L}(z) G(z, z') S(z') = \int dz' \delta(z - z') S(z') = S(z) \tag{61}$$

We can then solve equation (59) for a Green's function $G(z - z')$ by making a Fourier transformation :

$$L(ik)\widetilde{G}(k) = 1 \tag{62}$$

which has the solution :

$$\widetilde{G}(k) = \frac{1}{L(ik)} \tag{63}$$

However this is only a particular solution of (59), and the boundary conditions must be satisfied either by adding to equation (63) a solution of the homogeneous equation, or by integrating around the poles in the Fourier transform $\widetilde{G}(k)$ of $G(z - z')$. By inverting the Fourier transform, we obtain from equation (63) :

$$G(z - z') = \int \frac{dk}{2\pi} \frac{e^{ik(z-z')}}{L(ik)} \tag{64}$$

For the operator $\hat{L}(z)$ defined in equation (58), $L(ik)$ is a polynomial of nth order and the integrand in equation (64) contains n poles in the complex plane. Therefore we must use contour integration to evaluate this integral.

As a first example, we can apply this to the solution of Poisson's equation $\bigtriangledown^2 \phi(\mathbf{x}) = -\rho(\mathbf{x})/\epsilon_0$ for $\mathbf{x} = (x, y, z)$ so that the Green's function associated with the unit charge density at $\mathbf{x}' = (x', y', z')$ is given by :

$$\bigtriangledown^2 G(\mathbf{x}, \mathbf{x}') = -\delta(\mathbf{x} - \mathbf{x}')/\epsilon_0 \tag{65}$$

We look for a solution $G(\mathbf{x} - \mathbf{x}')$ by operating a Fourier transform, which can eventually be written $G(\mathbf{x}) = (4\pi r \epsilon_0)^{-1}$. Therefore we find :

$$\phi(\mathbf{x}) = \frac{1}{4\pi r \epsilon_0} \int d^3\mathbf{x}' \frac{\rho(\mathbf{x}')}{|\mathbf{x} - \mathbf{x}'|} \tag{66}$$

As a second example, we can apply our formalism to the solution of d'Alembert's equation $\frac{1}{c^2} \frac{\partial^2 \phi}{\partial t^2} - \bigtriangledown^2 \phi = 0$, so that the Green's function associated with the wave-equation for electromagnetic fields in vacuum is given by :

$$\left(\frac{1}{c^2}\frac{\partial^2}{\partial t^2} - \bigtriangledown^2\right) G(t-t', \mathbf{x}-\mathbf{x}') = \mu_0 \delta(t-t')\delta^3(\mathbf{x}-\mathbf{x}') \tag{67}$$

We look for a solution $G(t, \mathbf{x})$ by operating a Fourier transform, finding its solution, and inverting the Fourier transform, so that we eventually obtain $G(\mathbf{x} = (4\pi r \epsilon_0)^{-1}$. After some algebra [98, 99], we find :

$$G(t, \mathbf{x}) = -\mu_0 \int \frac{d\omega d^3\mathbf{k} e^{-i(\omega t - \mathbf{k}\cdot\mathbf{x})}}{(2\pi)^4(\omega^2/c^2 - |\mathbf{k}|^2)} \tag{68}$$

One can see that the integrand of this equation has two poles at $\omega = \pm kc$, if we write :

$$\frac{1}{\omega^2/c^2 - |\mathbf{k}|^2} = \frac{c}{2k}\left(\frac{1}{\omega - ck} - \frac{1}{\omega + ck}\right) \tag{69}$$

This can be overcome by a contour integration if we add an infinitesimal imaginary part $+i\theta$ to ω (we will see in section VI A 5 that this amounts to imposing the analyticity condition of *causality*). Now the step function $H(t) = [1 \quad \text{for} \quad t > 0, \quad 0 \quad \text{for} \quad t < 0]$ having a definite Fourier representation, we can find :

$$\int_{\mathbb{R}} \frac{d\omega}{2\pi} \frac{e^{-i\omega t}}{\omega \pm kc + i\theta} = -iH(t)e^{\pm ikct} \tag{70}$$

Now we can substitute equations (69-70) into equation (68), so that we eventually obtain the so-called *retarded Green's function* :

$$G_r(t, \mathbf{x}) = \frac{\mu_0 \delta(t - r/c)}{4r\pi} \tag{71}$$

Likewise, we can obtain the *advanced Green's function* by replacing ω with $\omega - i\theta$:

$$G_a(t, \mathbf{x}) = \frac{\mu_0 \delta(t + r/c)}{4r\pi} \tag{72}$$

The Green's function $G(t-t', \mathbf{x}-\mathbf{x}')$ describes the field at $(t, \mathbf{x})$ associated with the source at $(t', \mathbf{x}')$. The δ-function in equation (71) implies that t' is equal to the so-called *retarded time* t_r :

$$t_r \equiv t - \frac{|\mathbf{x} - \mathbf{x}'|}{c} \tag{73}$$

This means that the field at $(t, \mathbf{x})$ comes from the source at $(t', \mathbf{x}')$ where time t' is earlier than time t through the light propagation time from $\mathbf{x}$ to $\mathbf{x}'$. One can also apply this reasoning in a similar way to the advanced Green's function from equation (72).

Now we can describe the electromagnetic field using the *temporal gauge*, which is by setting $\phi = 0$ so that there is no scalar field. In the temporal gauge, the electric and magnetic vectors $\mathbf{E}$ and $\mathbf{B}$ can be described by the single vector $\mathbf{A}$. Then we can write a convenient reformulation of Maxwell's equations and write the wave equation such as :

$$\frac{\omega^2}{c^2}\mathbf{A}(\omega, \mathbf{k}) + \mathbf{k} \times [\mathbf{k} \times \mathbf{A}(\omega, \mathbf{k})] = -\mu_0 \mathbf{J}(\omega, \mathbf{k}) \tag{74}$$

for $\mathbf{E}(\omega, \mathbf{k}) = i\omega\mathbf{A}(\omega, \mathbf{k})$. Of course, it is not always convenient to use the temporal gauge, such as for example in the case of static uniform fields. The Green's function corresponding to the equation (74) above differs from the Green's functions associated with the Poisson and d'Alembert equations in the sense that it is here a tensor $\widetilde{G}_{ij}(\omega, \mathbf{k})$, and equation (74) must be re-written in tensorial form :

$$\left[\left(\frac{\omega^2}{c^2} - |\mathbf{k}|^2\right)\delta_{ij} + k_i k_j\right]\widetilde{G}_{jm}(\omega, \mathbf{k}) = -\mu_0 \delta_{im} \tag{75}$$

Eventually one can find :

$$\widetilde{G}_{ij}(\omega, \mathbf{k}) = -\frac{\mu_0}{\omega^2/c^2 - |\mathbf{k}|^2}\left(\delta_{ij} - \frac{c^2 k_i k_j}{\omega^2}\right) \tag{76}$$

Notice also that one can obtain the associated Green's function $G_{ij}(t, \mathbf{x})$ also through an inverse Fourier transform, but that it comes in an operator form instead of a function, and is rarely used. Now that the Green's function is obtained, we can solve equation (74) by separating the longitudinal and transverse parts, which are respectively given by :

$$\mathbf{k} \cdot \mathbf{A}(\omega, \mathbf{k}) = -\frac{\mu_0 c^2}{\omega^2}\mathbf{k} \cdot \mathbf{J}(\omega, \mathbf{k}) \tag{77}$$

$$\mathbf{k} \times \mathbf{A}(\omega, \mathbf{k}) = -\frac{\mu_0}{\omega^2/c^2 - |\mathbf{k}|^2}\mathbf{k} \times \mathbf{J}(\omega, \mathbf{k}) \tag{78}$$

Notice the singularities for $\omega^2/c^2 - |\mathbf{k}|^2 = 0$, which exist only for the transverse part of the field. The physical explanation for this is through emission of electromagnetic radiation : electromagnetic waves are transverse $\mathbf{k} \cdot \mathbf{A} = 0$, and obey the dispersion relation $\omega^2 = |\mathbf{k}|^2 c^2$, so that they correspond to the singularities of equation (78). The longitudinal part however plays no role in the emission of radiation and hence has no singularity at $\omega^2/c^2 - |\mathbf{k}|^2 = 0$.

Let's take as an example often used in radiative heat transfer the case of real-time *dyadic* or two-point Green functions with $n = 1$, which can be written in terms of the retarded G^{R} and advanced G^{A} Green functions, respectively :

$$G_R(\mathbf{x}t|\mathbf{x}'t') = i\langle[\psi(\mathbf{x},t),\overline{\psi}(\mathbf{x}',t')]\rangle\theta(t-t') \tag{79}$$

$$G_A(\mathbf{x}t|\mathbf{x}'t') = -i\langle[\psi(\mathbf{x},t),\overline{\psi}(\mathbf{x}',t')]\rangle\theta(t'-t) \tag{80}$$

where θ is the Theta function. This will be used as an application to our derivation of the near-field radiative heat transfer between nanogratings in section VI C 2.

We now define the time-ordered function in real time :

$$G_T(\mathbf{x}t|\mathbf{x}'t') = \int_{\mathbf{k}} d\mathbf{k} \int \frac{\mathrm{d}\omega}{2\pi} G_{\mathrm{T}}(\mathbf{k},\omega)\mathrm{e}^{\mathrm{i}\mathbf{k}\cdot(\mathbf{x}-\mathbf{x}')-\mathrm{i}\omega(t-t')} \tag{81}$$

Then the retarded and advanced Green functions can be related to the time-ordered Green function above, with wave-vector $\mathbf{k}$ and frequency ω by :

$$G_T(\mathbf{k},\omega) = [1+\chi n(\omega)]G_R(\mathbf{k},\omega) - \chi n(\omega)G_A(\mathbf{k},\omega) \tag{82}$$

where $n(x) = 1/(\mathrm{e}^{-\beta x} - \chi)$ is the Bose-Einstein or Fermi-Dirac distribution function, knowing that $\chi = 1$ for bosons and $\chi = -1$ for fermions, and where $\beta = \frac{\mu-\epsilon}{k_B T}$ for a particle chemical potential μ and energy ϵ. One should note that in the framework of radiative heat transfer, "particles" in these equations can be replaced with plates or any thermodynamical systems.

4. QED equation of motion and quantization

As we saw in the previous sections, quantum electrodynamics (QED) arose from Dirac's description of radiation and matter interaction through a correct formulation of relativistic quantum fields representing on one side the electromagnetic field as a set of harmonic oscillators, and on the other side the particles through the creation and annihilation operators [100].

The success of this theory was such that for a while Dirac's theory was believed to describe about any type of interaction between an electromagnetic field and charged particles. Nevertheless by the mid-forties, Willis Lamb

observed what is now known as the *Lamb shift* : a small energy difference between the two energy levels ${}^2s_{1/2}$ and ${}^2p_{1/2}$ of the Hydrogen atom, which Dirac's theory was not able to predict, since in its basic computations, quantum electrodynamics relied on a perturbative approach to determine the amplitudes, and the perturbation was correct up to the first order only.

But in 1947, Hans Bethe had an intuition, now called *renormalization*, which eventually allowed the perturbative approach related to quantum electrodynamics to be consistent up to any order of perturbation by reframing the infinite integrals appearing in the perturbation theory. This was later completed and optimized by Freeman Dyson, Sin-Itiro Tomonaga, Julian Schwinger, and especially Richard Feynman. For more information on the subject of renormalization, which was successfully applied to other field theories describing interactions others than electromagnetism —most notably the strong and weak interactions, as well as the electroweak interaction— we refer the reader to [97].

As for now, we can consider the electromagnetic field interacting with a half-spin charged particle as the real part of the following Lagrangian, known as the QED Lagrangian [101] :

$$\mathcal{L}_{QED} = \overline{\psi}(i\gamma^\mu D_\mu - m)\psi - \frac{1}{4}F_{\mu\nu}F^{\mu\nu} = i\overline{\psi}\gamma^\mu\partial_\mu\psi - e\overline{\psi}\gamma_\mu(A^\mu + B^\mu)\psi - m\overline{\psi}\psi - \frac{1}{4}F_{\mu\nu}F^{\mu\nu} \tag{83}$$

for $D_\mu \equiv \partial_\mu + ieA_\mu + ieB_\mu$ being the gauge covariant derivative associated with the coupling constant or electric charge of the particles e, A^μ the covariant four-potential of the electromagnetic field generated by the electron itself, and B_μ the field generated by the external source. Also, we have denoted $F_{\mu\nu} = \partial_\mu A_\nu - \partial_\nu A_\mu$ and $F^{\mu\nu}$ the covariant and contravariant components of the electromagnetic field tensor, respectively. In an inertial frame, these are given in natural units for two electric and magnetic fields E and H by :

$$F_{\mu\nu} = \begin{bmatrix} 0 & E_x & E_y & E_z \\ -E_x & 0 & -H_z & H_y \\ -E_y & H_z & 0 & -H_x \\ -E_z & -H_y & H_x & 0 \end{bmatrix} \qquad F^{\mu\nu} = \begin{bmatrix} 0 & -E_x & -E_y & -E_z \\ E_x & 0 & -H_z & H_y \\ E_y & H_z & 0 & -H_x \\ E_z & -H_y & H_x & 0 \end{bmatrix} \tag{84}$$

Replacing expression (83) in the Euler-Lagrange equation for the field (31), one can thus recover the field equations of motions :

$$i\gamma^\mu\partial_\mu\psi - m\psi = e\gamma_\mu(A^\mu + B^\mu)\psi \tag{85}$$

where the l.h.s of the equation corresponds to Dirac's equation (34), and the r.h.s describes the interaction with the electromagnetic field.

Now if we apply in a similar way the Euler-Lagrange equation to the quantum electrodynamic Lagrangian (83), but this time as applied to the four-potential A^μ of the field, we can obtain :

$$\partial_\nu F^{\nu\mu} = e\overline{\psi}\gamma^\mu\psi \tag{86}$$

This said, we are now in a position to derive our quantum field theory to the electromagnetic field in free space, based on our quantum field theory formalism in a step-by-step approach. With these notations, Maxwell's equations can be written in tensorial form :

$$\mu_0 \mathcal{J}^\mu = \partial_\nu F^{\mu\nu} \tag{87}$$

$$\partial_\xi F_{\mu\nu} + \partial_\nu F_{\xi\mu} + \partial_\mu F_{\nu\xi} = 0 \tag{88}$$

Shifting from a natural units system to SI units, these Maxwell's equations can be written in the classical description of the field as the following :

$$\nabla \times \mathbf{E} = -\frac{\partial \mathbf{B}}{\partial t} \qquad \text{(Faraday's law for magnetism)} \tag{89}$$

$$\nabla \times \mathbf{H} = \frac{\partial \mathbf{D}}{\partial t} \qquad \text{(Ampère's circuital law)} \tag{90}$$

$$\nabla \cdot \mathbf{D} = 0 \qquad \text{(Gauss's law)} \tag{91}$$

$$\nabla \cdot \mathbf{B} = 0 \qquad \text{(Gauss's law for magnetism)} \tag{92}$$

for electric and magnetic field vectors $\mathbf{E}$ and $\mathbf{H}$ respectively, and displacement and inductive vectors $\mathbf{D}$ and $\mathbf{B}$ respectively. For the free space permittivity ϵ_0 and permeability μ_0 such that $\epsilon_0\mu_0 = 1/c^2$, we have :

$$\mathbf{D} = \epsilon_0 \mathbf{E} \tag{93}$$

$$\mathbf{B} = \mu_0 \mathbf{H} \tag{94}$$

Here, equations (90, 91) are equivalent to the tensorial equation (87), and equations (89, 92) are equivalent to the tensorial equation (88). One can then find through the elementary expressions above :

$$\nabla^2 \mathbf{E} - \frac{1}{c^2}\frac{\partial^2 \mathbf{E}}{\partial t^2} = 0 \tag{95}$$

Following [102], we now consider the field confined within a cavity of length L, and with $\mathbf{E}$ being linearly polarized in the x-direction. We can write the electric and non-vanishing magnetic fields as the sums of $j = 1, 2, 3...$ normal modes of amplitude q_j within the cavity of eigenfrequency $\nu_j = j\pi c/L$ such that for $k_j = j\pi/L$ we have :

$$E_x(z,t) = \sum_j A_j q_j(t) sin(k_j z) \tag{96}$$

$$H_y = \sum_j A_j \frac{\dot{q}_j \epsilon_0}{k_j} cos(k_j z) \tag{97}$$

for a cavity volume V defined as the product of its length L and transverse area A, so that we can define :

$$A_j = \sqrt{\frac{2m_j\nu_j^2}{\epsilon_0 V}} \tag{98}$$

where the elements m_j have been included so as to show the analogy between this dynamical problem of single modes and the case of harmonic oscillators of mass m_j. One can then define the classical Hamiltonian of this field as :

$$\mathcal{H} = \frac{1}{2}\int_V d\tau \left(\epsilon_0 E_x^2 + \mu_0 H_y^2\right) = \frac{1}{2}\sum_j \left(m_j\nu_j^2 q_j^2 + \frac{p_j^2}{m_j}\right) \tag{99}$$

where one can also write the canonical momentum of the jth mode as $p_j = m_j\dot{q}_j$. In other words, each mode of the radiation field is the same dynamical equivalent to a mechanical harmonic oscillator, with the sum of all of the modes' independent energies being expressed as the Hamiltonian above.

Now we can quantize this field by recognizing that the position q_j and momentum operators p_j obey the following commutation relations :

$$[q_j, p_{j'}] = i\hbar\delta_{jj'} \tag{100}$$

$$[q_j, q_{j'}] = [p_j, p_{j'}] = 0 \tag{101}$$

We can switch to a_j and b_j, the annihilation and creation operators respectively, by setting :

$$a_j = e^{i\nu_j t}\frac{1}{\sqrt{2m_j\hbar\nu_j}}\left(m_j\nu_j q_j + ip_j\right) \tag{102}$$

$$b_j = e^{-i\nu_j t}\frac{1}{\sqrt{2m_j\hbar\nu_j}}\left(m_j\nu_j q_j - ip_j\right) \tag{103}$$

so that the Hamiltonian becomes simply :

$$\mathcal{H} = \hbar \sum_j \nu_j \left(b_j a_j + \frac{1}{2} \right) \tag{104}$$

and the commutation relations between the annihilation and creation operators follow from the commutation relations (100) and (101) :

$$[a_j, b_{j'}] = \delta_{jj'} \tag{105}$$

$$[a_j, a_{j'}] = [b_j, b_{j'}] = 0 \tag{106}$$

so that we can rewrite the electric and magnetic fields such as :

$$E_x(z,t) = \sum_j \mathcal{E}_j \left(a_j e^{-i\nu_j t} + b_j e^{i\nu_j t} \right) \sin k_j z \tag{107}$$

$$H_y(z,t) = -i\epsilon_0 c \sum_j \mathcal{E}_j \left(a_j e^{-i\nu_j t} - b_j e^{i\nu_j t} \right) \cos k_j z \tag{108}$$

for $\mathcal{E}_j = \sqrt{\hbar\nu_j/\epsilon_0 V}$. Thus we have quantized the electromagnetic field within a finite one-dimensional cavity of volume V. Nevertheless a full theory in free space still needs to be derived. For this, let's consider that the field is within a cubic cavity of very large (but finite) side L. We will switch from standing-wave to running-wave solutions, and impose period boundary conditions such that :

$$k_x = \frac{2\pi n_x}{L}, \qquad k_y = \frac{2\pi n_y}{L}, \qquad k_z = \frac{2\pi n_z}{L} \tag{109}$$

for n_x, n_y, n_z being integers, so that the set n_x, n_y, n_z fully defines a given electromagnetic mode by its wave-vector $\mathbf{k} = k_x, k_y, k_z$ with the condition imposed by Gauss's law (91), that this wave-vector is perpendicular to the unit polarization vector $\epsilon_{\mathbf{k}}$, so that the fields are purely transverse :

$$\mathbf{k} \cdot \epsilon_k = 0 \tag{110}$$

This implies that for each wave vector $\mathbf{k}$ there are two independent directions of polarization for ϵ_k. We shall denote these two polarizations ϕ by s and p, respectively called *transverse electric* (or TE) and *transverse magnetic* (or TM).

In the free space case, one can also expect the summation to occur over these modes, defined by their respective wave-vectors, within the large but finite cubic cavity of side L. Therefore this summation over modes also has to

contain a summation over the possible polarizations. One can then switch from a discrete summation over these modes to a continuous distribution by integrating :

$$\sum_{\mathbf{k}} \quad \longrightarrow \quad \sum_{\phi=s,p} \frac{L^3}{8\pi^3} \int d^3k = 2 \cdot \frac{L^3}{8\pi^3} \int d^3k \tag{111}$$

Then we can write the quantized electric and magnetic fields $\mathbf{E}(\mathbf{r},t) = \mathbf{E}^{(-)}(\mathbf{r},t) + \mathbf{E}^{(+)}(\mathbf{r},t)$ and $\mathbf{H}(\mathbf{r},t) = \mathbf{H}^{(-)}(\mathbf{r},t) + \mathbf{H}^{(+)}(\mathbf{r},t)$ such that :

$$\mathbf{E}(\mathbf{r},t) = \left[\sum_{\phi=s,p} \sum_{\mathbf{k}} \epsilon_k(\phi) \mathcal{E}_{\mathbf{k}} a_{\mathbf{k}}(\phi) e^{-i\nu_k t + i\mathbf{k}\cdot\mathbf{r}} \right] + \left[\sum_{\phi=s,p} \sum_{\mathbf{k}} \epsilon_k(\phi) \mathcal{E}_{\mathbf{k}} b_{\mathbf{k}}(\phi) e^{+i\nu_k t - i\mathbf{k}\cdot\mathbf{r}} \right] \tag{112}$$

$$\mathbf{H}(\mathbf{r},t) = \left[\sum_{\phi=s,p} \sum_{\mathbf{k}} \frac{\mathbf{k} \times \epsilon_k(\phi)}{\mu_0 \nu_k} \mathcal{E}_{\mathbf{k}} a_{\mathbf{k}}(\phi) e^{-i\nu_k t + i\mathbf{k}\cdot\mathbf{r}} \right] + \left[\sum_{\phi=s,p} \sum_{\mathbf{k}} \frac{\mathbf{k} \times \epsilon_k(\phi)}{\mu_0 \nu_k} \mathcal{E}_{\mathbf{k}} b_{\mathbf{k}}(\phi) e^{+i\nu_k t - i\mathbf{k}\cdot\mathbf{r}} \right] \tag{113}$$

where we have used the annihilation and creation operators $a_{\mathbf{k}}$ and $b_{\mathbf{k}}$ respectively, which satisfy the commutation relation $[a_{\mathbf{k}}, b_{\mathbf{k}}] = 1$. Also, we have used $\mathcal{E}_{\mathbf{k}} = \sqrt{\hbar\nu_k / 2\epsilon_0 V}$.

Notice that by writing the expressions of the electric and magnetic fields in two parts, we conveniently have $\mathbf{E}^{(-)}(\mathbf{r},t)$ and $\mathbf{H}^{(-)}(\mathbf{r},t)$ containing only annihilation operators, and their respective Hermitian conjugates $\mathbf{E}^{(+)}(\mathbf{r},t)$ and $\mathbf{H}^{(+)}(\mathbf{r},t)$ containing only creation operators. These respectively represent the positive and negative frequency parts of the given field operator E or H.

Nevertheless, equations above are complete only provided we supply a sum on the polarizations s and p, because certain components of the electric and magnetic fields do not commute and thus cannot be measured at the same time. To show this, we give the commutation relations for indices $i, j, k \in \{x, y, z\}$ based on [102] :

$$[E_i(\mathbf{x},t), H_j(\mathbf{x}',t)] = -i\hbar c^2 \frac{\partial}{\partial k} \delta^{(3)}(\mathbf{x} - \mathbf{x}') \tag{114}$$

$$[E_i(\mathbf{x},t), H_i(\mathbf{x}',t)] = 0 \tag{115}$$

What can be understood from these is that the perpendicular components of E and H cannot be measured at the same time, whereas the parallel components can.

Let's now consider a single mode of frequency ν with annihilation and creation operators a and b, respectively. We will now study a given energy eigenstate $|n\rangle$ corresponding to an energy of eigenvalue E_n given by equation (104) :

$$\mathcal{H}|n\rangle = \hbar\nu \left(ba + \frac{1}{2} \right) |n\rangle = E_n|n\rangle \tag{116}$$

Our goal [103] is to successively apply the annihilation operator a to that eigenstate $|n\rangle$ by virtue of equation (105), and arrive to the quantum definition of the vacuum state $|0\rangle$. We get :

$$\mathcal{H}a|n\rangle = (E_n - \hbar\nu)\, a|n\rangle \tag{117}$$

Then for a given normalization constant α_n determined by $\langle n-1|n-1\rangle = 1$, the state

$$|n-1\rangle = \frac{a}{\alpha_n}|n\rangle \tag{118}$$

is an energy eigenstate as well, with lowered energy eigenvalue $E_{n-1} = E_n - \hbar\nu$. We are now in a position to determine our lowest state energy E_0 and thus the quantum vacuum state by repeating this simple procedure n times, each time lowering the energy eigenvalue by $\hbar\nu$. We thus find :

$$\mathcal{H}a|0\rangle = (E_0 - \hbar\nu)\, a|0\rangle \tag{119}$$

Since energies below E_0 cannot exist for the oscillator, $(E_0 - \hbar\nu)$ cannot exist, and we postulate the existence of the vacuum state already encountered in the free field theory [104, 104, 105] of section V B 1 :

$$a|0\rangle = 0 \tag{120}$$

Plugging this back into the Hamiltonian, we get the *zero-point energy*, or *vacuum energy* E_0 :

$$\mathcal{H}|0\rangle = \frac{1}{2}\hbar\nu|0\rangle = E_0|0\rangle \qquad \Longrightarrow \qquad E_0 = \frac{1}{2}\hbar\nu \tag{121}$$

and therefore we find the following very important result, which correspond to the presence of n *quanta* of energy $\hbar\nu$ (or photons) :

$$E_n = \left(n + \frac{1}{2} \right) \hbar\nu \tag{122}$$

Now from equation (116) we can find $ba|n\rangle = n|n\rangle$ so that $|n\rangle$ is also an eigenstate of the so-called *particle number operator*, which is used to count the number of particles :

$$n = ba \tag{123}$$

This now allows us to determine the normalization constant α_n :

$$\langle n-1|n-1\rangle = \frac{n}{|\alpha_n|^2} = 1 \qquad \Longrightarrow \qquad \alpha_n = \sqrt{n} \tag{124}$$

Hence we can eventually find for a (and similarly for b) :

$$a|n\rangle = \sqrt{n}|n-1\rangle \tag{125}$$

$$b|n\rangle = \sqrt{n+1}|n+1\rangle \tag{126}$$

The latter equation can be repeated to give the *Fock states*, or *photon number states* :

$$|n\rangle = \frac{b^n}{\sqrt{n!}}|0\rangle \tag{127}$$

which form a complete set $\sum_{n=0}^{\infty} |n\rangle\langle n| = 1$.

Equations (122) and (127) are two important results of QED. They predict, as we already saw in Section V A that energy eigenvalues are discrete, in contradiction with the classical description of electromagnetism, where energy can take on any real value. Of importance to the formulation of the Casimir energy, they predict a residual energy of $\hbar\nu/2$ corresponding to E_0, called the *zero-point energy* or *vacuum energy.* In other words, the vacuum itself has a non-zero energy, as shown in FIG. 9.

Now if we consider the electric field operator from equation (112), but this time applied to a linearly polarized single-mode, we can show that the expectation value and hence variance are respectively given by :

$$\langle n|E|n\rangle = 0 \tag{128}$$

$$\langle n|E^2|n\rangle = 2|\mathcal{E}|^2\left(n+\frac{1}{2}\right) \tag{129}$$

This is an important property of the number state $|n\rangle$, because it means that there are fluctuations in the field around its zero mean $\langle n|E|n\rangle$, *including for the vacuum state* $|0\rangle$.

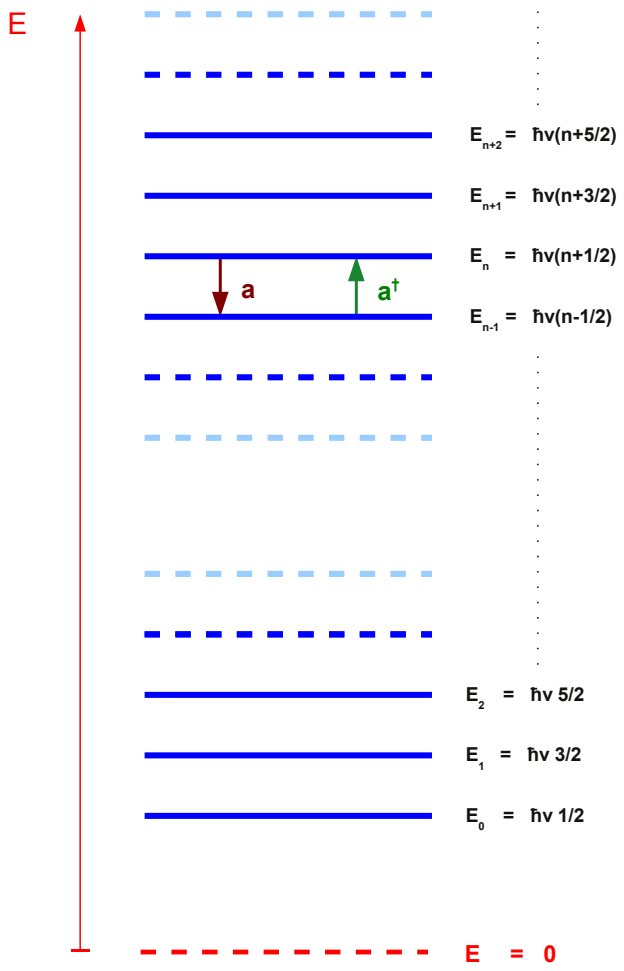

FIG. 9: Energy levels of the quantum harmonic oscillators describing the electromagnetic field, where each annihilation operator a lowers the energy by a quantum of energy $\hbar\nu$ (by repetition, all the way to the zero-point energy, which is the non-zero vacuum energy), and where each creation operator b increases the energy by a quantum of energy $\hbar\nu$. For this reason the annihilation and creation operators are collectively called the ladder operators

Another way to express it, is that the particle number operator n from equation (123) does not in general commute with the Hamiltonian of the system, and therefore following the general quantum description, the number of particles in a given spatial volume have fluctuations.

We conclude by generalizing our former single-mode field study to multi-mode fields, by rewriting our Hamiltonian of equation (104) such that :

$$\mathcal{H} = \sum_{\mathbf{k}} \mathcal{H}_{\mathbf{k}} = \sum_{\mathbf{k}} \hbar\nu_{\mathbf{k}} \left(b_{\mathbf{k}} a_{\mathbf{k}} + \frac{1}{2} \right) \tag{130}$$

with an energy eigenstate $|n_{\mathbf{k}}\rangle$ associated to that Hamiltonian :

$$\mathcal{H}_{\mathbf{k}} |n_{\mathbf{k}}\rangle = \hbar\nu_{\mathbf{k}} \left(n_{\mathbf{k}} + \frac{1}{2} \right) |n_{\mathbf{k}}\rangle \tag{131}$$

Therefore, the general eigenstate of the Hamiltonian $\mathcal{H}_{\mathbf{k}}$ from equation (130) can have in its first mode $n_{\mathbf{k};1}$ photons, in its second mode $n_{\mathbf{k};2}$ photons, in its third mode $n_{\mathbf{k};3}$ photons, etc... and can therefore be written as $|\{n_{\mathbf{k}}\}\rangle \equiv |n_{\mathbf{k};1}, n_{\mathbf{k};2}, n_{\mathbf{k};3}, ...\rangle$.

6. Conclusion

So we have seen how, based on Dirac's attempt to describe the electromagnetic field in a quantum formalism and his subsequent derivation of the Dirac equation (34), we found that these fields were Lorentz-invariant, and could be quantized by the process of second-quantization. We saw how this was done through the introduction of annihilation and creation operators and their associated anti-commutation relations (43), so that we could likewise require the fields to also obey the anti-commutation relations (45) and (46). We also saw the important consequence in the apparition of these operators as their prediction through Dirac's equation of antimatter.

Based on the principle of least action, we derived Noether's theorem in equation (47) which gave the separate conservation law of four currents : one as energy in equation (56), and three as momenta in equation (57). These four currents gave the formal definition of the stress-energy tensor in equation (55), which is at the foundation of the derivation of the Casimir energy and of the near-field heat transfer.

We continued with the definition of Green's functions to describe the correlation between two points of a given field in space, and we then derived the full theory of QED by considering modes as harmonic oscillators. Using second quantization onto QED, we derived the annihilation and creation operators commutation relations (105) and (106) for these modes, found the expression of the particle number operator in equation (123), and the Fock states in equation (127). Most importantly, we saw the QED prediction of a non-zero energy for the vacuum state in equation (121). Form this, we also derived a zero expectation value and non-zero variance of the vacuum state, thereby establishing the existence of vacuum fluctuations in equations (128) and (129).

VI. THEORY : SCATTERING THEORY APPLIED TO CASIMIR AND NEAR-FIELD HEAT TRANSFER

A. Casimir effect in the plane-plane geometries

1. *Complex permittivity and fitting models*

From now on we will consider the magnetic permeability to be equal to its vacuum value ($\mu = 1$). Each medium is characterized by an index of refraction $n(\omega)$ or by a permittivity $\epsilon(\omega) = n^2(\omega)$, which are both frequency-dependent. Unlike vacuum, the optical response of usual materials depends on the wave frequency, due to the fact that the polarization of those materials does not respond instantaneously to the incident wave. Therefore there is a *principle of causality*, appearing mathematically in the form of a phase difference. This is why permittivity rigorously must be treated as a complex function of frequency :

$$\epsilon(\omega) = \epsilon'(\omega) + i\epsilon''(\omega) \tag{132}$$

where the real part $\epsilon'(\omega)$ indicates how well the material can polarize, and where the imaginary part $\epsilon''(\omega)$ corresponds to the dissipation within the material. In general, the complex permittivity is a complicated function of ω, since it is a superposition of multiple dispersion phenomena occurring at different frequencies.

As a general rule, most of the materials we will be interested in can be divided into two groups : metals which are conductors, and dielectrics (or *polar materials*) which are insulators.

Metals are also good conductors of heat and are malleable at the nano-scale, which is why they are often used in precision measurements of the Casimir force. They furthermore are very reflective, therefore a tiny slab of metal such as gold or silver is enough to stop most of the modes, which form these quantities. We show in FIG. 10 the complex permittivity of gold as function of wavelength.

Dielectrics can be polarized by applying an electric field, so that the electric charges shift from their usual position at equilibrium, instead of flowing throughout the dielectric itself like for conductivity in metals. This causes the phenomenon of *dielectric polarization*, where positive charges shift towards the electric field and negative charges in the opposite direction, so that there appears an internal electric field altering the first field within the material itself.

In contrast, at the interface between a metal and a dielectric such as air, coherent electron oscillations are found which are called *surface plasmons*. These surface plasmons play an important role in the value of the Casimir force [29, 106–110] and radiative heat transfer, as they can couple to *polaritons*, which are *quasiparticles* coming from

the coupling of the modes with an electric or magnetic dipole-carrying excitation. In certain regimes, the permittivity function of metals will thus display certain resonant frequencies known as *surface plasmon-polaritons*. Likewise, some dielectrics have the property of displaying *exciton-polaritons* or *phonon-polaritons*. We will see this in more detail at the end of this chapter.

The permittivity function of metals and dielectrics can be obtained in two ways : either by tables of optical data such as [111, 112], where the permittivity is given for different frequencies, or by analytical expressions coming from solid state models such as the *Drude* and *plasma* models for conducting materials (like metals, semiconductors, and doped surfaces), the *Drude-Lorentz model* for certain dielectrics, or the *Sellmeier equation* for transparent materials. For precision measurements, having an exact model for the optical properties of the material is crucial [113, 114].

The most general way [115] to model the permittivity function $\epsilon(\omega)$ is by the expression :

$$\epsilon(\omega) = 1 - \sum_n \frac{\alpha_n}{\omega^2 - \omega_n^2 + i\gamma_n\omega} \tag{133}$$

which describes n damped harmonic oscillators, and is based on the Lorentz atom model. Each damped oscillator is defined by the triplet $(\alpha_n, \omega_n, \gamma_n)$, where α_n is the coefficient associated with the chosen model (plasma frequency for Drude, Sellmeier coefficient for silica...), ω_n stands for the resonance frequency of the given oscillator, and γ_n is the associated damping constant. This damping constant measures the material's dissipation. In order to describe a given material, the first step is thus to determine its number of resonance frequencies and therefore fix the index n.

The model defined in equation (133) has the following two limits at high and low frequencies :

$$\lim_{\omega\to\infty} \epsilon(\omega) = 1 \quad \text{and} \quad \lim_{\omega\to 0} \epsilon(\omega) = 1 + \sum_n \frac{\alpha_n}{\omega_n^2} > 1 \tag{134}$$

which correspond to the material's transparency at high frequencies, and the reaching of the so-called *static permittivity* at ultra-low frequencies.

Based on equation (133) we will now derive in real frequencies the expressions of the Drude and plasma models ($n = 0$) describing conductors, of the Drude-Lorentz model ($n = 1$) describing materials having one resonance frequency, and of the Sellmeier model ($n = 2$) describing transparent materials having two resonance frequencies.

The Drude model is then derived from equation (133) by considering only one oscillator ($n = 0$), and by letting the resonance frequency $\omega_0 \to 0$. This gives :

$$\epsilon(\omega) = 1 - \frac{\alpha_0}{\omega^2 + i\gamma_0\omega} = 1 - \frac{\omega_p^2}{\omega(\omega + i\gamma)} \tag{135}$$

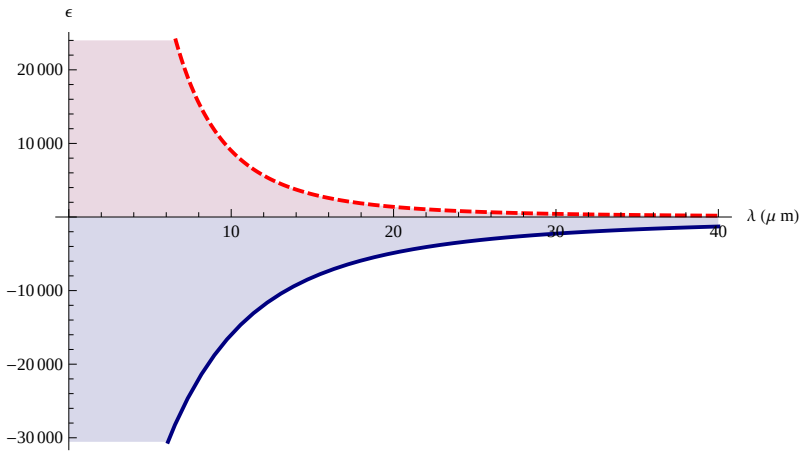

FIG. 10: Complex permittivity function of gold according to the Drude model from equation (135) and FIG. 11, with real part in blue and imaginary part in dashed red.

Metal	$\omega_\mathbf{p}$	γ
Gold	9.000 eV	35.000 meV
Copper	9.091 eV	30.000 meV
Aluminum	11.500 eV	50.000 meV
Tungsten	5.990 eV	53.773 meV

FIG. 11: Parameters ω_p and γ for the Drude (and hence plasma) model of equation (135), for different metals. These values come from [26] for gold, copper, and aluminum, and from [116] for tungsten.

where $\omega_p^2 \equiv \alpha_0$ is the characteristic frequency of *plasma waves* in the given conducting material, which is the frequency of the oscillation of the electric charges in the conductor. The parameter $\gamma \equiv \gamma_0$ defines the waves' *dissipation* inside the material.

A difference between metals and dielectrics arises from the static permittivity $\lim_{\omega\to 0} \epsilon(\omega)$ of equation (134), which is infinite for metals and finite for dielectrics.

The plasma model is similar to the Drude model except that the dissipation γ now tends to zero. We give in FIG. 11 the parameters ω_p and γ for different metals, and show also the real and imaginary part of the complex permittivity function of gold in FIG.10.

More interesting classes of materials are semiconductors subject to *doping*, which is the intentional infiltration of impurities into a pure semiconductor so as to shift it from the state of electric isolator to conductor. Before doping, the material is referred to as *intrinsic*, and as it becomes doped it is referred to as *extrinsic*. Eventually, the doping can be increased to the point of the material behaving more like a conductor than a semiconductor, in which case it is called *degenerate*.

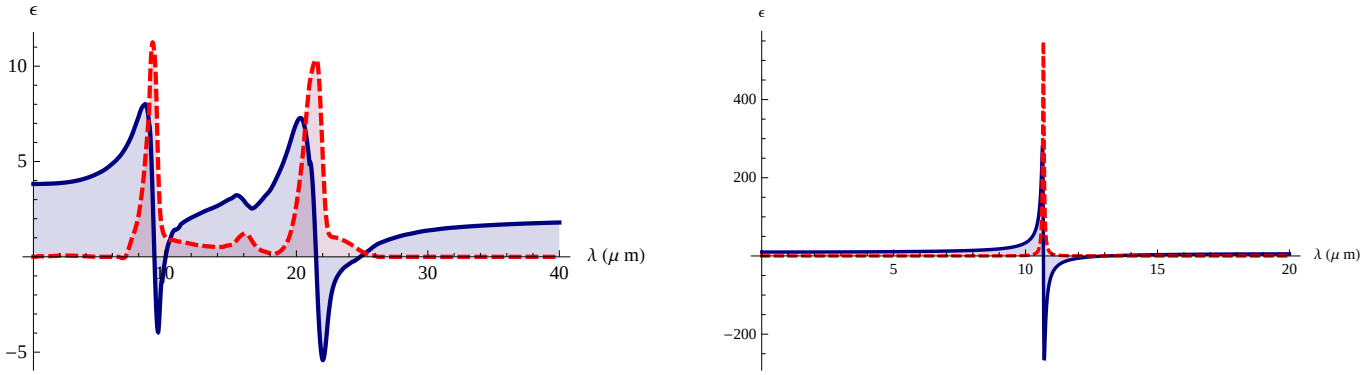

FIG. 12: Complex permittivity functions of SiO_2 on the left (according to the optical data found in [111]), and of SiC on the right (according to equation (140)), with real part in blue and imaginary part in red. Notice the presence of two resonances for SiO_2 at $\lambda = 8.75\mu$m and 21μm and one for SiC at $\lambda = 10.5\mu$m, due to surface phonon-polaritons.

Intrinsic silicon Si, has one resonance frequency around $\lambda = 0.3\mu$m, it is described by a Drude-Lorentz model, which is a Sellmeier model (141) with only one oscillator. In its general form, it is derived from equation (133) such that :

$$\epsilon(\omega) = 1 - \frac{\alpha_0}{\omega^2 + \omega_0^2} \tag{136}$$

Intrinsic silicon is modeled by :

$$\epsilon_{\text{IntSi}}(\omega) = \epsilon_\infty + \frac{(\epsilon_0 - \epsilon_\infty)\omega_0^2}{\omega^2 + \omega_0^2} \tag{137}$$

where the cut-off frequency is $\omega_0 = 4.345$ eV, with asymptotic values $\epsilon_\infty = 1.035$, and $\epsilon_0 = 11.87$.

Doped silicon is described by equation (133) with two oscillators : the first one describing the dielectric aspect of the silicon, and the second one describing the metallic aspect at low frequencies due to doping. It is then a sum of the former equation (137) with the Drude model's second term from equation (135) :

$$\epsilon(\omega) = 1 - \frac{\alpha_0}{\omega^2 - \omega_0^2} - \frac{\alpha_1}{\omega^2 + i\gamma_1\omega} \tag{138}$$

We obtain :

$$\epsilon_{\text{ExtSi}}(\omega) = \epsilon_{\text{IntSi}}(\omega) + \frac{\omega_p^2}{\omega(\omega + i\gamma)} \tag{139}$$

where now the parameters ω_p and γ depend on the doping itself, which is a measure of the density of charge carriers [27, 117].

Notice that we may want to take into account the dissipation of dielectrics by considering several oscillators, and as for the case of doped silicon, add a metallic part to the expression [118]. In this case, we can use the general formula (133) for permittivity. This is the case of certain materials such as Al_2O_3 and VO_2 [68].

We also give the Drude-Lorentz model describing SiC [65], whose permittivity shown in FIG.12 displays a resonance frequency at around 0.3μm :

$$\epsilon(\omega) = \epsilon_\infty \frac{\omega_l^2 - \omega^2 - i\gamma\omega}{\omega_t^2 - \omega^2 - i\gamma\omega} \tag{140}$$

with $\epsilon_\infty = 6.7$, $\omega_l = 182.7 \cdot 10^{12} s^{-1}$, $\omega_t = 149.5 \cdot 10^{12} s^{-1}$, and $\gamma = 0.9 \cdot 10^{12} s^{-1}$.

Finally the Sellmeier model, which describes transparent materials such as SiO_2 silicon dioxide, is derived from equation (133) by assuming that the dissipations γ_n are negligible in comparison with the resonance frequencies ω_n. This gives :

$$\epsilon(\omega) = 1 - \sum_n \frac{\alpha_n}{\omega^2 - \omega_n^2} \tag{141}$$

For fused silica SiO_2, whose permittivity function is shown in in FIG. 12, this can be expressed as a function of the wavelength λ, such that :

$$\epsilon(\lambda) \simeq 1 + \frac{a_1\lambda^2}{\lambda^2 - b_1} + \frac{a_2\lambda^2}{\lambda^2 - b_2} + \frac{a_3\lambda^2}{\lambda^2 - b_3} \tag{142}$$

where $a_n \equiv \alpha_n/\omega_n^2$ and $b_n \equiv c^2/\omega_n^2$ are the Sellmeier coefficients, which are determined experimentally [119] : $a_1 = 0.696$, $a_2 = 0.408$, $a_3 = 0.897$, $b_1 = 4.679 \cdot 10^{-3}\mu m^2$, $b_2 = 1.351 \cdot 10^{-2}\mu m^2$, $b_3 = 97.934\mu m^2$.

The first two terms in a_1 and a_2 correspond to the resonance frequencies of silicon dioxide SiO_2 at 8.75μm and 21μm, and the third term in a_3 is a convergence term so that $\epsilon(\lambda) \to 1$ at high frequencies.

2. Fresnel-Stokes amplitudes and S-matrices

We consider two distinct media of refraction indices n_0 and n_1, as illustrated in FIG. 13. The Snell-Descartes law comes from the conservation of frequency ω and transverse wave-vector k_z, giving the angles of reflection θ_0 and θ_1 by :

$$n_0 \sin\theta_0 = n_1 \sin\theta_1 = \frac{c|\mathbf{k}|}{\omega} \tag{143}$$

where we have considered the incident wave to be in the xz plane, so that the azimuthal angle is zero, with $k_x = |\mathbf{k}|$ and $k_y = 0$.

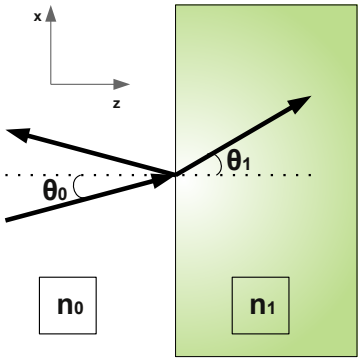

FIG. 13: Interface between two media of refraction indices n_0 and n_1, where the two angles θ_0 and θ_1 are related through Snell-Descartes law of equation (143).

Now we know that the longitudinal wave-vector κ changes according to the index of the medium in which the mode travels. For the two media 0 (which in our notation will denote vacuum) and 1 respectively, we hence have :

$$\kappa_0 = \sqrt{\epsilon_0 \frac{\xi^2}{c^2} + \mathbf{k}^2} \qquad \text{and} \qquad \kappa_1 = \sqrt{\epsilon_1 \frac{\xi^2}{c^2} + \mathbf{k}^2} \tag{144}$$

These determine the amplitudes of the scattering at interface, which are called the *Fresnel-Stokes amplitudes*, and which depend on the polarization TE or TM. The Fresnel-Stokes amplitudes come from the equations of continuity of the transverse field components at the interface, and from the properties of the plane waves in both media. The scattering amplitudes r_{01} and t_{01} are the reflection and transmission coefficients, sometimes called *Fresnel coefficients*, describing the scattering at the interface of a given incident wave ϵ_0^{in} coming from medium 0. A part of that wave is transmitted in the medium 1 as ϵ_1^{tr}, and a part is reflected back in medium 0 as ϵ_0^{ref}, as shown in FIG. 13.

Since this depends on the given polarization TE or TM of the wave, we give these Fresnel coefficients as the refraction amplitudes r_{01} and t_{01} of a wave coming from medium 0 onto medium 1, and conversely as the reciprocal amplitudes $\overline{r}_{01}$ and $\overline{t}_{01}$ of a wave coming from medium 1 onto medium 0 for both polarizations, as shown in FIG. 14 :

$$r_{01}^{\mathrm{TE}} = \frac{1 - z_{01}^{\mathrm{TE}}}{1 + z_{01}^{\mathrm{TE}}} \quad \text{and} \quad t_{01}^{\mathrm{TE}} = 1 + r_{01}^{\mathrm{TE}} = (1 - r_{01}^{\mathrm{TE}}) \frac{n_0 \cos\theta_0}{n_1 \cos\theta_1}, \quad \text{for} \quad z_{01}^{\mathrm{TE}} \equiv \frac{1 - r_{01}^{\mathrm{TE}}}{1 + r_{01}^{\mathrm{TE}}} = \frac{n_1 \cos\theta_1}{n_0 \cos\theta_0} = \frac{\kappa_1}{\kappa_0} \tag{145}$$

$$r_{01}^{\mathrm{TM}} = \frac{1 - z_{01}^{\mathrm{TM}}}{1 + z_{01}^{\mathrm{TM}}} \quad \text{and} \quad t_{01}^{\mathrm{TM}} = (1 + r_{01}^{\mathrm{TM}}) \frac{\cos\theta_0}{\cos\theta_1} = (1 - r_{01}^{\mathrm{TM}}) \frac{n_0}{n_1}, \quad \text{for} \quad z_{01}^{\mathrm{TM}} \equiv \frac{1 - r_{01}^{\mathrm{TM}}}{1 + r_{01}^{\mathrm{TM}}} = \frac{n_1 \cos\theta_0}{n_0 \cos\theta_1} = \frac{\epsilon_1 \kappa_0}{\epsilon_0 \kappa_1} \tag{146}$$

$$\overline{r}_{01}^{\mathrm{TE}} = -r_{01}^{\mathrm{TE}} \quad \text{and} \quad \overline{t}_{01}^{\mathrm{TE}} = 1 + \overline{r}_{01}^{\mathrm{TE}} = (1 - \overline{r}_{01}^{\mathrm{TE}}) \frac{n_1 \cos\theta_1}{n_0 \cos\theta_0}, \quad \text{for} \quad \overline{z}_{01}^{\mathrm{TE}} = 1/z_{01}^{\mathrm{TE}} \tag{147}$$

$$\overline{r}_{01}^{\mathrm{TM}} = -r_{01}^{\mathrm{TM}} \quad \text{and} \quad \overline{t}_{01}^{\mathrm{TM}} = (1 + \overline{r}_{01}^{\mathrm{TM}}) \frac{\cos\theta_1}{\cos\theta_0} = (1 - \overline{r}_{01}^{\mathrm{TM}}) \frac{n_1}{n_0}, \quad \text{for} \quad \overline{z}_{01}^{\mathrm{TM}} = 1/z_{01}^{\mathrm{TM}} \tag{148}$$

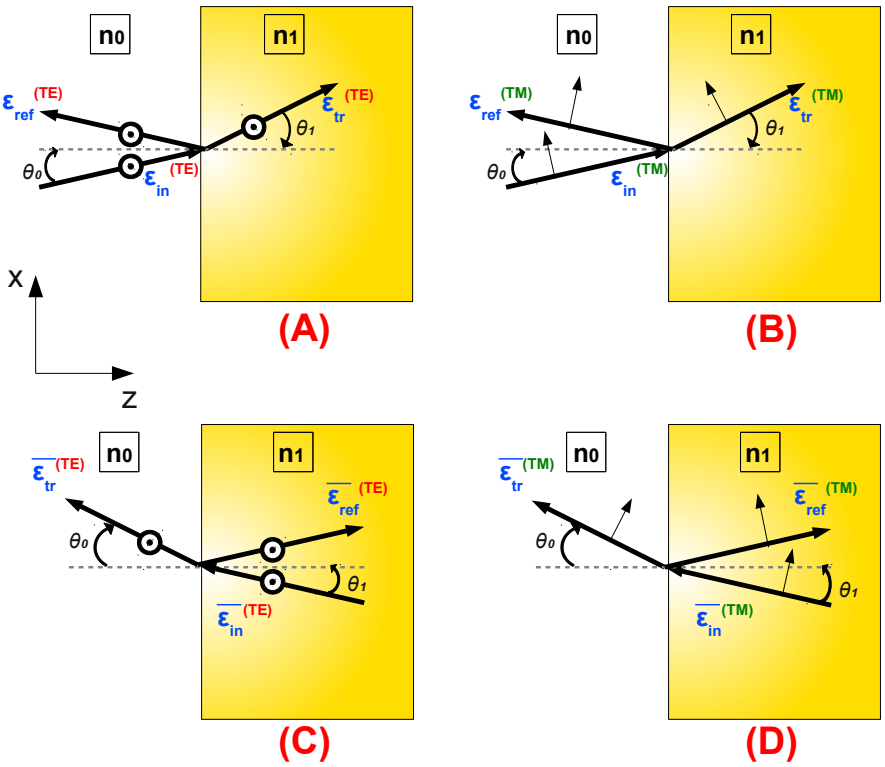

FIG. 14: Refraction scatterings of a TE-polarized mode (A) and of a TM-polarized mode (B), and reciprocal scatterings of a TE-polarized mode (C) and of a TM-polarized mode (D). The reflection and transmission coefficients of these four are respectively given by equations (145), (146), (147), and (148).

We denote the fields propagating away from the interface as $|\epsilon^{\text{out}}\rangle$, and towards the interface as $|\epsilon^{\text{in}}\rangle$, as shown in FIG. 15. For a chosen polarization, these coefficients of reflections r and $\overline{r}$, and coefficients of transmission t and $\overline{t}$ can be written together in a so-called *scattering matrix*, or *S-matrix*, of the form :

$$S_{\text{in/out}} = \begin{pmatrix} r = c/a & \overline{t} = (ad - bc)/a \\ t = 1/a & \overline{r} = -b/a \end{pmatrix} \tag{149}$$

where the coefficients a, b, c, and d, will be explained shortly. This S-matrix links the fields $|\epsilon^{\text{in}}\rangle = \begin{pmatrix} \epsilon_0^{\text{in}} \\ \epsilon_1^{\text{in}} \end{pmatrix}$ and $|\epsilon^{\text{out}}\rangle = \begin{pmatrix} \epsilon_0^{\text{out}} \\ \epsilon_1^{\text{out}} \end{pmatrix}$ such that :

$$|\epsilon^{\text{out}}\rangle = S\,|\epsilon^{\text{in}}\rangle \tag{150}$$

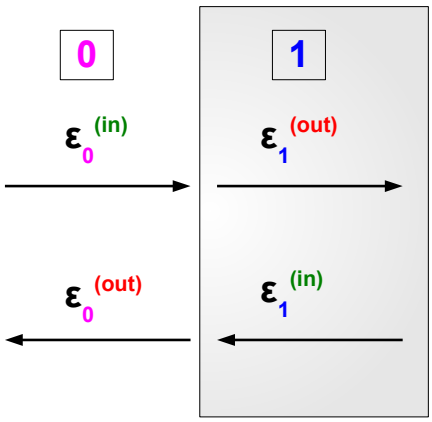

FIG. 15: Notations of the different fields propagating *in* and *out* of the interface according to the index of the material in which they travel. If we want to put the emphasis on the material in which the mode travels (as is done in the derivation of the Casimir energy between nanogratings), it is more convenient to use a S-matrix formalism according to equation (149). But if we want to put the emphasis on the direction of the propagation of the mode (as in the case of slabs, or coated materials), it is more convenient to use a T-matrix formalism according to equation (151).

However, instead of the direction of propagation with respect to the interface, it is often more convenient in numerical computations to identify the fields by the medium in which they travel : $|\epsilon_0\rangle$ for those in medium 0, and $|\epsilon_1\rangle$ for those in medium 1. Then we can define the so-called *transmission matrix*, or *T-matrix*, of the form :

$$T_{0/1} = \begin{pmatrix} a = 1/t & b = -\bar{r}/t \\ c = r/t & d = (t\bar{t} - r\bar{r})/t \end{pmatrix} \tag{151}$$

This T-matrix links the fields $|\epsilon^0\rangle = \begin{pmatrix} \epsilon_0^{\text{in}} \\ \epsilon_0^{\text{out}} \end{pmatrix}$ and $|\epsilon^1\rangle = \begin{pmatrix} \epsilon_1^{\text{out}} \\ \epsilon_1^{\text{in}} \end{pmatrix}$ such that :

$$|\epsilon^0\rangle = T_{0/1}\,|\epsilon^1\rangle \tag{152}$$

Clearly, the S- and T-matrices are related to one another. An important property is that the S-matrix is symmetrical if and only if the T-matrix has a unit determinant. The T-matrix is useful when one studies the propagation of modes through *optical networks* : slabs, coatings, layered materials, etc... In this latter case, it is possible to link the incoming fields from a medium A through B to another C by joining them through a T-matrix $T_{AC} = T_{AB} \cdot T_{BC}$ such that :

$$|\epsilon^{\text{A}}\rangle = T_{AB}\,|\epsilon^{\text{B}}\rangle \quad \text{and} \quad |\epsilon^{\text{B}}\rangle = T_{BC}\,|\epsilon^{\text{C}}\rangle \quad \Longrightarrow \quad |\epsilon^{\text{A}}\rangle = T_{AC}\,|\epsilon^{\text{C}}\rangle = T_{AB} \cdot T_{BC}\,|\epsilon^{\text{C}}\rangle \tag{153}$$

These results allow us to consider the case of a slab in vacuum. The slab is built by stacking a vacuum-matter interface (01 in our notation), a propagation over a length L inside matter 1, and again a matter-vacuum interface (10), as shown on FIG. 16. Then we can write the T-matrix of the slab such as :

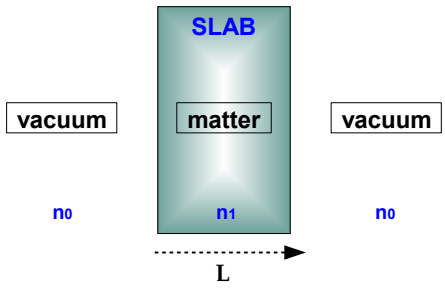

FIG. 16: Slab built by stacking a vacuum-matter interface, a propagation over a length ℓ inside matter, and again a matter-vacuum interface.

$$T^{\text{slab}} = T_{01}^{\text{int}} \cdot T_1^{\text{prop}} \cdot T_{10}^{\text{int}} = \begin{pmatrix} \frac{\sinh(\alpha+\beta)}{\sinh\beta} & \frac{\sinh\alpha}{\sinh\beta} \\ -\frac{\sinh\alpha}{\sinh\beta} & \frac{\sinh(\beta-\alpha)}{\sinh\beta} \end{pmatrix} \tag{154}$$

where we have for $-e^{-\beta} \equiv r_{01}^{int} = -\overline{r}_{01}^{int}$, and $\epsilon_0 = 1$:

$$T_{01}^{\text{int}} = \sqrt{\frac{\kappa_1}{\kappa_0}} \frac{1}{\sqrt{2\sinh\beta}} \cdot \begin{pmatrix} e^{\beta/2} & -e^{-\beta/2} \\ -e^{-\beta/2} & e^{\beta/2} \end{pmatrix} \quad \text{and} \quad T_1^{\text{prop}} = \begin{pmatrix} e^{\kappa_1 L} & 0 \\ 0 & e^{-\kappa_1 L} \end{pmatrix} \tag{155}$$

From these we can recover the scattering amplitudes through the S-matrix, and see that these correspond to the amplitudes of a *Fabry-Pérot cavity*, or *Fabry-Pérot resonator*, where the mirrors correspond to the interfaces and the cavity itself is "filled" by the medium.

Now we have considered so far only the scattering of ordinary propagative waves only in both media. But one can also encounter waves coming from the more refractive medium into the less refractive one, with an incident angle larger than the limit angle : $n_1 > n_0$, $n_1 \sin\theta_1 > n_0$, and $\sin\theta_0 > 1$.

This is the case of totally reflected and evanescent waves, which can be understood from our calculations above if we use the physical domain of complex frequencies Re ξ, with the branch of the square root chosen such that Re $\kappa > 0$.

Now the Fresnel-Stokes previously computed above are for classical fields only. In the case of a lossless slab, we can show [120] that :

$$|r|^2 + |t|^2 = 1 \qquad \text{and} \qquad rt^* + tr^* = 0 \tag{156}$$

These two unitary relations imply that $|r| < 1$, and that the S-matrices are unitary 2×2 matrices :

$$S^\dagger S = \begin{pmatrix} |r|^2 + |t|^2 & rt^* + tr^* \\ rt^* + tr^* & |r|^2 + |t|^2 \end{pmatrix} = I \tag{157}$$

For a lossless slab, the eigenvalues $r \pm t$ of the matrix S have a unit modulus. But for a lossy slab these eigenvalues have a modulus smaller than unity. This means that additional fluctuations must be taken into account.

3. Quantization and Airy function

So in order to fully describe optical networks, one must take into account the additional fluctuations which are associated with the noise lines coming from absorption. Mathematically, we will see that these appear in the form of a perturbation added to the S-matrix. Physically, we will now consider the contributions coming from the *evanescent waves* to the scattering. Evanescent waves are formed at an interface of two media with different permittivities. They are near-field standing waves that exponentially decay in intensity with regards to the distance from the interface where they were formed, as shown in FIG. 17 —they are usually most intense within a range of one third of a wavelength from the surface. By opposition to the evanescent waves, the equations we have given in the previous section concern *propagative waves*, which are the waves freely propagating (for example within the vacuum) and not subject to exponential decay in intensity with distance.

Now this full description which involves additional fluctuations is described by the case of lossy mirrors such as those forming a Fabry-Pérot cavity as shown on FIG. 18, where the S-matrix computed for the classical fields is no longer unitary as in equation (157). In this case, it is the restriction to the modes of interest contained in a larger S-matrix which is unitary.

Let's define the indices $m \equiv (\omega, \mathbf{k}, p)$ for a given polarization $p = TE, TM = s, p$, and $\phi = \pm$ the rightward/leftward direction of propagation. We have already seen in section V the anticommutation relations (43) of the annihilation and creation operators a_m^ϕ and b_m^ϕ, or field amplitudes corresponding to the normalized positive and negative frequency components. We saw in equations (41) and (42) that these operators could be used to define the electric and magnetic fields.

We now rewrite them by setting $a_m^{\phi\,\mathrm{in}}$ and $a_m^{\phi\,\mathrm{out}}$ as defining the input fields coming to the mirror and the output fields going away from the mirror, respectively —and similarly for $b_m^{\phi\,\mathrm{in}}$ and $b_m^{\phi\,\mathrm{out}}$. In the case of amplitudes a_m^ϕ and b_m^ϕ corresponding to positive and negative frequency components (that are hence normalized so that they correspond to the definition of annihilation and creation operators), these canonical relations are then written :

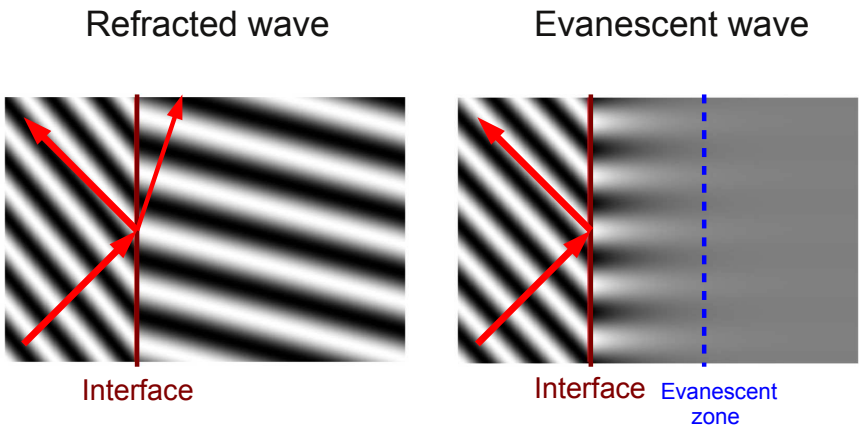

FIG. 17: Comparison at a given interface between a refracted incident wave and an evanescent wave. The exponential decay in intensity of the evanescent wave with the distance from the interface is clearly shown, being roughly delimited by the evanescent zone.

$$[a_{m'}^{\phi' \text{ in}}, b_m^{\phi \text{ in}}] = \delta_{mm'}\,\delta_{\phi\phi'} = 8\pi^3\,\delta^{(2)}(\mathbf{k}-\mathbf{k}')\,\delta(k_z-k_z')\,\delta_{pp'}\,\delta_{\phi\phi'} \tag{158}$$

$$[a_{m'}^{\phi' \text{ in}}, a_m^{\phi \text{ in}}] = [b_{m'}^{\phi' \text{ in}}, b_m^{\phi \text{ in}}] = 0 \tag{159}$$

for the input fields, and similarly for the output fields. The unitarity of scattering implies that the output fields have the same commutators as the input ones. This is true for optical networks, but not in the specific case of a Fabry-Pérot cavity.

In the case of lossless mirrors, the output fields can be obtained from the input ones by using the classical equations (156). But in the case of lossy mirrors, one must add additional fluctuations F_1 and F_2 at the interface 01 such that :

$$\begin{pmatrix} e_0^{\text{out}} \\ e_1^{\text{out}} \end{pmatrix} = S \begin{pmatrix} e_0^{\text{in}} \\ e_1^{\text{in}} \end{pmatrix} + \begin{pmatrix} F_1 \\ F_2 \end{pmatrix} \tag{160}$$

These additional fluctuations F_1 and F_2 also depend on m, and are a superposition of all the modes that are coupled to the main modes e_m^{ϕ} by the microscopic couplings causing the absorption. As already said, we can define these fluctuations by writing the unitary property for a large S-matrix that would take all the modes into account [29, 120]. Let's write therefore :

$$\begin{pmatrix} F_1 \\ F_2 \end{pmatrix} = S' \begin{pmatrix} f_1 \\ f_2 \end{pmatrix} = \begin{pmatrix} r' & \bar{t}' \\ t' & \bar{r}' \end{pmatrix} \begin{pmatrix} f_1 \\ f_2 \end{pmatrix} \tag{161}$$

where $\begin{pmatrix} f_1 \\ f_2 \end{pmatrix}$ represents the noise modes, and S' is the noise matrix, whose elements are the noise amplitudes. Then we can use the *optical theorem* to show that the norm matrix $S'S'^{\dagger}$ obeys the unitary condition on the whole scattering process :

$$SS^{\dagger} + S'S'^{\dagger} = I \tag{162}$$

The noise modes have similar canonical commutators to the input fields of the main modes, being in fact a linear superposition of the true input vacuum fields coupled to the main modes. Nevertheless if we fully develop the matrix elements of equation (162), we can see that they do not fully determine the noise amplitudes, but only describe the statistical characteristics of the additional fluctuations. This is due to the definition of the canonical noise modes f_1 and f_2.

As a side note, it is also noteworthy that the S-matrix of an absorbing slab has a particularly symmetrical form $r = \overline{r}$ and that the noise matrix S' may thus be written in the same form $r' = \overline{r}'$.

The S-matrix scattering formalism above can be derived for T-matrices as well :

$$|e_0\rangle = T|e_1\rangle + |G\rangle, \qquad \text{for} \qquad |G\rangle = M|F\rangle = \begin{pmatrix} 0 & -a \\ 1 & -c \end{pmatrix} |F\rangle \tag{163}$$

where G_1 and G_2 are additional fluctuations appearing as linear superpositions of F_1 and F_2. These expressions allow us to study the case of the modes scattering in the Fabry-Pérot cavity as shown in FIG. 18, where unitarity of the scattering is no longer valid, so that the input and output fields do not have the same anticommutators.

We can write in the classical case the transfer equation for the whole cavity :

$$|e_L\rangle = T_1 T_L T_2 |e_R\rangle + |G_1\rangle + T_1 T_L |G_2\rangle \tag{164}$$

for a matrix T_L of propagation within the cavity given by :

$$T_L = \begin{pmatrix} e^{\kappa_0 L} & 0 \\ 0 & e^{-\kappa_0 L} \end{pmatrix} \tag{165}$$

We now consider the Fabry-Pérot cavity as a composition of two networks : A, containing mirror 1 and propagation of the modes over length L_A, and B, containing the propagation of the modes over length L_B and mirror 2. Then we can write our result (164) over the distance $L = L_A + L_B$ within the cavity C such that :

$$|e_L\rangle = T_1 T_{L_A} |e_C\rangle + |G_1\rangle \quad \text{with} \quad T^A = T_1 T_{L_A} \quad \text{and} \quad |G^A\rangle = |G_1\rangle \tag{166}$$

$$|e_C\rangle = T_{L_B} T_2 |e_C\rangle + T_{L_B} |G_2\rangle \quad \text{with} \quad T^B = T_{L_B} T_2 \quad \text{and} \quad |G^B\rangle = T_{L_B} |G_2\rangle \tag{167}$$

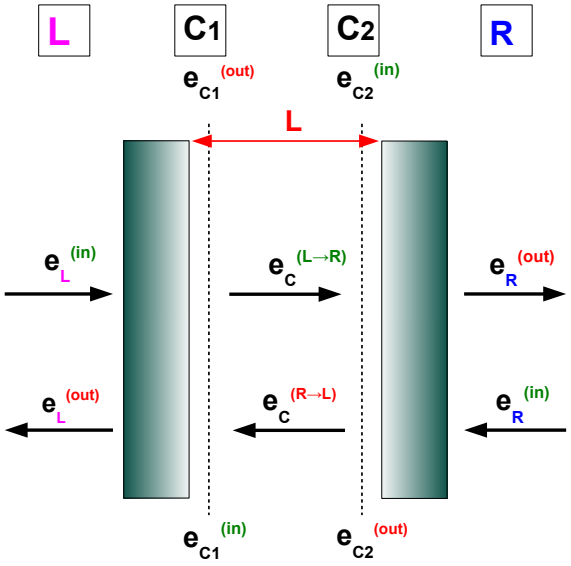

FIG. 18: Representation of a Fabry-Pérot cavity, where the fields at the left and at the right side of the cavity C are denoted by L and R respectively, and where the fields at the interface of the left-hand and right-hand mirrors inside of the cavity are denoted by C_1 and C_2, respectively.

In terms of the scattering amplitudes, these relations can be written as :

$$r_A = r_1 \quad \text{and} \quad r_B = r_2 e^{-2\kappa_0 L_B} \tag{168}$$

$$\overline{r}_A = \overline{r}_1 e^{-2\kappa_0 L_A} \quad \text{and} \quad \overline{r}_B = \overline{r}_2 \tag{169}$$

$$t_A = t_1 e^{-\kappa_0 L_A} \quad \text{and} \quad t_B = e^{-\kappa_0 L_B} t_2 \tag{170}$$

This allows us to evaluate $\mathcal{G}$, which is an indicator of the anticommutation of the input and output fields [29, 120] based on equation (162) :

$$\mathcal{G} = I + \frac{1}{\mathcal{D}} \begin{pmatrix} \overline{r}_A r_B & \overline{r}_A \\ r_B & \overline{r}_A r_B \end{pmatrix} + \frac{1}{\mathcal{D}^*} \begin{pmatrix} \overline{r}_A r_B & \overline{r}_A \\ r_B & \overline{r}_A r_B \end{pmatrix}^\dagger \tag{171}$$

with :

$$\mathcal{D} = 1 - \overline{r}_A r_B = 1 - \overline{r}_1 r_2 e^{-2\kappa_0 L} \tag{172}$$

Then the diagonal elements of $\mathcal{G}$ coincide with the so-called *Airy function* :

$$g = 1 + f + f^* = \frac{1 - |1 - \mathcal{D}|^2}{|\mathcal{D}|^2} \quad \text{and} \quad f = \frac{1 - \mathcal{D}}{\mathcal{D}} \tag{173}$$

which means that the commutators of the fields inside the cavity are not the same as those of the free fields. They correspond to a modified *spectral density*, which is the spectral density of the free fields multiplied by the Airy

function g. This is an important result, because the Casimir force is derived from a difference between the total pressure generated by the modes outside and inside of the cavity, as we will see in the following.

4. Derivation of the Casimir force between two planes

We derived through Noether's theorem the equation of the stress-energy tensor (55) in section V B 2. We now give an illustration of the physical meaning of its components in FIG. 19. The portion of the stress-energy tensor due to the electromagnetic field is the *electromagnetic stress–energy tensor*, which is a function of the electromagnetic field tensor $F^{\mu\nu}$ that we saw in equation (84) of section V B 4. It is given in SI units by :

$$T^{\mu\nu} = \frac{1}{\mu_0}[F^{\mu\alpha}F^{\nu}{}_{\alpha} - \frac{1}{4}\eta^{\mu\nu}F_{\alpha\beta}F^{\alpha\beta}] = \begin{bmatrix} \frac{1}{2}(\epsilon_0 E^2 + \frac{1}{\mu_0}H^2) & S_x/c & S_y/c & S_z/c \\ S_x/c & -\sigma_{xx} & -\sigma_{xy} & -\sigma_{xz} \\ S_y/c & -\sigma_{yx} & -\sigma_{yy} & -\sigma_{yz} \\ S_z/c & -\sigma_{zx} & -\sigma_{zy} & -\sigma_{zz} \end{bmatrix} \tag{174}$$

where $\eta^{\mu\nu}$ is the Minkowski metric tensor, which is a diagonal matrix with diagonal elements $(-1, 1, 1, 1)$. Here the matrix elements S_i are the components of the *Poynting vector* [121], which represents the electromagnetic field's directional energy flux density, or its rate of energy transfer per unit area in $W.m^{-2}$:

$$\mathbf{S} = \frac{1}{\mu_0}\mathbf{E} \times \mathbf{H} \tag{175}$$

The matrix elements σ_{ij} are the components of the so-called *Maxwell stress-tensor* :

$$\sigma_{ij} = \epsilon_0 E_i E_j + \frac{1}{\mu_0}H_i H_j - \frac{1}{2}\left(\epsilon_0 E^2 + \frac{1}{\mu_0}H^2\right)\delta_{ij} \tag{176}$$

where δ_{ij} is Kronecker's delta. The elements σ_{xx}, σ_{yy}, and σ_{zz} of the electromagnetic stress-energy tensor which form the diagonal elements of the Maxwell stress-tensor are hence akin to a pressure.

The elements ij of the Maxwell stress tensor represent the flux per unit of time of momentum which is parallel to the ith axis crossing a surface normal to the jth axis, in the negative direction. Alternatively, they also represent the force per area which is parallel to the ith axis, and experienced by a surface normal to the jth axis. So they are related to a negative pressure.

A given area in the electromagnetic field also experiences a force in a direction that is not normal to that area. Unlike forces coming from the pressure of an ideal gas, this gives rise to a shear or viscosity, which is represented by the non-diagonal elements of the Maxwell stress tensor.

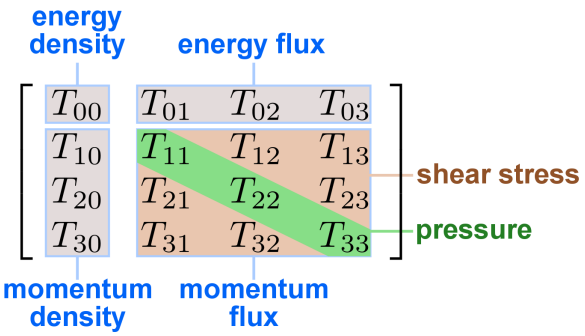

FIG. 19: Components of the general stress-energy tensor, with their physical meaning. The diagonal elements T_{11}, T_{22}, and T_{33} give the pressure responsible for the Casimir force. The shear stress is akin to viscosity.

In order to calculate the Casimir effect between two plates let us now assume a Fabry-Pérot cavity composed of perfectly plane mirrors. The index $m \equiv (\omega, \mathbf{k}, p)$ is preserved throughout the whole scattering process. The *vacuum impedance* in place of the electromagnetic constants in vacuum, is defined as $Z_0 = \mu_0 c = 1/\epsilon_0 c$. Then the component $T_{00} \equiv \sigma_{ii}$ of the Maxwell stress tensor gives the energy density per unit volume as a quadratic form of the free electric and magnetic fields :

$$T_{00} = \frac{1}{2cZ_0}\left(E_x^2 + E_y^2 + E_z^2 + c^2H_x^2 + c^2H_y^2 + c^2H_z^2\right) = \frac{1}{2cZ_0}\left(\mathbf{E}^T\mathbf{E} + c^2\mathbf{H}^T\mathbf{H}\right) \tag{177}$$

Based on equation (113) of the quantized free fields written as a linear superposition of the modes, we can find the quantum average of the energy density in vacuum state [120], such as :

$$\langle T_{00}\rangle_{vac} = \sum_{m\phi} \hbar\omega \;\; \langle a_m^\phi \cdot b_m^\phi\rangle_{vac} \tag{178}$$

In a thermal equilibrium state and at non-zero temperature T, the following anticommutator of the operators is :

$$\langle a_m^\phi \cdot b_m^\phi\rangle_{vac} \equiv \frac{\langle a_m^\phi b_m^\phi + b_m^\phi a_m^\phi\rangle_{vac}}{2} = \frac{1}{2} + \frac{1}{e^{\frac{\hbar\omega}{k_B T}} - 1} \tag{179}$$

In the case of vacuum at zero temperature, it reduces to $\frac{1}{2}$. We therefore recover the mean energy density in vacuum as the $\hbar\omega/2$ sum over the modes :

$$\langle T_{00}\rangle_{vac} = \sum_{m\phi} \frac{\hbar\omega}{2} \tag{180}$$

which is an infinite quantity reflecting the *vacuum energy catastrophe*, which fortunately does not influence our derivation of the Casimir energy [122].

We can now evaluate the T_{zz} component of the Maxwell stress tensor, which gives the pressure on the plane mirrors forming our Fabry-Pérot cavity and parallel to the xy-plane :

$$T_{zz} = \frac{1}{2Z_0}\left(E_x^2 + E_y^2 - E_z^2 + c^2H_x^2 + c^2H_y^2 - c^2H_z^2\right) = \frac{1}{2Z_0}\left(\mathbf{E}^T\Pi\mathbf{E} + c^2\mathbf{H}^T\Pi\mathbf{H}\right) \tag{181}$$

for Π a given diagonal matrix with diagonal elements $(+1, +1, -1)$. From this, we can similarly derive its quantum average :

$$\langle T_{zz}\rangle_{vac} = \sum_{m\phi} \hbar\omega_m \cos^2\theta_m \quad \langle a_m^\phi \cdot b_m^\phi\rangle_{vac} \tag{182}$$

where $\cos^2\theta_m$ is a projection factor arising from the polarization vectors with associated incidence angle θ in the xz-plane (equation 2-21 in [120]). Expression (182) represents the radiation pressure compared to that of energy density. As for equation (180), it is also infinite but this will not affect our derivation of the Casimir pressure in the Fabry-Pérot cavity.

By developing the sum over ϕ, we can then find the pressure endured by a given mirror, which is equal to the sum of the radiation pressure given by the contributions of the four following fields that are coupled in the scattering :

$$\langle P\rangle_{vac} = \sum_m \hbar\omega_m \cos^2\theta_m \quad \langle a_{m\ \mathrm{L}}^{\mathrm{in}} \cdot b_{m\ \mathrm{L}}^{\mathrm{in}} + a_{m\ \mathrm{L}}^{\mathrm{out}} \cdot b_{m\ \mathrm{L}}^{\mathrm{out}} - a_{m\ \mathrm{R}}^{\mathrm{out}} \cdot b_{m\ \mathrm{R}}^{\mathrm{out}} - a_{m\ \mathrm{R}}^{\mathrm{in}} \cdot b_{m\ \mathrm{R}}^{\mathrm{in}}\rangle_{vac} \tag{183}$$

We have already seen that for a given single mirror, the commutators are the same for the input and output fields even in the case of dissipation. Together with equation (179), we can then find :

$$\langle a_m^\phi \cdot b_m^\phi\rangle_{vac} = \frac{1}{2}\left[a_m^\phi b_m^\phi\right] = \frac{1}{2} \tag{184}$$

$$\langle a_{m\ \mathrm{L}}^{\mathrm{in}} \cdot b_{m\ \mathrm{L}}^{\mathrm{in}} - a_{m\ \mathrm{R}}^{\mathrm{in}} \cdot b_{m\ \mathrm{R}}^{\mathrm{in}}\rangle_{vac} = \langle a_{m\ \mathrm{L}}^{\mathrm{out}} \cdot b_{m\ \mathrm{L}}^{\mathrm{out}} - a_{m\ \mathrm{R}}^{\mathrm{out}} \cdot b_{m\ \mathrm{R}}^{\mathrm{out}}\rangle_{vac} = 0 \tag{185}$$

This implies that the radiation pressure is always zero for a single mirror, due to the equal roles played on both sides of the mirror, so that no mean force appears. Nevertheless, in the case of the two mirrors of the Fabry-Pérot cavity, we must calculate :

$$\langle P_1\rangle_{vac} = \sum_m \hbar\omega_m \cos^2\theta_m \quad \langle a_{m\ \mathrm{L}}^{\mathrm{in}} \cdot b_{m\ \mathrm{L}}^{\mathrm{in}} + a_{m\ \mathrm{L}}^{\mathrm{out}} \cdot b_{m\ \mathrm{L}}^{\mathrm{out}} - a_{m\ \mathrm{C}}^{\mathrm{L}\to\mathrm{R}} \cdot b_{m\ \mathrm{C}}^{\mathrm{L}\to\mathrm{R}} - a_{m\ \mathrm{C}}^{\mathrm{R}\to\mathrm{L}} \cdot b_{m\ \mathrm{C}}^{\mathrm{R}\to\mathrm{L}}\ \rangle_{vac} \tag{186}$$

$$\langle P_2\rangle_{vac} = \sum_m \hbar\omega_m \cos^2\theta_m \quad \langle a_{m\ \mathrm{C}}^{\mathrm{L}\to\mathrm{R}} \cdot b_{m\ \mathrm{C}}^{\mathrm{L}\to\mathrm{R}} + a_{m\ \mathrm{C}}^{\mathrm{R}\to\mathrm{L}} \cdot b_{m\ \mathrm{C}}^{\mathrm{R}\to\mathrm{L}} - a_{m\ \mathrm{R}}^{\mathrm{out}} \cdot b_{m\ \mathrm{R}}^{\mathrm{out}} - a_{m\ \mathrm{R}}^{\mathrm{in}} \cdot b_{m\ \mathrm{R}}^{\mathrm{in}}\rangle_{vac} \tag{187}$$

Whereas the anticommutators are the same for the input and output fields, they are related to the commutators multiplied by the Airy function from equation (184), for the fields within the cavity :

$$\langle a^{\phi}_{m\ \mathrm{C}} \cdot b^{\phi}_{m\ \mathrm{C}} \rangle_{vac} = \frac{1}{2} \left[a^{\phi}_{m\ \mathrm{C}} \ , \ b^{\phi}_{m\ \mathrm{C}} \right] = \frac{1}{2} g_m \tag{188}$$

Equations (184) and (188) allow us to simplify the expressions of the radiation pressure on both mirrors :

$$\langle P_1 \rangle_{vac} = \sum_m \hbar \omega_m \cos^2 \theta_m \quad (1 - g_m) \tag{189}$$

$$\langle P_2 \rangle_{vac} = \sum_m \hbar \omega_m \cos^2 \theta_m \quad (g_m - 1) = -\langle P_1 \rangle_{vac} \tag{190}$$

Notice that these two pressures have opposite values. This is a consequence of the translational invariance of vacuum : the global force of the vacuum suffered by the cavity is zero.

Now we are in a position to give the *Casimir force* acting on mirror 1 of surface A, with the assumption that $A \gg L^2$:

$$F \equiv A \langle P_1 \rangle_{vac} = A \sum_m \hbar \omega_m \cos^2 \theta_m \quad (1 - g_m) \tag{191}$$

This force has a positive sign, and is hence attractive.

Based on equation (111), we can write the summation symbol as :

$$\sum_m \omega_m \cos^2 \theta_m \ldots \quad \longmapsto \quad \sum_p \int \frac{d^2\mathbf{k}}{4\pi^2} \int \frac{d\omega}{2\pi} k_z \ldots \tag{192}$$

and therefore re-write the Casimir force as :

$$F = A\hbar \sum_p \int \frac{d^2\mathbf{k}}{4\pi^2} \int \frac{d\omega}{2\pi} k_z \left[1 - g^p_{\mathbf{k}}(\omega) \right] \tag{193}$$

5. Analyticity conditions of the cavity function : causality, passivity, stability

We now have to define the correct integration boundaries and study the analytical properties of the functions. The domain of integration for the frequency should of course include the propagative waves, which are the waves such that

$\omega \geqslant c|\mathbf{k}|$. However the full description of the radiation pressure should also take into account the evanescent waves, which have $\omega \leqslant c|\mathbf{k}|$. This contribution of the evanescent sector is made by an *analytical continuation* over the whole axis of real frequencies of the propagative waves.

In order to perform this analytical continuation, we choose a function having well defined *analyticity properties*: *causality*, *stability*, and *passivity*. The Airy function $g^p_{\mathbf{k}}(\omega)$ does not have the property of causality, but it can be written as a sum of a *retarded* and an *advanced* part :

$$g^p_{\mathbf{k}}(\omega) = 1 + f^p_{\mathbf{k}}(\omega) + f^p_{\mathbf{k}}(\omega)^* \tag{194}$$

$$\text{for} \quad f^p_{\mathbf{k}}(\omega) = \frac{\rho^p_{\mathbf{k}}(\omega)}{1 - \rho^p_{\mathbf{k}}(\omega)} \tag{195}$$

$$\text{and} \quad \rho^p_{\mathbf{k}}(\omega) = r^p_{\mathbf{k},1}(\omega) r^p_{\mathbf{k},2}(\omega) e^{-2\kappa_0 L} \tag{196}$$

where the function $\rho^p_{\mathbf{k}}(\omega)$ is given as the product of the reflection amplitudes $r^p_{\mathbf{k},1}(\omega)$ and $r^p_{\mathbf{k},2}(\omega)$ associated with each mirror, and the *propagation phaseshift* $e^{-2\kappa_0 L} = e^{-\kappa_0 L} e^{-\kappa_0 L}$ associated with the two-fold propagation of the modes from one mirror to the other through the cavity of length L. Partly because of causality, the *cavity function* $f^p_{\mathbf{k}}(\omega)$ is now an analytical function.

A way to understand the physical meaning of $\rho^p_{\mathbf{k}}(\omega)$ in the scattering approach is to say that it describes the reflection of the modes at the first mirror through $r^p_{\mathbf{k},1}(\omega)$, then the propagation of these modes over the cavity length by a factor $e^{-\kappa_0 L}$, and finally reaching the second mirror, these modes are reflected with a reflection coefficient $r^p_{\mathbf{k},2}(\omega)$ and propagate back to the first mirror along $e^{-\kappa_0 L}$. The cavity function $f^p_{\mathbf{k}}(\omega)$ can thus be seen as an open loop function.

The order of the product of these factors is not important in the plane-plane configuration, since all quantities are scalar, but in non-planar geometries, the diffraction process will be described by S-matrices instead of simple reflection coefficients, and the order of matrix multiplication will be important.

We now rewrite expression of the Casimir force (193) by including the cavity function $f^p_{\mathbf{k}}(\omega)$, and decompose it into a sum of two conjugated parts :

$$F = \mathcal{F} + \mathcal{F}^*, \qquad \text{for} \qquad \mathcal{F} = -A\hbar \sum_p \int \frac{d^2\mathbf{k}}{4\pi^2} \int \frac{d\omega}{2\pi} k_z f^p_{\mathbf{k}}(\omega) \tag{197}$$

Each part $\mathcal{F}$ and $\mathcal{F}^*$ has well defined analyticity properties.

Coming from the additional fluctuations arising from the noise lines, evanescent waves are present by necessity in the vicinity of a dispersive medium. Ordinary propagative waves correspond to real frequencies ω and real wave-vector k_z (or imaginary values for ξ and κ), whereas evanescent waves correspond to imaginary wave-vector k_z (or real values for ξ and κ).

The causal response function must obey the analyticity properties of causality, passivity, and stability in the physical domain of the complex frequency plane, according to equation (211). Causality is determined if we determine the conditions of extinction for waves propagating in a dissipative medium, and for evanescent waves confined to the vicinity of an interface between two media. We can find the properties of evanescent waves simply by extending the scattering amplitudes from propagative to evanescent waves. Let's consider for example the set of equations (145-148), with transmission coefficients $t_{01} = \left[\frac{\kappa_0}{\kappa_1}(1 - r_{01}^2)\right]^{\frac{1}{2}} = \bar{t}_{01}\frac{\kappa_0}{\kappa_1}$.

Then for evanescent waves coming from a non-absorbing medium $\epsilon_1 \in \mathbb{R}$, the quantity κ_1 is imaginary, and so κ_0 is real. Therefore z_{01}^{TE} is imaginary, which implies that $r_{01}, \bar{r}_{01} \in \mathbb{C}$ has a unit modulus, and hence that they are pure phases. The fields coming from within the medium is therefore totally reflected.

But since the transmission amplitudes t_{01} and $\bar{t}_{01}$ do not vanish, the fields coming from within the medium at an incident angle larger than the limit angle feed the evanescent field in vacuum. So we see that the unitary condition $|r|^2 + |t|^2 \leqslant 1$ does not apply, and the energy condition is complex to write for evanescent waves.

The condition of stability is established by considering TE evanescent waves, for which we have a condition on the modulus of the reflection amplitude $|r_{01}^{\mathrm{TE}}| \leqslant 1$. In section VI A 6 we will study *Wick's rotation* and how to properly switch from real frequencies ω to imaginary frequencies $\omega \to i\xi$, with $\mathrm{Re}\xi > 0$. But for now, it can be shown [123] that this property of stability is not only true for propagative waves or imaginary frequencies, but for the entire physical domain of the complex plane also. Eventually we can show that :

$$\mathrm{Re}\ \xi > 0 \quad \Longrightarrow \quad |r_{\mathbf{k}}^{\mathrm{TE}}(i\xi)| \leqslant 1 \quad \Longrightarrow \quad |\rho_{\mathbf{k}}^{\mathrm{TE}}(i\xi)| \leqslant 1 \tag{198}$$

This implies that the closed loop cavity function $f_{\mathbf{k}}^{p}(i\xi)$, which is built on the closed loop function $\rho_{\mathbf{k}}^{p}(i\xi)$, is analytic with no *pole* in the domain $\mathrm{Re}\ \xi > 0$. Here we define by pole the type of complex singularity behaving like ξ^{-n} when $\xi = 0$, for a given integer n.

This means that we are considering a closed loop function in a situation where the open loop function's gain is smaller than one, so that the closed loop function cannot reach the oscillation threshold.

The last inequality from equation (198) expresses the desired property of stability, which is obeyed by the fluctuations of vacuum scattered by the Fabry-Perot cavity : neither the mirrors nor the fields in the cavity can sustain any potential oscillation [124], which would otherwise be generated by a pole in the physical domain $\mathrm{Re}\ \xi > 0$.

Finally, this same equation (198) also implies a property of *passivity* [124], since the poles of the cavity function $f^p_{\mathbf{k}}(i\xi)$ are given by the equation $\rho^{\mathrm{TE}}_{\mathbf{k}}(i\xi) = 1$, which depends on the modulus *and* phase of $\rho^{\mathrm{TE}}_{\mathbf{k}}(i\xi)$.

Indeed, if the phase of $\rho^{\mathrm{TE}}_{\mathbf{k}}(i\xi)$ is such that it prevents the oscillation from reaching its threshold, then the stable closed loops can be formed out of open loop amplitudes lager than the unit modulus.

Therefore, by recalling equations (194-195), we can specify the property of passivity by the inequality :

$$\mathrm{Re}\,\xi > 0 \qquad \Longrightarrow \qquad g^p_{\mathbf{k}}(\omega) \geqslant 0 \tag{199}$$

The Airy function $g^p_{\mathbf{k}}(\omega)$, which is a spectral density defined on the propagative sector, hence remains positive over the whole physical domain of the complex frequency plane. If the condition of passivity was not met, then this Airy function would be positive only in the propagative sector, but not in the evanescent one.

So we have derived the necessary analyticity conditions : the property of causality is formulated by equations (194-196), the property of stability by equation (198), and the property of passivity by equation (199).

Now in the case of TM modes, the property of stability holds but passivity is not always respected. In order to show this let's consider a metallic *bulk*, which is an infinitely thick mirror, described by a plasma model with plasma frequency ω_p. It is described by the amplitudes given in equations (146) and (148), with $\epsilon_0 = 1$ for vacuum, and $\epsilon_1 = 1 - \frac{\omega_p^2}{\omega^2}$.

The violation of passivity happens in the divergence of $|r^{\mathrm{TM}}_{01}|$, which corresponds to a pole that is attained for the *surface plasmon* resonance condition :

$$z^{\mathrm{TM}}_{01} = -1 \qquad \text{and} \qquad \epsilon_1\kappa_0 + \kappa_1 = 0 \tag{200}$$

As we see in section VI A 9, surface plasmons are collective oscillations of electrons propagating on the interface between the vacuum and a conductive material. If we couple expression (200) with the *Brewster angle* for a vanishing reflection amplitude such that $z^{\mathrm{TM}}_{01} = +1$, we can then write the two expressions $(z^{\mathrm{TM}}_{01})^2 = +1$ such as :

$$\epsilon\xi^2 + c^2\mathbf{k}^2 = \epsilon^2\left(\xi^2 + c^2\mathbf{k}^2\right) \tag{201}$$

with $\epsilon_1 = \epsilon \neq 1$. This can also be written for the plasma frequency ω_p :

$$\omega^4 - \omega^2\left(\omega_p^2 + 2c^2\mathbf{k}^2\right) + \omega_p^2 c^2\mathbf{k}^2 = 0 \tag{202}$$

Then the solution of the equation above with larger frequency corresponds to the propagative waves having a Brewster angle ω_B, and the solution with smaller frequency corresponds to the evanescent waves having plasmon

resonance frequency ω_S :

$$\omega_B^2 = \frac{1}{2}\left(\omega_p^2 + 2c^2\mathbf{k}^2 + \sqrt{\omega_p^4 + 4c^4\mathbf{k}^4}\right) \tag{203}$$

$$\omega_S^2 = \frac{1}{2}\left(\omega_p^2 + 2c^2\mathbf{k}^2 - \sqrt{\omega_p^4 + 4c^4\mathbf{k}^4}\right) \tag{204}$$

The latter can also be written as the surface plasmon frequency, describing the well-known dispersion relation for surface plasmons :

$$\omega_S^2 = \frac{\omega_p^2}{2} \quad \text{for} \quad \omega_p^2 \ll c^2\mathbf{k}^2 \tag{205}$$

In this limit, we have $\kappa_0, \kappa_1 \sim |\mathbf{k}|$. This implies :

$$r_{01}^{\mathrm{TM}} \simeq \frac{1-\epsilon_1}{1+\epsilon_1} \simeq \frac{\omega_p^2}{2\omega^2 - \omega_p^2} \simeq \frac{\omega_S^2}{\omega^2 - \omega_S^2} \quad \Longrightarrow \quad \rho^{\mathrm{TM}} = \left(\frac{\omega_S^2}{\omega^2 - \omega_S^2}\right)^2 e^{-2\kappa_0 L} \tag{206}$$

The function ρ^{TM} is an open loop function. This means that the closed loop cavity function f^{TM} diverges for $\rho^{\mathrm{TM}} = 1$. Solving, we find :

$$\omega_{S\pm} = \omega_S\sqrt{1 \pm e^{-\kappa_0 L}} \tag{207}$$

The frequencies $\omega_{S\pm}$ are the perturbed plasmon frequencies that are the poles of the closed loop cavity function f^{TM}, lying outside the physical domain $\mathrm{Im}\,\omega < 0$. It means that the surface plasmons corresponding to the two mirrors are coupled by evanescent waves through the cavity, and are thus displaced from their usual plasmon frequency ω_S to perturbed frequencies $\omega_{S\pm}$.

Notice that we considered here a plasma model, and therefore no dissipation. It is possible to derive the same results in the dissipative case by using a Drude model for metals [120].

6. The Casimir force over imaginary frequencies and Cauchy's theorem

As we have now established the analyticity properties of the open and closed loop functions, we may now derive the expression of the Casimir force (197) over imaginary frequencies $\xi \equiv -i\omega$. This will be a mathematically equivalent expression, but much better suited to numerical evaluation. In order to do this, we use the *Cauchy theorem* from complex analysis over the complex plane, as shown on FIG. 20.

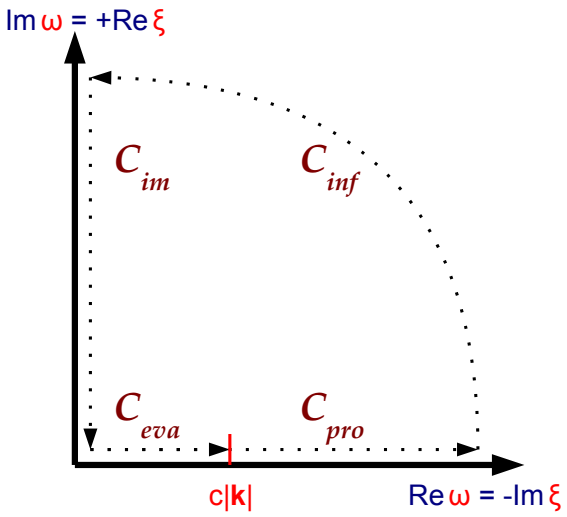

FIG. 20: Complex plane for which the expression of the Casimir force over real frequencies ω is switched to imaginary frequencies ξ. The quantities $\mathcal{C}_{\rm eva}$ and $\mathcal{C}_{\rm pro}$ correspond to the real evanescent and propagative waves, respectively. Then $\mathcal{C}_{\rm im}$ represents imaginary frequencies, and $\mathcal{C}_{\rm inf}$ represents the quarter circle with radius going to infinity.

We can define the contour integration $\mathcal{C}$ such as :

$$\mathcal{C} = \mathcal{C}_{\rm eva} + \mathcal{C}_{\rm pro} + \mathcal{C}_{\rm inf} + \mathcal{C}_{\rm im} \tag{208}$$

Assuming transparency of materials for $\omega \to \infty$, the contribution of $\mathcal{C}_{\rm inf}$ vanishes. Since Cauchy's theorem establishes :

$$\int \frac{d^2\mathbf{k}}{4\pi^2} \int_{\mathcal{C}} dz f^p_{\mathbf{k}}(z) = 0 \tag{209}$$

we deduce that the integrals over $\mathcal{C}_{\rm eva} + \mathcal{C}_{\rm pro}$ and $\mathcal{C}_{\rm im}$ are equal. Therefore we can write the Casimir force F as an integral expression over the real axis $[0, \infty[$ to an integral over the imaginary axis $[0, i\infty[$:

$$F = \mathcal{F} + \mathcal{F}^* \quad \text{for} \quad \mathcal{F} = -A \sum_p \int \frac{d^2\mathbf{k}}{4\pi^2} \int_0^{i\infty} \frac{d\omega}{2\pi} \hbar i \kappa f^p_{\mathbf{k}}(\omega) \tag{210}$$

Mathematically, the principle of causality implies that $\epsilon(\omega)$ is a function of ω in the upper-half of the complex frequency plane Im $\omega > 0$. Therefore we will often use imaginary frequencies ξ, as opposed to the real frequencies denoted by ω, by performing a *Wick's rotation* such that :

$$\omega \equiv i\xi \qquad \text{for} \quad \text{Re}\, \xi > 0 \tag{211}$$

Then the frequency is related to the wave vector by :

$$\epsilon\frac{\omega^2}{c^2} = k_x^2 + k_y^2 + k_z^2 = \mathbf{k}^2 + k_z^2 \tag{212}$$

So if we desire to switch to imaginary frequencies and then express k_z accordingly, we must be very cautious [120] in the way we chose the sign of the square root :

$$k_z = \pm\sqrt{\epsilon\frac{\omega^2}{c^2} - \mathbf{k}^2} \tag{213}$$

Indeed, k_z contains like ϵ an imaginary part, which means that the dephasing factor $\exp(ik_z z)$ which, as we will see, appears during the wave propagation in a given medium must include an extinction factor in the form of a *decreasing* exponential. This is done by selecting a specific root *depending on the direction of propagation* of the wave $\phi = \pm 1$:

$$k_z \equiv i\phi\kappa, \qquad \text{with} \quad \text{Re}\,\kappa > 0 \tag{214}$$

where from now on, we define :

$$\kappa = \sqrt{\epsilon\frac{\xi^2}{c^2} + \mathbf{k}^2} \tag{215}$$

Notice that the sign of k_z is changed under reflection with a medium, whereas the sign of κ does not. The wave's angle of incidence θ is thus written :

$$\cos\theta = \phi\frac{c\kappa}{n\xi} \tag{216}$$

If we write $\mathcal{F}$ in terms of complex frequencies $\xi = -i\omega$ (with Re $\xi > 0$ as usual), we find that $\mathcal{F} = \mathcal{F}^*$, so that the expression of the Casimir force over imaginary frequencies simplifies to :

$$F = 2\mathcal{F} = 2A\sum_p \int \frac{d^2\mathbf{k}}{4\pi^2}\int_0^\infty \frac{d\xi}{2\pi}\hbar\kappa f_{\mathbf{k}}^p(i\xi) \tag{217}$$

for $\mathbf{k} = \mathbf{k}_\perp = (k_x, k_z)$. This expression is equivalent to equation (197). The property of causality is ensured by the restriction to the first quadrant of the complex plane for frequencies Re $\omega > 0$ and Im $\omega > 0$.

Furthermore, when using imaginary frequencies we must change accordingly the permittivity function describing the material. One can derive equation (133) above for purely imaginary frequencies by the *Kramers-Kronig relations*,

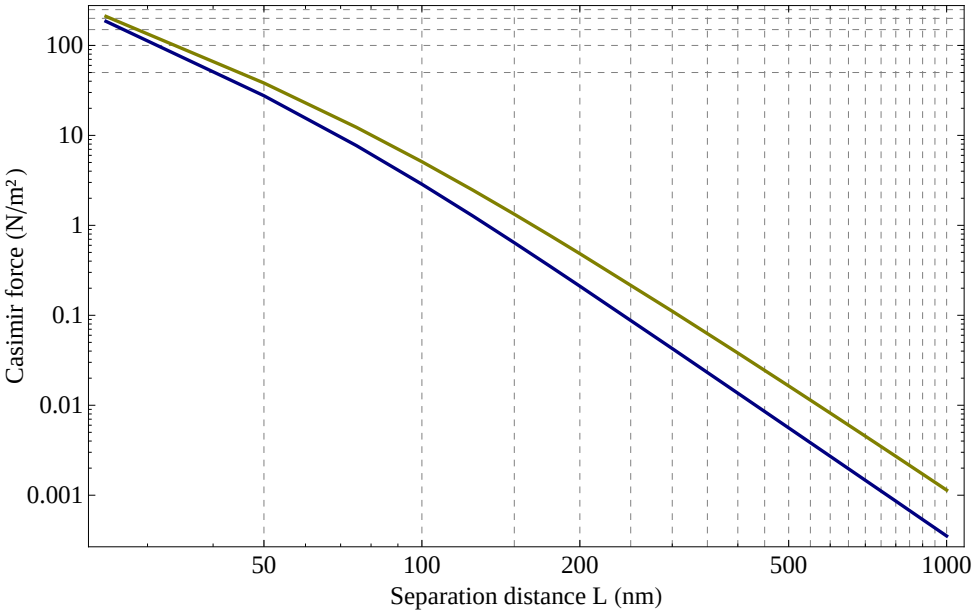

FIG. 21: Casimir force between two plates of gold (yellow curve) and two plates of intrinsic silicon (blue curve) forming a Fabry-Pérot cavity, as a function of their separation distance L. Notice that the force is in $\mathrm{N.m}^{-2} = \mathrm{pN}.\mu\mathrm{m}^{-2}$.

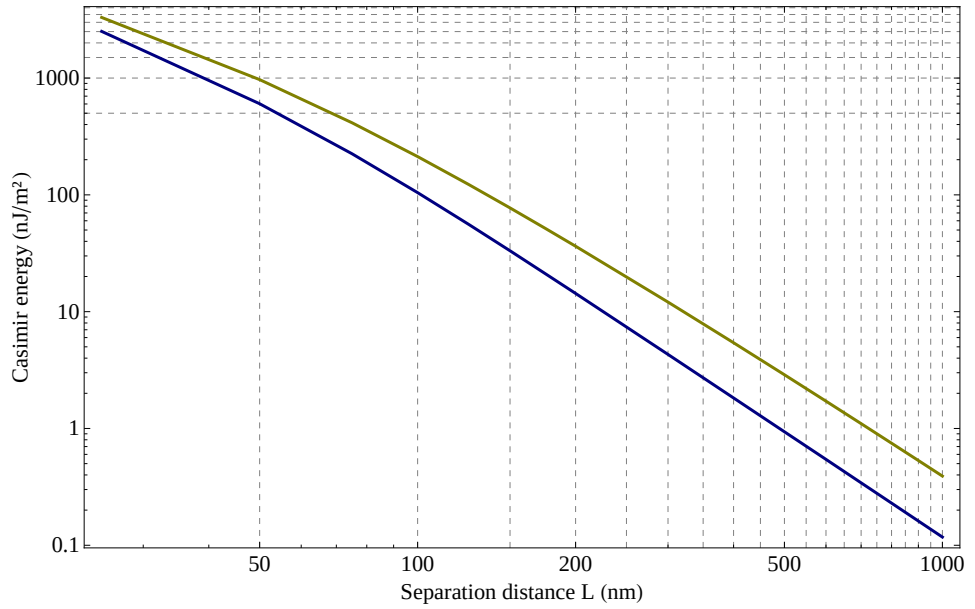

FIG. 22: Absolute value of the Casimir energy between two plates of gold (yellow curve) and two plates of intrinsic silicon (blue curve) forming a Fabry-Pérot cavity, as a function of their separation distance L.

which relate the real and imaginary parts to one another [125] by :

$$\epsilon(i\omega) = 1 + \frac{2}{\pi}\int_0^\infty \frac{\Omega\epsilon''(\Omega)}{\Omega^2+\omega^2}d\Omega \tag{218}$$

These relations imply causality, by performing the Wick rotation above in the complex frequency plane. Once expressed as a function of imaginary frequencies, the resonance frequencies do not appear in the plot of the permittivity.

Finally, we can choose the convention for the Casimir energy E to be negative and hence attractive :

$$E = -\int_L F(l)dl \tag{219}$$

so as to find the expression of the *Casimir energy* over real and imaginary frequencies, respectively :

$$E_{\mathbb{R}} = -A\sum_p \int \frac{d^2\mathbf{k}}{4\pi^2}\int_0^\infty \frac{d\omega}{2\pi}\frac{i\hbar}{2}\log\frac{1-\rho^p_{\mathbf{k}}(\omega)}{1-\rho^p_{\mathbf{k}}(\omega)^*} \tag{220}$$

$$E_{\mathbb{C}} = A\sum_p \int \frac{d^2\mathbf{k}}{4\pi^2}\int_0^\infty \frac{d\xi}{2\pi}\hbar\log\left[1-\rho^p_{\mathbf{k}}(i\xi)\right] \tag{221}$$

We present in FIG. 21 the Casimir force as a function of separation distance between two plates of gold, and two plates of intrinsic silicon. In FIG. 22 we also show the absolute value of the Casimir energy as a function of separation distance for these same plates. One can see the strong increase of both Casimir force and energy with shorter distances.

One can see through these plots that both the Casimir energy and force are much larger for gold than intrinsic silicon. We will see in the rest of this text that they are in general much larger for dielectrics than metals.

7. *Matsubara frequencies and Casimir for non-zero temperatures*

Had we not placed ourselves under the assumption of zero temperature, an extra factor equal to the r.h.s of equation (179) would appear in the integrand of equation (197). This integrand would then have poles at Matsubara frequencies [126, 127], which are given for an integer n by :

$$\xi_n = n\frac{2\pi k_B T}{\hbar} \tag{222}$$

In regards to the causality of the cavity function $f^p_{\mathbf{k}}(\omega)$, this implies that the physical domain of the complex plane is restricted to the first quadrant (Re $\xi > 0$ and Im $\xi > 0$), as shown on FIG. 20.

Indeed, the contribution of a non-zero temperature is taken into account by considering the field's thermal fluctuations [128], which are added to the zero temperature Casimir force. As already said in section VI A 4, for non-zero temperatures the pressure suffered by each mirror from equation (183) :

$$\langle P\rangle_{vac} = \sum_m \hbar\omega_m \cos^2\theta_m \quad \langle a^{\text{in}}_{m\ \text{L}} \cdot b^{\text{in}}_{m\ \text{L}} + a^{\text{out}}_{m\ \text{L}} \cdot b^{\text{out}}_{m\ \text{L}} - a^{\text{out}}_{m\ \text{R}} \cdot b^{\text{out}}_{m\ \text{R}} - a^{\text{in}}_{m\ \text{R}} \cdot b^{\text{in}}_{m\ \text{R}} \rangle_{vac} \tag{223}$$

must be multiplied by a factor $\mathcal{N}$ which comes from the r.h.s of the anticommutator seen in equation (179) :

$$\langle a^\phi_m \cdot b^\phi_m \rangle_{vac} \equiv \frac{\langle a^\phi_m b^\phi_m + b^\phi_m a^\phi_m \rangle_{vac}}{2} = \frac{1}{2} + \frac{1}{e^{\frac{\hbar\omega}{k_B T}} - 1} \tag{224}$$

which, in the case of vacuum at zero temperature, reduces to $\frac{1}{2}$. In order to switch to the case of non-zero temperatures, one must consider the vacuum energy as multiplied by this factor $\mathcal{N}$ such that :

$$\frac{1}{2}\hbar\omega \quad \longmapsto \quad \frac{1}{2}\hbar\omega \cdot \mathcal{N} \quad \text{for} \quad \mathcal{N} \equiv 1 + 2\overline{n}_\omega = 1 + 2\frac{1}{e^{\frac{\hbar\omega}{k_B T}} - 1} = \coth\frac{\hbar\omega}{2k_B T} \tag{225}$$

where the function $\overline{n}_\omega$ is the energy of the mean number of photons per mode given by Planck's law (4). This factor $\mathcal{N}$ appears in the integrand of the Casimir force, and when we switch from real to imaginary frequencies, it accounts for regularly spaced poles on the imaginary axis, which are in effect the Matsubara frequencies given in equation (222).

When calculating the force, these poles must be avoided by careful contours in the integration. The zero temperature limit is recovered [129] when :

$$\omega_T = \frac{2\pi k_B T}{\hbar} \to 0 \tag{226}$$

This implies that the thermal contribution to the zero-temperature Casimir force stays negligible for wavelengths λ smaller than the *thermal wavelength* λ_T :

$$\lambda_T = \hbar c\beta = \hbar c\frac{1}{k_B T} = \frac{2\pi c}{\omega_T} \tag{227}$$

At ambient temperature $T = 300\text{K}$, this wavelength is equal to $\sim 7\mu\text{m}$. So for distances beyond this value of $\lambda_T/2$, the thermal contributions to the zero temperature Casimir force become important.

Now since for non-zero temperatures, the pressure suffered by each mirror given in equation (183) must be multiplied by $\mathcal{N}$, we can derive the Casimir force in a straight-forward way by multiplying its integrand in equation (197) by this same factor $\mathcal{N}$:

$$F = A\hbar\sum_p \int \frac{d^2\mathbf{k}}{4\pi^2}\int_0^\infty \frac{d\omega}{2\pi} k_z \coth\frac{\hbar\omega}{2k_B T}\left[-f^p_{\mathbf{k}}(\omega) - f^p_{\mathbf{k}}(\omega)^*\right] \tag{228}$$

Then if we expand the function coth appearing in $\mathcal{N}$ as a series of exponentials depending on the thermal frequency ω_T, we get :

$$\mathcal{N} = 1 + 2\overline{n}_\omega = \coth\frac{\hbar\omega}{2k_BT} = \coth\frac{\pi\omega}{\omega_T} \simeq 1 + 2\sum_{n=1}^{\infty}\exp\left[-\frac{2n\pi(\omega+\eta)}{\omega_T}\right] \tag{229}$$

where the factor $\eta \in \mathbb{R}_+^*$ is to ensure uniform convergence and proper analyticity properties [129] such that $\eta \to 0$. Nevertheless, since by definition η is strictly positive, the frequency $\omega = 0$ is now part of the convergence domain of the series.

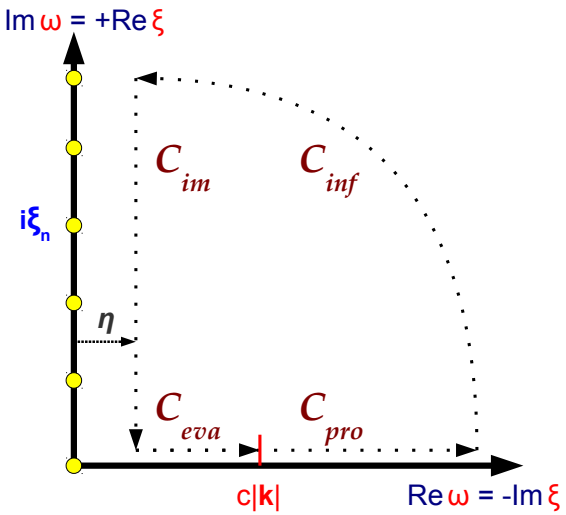

FIG. 23: Complex plane for which the expression of the Casimir force over real frequencies ω *at non zero temperature* is switched to imaginary frequencies ξ. The quantities $\mathcal{C}_{\rm eva}$ and $\mathcal{C}_{\rm pro}$ correspond to the real evanescent and propagative waves, respectively, $\mathcal{C}_{\rm im}$ represents imaginary frequencies, and $\mathcal{C}_{\rm inf}$ represents the quarter circle with radius going to infinity. The major difference with FIG. 20 is the convergence factor $\eta \to 0$ appearing in the series of exponential (229) so that the imaginary frequencies are not on the pure imaginary axis but on $z = i\xi + \eta$. Also notice the equidistant poles of the Matsubara frequencies along Im ω, including the one at $\omega = 0$.

Now following the traditional Lifshitz notation [130], we take :

$$\sum_n{}' \phi(n) \equiv \frac{1}{2}\phi(0) + \sum_{n=1}^{\infty}\phi(n) = \frac{1}{2}\sum_{n=-\infty}^{+\infty}\phi(|n|) \tag{230}$$

so that we obtain an expression of the Casimir force :

$$F = \lim_{n\to 0_+}\frac{\hbar A}{\pi}\sum_n{}'\sum_p\int\frac{d^2\mathbf{k}}{4\pi^2}\int_0^\infty d\omega\exp\left[-\frac{2n\pi(\omega+\eta)}{\omega_T}\right]k_z\left[-f_{\mathbf{k}}^p(\omega) - f_{\mathbf{k}}^p(\omega)^*\right] \tag{231}$$

On FIG. 24, we can see the Casimir energy as a function of separation distance L between two planes of intrinsic silicon Si, and between two planes of gold, at $T = 0$ K and at $T = 300$ K. One can see that a larger temperature

increases the Casimir energy. beyond 6μm, the Casimir energy associated with the dielectric profiles at $T = 300$ K is even larger than for the metallic profiles at $T = 0$ K.

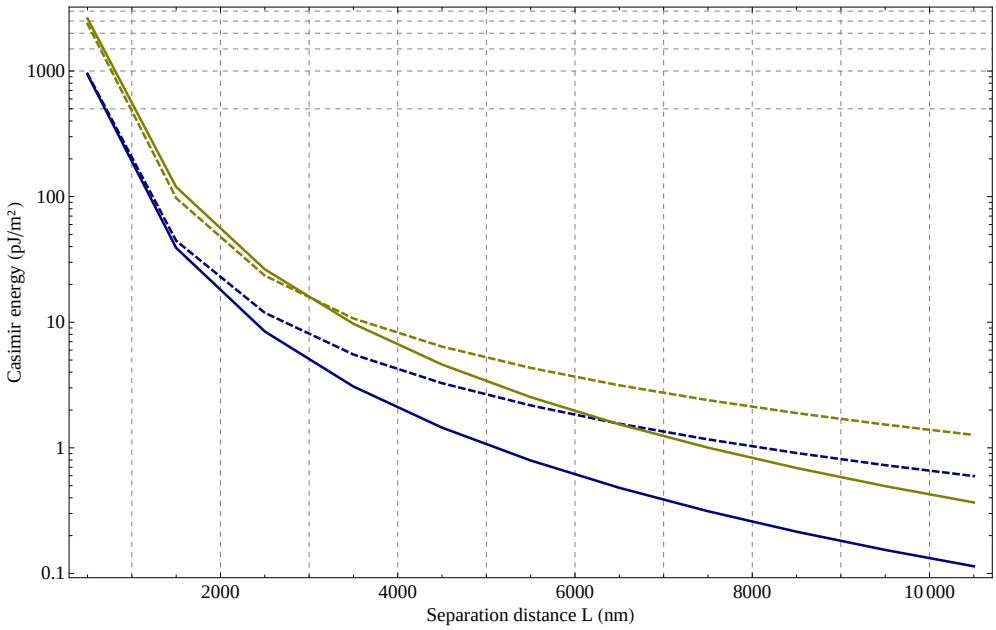

FIG. 24: Casimir energy as a function of separation distance L between two planes of intrinsic silicon Si (blue curve) and between two planes of gold Au (yellow curve), at zero temperature (respective solid curves) and at $T = 300$ K (respective dashed curves).

With the same conditions for analyticity than for case with zero temperature, we restrict ourselves to the first quadrant of the complex frequency plane Re $(\omega) = -$Im $(\xi) > 0$ and Im $(\omega) =$ Re $(\xi) > 0$. This is for the cavity function $f^p_{\mathbf{k}}(i\xi)$. In the case of the advanced function $f^p_{\mathbf{k}}(i\xi)^*$ appearing in equation (231), the contour must be found in Re $(\omega) = -$Im $(\xi) < 0$ and Im $(\omega) =$ Re $(\xi) > 0$.

Wanting to switch to imaginary frequencies, we use the Cauchy theorem. But the convergence factor η implies that the part corresponding to $\mathcal{C}_{\text{im}}$ from equation (208) is not the imaginary axis anymore but the axis $z = i\xi + \eta$, as shown on FIG. 23.

The function coth $\frac{\pi z}{\omega_T}$ which now is included in the expression of the Casimir force has poles on the imaginary axis. These are Matsubara frequencies (222), now rewritten as a function of the thermal frequency such that :

$$z_n = in\omega_T \tag{232}$$

We can therefore eventually write :

$$F = \lim_{n\to 0_+} \frac{\hbar A}{\pi} {\sum_n}' \sum_p \int \frac{d^2\mathbf{k}}{4\pi^2} \int_0^\infty d\xi e^{-\frac{2n\pi\eta}{\omega_T}} \kappa \left[e^{-\frac{2in\pi\omega}{\omega_T}} f^p_{\mathbf{k}}(i\xi + \eta) + e^{\frac{2in\pi\omega}{\omega_T}} f^p_{\mathbf{k}}(i\xi - \eta) \right] \tag{233}$$

When $f^p_{\mathbf{k}}(i\xi)$ does not contain poles on the imaginary frequency axis, one can set $\eta = 0$ in the functions $f^p_{\mathbf{k}}(i\xi + \eta)$ and $f^p_{\mathbf{k}}(i\xi - \eta)$. Often [129], the response functions can be ill-defined around $\omega = 0$.

8. Derjaguin's Proximity Approximation

The Proximity Approximation (PA), sometimes called Proximity Force Approximation (PFA), was originally developed [131] as a model to colloidal solutions, and later applied to nuclear physics [132] and Casimir physics [133, 134] as a planar approximation to non-planar geometries.

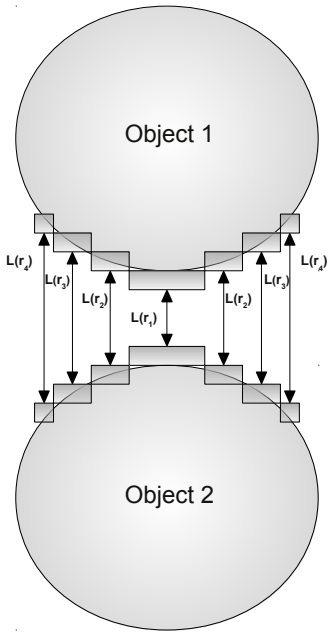

FIG. 25: Approximation of the arbitrary surfaces of two objects (here two spheres) in the Derjaguin Proximity Approximation. Notice that the unit cells locally approximating the arbitrary surfaces are taken as parallel to those of the opposite object.

It gives the general force of interaction F between two objects of arbitrary shapes, separated by a distance L which should not change too abruptly as one locally considers the surfaces of the objects. The PA takes the shape of the objects as a mosaic of small planar surfaces that are parallel to those of the other object, as shown in FIG. 25.

In this case, one can decompose the force F as a sum of local forces such that :

$$F = \int d^2\mathbf{r} \frac{F_{\text{p-p}}}{A} \left(L(\mathbf{r})\right) + \cdots \tag{234}$$

where $F_{\text{p-p}}/A$ is the force per unit area of the two parallel planar cells locally modeling the surface, and separated by the specific distance $L(\mathbf{r})$. In our case the Casimir force $F_{\text{p-p}}/A$ is easy to compute, the integral being replaced by a simple sum over all the different parallel unit cells.

9. Polariton coupling with surface-quasiparticles

So we saw that the Casimir energy is derived from the scattering matrices describing the mirrors. These S-matrices in turn depend on two factors : the mirrors' geometry and the permittivity of the mirrors' materials. In practice, the permittivity functions describing these materials can be non-trivial due to surface-plasmons (in the case of conductive materials), and phonons (in the case of dielectrics). These in turn can also be coupled to polaritons, which are *quasiparticles* arising from the strong coupling of electromagnetic waves and electric or magnetic dipole-carrying excitations.

By quasiparticles we understand collective excitations that occur in a complex system, which behaves as if it contained weakly interacting particles. In FIG. 26, we show a list of quasiparticles with their associated definitions.

One of the most common quasiparticles in solid state physics are *phonons*, which are collective excitations in a periodic and elastic array of atoms or molecules within a material. These are a quantized excitation states of the modes of vibrations of elastic and interacting groups of particles. Phonons account for important characteristics of certain materials, such as their electrical conductivities, or thermal and acoustical properties.

More precisely, phonons describe a type of vibrational motions in which a lattice uniformly oscillates at the same frequency. It appears through Fourier analysis, that these lattice oscillations can in turn be seen as superpositions of elementary oscillations themselves. These are seen classically as waves, but display a particle-like nature when quantized.

Let's consider a series of two alternating ions (or atoms) of respective mass m_1 and m_2, separated by a length a, and connected by springs of spring constant K. Then for the vibration wave-vector $k = 2\pi/\lambda$, we have two modes of vibration as shown on FIG. 27 :

$$\omega_{\pm}^2(\omega) = K\left(\frac{1}{m_1} + \frac{1}{m_2}\right) \pm K\sqrt{\left(\frac{1}{m_1} + \frac{1}{m_2}\right)^2 - \frac{4\sin^2(ka/2)}{m_1 m_2}} \tag{235}$$

These are the dispersion relations, which are the relations between frequency ω and wave-vector $k(\omega)$. In the case of the plus sign, we deal with an *optical mode*, and in the case of the minus sign, we deal with an *acoustic mode*,

Quasiparticle	Definition
Polariton	*Coupling of a photon with other quasiparticles*
Plasmon	*Quantum of high frequency oscillations of the electron density in conductive materials*
Phonon	*Quantum of a collective excitation in a periodic and elastic lattice of atoms in condensed matter*
Exciton	*Bound state found in electric insulators of an electron and hole that are attracted to each other by the electrostatic Coulomb force*
Polaron	*Fermionic quasiparticle composed of a charge and its accompanying polarization field (should not be confused with polariton, which is a bosonic quasiparticle)*
Bipolaron	*Bound pair of two polarons*
Hole	*Absence of electron in a valence band*
Holon/chargon	*Quasiparticle created by electron spin-charge separation*
Fracton	*Quantum of a collective excitation that has a fractal nature on a substrate*
Magnon	*Coherent excitation of electron spins in a material*
Majorana fermion	*Quasiparticle that is equal to its own antiparticle, appearing as a midgap state in some superconductors*
Phason	*Vibrational modes in a quasicrystal associated with atomic reconfiguration*
Soliton	*Self-amplifying independent excitation wave*
Spinon	*Quasiparticle which, along with holons, is created from electron spin-charge separation*

FIG. 26: List of some quasiparticles that are often encountered in condensed matter physics. These may substantially change the value of the Casimir energy or of the radiative heat transfer, depending on the chosen material of the plates, through its associated permittivity function.

as shown in FIG. 27. From a geometrical perspective, the optical modes are characterized by the two ions or atoms moving against each other, and the acoustic modes are characterized by the two ions or atoms moving together.

Based on equation (235), one can determine the speed of propagation of an acoustic phonon, which is the speed of sound in that given material, as the slope of the acoustic dispersion relation $\partial\omega(k)/\partial k$.

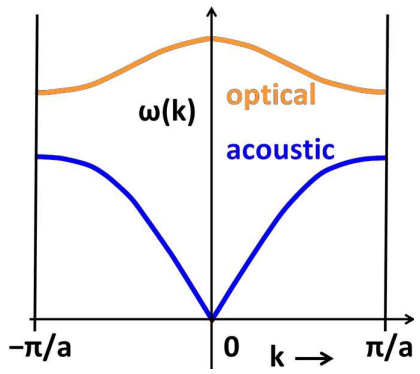

FIG. 27: Dispersion relation for phonons described through one-dimensional series of two alternating ions or atoms, as shown in equation (235). The boundaries at $-\pi/a$ and π/a are those of the first Brillouin zone[135].

In conductive materials such as metals, there exists high frequency oscillations of the electron density which are called *plasma oscillations*. These are practically described as a perturbation in the dielectric function of a free electron gas. The quantization of these plasma oscillations lead to quasiparticles called *plasmons*. So a plasmon is a quantum of plasma oscillation, just as phonons are quanta of mechanical vibrations, and photons are quanta of light (albeit photons are real particles, not quasiparticles).

Surface plasmons are guided waves trapped at the interface between a dielectric and a metal. They are created by the collective reactions of free electrons in a metal to electromagnetic perturbations. These perturbations can come from incident high energy electrons, or by electromagnetic radiation. For this reason, surface plasmons are both displaying the characteristics of electromagnetic waves and of surface charges, as shown in FIG. 28.

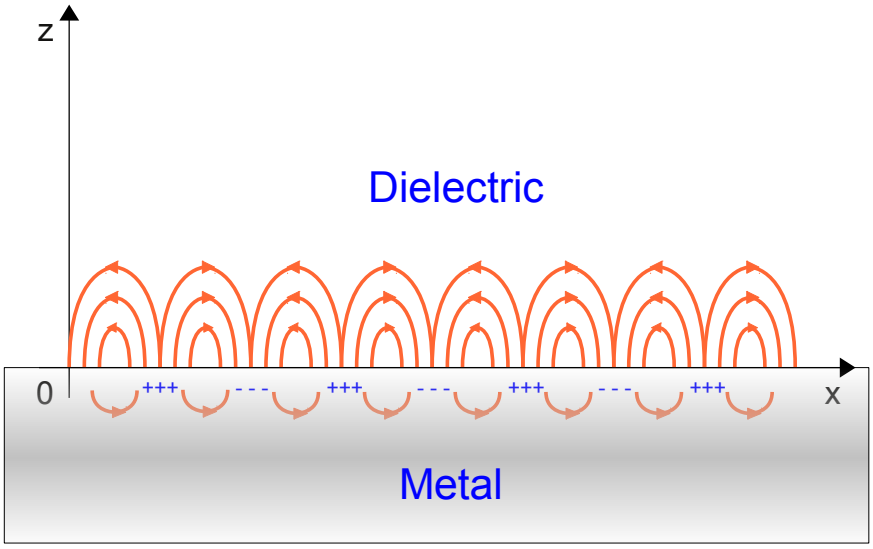

FIG. 28: Electric field lines and distributions of charges for a surface-plasmon located on the interface between a metal and a dielectric.

Each surface-plasmon has an evanescent field that is perpendicular to the surface [136, 137], and which decays exponentially on each side of the interface, both in the metal and in the dielectric. Nevertheless, it is noteworthy that the depth of the field's penetration within the metal is considerably smaller than for the dielectric due to the screening effect of the free charges.

It is noteworthy that surface-plasmons have a lower energy than plasmons present within the material bulk, since these quantize the oscillations of the electrons around positive ions present within the metal. If surface-plasmons couple with a photon, the produced excitation is called a surface-plasmon polariton. Surface-plasmon polaritons

propagate along the surface of a metal until their associated energy is lost either by dissipation or by radiation in free-space.

When surface-plasmons are created by incident high-energy electrons impacting the metal, the energy from the scattering of the electrons is transferred into the material, and the component of the scattering vector parallel to the surface brings about the formation of a surface plasmon. However the evanescent nature of surface-plasmons implies that the momenta of incident light and of surface-plasmons do not match. One can then artificially couple photons with surface-plasmons so as to create surface-plasmon polaritons, by using a grating coupler to match the respective photon and the surface-plasmon wave-vectors. This is done by increasing the parallel wave-vector component proportionally to the grating period, as shown in FIG. 29. This process can also be viewed as a tool to detect surface defects and rugosity, since the slightest corrugation or groove depth is enough to generate a surface-plasmon polariton.

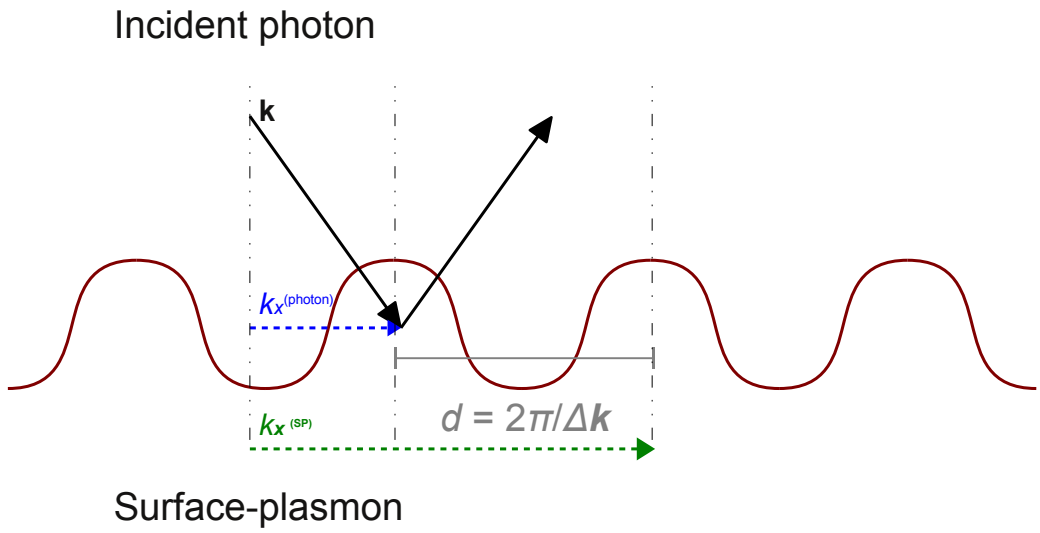

FIG. 29: Example of a sinusoidal grating coupler used to generate surface-plasmon polaritons by matching the wave-vectors $\mathbf{k}$ of the incident photons in their parallel component k_x^{photon} with those of the surface-plasmons k_x^{SP}, through an increase proportional to the grating period d.

When the wave-vector or frequency of the incident photons matches the frequency of the electrons on the material's surface which naturally oscillate against the positive atoms' nuclei, the surface-plasmons are described as resonant. So *surface-plasmon resonances* are the resonant and collective oscillation of the valence electrons within the metal bulk, which are excited by the incident photons. When surface-plasmon resonances are confined to nanostructures below the micrometer range, we speak of *localized* surface-plasmon resonances.

Finally, *excitons* are quasiparticles that can be seen as pairs of electron-hole bound by the Coulomb force (see FIG. 26). These exist in semiconductors, and in electric insulators such as dielectrics. In general, we can divide excitons in two large groups : *Mott-Wannier excitons* whose radii are much larger than the material's lattice constant, and *Frenkel excitons* whose radii are much smaller and which appear for small values of the material's dielectric constant.

Excitons are created when a semiconductor or dielectric absorbs a photon, thus exciting an electron from the valence band into the conduction band. This produces a localized and positively-charged hole, to which the electron in the conduction band is attracted by the Coulomb force. The produced exciton has a smaller energy than the unbound electron and hole, due to the fact that this attraction has an energy balance at equilibrium.

One can also describe excitons as neutral polarization waves within the material. For semiconductors, the presence of excitons appears as a peak of absorption at an energy smaller than the energy of the electronic band gap. The difference between these two energies is the exciton's binding energy, and the peak can be observed only when this binding energy is small compared to the thermal energy.

Now that we have defined phonons, excitons, and surface-plasmons, we can study their coupling with polaritons, which are bosonic quasiparticles arising from the strong coupling between a photon and an electric or magnetic dipole-carrying excitation. In general, polaritons and their associated excitation depend on the frequency of the photon involved :

- *Phonon-polaritons* result from the strong coupling of an infrared photon with an optical phonon.
- *Exciton-polaritons* result from the strong coupling of a visible photon with an exciton.
- *Surface-plasmon-polaritons* result from the strong coupling of surface-plasmons with photons of various frequencies.

Polaritons manifest the *principle of avoided crossing* (or *level repulsion*), and hence display the crossing of the dispersion of light with interacting resonances. This is important when we consider dielectrics such as silica glass SiO_2, which has resonances at $\lambda = 8.75\mu$m and $\lambda = 21\mu$m, or SiC [138], which has a resonance at $\lambda = 10.5\mu$m, as shown in FIG. 12.

10. Conclusion

Since we have seen that the Casimir force is derived from the Fresnel-Stokes amplitudes, the first step in order to compute it is to obtain an accurate permittivity function describing the mirrors's materials. We have seen how the complex permittivity of a given material could be obtained either from tables of optical constants available in literature [111, 112], or from specific models. These models can all be derived from equation (133), depending on the material's dissipation and number of oscillators or resonance frequencies. The one-oscillator Drude and plasma models are used to describe metals, the one-oscillator Drude-Lorentz model is used to describe materials such as intrinsic Si or SiC, and the two-oscillators Sellmeier model is used to describe transparent dielectrics such as SiO_2 glass.

After a careful choice of the transverse wave vector in equation (215), we went on to define the Fresnel-Stokes amplitudes for reflection and transmission coefficients of TE- and TM-polarized waves in equation (145-148). These results were generalized through S-matrices and T-matrices in equations (149) and (151) for plane mirrors. Then based on a violation of the unitary property of the S-matrix in equation (162), we derived a scattering formalism for the quantum description of the fields within the Fabry-Pérot cavity. This was done by taking into account the additional fluctuations associated with the noise lines coming from the absorption, and related to the contribution of evanescent waves. To measure this anticommutation of the fields, we defined the Airy function in equation (173), which showed that the fields commutators inside the cavity were not the same than those of the input and output fields.

We then established the Casimir force in equation (197) as a summation over all the modes, both evanescent and propagative, contributing to the pressure from vacuum outside of the Fabry-Pérot cavity being greater than the pressure inside, hence giving rise to an attractive force between the two plates. We saw how this pressure given in equation (186-187) was derived from the quantum average of the T_{zz} Maxwell stress tensor in equation (182), with commutators of the input and output fields within the cavity multiplied by the Airy function.

In order to find correct integration boundaries for these modes, and especially in order to perform an analytical continuation over the frequencies of propagative waves ($\omega \geqslant c|\mathbf{k}|$) to those of evanescent waves ($\omega \leqslant c|\mathbf{k}|$), we had then to substitute our Airy function by a function having well-defined analyticity properties : the property of causality was formulated by equations (194-196), the property of stability by equation (198), and the property of passivity by equation (199).

Finally we generalized the Casimir force to imaginary frequencies through the Cauchy theorem in equation (217), and integrated to derive the Casimir energy in equations (220-221). All this formalism having been performed for zero temperatures only, we derived in equation (231) the expression of the Casimir force for non-zero temperatures, as a function of Matsubara frequencies. This is because the zero-point energy for non-zero temperatures is multiplied by a factor (225) given by the mean number of photons per mode, according to Planck's law (4). Then we spoke of Derjaguin's Proximity Approximation, and of its domain of validity for non-planar surfaces. Finally, we concluded by a brief review of phonons, surface-plasmons, excitons, and their respective coupling with polaritons.

B. Casimir effect in non-planar geometries

1. *The RCWA method and associated reflection matrix for gratings*

In the previous section we have introduced the expression of the Casimir force between planar surfaces. The expression of the force is derived from the quantum vacuum fluctuations which are at the origin of vacuum radiation pressure. This pressure is expressed *via* the Maxwell stress tensor acting on the plates forming the Fabry-Pérot cavity.

In this formalism, the vacuum pressure was fully described by the Fresnel stokes amplitudes contained within the cavity's Airy function. This Airy function, and its associated open loop function $f^p_{\mathbf{k}}(\omega)$ displaying well-defined analyticity properties, could be written as a scalar function. Indeed the Casimir force acting on the plane mirrors originates in simple *specular* reflection, which leaves polarizations and transverse wavevectors invariant.

From now on we will consider infinitely long, one-dimensional periodic gratings separated by a vacuum slit, as shown on FIG. 30. One-dimensional implies the grating to be periodic in the x-direction and constant in the y-direction. Their temperature is assumed to be zero. Furthermore we consider the gratings' support to be bulks of infinite thickness along the $z-$axis.

The geometrical parameters are the corrugation period d, the filling factor p, the groove depth a, the gap d_1, the gratings' distance of separation L, and the lateral displacement δ along the x-axis.

As already mentioned, corrugated profiles are of importance to nanotechnological applications [54]. This especially concerns nanoelectromechanical systems (NEMS) and microelectromechanical systems (MEMS) design (see FIG. 2), as these devices are often subject to the problem of *stiction* [59, 139, 140] due to the Casimir force.

In the case of gratings, the expression of the Casimir force becomes more complex due to the fact that the scattering of the electromagnetic field on the grating is non specular, meaning the reflection process couples different polarizations and transverse wavevectors. From diffraction theory it is known that above and below the grooves, the solution for the electromagnetic field is given by a *Rayleigh expansion*.

This leads to a number of coupled modes equal to $2N+1$, which is the number of coefficients present in a Rayleigh expansion for an incident monochromatic wave, as the longitudinal field components above the grating are written as such an expansion. Following the procedure outlined in [28], we now derive the S-matrix associated with those gratings according to the *Rigorous Coupled-Wave Analysis* (RCWA) method described in [85].

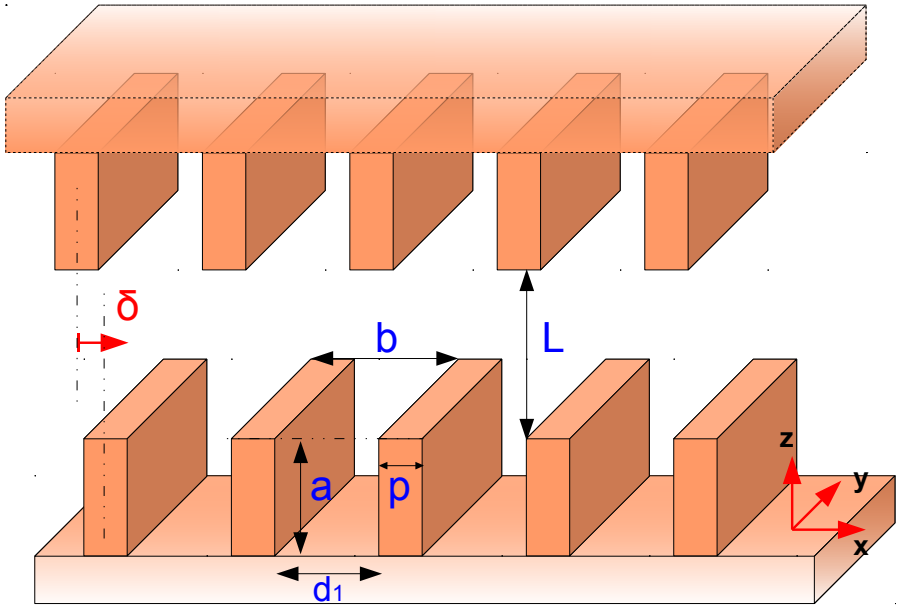

FIG. 30: Main geometrical parameters of corrugated plates forming a Fabry-Pérot cavity : we denote by d the corrugation period, p the filling factor (often expressed as a percentage of the period), a the groove depth, d_1 the space between corrugation ridges, L the separation distance of closest approach, δ the lateral translation along the $x-$axis of the plates before one another. Note that the plates are extended to infinity in both the $x-$ and $y-$direction.

Using the $t-$ and $y-$invariance of the problem, we can consider the electric and magnetic fields only along the x and z directions :

$$E_i(x,y,z,t) = E_i(x,z)e^{i(k_y y-\omega t)} \tag{236}$$

$$H_i(x,y,z,t) = H_i(x,z)e^{i(k_y y-\omega t)} \tag{237}$$

The mathematical advantage of considering infinite *periodic* nanogratings is that we can restrain ourselves in our derivation of the Casimir energy to only one given period as the *first Brillouin zone*. Therefore we consider the wave vector as confined to $0 < k_x < 2\pi/d$. We now need to find the longitudinal components outside the corrugated region ($z > a$), and inside the transmitted region ($z \leqslant 0$).

$z > a$:

$$E_y(x,z) = I_p^{(e)} e^{i(\alpha_p x - \beta_p^{(1)} z)} + \sum_{n=-\infty}^{+\infty} R_{np}^{(e)} e^{i(\alpha_n x + \beta_n^{(1)} z)} \tag{238}$$

$$H_y(x,z) = I_p^{(h)} e^{i(\alpha_p x - \beta_p^{(1)} z)} + \sum_{n=-\infty}^{+\infty} R_{np}^{(h)} e^{i(\alpha_n x + \beta_n^{(1)} z)} \tag{239}$$

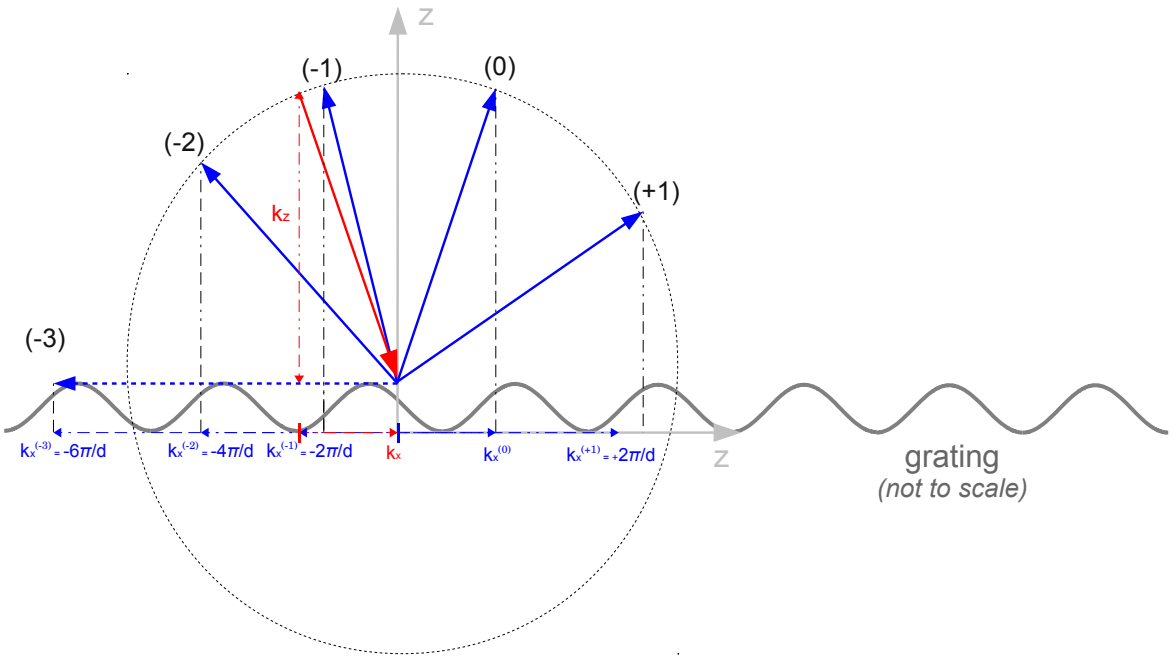

FIG. 31: Process of mode diffraction on (not to scale) gratings. After fixing an order of diffraction N so that both $p, n \in [-N, ..., -2, -1, 0, +1, +2, ..., +N]$, we consider for each incident mode p its associated n diffracted modes on the grating. Each n diffracted mode is generated along a specific orientation given by its lateral component $k_x^{(n)} = 2\pi n/d$ belonging to the associated Brillouin zone, and by its amplitude being fixed at $|\mathbf{k}| = \omega/c$. This amplitude appears as the radius of the dashed circle within each diffracted mode has an amplitude $|\mathbf{k}| < \omega/c$, and is thus propagative. When the diffracted modes exceed this limit $|\mathbf{k}| > \omega/c$, they belong to the evanescent sector. This is illustrated by the dashed mode, corresponding to $n = (-3)$. Notice that a *specular reflection* may appear when the incident mode has an angle of incidence equal to the *Bragg angle*, in which case the first diffracted mode $n = (0)$ comes back in the same direction than the incident mode. The Casimir energy in equation (296) is derived from an integration over all the modes components k_x, k_z, ω, within each Brillouin zone $k_x \in [0, 2\pi/d]$.

$$\alpha_p = k_x + \frac{2\pi p}{d} \quad \text{and} \quad \alpha_n = k_x + \frac{2\pi n}{d} \tag{240}$$

$$\beta_p^{(1)2} = \omega^2 - k_y^2 - \alpha_p^2 \quad \text{and} \quad \beta_n^{(1)2} = \omega^2 - k_y^2 - \alpha_n^2 \tag{241}$$

$$\beta_n^{(2)2} = \omega^2 \epsilon\mu - k_z^2 - \alpha_n^2 \tag{242}$$

where p is an integer. For each incident mode p we consider $n \in \{2N+1\}$ diffracted modes, where $2N+1$ is the number of Rayleigh coefficients, as shown on FIG. 31. For $n = 0$, specular diffraction reflection is recovered. Below the grating the field obeys the following expansion :

$z \leqslant 0$:

$$E_y(x, z) = \sum_{n=-\infty}^{+\infty} T_{np}^{(e)} e^{i(\alpha_n x - \beta_n^{(2)} z)} \tag{243}$$

$$H_y(x,z) = \sum_{n=-\infty}^{+\infty} T_{np}^{(h)} e^{i(\alpha_n x - \beta_n^{(2)} z)} \tag{244}$$

I_p, R_{np}, T_{np} are the incidence, reflection, and transmission matrices respectively, all of dimension $2N+1$.

The sums are performed over all integers n. By symmetry, the other field components of the electric and magnetic fields can each be expressed through the z-components of *both* fields. For example, we have :

$$E_x = \frac{ik_y}{\kappa^2}\partial_x E_y + \frac{i\omega}{\kappa^2}\partial_z H_y \tag{245}$$

$$H_x = \frac{ik_y}{\kappa^2}\partial_x H_y + \frac{i\omega\epsilon}{\kappa^2}\partial_z E_y \tag{246}$$

$$\kappa^2 = \frac{\epsilon\omega^2}{c^2} - k_y^2 \tag{247}$$

We now need to calculate the reflection coefficients R_{np} associated with these rectangular gratings. First, we must rewrite the Maxwell equations inside the corrugated region $0 < z < a$ through a set of first-order differential equations :

$$\partial_z \mathbf{F} = \mathbf{M}\mathbf{F} \tag{248}$$

for $\mathbf{F}^\top = (E_y, E_x, H_y, H_x)$ and $\mathbf{M}$ a constant square matrix of dimension $8N+4$. The solution of the fields is then of the form :

$$\mathbf{F}(z) = e^{\mathbf{M}z}\mathbf{F}(0) \tag{249}$$

From now on, our strategy will be to write the fields inside the grating in this form, and match them by continuity relations for each E_y, H_y, E_x, H_x, with our previous equations at boundary $z = a$ for $z > a$, and at boundary $z = 0$ for $z \leqslant 0$. Eventually we will find solutions written in terms of transmission matrices T_{np}, which we will rewrite in terms of the wanted reflection matrices R_{np} through the continuity relations at $z = a$.

We start by writing the four continuity relations for $z = 0$, and the other four for $z = a$, and match them with the solutions to Maxwell's equation. The electromagnetic field inside the corrugation region $0 < z \leqslant a$ can be written as :

$$E_y = \sum_n S_n^{e_y}(z) e^{i\alpha_n x} \tag{250}$$

$$E_x = \sum_n S_n^{e_x}(z) e^{i\alpha_n x} \tag{251}$$

$$H_y = \sum_n S_n^{h_y}(z) e^{i\alpha_n x} \tag{252}$$

$$H_x = \sum_n S_n^{h_x}(z) e^{i\alpha_n x} \tag{253}$$

We then find the quantities $\{S_n^{e_y}(0), S_n^{e_x}(0), S_n^{h_y}(0), S_n^{h_x}(0)\}$ by applying the following boundary conditions at $z = 0$:

Continuity of E_y *at* $z = 0$:

$$S_n^{e_y}(0) = T_{np}^{(e)} \tag{254}$$

Continuity of E_x *at* $z = 0$:

$$S_n^{e_x}(0) = -\alpha_n \frac{k_y}{\kappa^2} T_{np}^{(e)} + \frac{\omega}{\kappa^2} \beta_n^{(2)} T_{np}^{(h)} \tag{255}$$

Continuity of H_y *at* $z = 0$:

$$S_n^{h_y}(0) = T_{np}^{(h)} \tag{256}$$

Continuity of H_x *at* $z = 0$:

$$S_n^{h_x}(0) = -\alpha_n \frac{k_y}{\kappa^2} T_{np}^{(h)} - \frac{\epsilon\omega}{\kappa^2} \beta_n^{(2)} T_{np}^{(e)} \tag{257}$$

Likewise, we can use equations (250-253) to find $\{S_n^{e_y}(a), S_n^{e_x}(a), S_n^{h_y}(a), S_n^{h_x}(a)\}$ by applying the boundary conditions at $z = a$. The continuity of E_y at $z = a$ can be written :

$$\sum_n S_n^{e_y}(z) e^{i\alpha_n x}\Big|_{z=a} = \left(I_p^{(e)} e^{i(\alpha_p x - \beta_p^{(1)} z)} + \sum_n R_{np}^{(e)} e^{i(\alpha_n x + \beta_n^{(1)} z)} \right)\Big|_{z=a} \tag{258}$$

which implies that for $n = p$ we have $S_p^{e_y}(a) = I_p^{(e)} e^{-i\beta_p^{(1)} a} + R_{pp}^{(e)} e^{i\beta_p^{(1)} a}$, and for $n \neq p$ we have $S_n^{e_y}(a) = R_{np}^{(e)} e^{i\beta_n^{(1)} a}$. This can be done in a similar way for $S_n^{e_x}(a), S_n^{h_y}(a)$, and $S_n^{h_x}(a)$, so that after some calculations we get for $\kappa_0^2 = \omega^2/c^2 - k_z^2$:

Continuity of E_y *at* $z = a$:

$$R_{np}^{(e)} = e^{-i\beta_n^{(1)} a} \left(S_n^{e_y}(a) - \delta_{np} I_p^{(e)} e^{-i\beta_p^{(1)} a} \right) \tag{259}$$

Continuity of E_x *at* $z = a$:

$$S_n^{e_x}(a) = -\frac{k_y}{\kappa_0^2}\left(\alpha_n R_{np}^{(e)} e^{i\beta_n^{(1)}a} + \delta_{np}\alpha_p I_p^{(e)} e^{-i\beta_p^{(1)}a}\right) - \frac{\omega}{\kappa_0^2}\left(\beta_n^{(1)} R_{np}^{(h)} e^{i\beta_n^{(1)}a} - \delta_{np}\beta_p^{(1)} I_p^{(h)} e^{-i\beta_p^{(1)}a}\right) \tag{260}$$

Continuity of H_y *at* $z = a$:

$$R_{np}^{(h)} = e^{-i\beta_n^{(1)}a}\left(S_n^{h_y}(a) - \delta_{np} I_p^{(h)} e^{-i\beta_p^{(1)}a}\right) \tag{261}$$

Continuity of H_x *at* $z = a$:

$$S_n^{h_x}(a) = -\frac{k_y}{\kappa_0^2}\left(\alpha_n R_{np}^{(h)} e^{i\beta_n^{(1)}a} + \delta_{np}\alpha_p I_p^{(h)} e^{-i\beta_p^{(1)}a}\right) - \frac{\omega}{\kappa_0^2}\left(\beta_n^{(1)} R_{np}^{(e)} e^{i\beta_n^{(1)}a} - \delta_{np}\beta_p^{(1)} I_p^{(e)} e^{-i\beta_p^{(1)}a}\right) \tag{262}$$

We now come back to Maxwell's equations (248), and write the l.h.s as :

$$\partial_z E_y = i\omega H_x + \frac{k_z}{\omega\epsilon(x)}\left(\partial_x H_y - ik_y H_x\right) \tag{263}$$

$$\partial_z E_x = \partial_x\left(\frac{\partial_x H_y - ik_y H_x}{i\omega\epsilon(x)}\right) - i\omega H_y \tag{264}$$

$$\partial_z H_y = \frac{i}{\omega}\left(k_y^2 - \epsilon\omega^2\right) E_x - \frac{k_y}{\omega}\partial_x E_y \tag{265}$$

$$\partial_z H_x = i\omega\epsilon(x) E_y + \partial_x\left(\frac{ik_y E_x - \partial_x E_y}{i\omega}\right) \tag{266}$$

Indeed, since the dielectric function $\epsilon(x)$ is periodic for a grating with period d, it can be written as a Fourier series :

$$\epsilon(x) = \sum_{m=-N}^{N} \varepsilon_m e^{2\pi imx/d} \qquad \text{and} \qquad \frac{1}{\epsilon(x)} = \sum_{m=-N}^{N} \widetilde{\varepsilon}_m e^{2\pi imx/d} \tag{267}$$

We can now substitute equations (250-253) into equations (263-266) in order to determine $\partial_z S_n^{e_y}$, $\partial_z S_n^{e_x}$, $\partial_z S_n^{h_y}$, $\partial_z S_n^{h_x}$.

We first derive $\partial_z S_n^{e_y}$. We use the permittivity expressions (267) together with equations (252-253), and substitute those in equation (263). This gives :

$$\sum_n \partial_z S_n^{e_y}(z) e^{i\alpha_n x} = \sum_n i\omega S_n^{h_x}(z) e^{i\alpha_n x} + \frac{k_y}{\omega}\sum_m \widetilde{\varepsilon}_m e^{2\pi imx/d}\left(\sum n' i\alpha_{n'} S_{n'}^{h_y}(z) e^{i\alpha_{n'}x} - ik_y \sum n' S_{n'}^{h_x}(z) e^{i\alpha_{n'}x}\right) \tag{268}$$

Then we can take the series index $n' = n - m$ and compare it with the n-th coefficient of the sum. Proceeding in a similar way for $\partial_z S_n^{e_x}, \partial_z S_n^{h_y}$, and $\partial_z S_n^{h_x}$, we find :

$$\partial_z S_n^{e_y} = i\omega S_n^{h_x}(z) - \frac{ik_y}{\omega} \sum_m \widetilde{\varepsilon}_m \left(k_y S_{n-m}^{h_x} - \alpha_{n-m} S_{n-m}^{h_y} \right) \tag{269}$$

$$\partial_z S_n^{e_x} = \frac{i\alpha_n}{\omega} \sum_m \widetilde{\varepsilon}_m \left(-k_y S_{n-m}^{h_x} + \alpha_{n-m} S_{n-m}^{h_y} \right) - i\omega S_n^{h_y} \tag{270}$$

$$\partial_z S_n^{h_y} = \frac{ik_y^2}{\omega} S_n^{e_x} - i\omega \sum_m \varepsilon_m S_{n-m}^{e_x} - \frac{ik_y}{\omega} \alpha_n S_n^{e_y} \tag{271}$$

$$\partial_z S_n^{h_x} = \frac{i\alpha_n}{\omega} \left(k_y S_n^{e_x} - \alpha_n S_n^{e_y} \right) + i\omega \sum_m \varepsilon_m S_{n-m}^{e_y} \tag{272}$$

These four expressions form together the vector $\partial_z \mathbf{F}$ from the l.h.s of equation (248), which is of dimension $8N + 4$. For a fixed $n = m + n'$, it can be written as :

$$\partial_z \mathbf{F} = \begin{pmatrix} \partial_z S^{(n,1)} \\ \partial_z S^{(n,2)} \\ \partial_z S^{(n,3)} \\ \partial_z S^{(n,4)} \\ \vdots \end{pmatrix} = \begin{pmatrix} i\omega\delta_{n,n'} S^{(n',4)}(z) - \frac{ik_y}{\omega} \widetilde{\varepsilon}_{n-n'} \left(k_y S^{(n',4)} - \alpha_{n'} S^{(n',3)} \right) \\ \frac{i\alpha_n}{\omega} \widetilde{\varepsilon}_{n-n'} \left(-k_y S^{(n',4)} + \alpha_{n'} S^{(n',3)} \right) - i\omega\delta_{n,n'} S^{(n',3)} \\ \frac{ik_y^2}{\omega} \delta n, n' \left(k_y S^{(n',2)} - \alpha_{n'} S^{(n',1)} \right) - i\omega\varepsilon_{n-n'} S^{(n',2)} \\ \frac{i\alpha_n}{\omega} \delta n, n' \left(k_y S^{(n',2)} - \alpha_{n'} S^{(n',1)} \right) + i\omega\varepsilon_{n-n'} S^{(n',1)} \end{pmatrix} \tag{273}$$

which is to be matched with the r.h.s of equation (248) :

$$\mathbf{MF} = \begin{pmatrix} M^{(n,1;n',1)} & M^{(n,1;n',2)} & M^{(n,1;n',3)} & M^{(n,1;n',4)} & M^{(n,1;n'+1,1)} & \dots \\ M^{(n,2;n',1)} & M^{(n,2;n',2)} & M^{(n,2;n',3)} & M^{(n,2;n',4)} & & \\ M^{(n,3;n',1)} & M^{(n,3;n',2)} & M^{(n,3;n',3)} & M^{(n,3;n',4)} & & \\ M^{(n,4;n',1)} & M^{(n,4;n',2)} & M^{(n,4;n',3)} & M^{(n,4;n',4)} & & \\ M^{(n+1,1;n',1)} & & & & & \\ \vdots & & \vdots & & & \ddots \end{pmatrix} \begin{pmatrix} S^{(n',1)} \\ S^{(n',2)} \\ S^{(n',3)} \\ S^{(n',4)} \\ S^{(n'+1,1)} \\ \vdots \end{pmatrix} \tag{274}$$

Here we have used the following notation : e_y, e_x, h_y, h_x are now denoted by the index $j = 1, 2, 3, 4$, respectively, so that each element is now associated with $l = (n, j)$.

We now see that our next logical step is to determine the matrix $\mathbf{M}$. First off, each element i of the product $\mathbf{MF}$ above can be obtained through the sum $\sum_k M_{ik} F_k$, where the sum over the components of $\mathbf{F}$ is $\sum_{n'} \sum_{j=1}^{4}$. For

example we can calculate the first component of $\mathbf{MF}$ for a fixed n as :

$$(\mathbf{MF})^{(n,1)} = \sum_{n'} \left(M^{(n,1;n',1)S^{(n',1)}} + M^{(n,1;n',2)S^{(n',2)}} + M^{(n,1;n',3)S^{(n',3)}} + M^{(n,1;n',4)S^{(n',4)}} \right) \tag{275}$$

Therefore by identification with the first element of $\partial\mathbf{F}/\partial z$ in equation (273), we find :

$$M^{(n,1;n',1)} = 0 \tag{276}$$

$$M^{(n,1;n',2)} = 0 \tag{277}$$

$$M^{(n,1;n',3)} = \frac{ik_y}{\omega}\widetilde{\varepsilon}_{n-n'}\alpha n' \tag{278}$$

$$M^{(n,1;n',4)} = i\omega\delta n, n' - \frac{ik_y^2}{\omega}\widetilde{\varepsilon}_{n-n'} \tag{279}$$

Proceeding likewise for the other elements, we eventually find the matrix $\mathbf{M}$ of dimension $8N+4$:

$$\mathbf{M}^{(n,n')} = \begin{pmatrix} 0 & 0 & \frac{ik_y}{\omega}\widetilde{\varepsilon}_{n-n'}\alpha_{n'} & i\omega\delta_{n,n'} - \frac{ik_y^2}{\omega}\widetilde{\varepsilon}_{n-n'} \\ 0 & 0 & \frac{i}{\omega}\alpha_n\alpha_{n'}\widetilde{\varepsilon}_{n-n'} - i\omega\delta_{n,n'} & -\frac{ik_y}{\omega}\alpha_n\widetilde{\varepsilon}_{n-n'} \\ -\frac{ik_y}{\omega}\alpha_{n'}\delta_{n,n'} & -i\omega\widetilde{\varepsilon}_{n-n'} + \frac{ik_y^2}{\omega}\delta_{n,n'} & 0 & 0 \\ i\omega\widetilde{\varepsilon}_{n-n'} - \frac{i\alpha_{n'}^2}{\omega}\delta_{n,n'} & \frac{ik_y}{\omega}\alpha_{n'}\delta_{n,n'} & 0 & 0 \end{pmatrix} \tag{280}$$

It is convenient to label each row and column as $4(i-1)+j$, for $i \in [1, ..., 2N]$ and $j \in [1, 2, 3, 4]$. Now that we have established $\mathbf{M}$, we can find the solution $\mathbf{F}(z)$ to our differential equation (249), with $\mathbf{F}(0)$ now obtained through the continuity conditions at $z = 0$:

$$\mathbf{F}(0) = \begin{pmatrix} T_{np}^{(e)} \\ -\alpha_n \frac{k_y}{\kappa^2} T_{np}^{(e)} + \frac{\omega}{\kappa^2}\beta_n^{(2)} T_{np}^{(h)} \\ T_{np}^{(h)} \\ -\alpha_n \frac{k_y}{\kappa^2} T_{np}^{(h)} - \frac{\omega\epsilon}{\kappa^2}\beta_n^{(2)} T_{np}^{(e)} \end{pmatrix} \tag{281}$$

Our goal being to obtain the reflection matrices, let us now determine the continuity conditions at $z = a$ through equation (249) now written as :

$$\mathbf{F}(a) = e^{\mathbf{M}a}\mathbf{F}(0) \tag{282}$$

The l.h.s has been obtained through the continuity conditions at $z = a$ from equations (254-257), and the r.h.s by identification with the matrix elements. These two are hence respectively given by :

$$\mathbf{F}(a) = \begin{pmatrix} S_n^{e_y}(a) \\ S_n^{e_x}(a) \\ S_n^{h_y}(a) \\ S_n^{h_x}(a) \end{pmatrix} \tag{283}$$

and

$$\mathbf{F}_{nj}(a) = \sum_{n',j'} \left(e^{\mathbf{M}a}\right)_{n,j;n',j'} \mathbf{F}_{n',j'}(0) \tag{284}$$

At this point, we must take into account the two polarizations independently. For example, for electric waves ($H_y = 0$) we take $I_p^{(h)} = 0$ and $I_p^{(e)} = 1$ so that $\mathbf{F}(a)$ becomes :

$$\mathbf{F}(a) = \begin{pmatrix} R_{np}^{(e,e)} e^{i\beta_n^{(1)}a} + \delta_{np} e^{-i\beta_p^{(1)}a} \\ -\frac{k_y}{\kappa_0^2}\left(\alpha_n R_{np}^{(e,e)} e^{i\beta_n^{(1)}a} + \delta_{np}\alpha_p e^{-i\beta_p^{(1)}a}\right) - \frac{\omega}{\kappa_0^2}\beta_n^{(1)} R_{np}^{(h,e)} e^{i\beta_n^{(1)}a} \\ R_{np}^{(h,e)} e^{i\beta_n^{(1)}a} \\ -\frac{k_y}{\kappa_0^2}\alpha_n R_{np}^{(h,e)} e^{i\beta_n^{(1)}a} + \frac{\omega}{\kappa_0^2}\left(\beta_n^{(1)} R_{np}^{(e,e)} e^{i\beta_n^{(1)}a} - \delta_{np}\beta_p^{(1)} e^{-i\beta_p^{(1)}a}\right) \end{pmatrix} \tag{285}$$

Notice that we changed our notation of the reflection matrices R_{np}, so that they now have two indices in their superscript. The first index refers to the polarization of the reflected field (which for a diffraction process on nanogratings can either be e or h), and the second index refers to the incident field (e in our above equation).

We now enter into the final step of our calculations to determine the reflection matrices, which we do by rewriting the vectors $\mathbf{F}(0)$ and $\mathbf{F}(a)$ such as :

$$\mathbf{F}(a) = TX + Z \quad \text{and} \quad \mathbf{F}(0) = SX \qquad \text{for} \qquad X = \begin{pmatrix} R_{np}^{e} \\ R_{np}^{h} \\ T_{np}^{e} \\ T_{np}^{h} \\ \vdots \end{pmatrix} \tag{286}$$

Hence the solutions can conveniently be expressed as $X = \left(e^{\mathbf{M}a}S - T\right)Z$. The vector Z, which is variable-independent, contains the polarization of incident waves. Therefore it characterizes the two different solutions for $e-$waves and $h-$waves, respectively :

$$X\left(I_p^{(e)} = 1, I_p^{(h)} = 0\right) = \begin{pmatrix} R_{np}^{(e,e)} \\ R_{np}^{(h,e)} \\ \vdots \end{pmatrix} \quad \text{and} \quad X\left(I_p^{(h)} = 1, I_p^{(e)} = 0\right) = \begin{pmatrix} R_{np}^{(e,h)} \\ R_{np}^{(h,h)} \\ \vdots \end{pmatrix} \tag{287}$$

As already said, because the fields E_y and H_z are not decoupled for $k_y \neq 0$, we obtain our final solution :

$$\mathcal{R}_1(\omega) = \begin{pmatrix} R_{np}^{(e,e)} = R_{n_1q_1}^{(e)}(I_p^{(e)} = \delta_{pq_1}, I_p^{(h)} = 0) & R_{np}^{(e,h)} = R_{n_2q_2}^{(e)}(I_p^{(e)} = 0, I_p^{(h)} = \delta_{pq_2}) \\ R_{np}^{(h,e)} = R_{n_3q_3}^{(e)}(I_p^{(e)} = \delta_{pq_3}, I_p^{(h)} = 0) & R_{np}^{(h,h)} = R_{n_4q_4}^{(e)}(I_p^{(e)} = 0, I_p^{(h)} = \delta_{pq_4}) \end{pmatrix} \tag{288}$$

This is the reflection matrix $R_{1\text{down}}$ for the reflection of a downward wave from the lower grating along the $z-$axis. We can likewise determine the reflection matrix $R_{2\text{up}}$ for the reflection of an upward wave from the upper grating, by performing a change of variable $z = -z' + L$ in equations (238-239).

Notice that we can laterally displace the two gratings with respect to another along the $x-$axis. This is specified by the parameter δ, as shown in FIG. 30, and practically done by another similar change of variable $x = x' - \delta$, with δ smaller than the corrugation period d. Then the upper grating will be laterally shifted by $\delta = \Delta x$. This allows us to probe the *lateral Casimir force*, which comes from the periodic variations of the normal Casimir force when the two gratings are laterally shifted with respect to one another. This lateral force is also at the origin of a *torque* so that the gratings are rotated parallely around the z-axis.

Applied to radiative heat transfer, which is calculated from a scattering formalism also, this lateral shift of the two gratings with δ will allow us to modulate the flux with δ, and eventually specify a thermal modulator for nanosystems in section IX C.

2. The Casimir energy for periodic gratings

In order to obtain the Casimir energy, we will first need to determine the eigenfrequencies of all stationary solutions of the generalized diffraction problem of all the subsequent diffraction processes on the two gratings. For this we use *Cauchy's argument principle* :

$$\frac{1}{2i\pi}\oint \psi(\omega)\frac{d}{d\omega}\ln f(\omega)d\omega = \sum \psi(\omega_0) - \sum \psi(\omega_\infty) \tag{289}$$

where ω_0 are zeros, ω_∞ are poles of $f(\omega)$ within the contour of integration, and degenerate eigenvalues are summed according to their multiplicities. In the case of the Casimir energy, we have $\psi(\omega) = \hbar\omega/2$, and the equation of eigenfrequencies for the associated problem from classical electrodynamics is $f(\omega) = 0$. Let us first stretch the procedure for the simple case of a planar Fabry-Pérot cavity. In this case, this equation writes in the following way for TE-modes :

$$f(\omega) = 1 - r_{1\text{TE}}(\omega)r_{1\text{TEup}}(\omega) = 0 \tag{290}$$

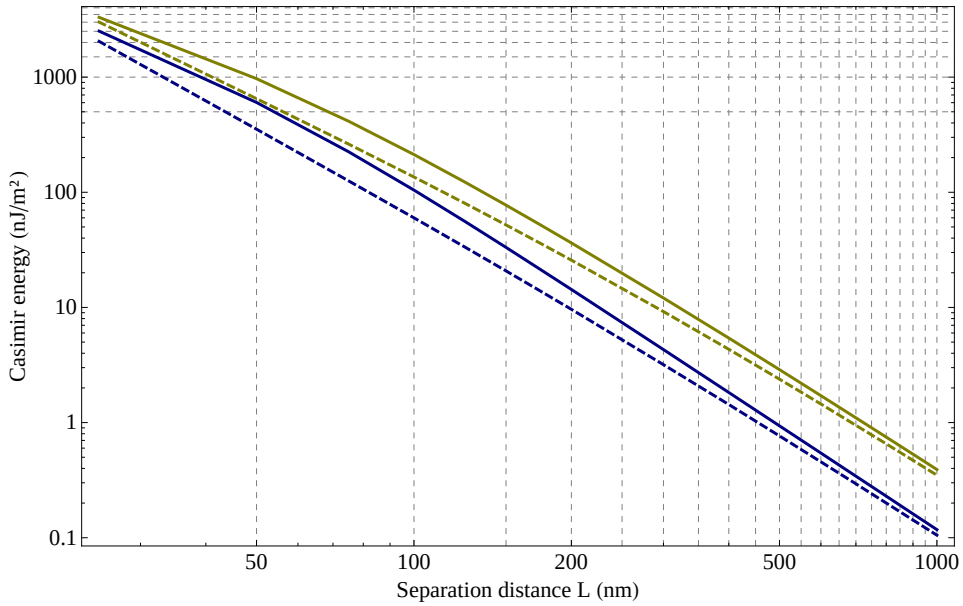

FIG. 32: Absolute value of the Casimir energy between two corrugated plates of gold (dashed yellow curve) and two corrugated plates of intrinsic silicon (dashed blue curve), as a function of their separation distance L. This is compared with the respective plane-plane results from FIG. 22 for these two materials (solid yellow curve for gold, and solid blue curve for intrinsic silicon). The gratings have a period $d = 100$nm, groove depth $a = 50$nm, and filling factor $p = 50\%$.

The two reflection coefficients correspond respectively to a downward plane wave reflecting on the lower grating, and to an upward plane wave reflecting on the upper grating.

If we now denote $r_{2\mathrm{TE}}(\omega)$ the reflection coefficient of a downward TE-mode reflected on the upper plate now located at $z < 0$, we can use Maxwell's equations to find $r_{2\mathrm{TEup}}(\omega) = r_{2\mathrm{TE}}(\omega) exp(2ik_z L)$. Writing the associated relations for the TM-modes together with equation (289-290), we can use the argument principle and recover *Lifshitz formula*.

Coming back to the gratings configuration, for an eigenvector Ψ_i describing a given normal mode of frequency ω_i, we can then use the equation for normal modes :

$$R_1(\omega_i) R_{2\mathrm{up}}(\omega_i) \Psi_i = \Psi_i \tag{291}$$

Then through this expression, we obtain instead of equation (290) the following condition for eigenfrequencies :

$$\det[I - R_1(\omega) R_{2\mathrm{up}}(\omega)] = 0 \tag{292}$$

In the case where the two gratings are aligned with respect to one another ($\delta = 0$), we can define a matrix equivalent of the factor of propagation within the cavity $e^{-\kappa_0 L}$ from the plane-plane case :

$$K(i\omega) = \begin{pmatrix} G & 0 \\ 0 & G \end{pmatrix} \tag{293}$$

$$G = \mathrm{diag}\left[\exp\left(-L\sqrt{\omega^2 + k_y^2 + [k_x + (2m\pi/d)]^2}\right)\right] \quad \text{and} \quad m = -N, \ldots, +N \tag{294}$$

Then we can write :

$$R_{2\mathrm{up}}(i\omega) = K(i\omega)R_2(i\omega)K(i\omega) \tag{295}$$

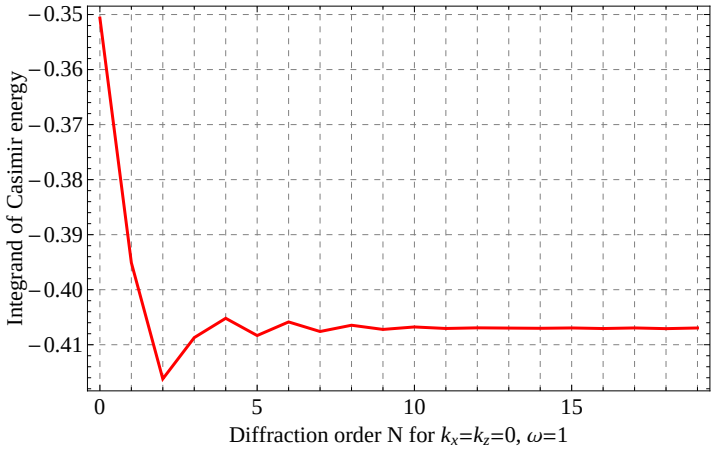

FIG. 33: Convergence with diffraction order N of the value of the integrand of the Casimir energy from equation (296). This is for gratings of intrinsic silicon with period $d = 400$nm, groove depth $a = 100$nm, filling factor $p = 50\%$, and separation distance $L = 200$nm. We took here a specific mode with $k_x = k_z = 0$ and $\lambda = 2.51\mu$m, which hence lies in the propagative sector.

The solution of equation (292) for each k_x and k_y gives the possible eigenfrequencies ω_i of the solutions of Maxwell's equations. These in turn must be replaced within the definition of the Casimir energy $E = \sum_i \hbar\omega_i/2$. One must ensure that these solutions vanish when z goes to infinity.

Eventually, we can sum over these eigenfrequencies by using the argument principle from equation (289). We then obtain the expression of the Casimir energy between two parallel gratings for the first Brillouin zone, of width equal to $2\pi d$:

$$E = \frac{\hbar c d}{8\pi^3}\int_0^\infty d\omega \int_{\mathbb{R}} dk_y \int_0^{2\pi/d} dk_x \ln\det[I - R_1(i\omega)K(i\omega)R_2(i\omega)K(i\omega)] \tag{296}$$

Note that since for a given *invertible* matrix A, we have the following property [141] :

$$\frac{\partial}{\partial z}\left(\ln\det A\right) = \mathrm{Tr}\left(A' A^{-1}\right) = \mathrm{Tr}\left(A^{-1}A'\right) \tag{297}$$

we can also write the expression of the Casimir force from equation (296) above as a trace of the associated integrand.

In FIG. 32, we show the absolute value of the Casimir energy as a function of separation distance between two corrugated plates of gold, and two corrugated plates of intrinsic silicon. We also compare it with the plane-plane cases for these two materials. One can see the strong increase with shorter distances for both plane and non-plane geometries, and especially at fixed distance, the greater Casimir energy for the plane-plane case than for the grating-grating case. Notice also the greater energy associated with gold plates, compared to intrinsic silicon plates. This is a general characteristic of metals compared to dielectrics, which have a smaller *skin depth* so that they are highly reflective, especially at small frequencies.

The order of diffraction N will determine the span of the parameter m in equation (293) and hence the dimension of the matrices K and R, since these are of dimension $4N + 2$. When performing numerical computations of the Casimir energy, the results of which will be presented in section VII, it is crucial to first ensure its convergence with diffraction order and hence to wisely choose N. We show in FIG. 33 the results of such a convergence in N for gratings of intrinsic silicon.

Also, each diffracted mode is integrated over its wavevector and frequency components within the first Brillouin zone, so that there is no overlap in the integration from one mode to another. Since the Casimir energy is fundamentally a near-field energy, it is by far the normal modes $n = (0)$ that have the largest contribution to the total value of the energy (this can be seen by how close the scattering results are to the Proximity Approximation). Nevertheless there is also an important contribution coming from the *lateral modes*, which are the modes with larger k_x components. As shown on FIG. 34, these appear for instance when we subtract the total mode contribution associated with non-shifted gratings (where the contribution of the normal modes is maximum due to the near-field contribution of the corrugation tops) to the one associated with gratings that are shifted by half a period. This is practically done by subtracting the integrand of equation (296) at $\delta = 0$ and at $\delta = d/2$.

3. The Casimir energy for arbitrary periodic gratings

We may now generalize the scattering formalism between rectangular gratings to gratings of arbitrary periodic profiles. This can be achieved by modeling the arbitrary profiles as stacks of K horizontal rectangular slices. The difference in the analytical expression of the Casimir energy then appears in the distance between the grating ridges d_1, which will now depend on y, such as shown on FIG. 35.

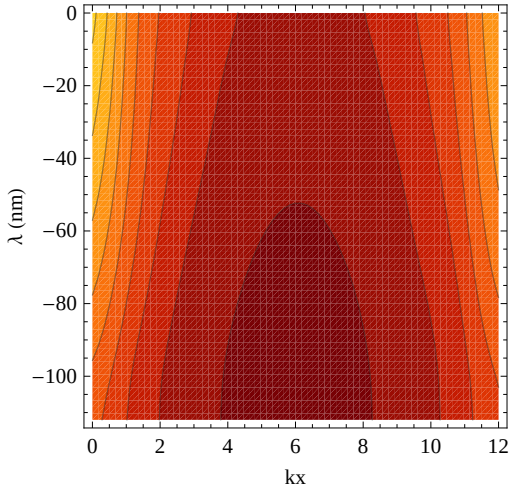

FIG. 34: Difference of the integrand of equation (296) at $\delta = 0$ and at $\delta = d/2$, showing the contribution of the lateral modes when the gratings are shifted by half a period. The components of the modes have been summed over a grid of values of k_z for each value of ω and k_x. The components k_x are here presented within half a Brillouin zone $[0, \pi/d]$, and the components k_y are of course set to zero by grating symmetry. This is for gratings of intrinsic silicon Si with period $d = 500$ nm, filling factor $p = 50\%$, corrugation depth $a = 500$ nm, and separated by a distance $L = 25$ nm.

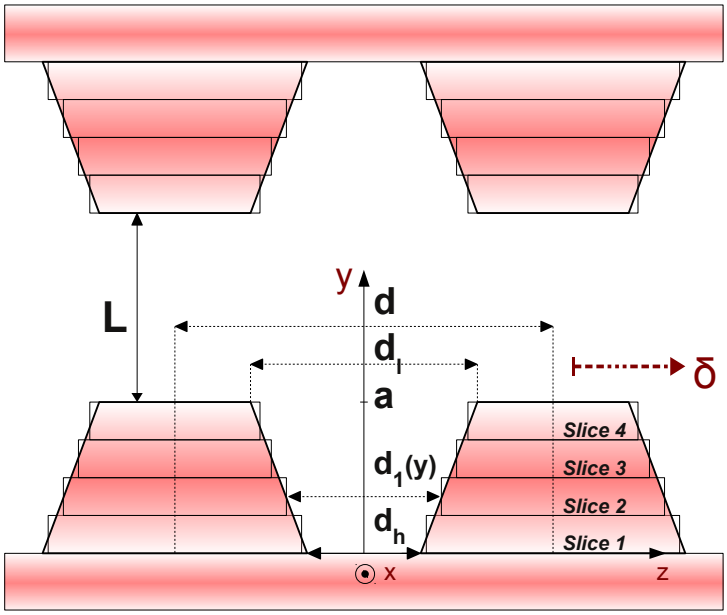

FIG. 35: Arbitrary gratings geometry and parameters in the approximation of vertical stacks of rectangular slices (here for $K = 4$).

For each slice (i), the spacing between the corrugation ridges is $d_1^{(i)}$, and the scattering formalism for rectangular corrugations can be applied. More specifically, a differential equation akin to equation (248) :

$$\partial_y \mathbf{F} = \mathbf{M}^{(i)} \mathbf{F} \tag{298}$$

can be solved within each slice (i) to relate the fields at boundary $y = i\frac{a}{K}$ and $y = (i+1)\frac{a}{K}$.

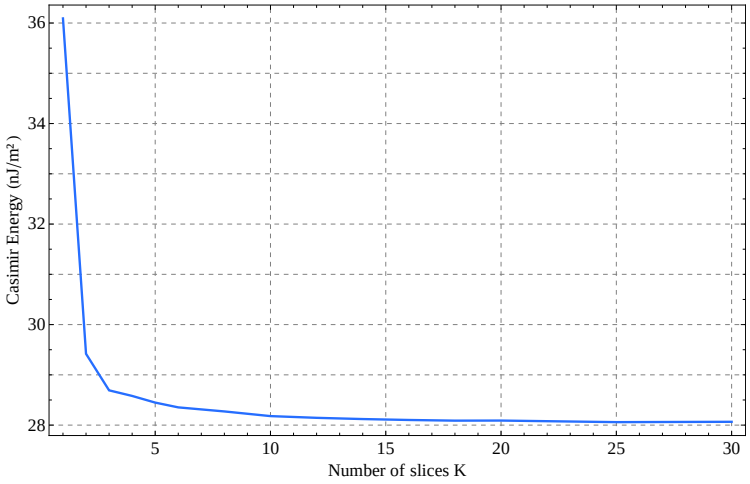

FIG. 36: Dependence of the Casimir energy to the number of slices K for the case of *sawtooth* gratings, with $L = 100$ nm, $d = 400$ nm, $a = 50$ nm, and $d_1(y) = 4y + 200$.

In a similar way to the case $K = 1$ above, the field at $y = a$ is thus related to the field at $y = 0$ *via* the relation :

$$\mathbf{F}(a) = \left[\prod_{i=K}^{1} e^{\mathbf{M}^{(i)} \frac{a}{K}} \right] \mathbf{F}(0) \tag{299}$$

where the product $\prod$ runs from $i = K$ to $i = 1$, in that order. The greater the number of slices K, the greater the fitting of the gratings' shape will be, and thus the accuracy of the overall model. This convergence in K is shown in Fig. 36 for given profiles shaped as *sawteeth* (see section VII E), with a separation distance $L = 100$ nm, grating period $d = 400$ nm, corrugation depth $a = 50$ nm, and distance between ridges $d_1(y) = 4y + 200$.

Hence a correct parametrization of the quantity d_1 as a function of y allows one to generate arbitrary symmetric profiles for the corrugations.

It is sometimes also useful to compare the results of the scattering theory for arbitrary periodic gratings with predictions from Derjaguin's Proximity Approximation [131].

As explained in section VI A 8, the Proximity Approximation comes from the weighted sum of the planar normal contributions $E_{\mathrm{PP}}(L)$ depending on the local separation distances L within each period, and hence on the lateral displacement δ between the gratings. If we express the shapes of the arbitrary periodic gratings in an analytical form such as $y = f(x, \delta)$ for the lower grating and $y = L + 2a - f(x, \delta = 0)$ for the upper grating in the xy-plane shown on Fig. 35, we can define the function $h(x, \delta) = L + 2a - f(x, \delta = 0) - f(x, \delta)$ expressing the local distance of separation between the two profiles, as a function of x and δ.

Dividing the period d in a number $\eta \to \infty$ of intervals of individual widths $d/\eta \to 0$, we obtain a general expression

of the Casimir energy in the Proximity Approximation for arbitrary gratings as a function of the lateral shift δ :

$$E^{\mathrm{PFA}}(L,\delta) \;=\; \frac{1}{d}\int_0^d E_{\mathrm{PP}}\left(h(x,\delta)\right)dx = \frac{1}{\eta}\sum_{i=1}^{\eta} E_{\mathrm{PP}}\left(L = h\left(x = i\frac{d}{\eta},\delta\right)\right) \tag{300}$$

When compared to the scattering results outlined in the previous section, equation (300) above will allow us to explore the contribution of the lateral modes compared to the normal modes. We will see this in more details in section VII.

C. Out-of-thermal equilibrium phenomena

1. The Casimir energy for periodic gratings

In the previous section we have derived the Casimir energy for corrugated plates at zero temperature. Earlier in section VI A 7, we have also considered the Casimir energy at thermal equilibrium, where the two mirrors have the same non-zero temperature, which was given as a sum over the Matsubara frequencies. We now consider two gratings out-of-thermal equilibrium, each with a different temperature, with the aim to obtain an expression of the Casimir force. There exists more than eleven different ways to derive the expression of the Casimir force [142–144]. However we will here focus on the derivation of the Casimir force through the exact method of scattering theory. We can hence use our earlier scattering results of the reflection and transmission matrices developed for gratings. We will consider the general case as applied to gratings but this formalism can be applied to the simpler case of planar surfaces by considering the scattering matrices as scalars.

Based on [61, 145], we consider a Fabry-Pérot cavity made of two bulks of infinite surface and width along the $z-$axis. Our aim is to determine the correlators of the field inside the cavity, based on Rytov's theory [146]. Because the field fluctuations have a local polarization, the two mirrors radiate independently from each other. This means that when stationary, each mirror's radiation is the same as if it were placed in thermal equilibrium with its environment, the other mirror being absent.

This allows us to obtain the expression of the cavity field firstly by deriving the radiation of one plate at thermal equilibrium with its environment, and then secondly by considering these scattered independent contributions. We use

the same geometrical parameters and spatial coordinates than in FIG. 30. We will work with real positive frequencies ω, and consider the electric field $\mathbf{E}(t,\mathbf{r})$ only, the magnetic field $\mathbf{H}(t,\mathbf{r})$ being obtained through Maxwell's equations. In the cavity, $\mathbf{E}(t,\mathbf{r})$ can be expressed as a sum of plane-wave contributions of amplitudes b :

$$\mathbf{E}^{(\pm)}_{\alpha,\mathbf{k}_\perp}(t,\mathbf{r}) = 2\mathrm{Re}\left[b^{(\pm)}_{\alpha,\mathbf{k}_\perp}\mathcal{E}^{(\pm)}_{\alpha,\mathbf{k}_\perp}(\omega,\mathbf{r})e^{-i\omega t}\right] \tag{301}$$

for

$$\mathcal{E}^{(\pm)}_{\alpha,\mathbf{k}_\perp}(\omega,\mathbf{r}) \equiv \mathbf{e}^{(\pm)}_{\alpha,\mathbf{k}_\perp}(\omega)e^{i\mathbf{k}^{(\pm)}\cdot\mathbf{r}} \tag{302}$$

We identify here $(+)$ and $(-)$ with the direction of propagation of the modes along the $z-$axis in the positive and negative directions, respectively, and $\alpha = s,p$ with the TE and TM polarizations, respectively. We have $\mathbf{k}^{(\pm)} = \mathbf{k}_\perp \pm k_z\hat{\mathbf{z}}$ with again an important condition on k_z :

$$k_z = \sqrt{\omega^2/c^2 - k_\perp^2} \qquad \text{for} \qquad -\frac{\pi}{2} < \arg k_z \leqslant +\frac{\pi}{2} \tag{303}$$

Notice that the restriction is done so that in the case where k_z is a pure imaginary number, the negative part of the imaginary axis is excluded. This said, we set :

$$\mathbf{e}^{(\pm)}_{s,\mathbf{k}_\perp}(\omega) = \hat{\mathbf{z}} \times \hat{\mathbf{k}}_\perp \tag{304}$$

$$\mathbf{e}^{(\pm)}_{p,\mathbf{k}_\perp}(\omega) = \frac{c}{\omega}\mathbf{k}^{(\pm)} \times \mathbf{e}^{(\pm)}_{s,\mathbf{k}_\perp} \tag{305}$$

As usual, for real k_z and $k_\perp < \omega/c$ we have propagative waves, and for imaginary k_z and $k_\perp > \omega/c$ we have evanescent waves.

We will also use a roman index i to denote both the position $\mathbf{r}$ and the ith component of a vector, and a greek index ρ to denote both the wave vector $\mathbf{k}_\perp$ and the polarization α. So for example $\mathcal{E}^{(\pm)}_{\alpha,\mathbf{k}_\perp}(\omega,\mathbf{r}) \Leftrightarrow \mathcal{E}^{(\pm)}_{i\rho}(\omega)$.

Because of the periodicity of the corrugations, we can defined $\mathbf{k}_\perp$ through two integers n_x and n_y such as $k_x = 2\pi n_x/L_x$ and $k_y = 2\pi n_y/L_y$, where L_x and L_y are the lateral lengths of the plates, each plate having an area $\mathcal{A} = L_xL_y$. Then we define the following notations for a given kernel $X_{\alpha,\mathbf{k}_\perp;\alpha',\mathbf{k'}_\perp}(\omega) = X_{\rho,\rho'}(\omega)$:

$$\sum_\omega \equiv \int \frac{d\omega}{2\pi} \qquad \text{and} \qquad \sum_\rho \equiv \frac{1}{\mathcal{A}}\sum_{n_x,n_y}\sum_\rho \tag{306}$$

$$\delta_{\omega,\omega'} \equiv 2\pi\delta(\omega-\omega') \qquad \text{and} \qquad \delta_{\rho,\rho'} \equiv A\delta_{n_x,n'_x}\delta_{n_y,n'_y}\delta_{\rho,\rho'} \tag{307}$$

$$\mathrm{Tr}_\rho X = \sum_\rho X_{\rho;\rho'} \equiv \frac{1}{\mathcal{A}} \sum_{n_x,n_y} \sum_\alpha X_{\alpha,\mathbf{k}_\perp;\alpha',\mathbf{k'}_\perp} \tag{308}$$

Then we can derive the expression of the field radiated by a single grating at thermal equilibrium with its environment, and in the absence of the second grating. Let's denote our two plates by index $A = (1), (2)$, and $\mathcal{E}_i^A(\omega)$ the time Fourier transform of the field radiated by plate A.

The total radiation field $\mathcal{E}_i^{\mathrm{eq},A}(\omega)$ existing inside of the cavity when each plate is individually considered as in equilibrium with the environment at temperature T_A is equal to the sum of each plate's individual radiation $\mathcal{E}_i^A(\omega)$, of the environment radiation (which includes both the fluctuations of vacuum as well as the Stefan-Boltzmann radiation) suffered by each plate from the cavity $\mathcal{E}_i^{\mathrm{env},A}(\omega)$, and of the ensuing scattered radiation $\mathcal{E}_i^{\mathrm{scat},A}(\omega)$:

$$\mathcal{E}_i^{\mathrm{eq},A}(\omega) = \mathcal{E}_i^A(\omega) + \mathcal{E}_i^{\mathrm{env},A}(\omega) + \mathcal{E}_i^{\mathrm{scat},A}(\omega) \tag{309}$$

We can expand these three fields as :

$$\mathcal{E}_i^A(\omega) = \sum_\rho \mathcal{E}_{i\rho}^{(\pm)}(\omega) b_\rho^A(\omega) \tag{310}$$

$$\mathcal{E}_i^{\mathrm{env},A}(\omega) = \sum_\rho \mathcal{E}_{i\rho}^{(\mp)}(\omega) b_\rho^{\mathrm{env}}(\omega) \tag{311}$$

$$\mathcal{E}_i^{\mathrm{scat},A}(\omega) = \sum_{\rho,\rho'} \mathcal{E}_{i\rho}^{(\pm)}(\omega) S_{\rho,\rho'}^A(\omega) b_{\rho'}^{\mathrm{env}}(\omega) \tag{312}$$

The upper sign in the superscript of $\mathcal{E}$ corresponds to plate (1), and the lower sign to plate (2). The S-matrix of plate A for the field coming onto it from the cavity is given by $S_{\rho,\rho'}^A$. In general, $S_{\rho,\rho'}^A$ depends on the position $\mathbf{x}^A$ of some fixed reference point Ω^A selected on plate A. Then for $\widetilde{S}_{\rho,\rho'}^A$ the S-matrix of plate A related to the coordinate system with origin at Ω^A, we have :

$$S_{\rho,\rho'}^A = e^{-i\mathbf{k}^{(\pm)}\cdot\mathbf{x}^A} \widetilde{S}_{\rho,\rho'}^A e^{i\mathbf{k'}^{(\mp)}\cdot\mathbf{x}^A} \tag{313}$$

Now we can expand the indices and the $\pm$ amplitudes of the total equilibrium field for $\gamma, \gamma' = \pm$, such as :

$$b_{\alpha,-}^{\mathrm{eq},A}(\mathbf{k}_\perp,\omega) = b_\alpha^{\mathrm{env},A}(\mathbf{k}_\perp,\omega) \tag{314}$$

$$b_{\alpha,+}^{\mathrm{eq},A}(\mathbf{k}_\perp,\omega) = b_\alpha^{\mathrm{scat},A}(\mathbf{k}_\perp,\omega) + b_\alpha^{\mathrm{rad},A}(\mathbf{k}_\perp,\omega) \tag{315}$$

where $b^{\mathrm{env},A}_{\alpha,\gamma}(\mathbf{k}_\perp,\omega)$ represents the environment radiation suffered by A, $b^{\mathrm{scat},A}_{\alpha}(\mathbf{k}_\perp,\omega)$ the corresponding scattered radiation, and $b^{\mathrm{rad},A}_{\alpha}(\mathbf{k}_\perp,\omega)$ is the field radiated by A. In the general case, these three radiations have positive and negative contributions, but here we deal with one infinite body so that they simplify to the form expressed in equations (314-315).

In an equilibrium situation, it is usually of no interest to calculate the individual contributions to $b^{\mathrm{eq},A}_{\alpha,\gamma}(\mathbf{k}_\perp,\omega)$, but here we consider such an equilibrium situation for the sake of obtaining the radiated contribution $b^{\mathrm{rad},A}_{\alpha}(\mathbf{k}_\perp,\omega)$.

From equations (314-315), we see that :

$$\sum_{\gamma,\gamma'}\langle b^{\mathrm{eq},A}_{\alpha,\gamma}(\mathbf{k}_\perp,\omega)b^{\mathrm{eq},A\,\dagger}_{\alpha,\gamma'}(\mathbf{k}_\perp,\omega')\rangle = \langle b^{\mathrm{rad},A}_{\alpha}(\mathbf{k}_\perp,\omega)b^{\mathrm{rad},A\,\dagger}_{\alpha}(\mathbf{k}_\perp,\omega')\rangle + 8 \text{ terms} \tag{316}$$

where the "8 terms" represent all the other possible correlations involving the r.h.s of equations (314-315). If we assume that the environment is not coupled to the field radiated by the body, we then have :

$$\langle b^{\mathrm{env},A}_{\alpha}(\mathbf{k}_\perp,\omega)b^{\mathrm{rad},A\,\dagger}_{\alpha'}(\mathbf{k}'_\perp,\omega')\rangle = \langle b^{\mathrm{scat},A}_{\alpha}(\mathbf{k}_\perp,\omega)b^{\mathrm{rad},A\,\dagger}_{\alpha'}(\mathbf{k}'_\perp,\omega')\rangle = 0 \tag{317}$$

and so, by isolating the radiative part and using the previous equation we can rewrite equation (316) such as :

$$\begin{aligned}\langle b^{\mathrm{rad},A}_{\alpha}(\mathbf{k}_\perp,\omega)b^{\mathrm{rad},A\,\dagger}_{\alpha}(\mathbf{k}_\perp,\omega')\rangle = \quad & \langle b^{\mathrm{eq},A}_{\alpha,\gamma}(\mathbf{k}_\perp,\omega)b^{\mathrm{eq},A\,\dagger}_{\alpha,\gamma'}(\mathbf{k}_\perp,\omega')\rangle \\ & -\langle b^{\mathrm{env},A}_{\alpha}(\mathbf{k}_\perp,\omega)b^{\mathrm{env},A\,\dagger}_{\alpha}(\mathbf{k}_\perp,\omega')\rangle \\ & -\langle b^{\mathrm{scat},A}_{\alpha}(\mathbf{k}_\perp,\omega)b^{\mathrm{scat},A\,\dagger}_{\alpha}(\mathbf{k}_\perp,\omega')\rangle \\ & -\langle b^{\mathrm{env},A}_{\alpha}(\mathbf{k}_\perp,\omega)b^{\mathrm{scat},A\,\dagger}_{\alpha}(\mathbf{k}_\perp,\omega') + c.c.\rangle\end{aligned} \tag{318}$$

where from now on we implicitly use the summation in γ,γ'. Now we can define the amplitudes $b^{(\mathrm{env})}_{\alpha}(\omega)$ of the environment radiation by the well-known correlators given by the second term of equation (318) above, which is just the free-field result :

$$\langle b^{\mathrm{env}}_{\rho}(\omega)b^{\mathrm{env}*}_{\rho'}(\omega')\rangle = \frac{2\pi\omega}{c^2}F(\omega,T_A)\mathrm{Re}\left(\frac{1}{k_z}\right)\delta_{\omega\omega'}\delta_{\rho\rho'} \tag{319}$$

for

$$F(\omega,T) = \frac{\hbar\omega}{2}\coth\left(\frac{\hbar\omega}{2k_BT}\right) \tag{320}$$

Then by defining the projection operators :

$$\Pi^{pw}_{\alpha,\alpha'}(\mathbf{k}_\perp,\mathbf{k}'_\perp) = \frac{1+s_\alpha}{2}\delta_{\mathbf{k}_\perp,\mathbf{k}'_\perp}\delta_{\alpha,\alpha'} \tag{321}$$

$$\Pi^{ew}_{\alpha,\alpha'}(\mathbf{k}_\perp,\mathbf{k}'_\perp) = i\frac{1-s_\alpha}{2}\delta_{\mathbf{k}_\perp,\mathbf{k}'_\perp}\delta_{\alpha,\alpha'} \tag{322}$$

where $s_\alpha = \mathrm{sgn}[k_z^2] = \mathrm{sgn}[\omega^2/c^2 - \mathbf{k}_\perp^2]$, we can expand again and rewrite equation (319) such as :

$$\langle b^{\mathrm{env},A}_\alpha(\mathbf{k}_\perp,\omega) b^{\mathrm{env},A\,\dagger}_{\alpha'}(\mathbf{k}'_\perp,\omega')\rangle = \frac{2\pi\omega}{c^2 k_z}F(\omega,T)\delta(\omega-\omega')\Pi^{pw}_{\alpha,\alpha'}(\mathbf{k}_\perp,\mathbf{k}'_\perp). \tag{323}$$

The correlations involving the scattered field can be written in terms of the scattering matrix S_A associated with the medium :

$$\langle b^{\mathrm{scat},A}_\alpha(\mathbf{k}_\perp,\omega) b^{\mathrm{env},A\,\dagger}_{\alpha'}(\mathbf{k}'_\perp,\omega')\rangle = \frac{2\pi\omega}{c^2}F(\omega,T_A)\delta(\omega-\omega')\sum_{\mathbf{k}''_\perp,\alpha''} S_A^{\alpha,\alpha''}(\mathbf{k}_\perp,\mathbf{k}''_\perp,\omega)\frac{1}{k''_z}\Pi^{pw}_{\alpha'',\alpha'}(\mathbf{k}''_\perp,\mathbf{k}'_\perp) \tag{324}$$

$$\begin{aligned}\langle b^{\mathrm{scat},A}_\alpha(\mathbf{k}_\perp,\omega) b^{\mathrm{scat},A\,\dagger}_{\alpha}(\mathbf{k}'_\perp,\omega')\rangle = \frac{2\pi\omega}{c^2} \quad & F(\omega,T_A)\delta(\omega-\omega') \\ & \times \sum_{\mathbf{k}''_\perp,\alpha''}\sum_{\mathbf{k}'''_\perp,\alpha'''} S_A^{\alpha,\alpha'}(\mathbf{k}_\perp,\mathbf{k}''_\perp)\frac{1}{k''_z}\Pi^{pw}_{\alpha,\alpha'}(\mathbf{k}''_\perp,\mathbf{k}'''_\perp)(S_A^\dagger)^{\alpha''',\alpha'}(\mathbf{k}'''_\perp,\mathbf{k}'_\perp)\end{aligned} \tag{325}$$

where we define S_A through the relation :

$$b^{\mathrm{scat},A}_\alpha(\mathbf{k}_\perp,\omega) = \sum_{\mathbf{k}'_\perp,\alpha'} S_A^{\alpha,\alpha'}(\mathbf{k}_\perp,\mathbf{k}'_\perp,\omega) b^{\mathrm{env},A}_{\alpha'}(\mathbf{k}'_\perp,\omega) \tag{326}$$

We must now find the first term on the r.h.s of equation (318).

First, we can notice that the amplitudes $\mathcal{E}(\mathbf{r},\omega)$ obey the fluctuation-dissipation theorem, so that we have the following relations :

$$\langle \mathcal{E}_\alpha(\mathbf{r},\omega)\mathcal{E}^\dagger_{\alpha'}(\mathbf{r}',\omega')\rangle = \frac{2}{\omega}F(\omega,T_A)\delta(\omega-\omega')\mathrm{Im}G(\mathbf{r},\mathbf{r}',\omega) \tag{327}$$

where $G(\mathbf{r},\mathbf{r}',\omega)$ is the Green function in the cavity associated with the interface with plate A. By expanding both sides in their transverse Fourier components, we obtain :

$$\langle b_j^{\mathrm{eq},A}(\mathbf{k}_\perp,\omega) b_j^{\mathrm{eq},A\,\dagger}(\mathbf{k}'_\perp,\omega)\rangle = \frac{2}{\omega} F(\omega,T_A)\delta(\omega-\omega')\mathrm{Im}G(\mathbf{k}_\perp,\mathbf{k}'_\perp,\omega) \tag{328}$$

The Green function can then be given in terms of the scattering matrix in the following way. First let's recall that in the absence of any radiated field from the plate, we have by using equation (326) :

$$b^A = b^{\mathrm{env},A} + b^{\mathrm{scat},A} = b^{\mathrm{env},A} + \mathbf{S}_A b^{\mathrm{env},A} \tag{329}$$

where we did not write the arguments in ω for sake of simplicity. Then by comparing this expression to the iterative solution of the Lipmann-Schwinger equation :

$$b^A = b^{\mathrm{env},A} - \mathbf{G}_0 \mathbf{T}_A b^{\mathrm{env},A} \tag{330}$$

for T_A the so-called T-operator [147] associated with plate A, we see that $\mathbf{S}_A = -\mathbf{G}_0(\omega)\mathbf{T}_A$. Therefore :

$$\mathbf{G} = \mathbf{G}^0 - \mathbf{G}^0\mathbf{T}_A\mathbf{G}^0 = \mathbf{G}^0 + \mathbf{S}_A\mathbf{G}^0 = \mathbf{G}^0 + \mathbf{G}^A \tag{331}$$

where in the last equation we defined $\mathbf{G}^{\mathrm{scat}}$. The retarded Fourier-transformed Green function in free-space is then written :

$$G^0(\mathbf{k}_\perp,\mathbf{k}'_\perp,\omega) = \frac{2\pi i\omega^2}{c^2}\frac{1}{k'_z}\,\delta_{\mathbf{k}_\perp,\mathbf{k}'_\perp}\,\delta_{\alpha,\alpha'} \tag{332}$$

where from now on $k_z = \sqrt{\omega^2/c^2 - \mathbf{k}_\perp^2}$, so that k_z is no longer defined by equation (303)). From equation (331), we then obtain the retarded dyadic Green function associated with mirror A, from equation (79) :

$$G^A(\mathbf{k}_\perp,\mathbf{k}'_\perp,\omega) = \frac{2\pi i\omega^2}{c^2}\sum_{\mathbf{k}''_\perp,\alpha''} S_A^{\alpha,\alpha''}(\mathbf{k}_\perp,\mathbf{k}''_\perp)\delta_{\mathbf{k}''_\perp,\mathbf{k}'_\perp}\,\delta_{\alpha'',\alpha'}\frac{1}{k'_z} \tag{333}$$

We can expand the indices and rewrite equation (327) as :

$$\langle \mathcal{E}_i^{\mathrm{eq},A}(\omega)\mathcal{E}_{i'}^{\mathrm{eq},A*}(\omega')\rangle = \frac{2}{\omega}F(\omega,T_A)\delta_{\omega\omega'}\mathrm{Im}G^A_{ii'}(\omega) \tag{334}$$

The dyadic retarded Green function $G^A_{ii'}(\omega)$ can then be written in terms of $S^A_{\rho\rho'}$ for each mirror's interface with the cavity, as a function of the retarded Green function in free space $G^0_{ii'}(\omega)$:

$$G^A_{ii'}(\omega) = G^{(0)}_{ii'}(\omega) + \frac{2i\pi\omega^2}{c^2} \sum_{\rho,\rho'} \mathcal{E}^{(\pm)}_{i\rho} S^A_{\rho\rho'} \mathcal{E}^{(\mp)}_{J(i')\rho'} \frac{1}{k'_z} \tag{335}$$

for

$$G^0_{ii'}(\omega) = \frac{2i\pi\omega^2}{c^2} \sum_{\rho} \frac{1}{k_z} \left[\theta(z-z') \mathcal{E}^{(+)}_{i\rho} \mathcal{E}^{(+)}_{J(i')\rho} + \theta(z'-z) \mathcal{E}^{(-)}_{i\rho} \mathcal{E}^{(-)}_{J(i')\rho} \right] \tag{336}$$

where $\theta(z) \equiv [\theta(z) = 1 \text{ for } z \geqslant 0, \theta(z) = 0 \text{ for } z < 0]$ is the Heaviside function, and J is the inversion operator :

$$J(i) \equiv J(i, \mathbf{r}) = (i, -\mathbf{r}) \tag{337}$$

$$J(\rho) \equiv J(\alpha, \mathbf{k}_\perp) = (\alpha, -\mathbf{k}_\perp) \tag{338}$$

$$J((\pm)) \equiv (\mp) \tag{339}$$

Then we can define :

$$s_\alpha \equiv \text{sgn}(\omega^2/c^2 - k_\perp^2) \tag{340}$$

so that we have :

$$\mathcal{E}^{(\pm)*}_{i\rho} = \mathcal{E}^{(\pm)}_{J(i)\rho} \frac{1+s_\alpha}{2} + \mathcal{E}^{(\mp)}_{J(i)\rho} \frac{1-s_\alpha}{2} \tag{341}$$

$$\mathcal{E}^{(\pm)}_{J(i)J(\rho)} = (-1)^{P(\alpha)} \mathcal{E}^{(\mp)}_{i\rho} \tag{342}$$

with $P(\alpha) = 1$ for TE modes, and 0 for TM modes. Then microscopic reversibility implies that $G^A_{ii'}(\omega) = G^A_{i'i}(\omega)$, and together with equation (335) gives the Onsager's reciprocity relations, which we already saw in equation (16) of Section V A 2, for any S-matrix :

$$S^A_{\rho\rho'} = \frac{k'_z}{k_z} (-1)^{P(\alpha)+P(\alpha')} S^A_{J(\rho')J(\rho)} \tag{343}$$

Then we can replace the expression of $\mathcal{E}^{\text{eq},A}_i(\omega)$ given in equations (309-312) into the l.h.s of equation (334), and replace the expression of $G^A_{ii'}(\omega)$ given in equation (335) into the r.h.s of equation (334). Then using equations (319) and (341-343), we can find the non-vanishing correlators of $b^A_\rho(\omega)$.

In order to do so, the expressions (332-333) may be rewritten with the help of the following projections operators :

$$\left[\frac{1}{k_z} \Pi^{\text{pw}}_{\alpha,\alpha'}(\mathbf{k}_\perp, \mathbf{k}'_\perp) \right]^\dagger = \frac{1}{k_z} \Pi^{\text{pw}}_{\alpha,\alpha'}(\mathbf{k}_\perp, \mathbf{k}'_\perp) \tag{344}$$

$$\left[\frac{1}{k_z}\Pi^{\mathrm{ew}}_{\alpha,\alpha'}(\mathbf{k}_\perp,\mathbf{k}'_\perp)\right]^\dagger = -\frac{1}{k_z}\Pi^{\mathrm{ew}}_{\alpha,\alpha'}(\mathbf{k}_\perp,\mathbf{k}'_\perp) \tag{345}$$

and by defining $\Sigma^{\mathrm{pw/ew}}_{-1}$ through the relations :

$$\left[\Sigma^{\mathrm{pw/ew}}_{-1}(\mathbf{k}_\perp,\mathbf{k}'_\perp)\right]_{\alpha,\alpha'} = \frac{1}{k_z}\Pi^{\mathrm{pw/ew}}_{\alpha,\alpha'}(\mathbf{k}_\perp,\mathbf{k}'_\perp) \tag{346}$$

we then can write our dyadic Green functions :

$$\mathrm{Im}G^0(\mathbf{k}_\perp,\mathbf{k}'_\perp,\omega) = \frac{2\pi\omega^2}{c^2}\mathrm{Re}\left[\Sigma^{\mathrm{pw}}_{\alpha,\alpha'}(\mathbf{k}_\perp,\mathbf{k}'_\perp)+\Sigma^{\mathrm{ew}}_{\alpha,\alpha'}(\mathbf{k}_\perp,\mathbf{k}'_\perp)\right] = \frac{2\pi\omega^2}{c^2}\Sigma^{\mathrm{pw}}_{\alpha,\alpha'}(\mathbf{k}_\perp,\mathbf{k}'_\perp) \tag{347}$$

$$\begin{aligned}\mathrm{Im}G^A(\mathbf{k}_\perp,\mathbf{k}'_\perp,\omega) &= \frac{2\pi\omega^2}{c^2}\mathrm{Re}\sum_{\mathbf{k}''_\perp,\alpha''} S_A^{\alpha,\alpha''}(\mathbf{k}_\perp,\mathbf{k}''_\perp)\left[\Sigma^{\mathrm{pw}}_{\alpha'',\alpha'}(\mathbf{k}''_\perp,\mathbf{k}'_\perp)+\Sigma^{\mathrm{ew}}_{\alpha'',\alpha'}(\mathbf{k}''_\perp,\mathbf{k}'_\perp)\right] \qquad (348)\\ &= \frac{2\pi\omega^2}{c^2}\sum_{\mathbf{k}''_\perp,\alpha''}\frac{1}{2}\left\{S_A^{\alpha,\alpha''}(\mathbf{k}_\perp,\mathbf{k}''_\perp)\Sigma^{\mathrm{pw}}_{\alpha'',\alpha'}(\mathbf{k}''_\perp,\mathbf{k}'_\perp)+{\Sigma^{\mathrm{pw}}_{\alpha'',\alpha'}}^\dagger(\mathbf{k}''_\perp,\mathbf{k}'_\perp)S_A^{\alpha,\alpha''\dagger}(\mathbf{k}_\perp,\mathbf{k}''_\perp)+(\mathrm{pw}\leftrightarrow\mathrm{ew})\right\}\end{aligned}$$

where we used the fact that the first term in equation (347) is real, and the second term is purely imaginary. Finally, we can replace directly equations (347) and (348) into equation (328), so that we get :

$$\begin{aligned}\langle b^{\mathrm{eq},A}_\alpha(\mathbf{k}_\perp,\omega)b^{\mathrm{eq},A\,\dagger}_{\alpha'}(\mathbf{k}'_\perp,\omega')\rangle = 2\frac{2\pi\omega}{c^2}F(\omega,T_A)\delta(\omega-\omega')\Bigg\{&\frac{1}{k_z}\Pi^{\mathrm{pw}}_{\alpha,\alpha'}(\mathbf{k}_\perp,\mathbf{k}'_\perp)+\\ &\frac{1}{2}\sum_{\mathbf{k}''_\perp,\alpha''}S_A^{\alpha,\alpha''}(\mathbf{k}_\perp,\mathbf{k}''_\perp,\omega)\left[\frac{1}{k''_z}\Pi^{\mathrm{pw}}_{\alpha'',\alpha'}(\mathbf{k}''_\perp,\mathbf{k}'_\perp)+\frac{1}{k''_z}\Pi^{\mathrm{ew}}_{\alpha'',\alpha'}(\mathbf{k}''_\perp,\mathbf{k}'_\perp)\right]+\mathrm{h.c.}\Bigg\},\end{aligned} \tag{349}$$

A direct substitution of equations (324-325), (327) and (349) into equation (318) finally gives :

$$\begin{aligned}\langle b^{\mathrm{rad},A}_\alpha(\mathbf{k}_\perp,\omega)b^{\mathrm{rad},A\,\dagger}_{\alpha'}(\mathbf{k}'_\perp,\omega')\rangle = \frac{2\pi\omega}{c^2}F(\omega,T_A)\delta(\omega-\omega')\Bigg\{&\frac{1}{k_z}\Pi^{\mathrm{pw}}_{\alpha,\alpha'}(\mathbf{k}_\perp,\mathbf{k}'_\perp)\\ &+\sum_{\mathbf{k}''_\perp,\alpha''}\left[S_A^{\alpha,\alpha''}(\mathbf{k}_\perp,\mathbf{k}''_\perp,\omega)\frac{1}{k''_z}\Pi^{\mathrm{ew}}_{\alpha'',\alpha'}(\mathbf{k}''_\perp,\mathbf{k}'_\perp)-\frac{1}{k''_z}\Pi^{\mathrm{ew}}_{\alpha'',\alpha'}(\mathbf{k}''_\perp,\mathbf{k}'_\perp)S^{A\,\dagger}_{\alpha,\alpha''}(\mathbf{k}_\perp,\mathbf{k}''_\perp,\omega)\right.\\ &\left.-\sum_{\mathbf{k}'''_\perp,\alpha'''}S^A_{\alpha,\alpha''}(\mathbf{k}_\perp,\mathbf{k}''_\perp,\omega)\frac{1}{k''_z}\Pi^{\mathrm{pw}}_{\alpha'',\alpha'''}(\mathbf{k}''_\perp,\mathbf{k}'''_\perp)(S^\dagger_A)^{\alpha''',\alpha'}(\mathbf{k}'''_\perp,\mathbf{k}'_\perp,\omega)\right]\Bigg\}\end{aligned} \tag{350}$$

By contracting the indices using the product of operators, we can hence rewrite equation (350) as :

$$\langle b_\alpha^{\mathrm{rad},A}(\mathbf{k}_\perp,\omega) b_{\alpha'}^{\mathrm{rad},A\,\dagger}(\mathbf{k}'_\perp,\omega')\rangle = \frac{2\pi\omega}{c^2} F(\omega,T_A)\delta(\omega-\omega') \left[\boldsymbol{\Sigma}_{-1}^{\mathrm{pw}} - \mathbf{S}_A\boldsymbol{\Sigma}_{-1}^{\mathrm{pw}}\mathbf{S}_A^\dagger + \mathbf{S}_A\boldsymbol{\Sigma}_{-1}^{\mathrm{ew}} - \boldsymbol{\Sigma}_{-1}^{\mathrm{ew}}\mathbf{S}_A^\dagger\right]_{\mathbf{k}_\perp,\mathbf{k}'_\perp,\alpha,\alpha'} \tag{351}$$

Now that we obtained the correlation function for one plate, we can proceed to the two-plates calculation.

This expression of the non-vanishing correlators of $b_\rho^A(\omega)$ can also be rewritten :

$$\langle b^A(\omega) b^{B\dagger}(\omega')\rangle = \delta_{AB}\frac{2\pi\omega}{c^2}F(\omega,T_A)\delta_{\omega\omega'} \times \left(\Sigma_{-1}^{\mathrm{pw}} - S^A\Sigma_{-1}^{\mathrm{pw}}S^{A\dagger} + S^A\Sigma_{-1}^{\mathrm{ew}} - \Sigma_{-1}^{\mathrm{ew}}S^{A\dagger}\right) \tag{352}$$

for $b^A(\omega)$ the column vector made out of the amplitudes $b_\rho^A(\omega)$. Now let's rewrite the projectors on the propagative and evanescent sectors from equations (344-345), respectively as :

$$\Sigma_n^{\mathrm{pw}} = k_z^n \Pi^{\mathrm{pw}} \qquad \text{for} \qquad \Pi_{\rho\rho'}^{\mathrm{pw}} = \delta_{\rho\rho'}\frac{1+s_\alpha}{2} \tag{353}$$

$$\Sigma_n^{\mathrm{ew}} = k_z^n \Pi^{\mathrm{ew}} \qquad \text{for} \qquad \Pi_{\rho\rho'}^{\mathrm{ew}} = \delta_{\rho\rho'}\frac{1-s_\alpha}{2} \tag{354}$$

The non-vanishing correlators of the amplitudes $b_\rho^A(\omega)$ are a generalization of Kirchoff's law that we saw in equation (309) to non-planar geometries. One can say that the flux coming from plate A is fully defined by the associated scattering matrix S^A.

This said, we are in a position to now derive the field within the cavity, as a superposition of waves :

$$\mathcal{E}_{i\rho}(\omega) = b_\rho^{(+)}(\omega)\mathcal{E}_{i\rho}^{(+)}(\omega) + b_\rho^{(-)}(\omega)\mathcal{E}_{i\rho}^{(-)}(\omega) \tag{355}$$

Now the field within the cavity arises from the scattering coming from each of the two plates' emitted radiation, and the amplitudes $b^{(\pm)}(\omega)$ are thus defined by :

$$b^{(+)} = b^{(1)} + \mathbf{S}^{(1)}b^{(-)} = \mathbf{U}^{(12)}b^{(1)} + \mathbf{S}^{(1)}\mathbf{U}^{(21)}b^{(2)} \tag{356}$$

$$b^{(-)} = b^{(2)} + \mathbf{S}^{(2)}b^{(+)} = \mathbf{U}^{(21)}b^{(2)} + \mathbf{S}^{(2)}\mathbf{U}^{(12)}b^{(1)} \tag{357}$$

For

$$\mathbf{U}^{AB} = \left(1 - \mathbf{S}^A\mathbf{S}^B\right)^{-1} \tag{358}$$

This operational form can also be expanded in indices and written :

$$b_{\alpha,+}(\mathbf{k}_\perp,\omega) = b_\alpha^{\mathrm{rad},A}(\mathbf{k}_\perp,\omega) + \sum_{\mathbf{k}'_\perp,\alpha'} S_A^{\alpha,\alpha'}(\mathbf{k}_\perp,\mathbf{k}'_\perp) b_{\alpha',-}(\mathbf{k}'_\perp,\omega) \tag{359}$$

$$b_{\alpha,-}(\mathbf{k}_\perp,\omega) = b_\alpha^{\mathrm{rad},B}(\mathbf{k}_\perp,\omega) + \sum_{\mathbf{k}'_\perp,\alpha'} S_B^{\alpha,\alpha'}(\mathbf{k}_\perp,\mathbf{k}'_\perp) b_{\alpha',+}(\mathbf{k}'_\perp,\omega), \tag{360}$$

Since $\langle b^A b^{A\,\dagger}\rangle$ and $\langle b^B b^{B\,\dagger}\rangle$ are given by equation (351), and if we assume that the radiation coming from the two different bodies is uncorrelated, so that $\langle b^A b^{B\,\dagger}\rangle = \langle b^B b^{A\,\dagger}\rangle = 0$, we can then calculate $\langle b_\gamma b^\dagger_{\gamma'}\rangle$. After some algebra, we get :

$$\begin{aligned}\langle b_+(\omega) b_+^\dagger(\omega')\rangle = \frac{2\pi\omega}{c^2}\delta(\omega-\omega')\Big\{ & F(\omega,T_A)\mathbf{U}_{AB}\left[\boldsymbol{\Sigma}_{-1}^{\mathrm{pw}} - \mathbf{S}_A\boldsymbol{\Sigma}_{-1}^{\mathrm{pw}}\mathbf{S}_A^\dagger + \mathbf{S}_A\boldsymbol{\Sigma}_{-1}^{\mathrm{ew}} - \boldsymbol{\Sigma}_{-1}^{\mathrm{ew}}\mathbf{S}_A^\dagger\right]\mathbf{U}_{AB}^\dagger \\ & + F(\omega,T_B)\mathbf{S}_A\mathbf{U}_{BA}\left[\boldsymbol{\Sigma}_{-1}^{\mathrm{pw}} - \mathbf{S}_B\boldsymbol{\Sigma}_{-1}^{\mathrm{pw}}\mathbf{S}_B^\dagger + \mathbf{S}_B\boldsymbol{\Sigma}_{-1}^{\mathrm{ew}} - \boldsymbol{\Sigma}_{-1}^{\mathrm{ew}}\mathbf{S}_B^\dagger\right]\mathbf{U}_{BA}^\dagger\mathbf{S}_A^\dagger\Big\}\end{aligned} \tag{361}$$

$$\begin{aligned}\langle b_+(\omega) b_-^\dagger(\omega')\rangle = \frac{2\pi\omega}{c^2}\delta(\omega-\omega')\Big\{ & F(\omega,T_A)\mathbf{U}_{AB}\left[\boldsymbol{\Sigma}_{-1}^{\mathrm{pw}} - \mathbf{S}_A\boldsymbol{\Sigma}_{-1}^{\mathrm{pw}}\mathbf{S}_A^\dagger + \mathbf{S}_A\boldsymbol{\Sigma}_{-1}^{\mathrm{ew}} - \boldsymbol{\Sigma}_{-1}^{\mathrm{ew}}\mathbf{S}_A^\dagger\right]\mathbf{U}_{AB}^\dagger\mathbf{S}_B^\dagger \\ & + F(\omega,T_B)\mathbf{S}_A\mathbf{U}_{BA}\left[\boldsymbol{\Sigma}_{-1}^{\mathrm{pw}} - \mathbf{S}_B\boldsymbol{\Sigma}_{-1}^{\mathrm{pw}}\mathbf{S}_B^\dagger + \mathbf{S}_B\boldsymbol{\Sigma}_{-1}^{\mathrm{ew}} - \boldsymbol{\Sigma}_{-1}^{\mathrm{ew}}\mathbf{S}_B^\dagger\right]\mathbf{U}_{BA}^\dagger\Big\}\end{aligned} \tag{362}$$

$$\begin{aligned}\langle b_-(\omega) b_+^\dagger(\omega')\rangle = \frac{2\pi\omega}{c^2}\delta(\omega-\omega')\Big\{ & F(\omega,T_A)\mathbf{S}_B\mathbf{U}_{AB}\left[\boldsymbol{\Sigma}_{-1}^{\mathrm{pw}} - \mathbf{S}_A\boldsymbol{\Sigma}_{-1}^{\mathrm{pw}}\mathbf{S}_A^\dagger + \mathbf{S}_A\boldsymbol{\Sigma}_{-1}^{\mathrm{ew}} - \boldsymbol{\Sigma}_{-1}^{\mathrm{ew}}\mathbf{S}_A^\dagger\right]\mathbf{U}_{AB}^\dagger \\ & + F(\omega,T_B)\mathbf{U}_{AB}\left[\boldsymbol{\Sigma}_{-1}^{\mathrm{pw}} - \mathbf{S}_B\boldsymbol{\Sigma}_{-1}^{\mathrm{pw}}\mathbf{S}_B^\dagger + \mathbf{S}_B\boldsymbol{\Sigma}_{-1}^{\mathrm{ew}} - \boldsymbol{\Sigma}_{-1}^{\mathrm{ew}}\mathbf{S}_B^\dagger\right]\mathbf{U}_{BA}^\dagger\mathbf{S}_A^\dagger\Big\}\end{aligned} \tag{363}$$

$$\begin{aligned}\langle b_-(\omega) b_-^\dagger(\omega')\rangle = \frac{2\pi\omega}{c^2}\delta(\omega-\omega')\Big\{ & F(\omega,T_A)\mathbf{S}_B\mathbf{U}_{AB}\left[\boldsymbol{\Sigma}_{-1}^{\mathrm{pw}} - \mathbf{S}_A\boldsymbol{\Sigma}_{-1}^{\mathrm{pw}}\mathbf{S}_A^\dagger + \mathbf{S}_A\boldsymbol{\Sigma}_{-1}^{\mathrm{ew}} - \boldsymbol{\Sigma}_{-1}^{\mathrm{ew}}\mathbf{S}_A^\dagger\right]\mathbf{U}_{AB}^\dagger\mathbf{S}_B^\dagger \\ & + F(\omega,T_B)\mathbf{U}_{BA}\left[\boldsymbol{\Sigma}_{-1}^{\mathrm{pw}} - \mathbf{S}_B\boldsymbol{\Sigma}_{-1}^{\mathrm{pw}}\mathbf{S}_B^\dagger + \mathbf{S}_B\boldsymbol{\Sigma}_{-1}^{\mathrm{ew}} - \boldsymbol{\Sigma}_{-1}^{\mathrm{ew}}\mathbf{S}_B^\dagger\right]\mathbf{U}_{BA}^\dagger\Big\}\end{aligned} \tag{364}$$

It is then straightforward to derive $\langle b_{\alpha,\gamma}^{\mathrm{rad}}(\mathbf{k}_\perp,\omega) b_{\alpha,\gamma'}^{\mathrm{rad},\,\dagger}(\mathbf{k}'_\perp,\omega')\rangle$. The two equations (356-357) along with equation (352) fully define the field within the cavity, which is given by the matrix $C^{(KK')}$ of the non-vanishing correlators :

$$\langle b^{(K)}(\omega) b^{(K')\dagger}(\omega')\rangle = \delta_{\omega\omega'} C^{(KK')} \tag{365}$$

where $C^{(KK')}$ can be written in terms of the S-matrices $S^{(1)}$ and $S^{(2)}$ by using equations (356-357) together with equation (352).

We can now determine the average of any observables constructed from the field within the cavity. We will here be interested in the vacuum pressure so as to estimate the Casimir force out-of-thermal equilibrium, but we will see that we can also use this same formalism to determine other observables such as the flux, and hence obtain the radiative heat transfer between the plates. These observables are symmetric bilinears of the electric field, and of the form :

$$\overline{\chi} \equiv \sum_{ij} \int d^2\mathbf{r}_\perp \int d^2\mathbf{r'}_\perp E_i(t,\mathbf{r}) \chi_{ij}(\mathbf{r},\mathbf{r'}) E_j(t,\mathbf{r'}) \tag{366}$$

for $\chi_{ij}(\mathbf{r},\mathbf{r'}) = \chi_{ji}(\mathbf{r'},\mathbf{r})$. Now if we define the following matrix :

$$\chi^{(KK')}_{\rho,\rho'} = \sum_{ij} \int d^2\mathbf{r}_\perp \int d^2\mathbf{r'}_\perp \mathcal{E}^{(K)*}_{i\rho}(\omega,\mathbf{r}) \chi_{ij}(\mathbf{r},\mathbf{r'}) \mathcal{E}^{(K')}_{j\rho'}(\omega,\mathbf{r'}) \tag{367}$$

we can obtain the statistical average of $\overline{\chi}$:

$$\langle \overline{\chi} \rangle = 2 \sum_{\omega>0} \sum_{K,K'} \mathrm{Tr}_\rho \left[C^{(KK')} \chi^{(K'K)} \right] \tag{368}$$

Let's now compute the Casimir force by considering the $xy-$integral of the zz components of the Maxwell stress tensor T_{ij}. We can find :

$$\chi^{(KK')}\left[T_{zz}\right] = \frac{c^2 k_z^2}{4\pi\omega^2} \left(\delta_{KK'} \Pi^{\mathrm{pw}} + \delta_{KJ(K')} \Pi^{\mathrm{ew}} \right) \tag{369}$$

Substituting this in equation (368), we obtain the unrenormalized expression of the Casimir force out-of-thermal equilibrium $F_z^{(0\mathrm{neq})}$:

$$F_z^{(0\mathrm{neq})} = \sum_{\omega>0} \frac{1}{\omega} \left[F(\omega,T_1) \mathbf{J}(\mathbf{S}^{(1)},\mathbf{S}^{(2)}) + F(\omega,T_2) \mathbf{J}(\mathbf{S}^{(2)},\mathbf{S}^{(1)}) \right] \tag{370}$$

for :

$$\mathbf{J}(\mathbf{S}^A,\mathbf{S}^B) = \mathrm{Tr}_\rho (\quad \mathbf{U}^{AB} \left(\mathbf{\Sigma}^{\mathrm{pw}}_{-1} - \mathbf{S}^A \mathbf{\Sigma}^{\mathrm{pw}}_{-1} \mathbf{S}^{A\dagger} + \mathbf{S}^A \mathbf{\Sigma}^{\mathrm{ew}}_{-1} - \mathbf{\Sigma}^{\mathrm{ew}}_{-1} \mathbf{S}^{A\dagger} \right) \tag{371}$$

$$\cdot \quad \mathbf{U}^{AB\dagger} \left(\mathbf{\Sigma}^{\mathrm{pw}}_{2} + \mathbf{S}^{B\dagger} \mathbf{\Sigma}^{\mathrm{pw}}_{2} \mathbf{S}^{B} + \mathbf{S}^{B\dagger} \mathbf{\Sigma}^{\mathrm{ew}}_{2} + \mathbf{\Sigma}^{\mathrm{ew}}_{2} \mathbf{S}^{B} \right)) \tag{372}$$

Now we can add and subtract $\left(F(\omega,T_1) \mathbf{J}(\mathbf{S}^{(2)},\mathbf{S}^{(1)}) + F(\omega,T_2) \mathbf{J}(\mathbf{S}^{(1)},\mathbf{S}^{(2)}) \right)/2$ from the expression inside of the square brackets of equation (370). Then we can find :

$$F_z^{(0\text{neq})}(T_1,T_2)=\frac{1}{2}F_z^{(0\text{eq})}(T_1)+\frac{1}{2}F_z^{(0\text{eq})}(T_2)+\frac{1}{2}\Delta F_z^{(\text{neq})}(T_1,T_2) \tag{373}$$

Here we have used the following expressions :

$$F_z^{(0\text{eq})}=\sum_{\omega>0}\frac{1}{\omega}F(\omega,T)\left[\mathbf{J}(\mathbf{S}^{(1)},\mathbf{S}^{(2)}+\mathbf{J}(\mathbf{S}^{(2)},\mathbf{S}^{(1)})\right] \tag{374}$$

$$\begin{aligned}\Delta F_z^{(\text{neq})}(T_1,T_2) &= \sum_{\omega>0}\frac{1}{\omega}(F(\omega,T_1)-F(\omega,T_2))\left[\mathbf{J}(\mathbf{S}^{(1)},\mathbf{S}^{(2)})-\mathbf{J}(\mathbf{S}^{(2)},\mathbf{S}^{(1)})\right] &(375)\\ &= \hbar\sum_{\omega>0}\left[\overline{n}(\omega,T_1)-\overline{n}(\omega,T_2)\right]\left[\mathbf{J}(\mathbf{S}^{(1)},\mathbf{S}^{(2)})-\mathbf{J}(\mathbf{S}^{(2)},\mathbf{S}^{(1)})\right] &(376)\end{aligned}$$

for

$$F(\omega,T)=\hbar\omega\left[\frac{1}{2}+\overline{n}(\omega,T)\right]\quad\text{with}\quad\overline{n}(\omega,T)=\left[\exp\left(\frac{\hbar\omega}{k_BT}\right)-1\right]^{-1} \tag{377}$$

where we have already defined the function $F(\omega,T)$ in equation (320) and $\overline{n}(\omega,T)$ earlier in equation (225). If we then replace equation (372) in the r.h.s of equation (374), find after some algebra :

$$F_z^{(0\text{eq})}(T)=R^{(0)}(T)+F_z^{(\text{eq})}(T)\quad\text{for}\quad R^{(0)}(T)=2\sum_{\omega>0}\frac{F(\omega,T)}{\omega}\text{Tr}_\rho\left[k_z\Pi^{\text{pw}}\right] \tag{378}$$

Now the divergent quantity $R^{(0)}$ contains a temperature-dependent contribution giving rise to a pressure which is independent of the distance of separation. This pressure depends on the environment outside of the cavity, but not on the geometry nor on the permittivity of the gratings materials [71]. Since $R^{(0)}$ neither depends on the materials' permittivity, nor on the separation distance, we can neglect it.

Concerning the second term in equation (378) corresponding to the renormalized part, we can write it as :

$$F_z^{(\text{eq})}(T)=2\text{Re}\sum_{\omega>0}\frac{F(\omega,T)}{\omega}\text{Tr}_\rho\left[k_z\left(\mathbf{U}^{(12)}\mathbf{S}^{(1)}\mathbf{S}^{(2)}+\mathbf{U}^{(21)}\mathbf{S}^{(2)}\mathbf{S}^{(1)}\right)\right] \tag{379}$$

Based on equation (313) and using $F_z^{(\text{eq})}=\partial F(a,T)/\partial a$, we can readily check that $F_z^{(\text{eq})}(T)$ has an associated free energy :

$$F(a,T)=2\text{Im}\sum_{\omega>0}\frac{F(\omega,T)}{\omega}\text{Tr}_\rho\log\left[1-\mathbf{S}^{(1)}\mathbf{S}^{(2)}\right] \tag{380}$$

This is none other that the scattering expression of the Casimir force at thermal equilibrium which was hinted in equations (233) and (296), and is well documented in literature [28, 29, 148]. Notice however that it is here expressed in terms of real frequencies.

Putting all these results together in equation (373), we finally obtain the now normalized scattering expression of the Casimir force out-of-thermal equilibrium :

$$F_z^{(\mathrm{neq})}(T_1,T_2) = \frac{1}{2}F_z^{(\mathrm{eq})}(T_1) + \frac{1}{2}F_z^{(\mathrm{eq})}(T_2) + \frac{1}{2}\Delta F_z^{(\mathrm{neq})}(T_1,T_2) \tag{381}$$

Notice again that this expression is for real frequencies only. This matters greatly in the numerical computation of the force, because the associated integrand in equation (379) oscillates and is difficult to integrate. One could use again a contour integration and Cauchy's theorem, but the cavity integrand should again obey the analyticity properties explained earlier in section VI A 5, which is far from trivial.

Notice also the important property of $\Delta F_z^{(\mathrm{neq})}(T_1,T_2)$, already seen in equation (376), that it vanishes for two mirrors having the same S-matrices. This implies that two gratings made out of the same materials and same geometries will have a zero non-equilibrium force contribution, but that two gratings made out of the same material with different corrugation depths for example will not. Of course, in the case $T_1 = T_2$, this contribution vanishes [61, 71].

In the general case where the two equilibrium $F_z^{(\mathrm{eq})}(T)$ and non-equilibrium $\Delta F_z^{(\mathrm{neq})}(T_1,T_2)$ terms of the total Casimir force are computed separately, one should also be careful with the order in which the two plates are labeled $A = 1, 2$.

We can replace in equation (381) the scattering matrices between gratings that we have already derived in section VI B 1 through the RCWA method, and thus calculate the out-of-thermal equilibrium Casimir force between gratings, or we can set these S-matrices as diagonal matrices formed by the scalar Fresnel-Stokes amplitudes and hence obtain that same force for the plane-plane case.

2. Near-field radiative heat transfer for periodic gratings

Based on [61, 145], we now build on our earlier formalism developed in Section VI B 3, where we derived the correlation function $\langle b^{rad}_{\alpha,\gamma}(\mathbf{k}_\perp,\omega) b^{rad,\dagger}_{\alpha,\gamma'}(\mathbf{k}'_\perp,\omega')\rangle$ through equations (361-364). By obtaining the statistical average of any observables constructed out of the intracavity field in equation (368), and applying it to the Maxwell stress tensor T_{ij}, we could then derive the expression of the Casimir force out-of-thermal equilibrium within the cavity.

We now use a similar approach. Still considering the radiative heat transfer between two infinite corrugated plates $A = (1), (2)$, and using the same geometrical parameters and spatial coordinates than in FIG. 30, we assume these plates to be parallel to one another and kept at respective temperatures T_1, T_2. The general expression for the heat flux can be written [149] :

$$\mathrm{H_F}(T_1,T_2) = \frac{c}{4\pi}\int_A \mathbf{dA}\cdot\langle \mathbf{E}\times\mathbf{H}\rangle \tag{382}$$

where we assume the average to be at thermal equilibrium. The fact that we did not write equation (382) in a symmetric form and that $\mathbf{E}$ and $\mathbf{H}$ in general do not commute does not change our problem for now. We can then write the electric field $\mathbf{E}$ in the frequency domain :

$$\mathbf{E}(\mathbf{r},t) = \int_0^\infty d\omega \left[\tilde{\mathcal{E}}(\mathbf{r},\omega)e^{-i\omega t} + \tilde{\mathcal{E}}^\dagger(\mathbf{r},\omega)e^{i\omega t}\right] \tag{383}$$

Using Faraday's law from equation (89), we can rewrite $\mathbf{H}$ in terms of $\mathbf{E}$:

$$\mathrm{H_F}(T_1,T_2) = \frac{ic}{4\pi}\int_A \mathbf{dA}\cdot\int d\omega\frac{d\omega'}{\omega'}\{\langle -\tilde{\mathcal{E}}\times(\nabla\times\tilde{\mathcal{E}}')e^{-i(\omega+\omega')t} + \tilde{\mathcal{E}}\times(\nabla\times\tilde{\mathcal{E}}'^\dagger)e^{-i(\omega-\omega')t}\rangle - \text{c.c.}\} \tag{384}$$

Now for $j, j' = 1, 2, 3$ we have :

$$\langle\tilde{\mathcal{E}}_j(\omega)\tilde{\mathcal{E}}_{j'}(\omega')\rangle \sim \langle\tilde{\mathcal{E}}^\dagger_j(\omega)\tilde{\mathcal{E}}^\dagger_{j'}(\omega')\rangle = 0 \tag{385}$$

$$\langle\tilde{\mathcal{E}}_j(\omega)\tilde{\mathcal{E}}^\dagger_{j'}(\omega')\rangle \sim \langle\tilde{\mathcal{E}}^\dagger_j(\omega)\tilde{\mathcal{E}}_{j'}(\omega')\rangle \sim \delta(\omega-\omega') \tag{386}$$

Taking now the surface A as an $xy-$plane separating the two plates, we can write :

$$\mathrm{H_F}(T_1,T_2,a) = \frac{ic^2}{4\pi\omega}\int d\mathbf{r}_\perp\int\frac{d\omega}{\omega}\{\langle\tilde{\mathcal{E}}_j\partial_z\tilde{\mathcal{E}}^\dagger_j - \tilde{\mathcal{E}}_j\partial_j\tilde{\mathcal{E}}^\dagger_z\rangle - \text{c.c.}\}. \tag{387}$$

We will now show that the contribution coming from the second term vanishes. We have :

$$\frac{ic^2}{4\pi\omega}\int d\mathbf{r}_\perp \int \frac{d\omega}{\omega}\langle\tilde{\mathcal{E}}_j\partial_j\tilde{\mathcal{E}}_z^\dagger\rangle = \frac{1}{4\pi}\sum_{j,\gamma\gamma'}\Bigg[\sum_{\mathbf{k}_\perp,\mathbf{k}'_\perp<\omega\geq 0}\frac{c^2}{\omega}k_j^{\gamma'}\int d\mathbf{r}_\perp\langle b_{j,\gamma}(\mathbf{k}_\perp,\omega)b^\dagger_{j,\gamma'}(\mathbf{k}'_\perp,\omega)\rangle e^{i(\mathbf{k}_\perp-\mathbf{k}'_\perp)\cdot\mathbf{r}_\perp+i(\gamma k_z-\gamma' k'_z)z} + \text{c.c.}$$
$$+\sum_{\mathbf{k}_\perp>\omega\geq 0}\sum_{\mathbf{k}'_\perp>\omega\geq 0}\frac{c^2}{\omega}\tilde{k}_j^{\gamma'}\int d\mathbf{r}_\perp\langle b_{j,\gamma}(\mathbf{k}_\perp,\omega)b^\dagger_{j,\gamma'}(\mathbf{k}'_\perp,\omega)\rangle e^{i(\mathbf{k}_\perp-\mathbf{k}'_\perp)\cdot\mathbf{r}_\perp-(\gamma k_z+\gamma' k'_z)z} + \text{c.c.}$$
$$+\sum_{\mathbf{k}_\perp>\omega\geq 0}\sum_{\mathbf{k}'_\perp<\omega'\geq 0}...+\sum_{\mathbf{k}_\perp<\omega\geq 0}\sum_{\mathbf{k}'_\perp>\omega'\geq 0}...\Bigg] \tag{388}$$

$$\frac{ic^2}{4\pi\omega}\int d\mathbf{r}_\perp \int \frac{d\omega}{\omega}\langle\tilde{\mathcal{E}}_j\partial_j\tilde{\mathcal{E}}_z^\dagger\rangle = \frac{1}{4\pi}\sum_{j,\gamma\gamma'}\Bigg[\sum_{\mathbf{k}_\perp<\omega\geq 0}\sum_{\mathbf{k}'_\perp<\omega'\geq 0}\frac{c^2}{\omega}k_j^{\gamma'}\delta_{\mathbf{k}_\perp,\mathbf{k}'_\perp}\langle b_{j,\gamma}(\mathbf{k}_\perp,\omega)b^\dagger_{j,\gamma'}(\mathbf{k}'_\perp,\omega)\rangle e^{i(\gamma k_z-\gamma' k'_z)z} + \text{c.c.}$$
$$+\sum_{\mathbf{k}_\perp>\omega\geq 0}\sum_{\mathbf{k}'_\perp>\omega\geq 0}\frac{c^2}{\omega}\tilde{k}_j^{\gamma'}\delta_{\mathbf{k}_\perp,\mathbf{k}'_\perp}\langle b_{j,\gamma}(\mathbf{k}_\perp,\omega)b^\dagger_{j'}(\mathbf{k}'_\perp,\omega)\rangle e^{-(\gamma k_z+\gamma' k'_z)z} + \text{c.c.}\Bigg] \tag{389}$$

$$\frac{ic^2}{4\pi\omega}\int d\mathbf{r}_\perp \int \frac{d\omega}{\omega}\langle\tilde{\mathcal{E}}_j\partial_j\tilde{\mathcal{E}}_z^\dagger\rangle = \frac{1}{4\pi}\sum_{j,\gamma\gamma'}\Bigg[\sum_{\mathbf{k}_\perp<\omega\geq 0}\frac{c^2k_j^{\gamma'}}{\omega}\langle b_{j,\gamma}(\mathbf{k}_\perp,\omega)b^\dagger_{j,\gamma'}(\mathbf{k}_\perp,\omega)\rangle e^{i(\gamma-\gamma)k_z z} + \text{c.c.}$$
$$+\sum_{\mathbf{k}_\perp>\omega\geq 0}\frac{c^2\tilde{k}_j^{\gamma'}}{\omega}\langle b_{j,\gamma}(\mathbf{k}_\perp,\omega)b^\dagger_{j,\gamma'}(\mathbf{k}_\perp,\omega)\rangle e^{-(\gamma+\gamma')k_z z} + \text{c.c.}\Bigg] \tag{390}$$

where :

$$k^\gamma_{x,y} = \mathbf{k}_\perp \qquad \text{and} \qquad k^\gamma_z = \gamma k_z \tag{391}$$

But the Gauss law in vacuum from equation (91) gives :

$$\nabla\cdot\mathbf{E}(\mathbf{r},t) = \sum_{\omega,\mathbf{k}_\perp,\gamma} k_j^\gamma\, b_{j,\gamma}(\mathbf{k}_\perp,\omega)e^{i\mathbf{k}_\perp\cdot\mathbf{r}_\perp+i\gamma k_z z-i\omega t} = 0 \tag{392}$$

and has to hold for any $\mathbf{r}$ within the cavity. Therefore :

$$k_j^\gamma b_{j,\gamma}(\mathbf{k}_\perp,\omega) = 0 \tag{393}$$

from which we find that equation (390) vanishes. Therefore we can write equation (387) as :

$$\mathrm{H_F}(T_1,T_2,a) = \frac{ic^2}{4\pi\omega}\int d\mathbf{r}_\perp\int\frac{d\omega}{\omega}\{\langle\tilde{\mathcal{E}}_j\partial_z\tilde{\mathcal{E}}_j^\dagger - \text{c.c.}\} \tag{394}$$

Notice that we can write this decomposition as a sum only if the surfaces are transversally periodic, as depicted in FIG. 30. For non-periodic gratings, we have to replace the sums by integrals.

Hence expanding the field in its transverse Fourier components, we can write :

$$\tilde{\mathcal{E}}_j(\mathbf{r},\omega) = \sum_{\mathbf{k}_\perp} b_{j,\pm}(\mathbf{k}_\perp,\omega) e^{i\mathbf{k}_\perp\cdot\mathbf{r}_\perp \pm i k_z z} = \sum_{\mathbf{k}_\perp<\omega} b_{j,\pm}(\mathbf{k}_\perp,\omega) e^{i\mathbf{k}_\perp\cdot\mathbf{r}_\perp \pm i k_z z} + \sum_{\mathbf{k}_\perp>\omega} b_{j,\pm}(\mathbf{k}_\perp,\omega) e^{i\mathbf{k}_\perp\cdot\mathbf{r}_\perp \mp k_z z}$$

where the summation over $\pm$ is implicit. We can separate propagative and evanescent modes :

$$k_z = \begin{cases} \sqrt{-\mathbf{k}_\perp^2 + \omega^2/c^2} & \text{for} \quad \mathbf{k}_\perp < \omega/c \\ \\ \sqrt{+\mathbf{k}_\perp^2 - \omega^2/c^2} & \text{for} \quad \mathbf{k}_\perp > \omega/c \end{cases} \tag{395}$$

By substituting equation (395) into equation (383), and then into equation (387), we have :

$$\begin{aligned} \mathrm{H_F}(T_1,T_2,a) = \frac{1}{4\pi}\sum_{j,\gamma\gamma'} \Bigg[& \sum_{\mathbf{k}_\perp,\mathbf{k}'_\perp<\omega\geq 0} \frac{c^2}{\omega}\gamma' k'_z \int d\mathbf{r}_\perp \langle b_{j,\gamma}(\mathbf{k}_\perp,\omega) b^\dagger_{j,\gamma'}(\mathbf{k}'_\perp,\omega)\rangle e^{i(\mathbf{k}_\perp-\mathbf{k}'_\perp)\cdot\mathbf{r}_\perp + i(\gamma k_z - \gamma' k'_z)z} + \text{c.c.} \\ & - \sum_{\mathbf{k}_\perp>\omega\geq 0}\sum_{\mathbf{k}'_\perp>\omega\geq 0} i\frac{c^2}{\omega}\gamma' k'_z \int d\mathbf{r}_\perp \langle b_{j,\gamma}(\mathbf{k}_\perp,\omega) b^\dagger_{j,\gamma'}(\mathbf{k}'_\perp,\omega)\rangle e^{i(\mathbf{k}_\perp-\mathbf{k}'_\perp)\cdot\mathbf{r}_\perp - (\gamma k_z + \gamma' k'_z)z} + \text{c.c.} \\ & + \sum_{\mathbf{k}_\perp>\omega\geq 0}\sum_{\mathbf{k}'_\perp<\omega'\geq 0} \ldots + \sum_{\mathbf{k}_\perp<\omega\geq 0}\sum_{\mathbf{k}'_\perp>\omega'\geq 0} \ldots \Bigg] \end{aligned}$$

$$\begin{aligned} = \frac{1}{4\pi}\sum_{j,\gamma\gamma'} \Bigg[& \sum_{\mathbf{k}_\perp<\omega\geq 0}\sum_{\mathbf{k}'_\perp<\omega'\geq 0} \frac{c^2}{\omega}\gamma' k'_z \delta_{\mathbf{k}_\perp,\mathbf{k}'_\perp} \langle b_{j,\gamma}(\mathbf{k}_\perp,\omega) b^\dagger_{j,\gamma'}(\mathbf{k}'_\perp,\omega)\rangle e^{i(\gamma k_z - \gamma' k'_z)z} + \text{c.c.} \\ & - \sum_{\mathbf{k}_\perp>\omega\geq 0}\sum_{\mathbf{k}'_\perp>\omega\geq 0} i\frac{c^2}{\omega}\gamma' k'_z \delta_{\mathbf{k}_\perp,\mathbf{k}'_\perp} \langle b_{j,\gamma}(\mathbf{k}_\perp,\omega) b^\dagger_{j'}(\mathbf{k}'_\perp,\omega)\rangle e^{-(\gamma k_z + \gamma' k'_z)z} + \text{c.c.} \Bigg] \end{aligned}$$

$$\begin{aligned} = \frac{1}{4\pi}\sum_{j,\gamma\gamma'} \Bigg[& \sum_{\mathbf{k}_\perp<\omega\geq 0} \frac{c^2\gamma' k'_z}{\omega} \langle b_{j,\gamma}(\mathbf{k}_\perp,\omega) b^\dagger_{j,\gamma'}(\mathbf{k}_\perp,\omega)\rangle e^{i(\gamma-\gamma)k_z z} + \text{c.c.} \\ & - \sum_{\mathbf{k}_\perp>\omega\geq 0} i\frac{\gamma' c^2 k'_z}{\omega} \langle b_{j,\gamma}(\mathbf{k}_\perp,\omega) b^\dagger_{j,\gamma'}(\mathbf{k}_\perp,\omega)\rangle e^{-(\gamma+\gamma')k_z z} + \text{c.c.} \Bigg] \end{aligned} \tag{396}$$

where $\gamma,\gamma' = \pm$. Now we know that :

$$\langle b_{j,\gamma}(\mathbf{k}_\perp,\omega) b^\dagger_{j',\gamma'}(\mathbf{k}_\perp,\omega)\rangle \sim \langle b^\dagger_{j,\gamma}(\mathbf{k}_\perp,\omega) b_{j',\gamma'}(\mathbf{k}_\perp,\omega)\rangle \tag{397}$$

where by "$\sim$ ", we mean that the difference of the two quantities above are (the zero-point contribution) does not contribute to the heat flux.

Then by explicitly calculating the sums in γ, γ' in equation (396), we see that only the $\gamma = \gamma'$ terms survive in the propagative sector, and that only the $\gamma \neq \gamma'$ terms survive in the evanescent sector. Therefore equation (396) can be written :

$$\mathrm{H_F}(T_1, T_2, a) = \frac{2c^2}{4\pi}\left[\sum_{\mathbf{k}_\perp < \omega \geq 0} \frac{\gamma' k_z}{\omega}\delta_{\gamma,\gamma'}\langle b_{j,\gamma}(\mathbf{k}_\perp,\omega) b^\dagger_{j,\gamma'}(\mathbf{k}_\perp,\omega)\rangle + \sum_{\mathbf{k}_\perp > \omega \geq 0} \frac{\gamma' k_z}{i\omega}\delta_{\gamma,-\gamma'}\langle b_{j,\gamma}(\mathbf{k}_\perp,\omega) b^\dagger_{j,\gamma'}(\mathbf{k}_\perp,\omega)\rangle\right] \quad (398)$$

where we used Einstein's summation convention for the Cartesian indices, and implicitly summed over γ, γ' also.

Then if we denote the s, p polarization by indices $\alpha = 1, 2$, and still use Einstein's summation convention, we can also write equation (398) in the polarization basis :

$$\mathrm{H_F}(T_1, T_2, a) = \frac{2c^2}{4\pi}\left[\sum_{\mathbf{k}_\perp < \omega \geq 0} \frac{\gamma' k_z}{\omega}\delta_{\gamma,\gamma'}\langle b_{\alpha,\gamma}(\mathbf{k}_\perp,\omega) b^\dagger_{\alpha,\gamma'}(\mathbf{k}_\perp,\omega)\rangle + \sum_{\mathbf{k}_\perp > \omega \geq 0} \frac{\gamma' k_z}{i\omega}\delta_{\gamma,-\gamma'}\langle b_{\alpha,\gamma}(\mathbf{k}_\perp,\omega) b^\dagger_{\alpha,\gamma'}(\mathbf{k}_\perp,\omega)\rangle\right] \quad (399)$$

In principle, we should replace the total out-of-equilibrium electric field in the previous expression (399), but since in practice we evaluate this equation within an equilibrium framework, we can divide the field in a part due to the body radiation, and a part due to the environment and scattering radiations :

$$b_{\alpha,\gamma}(\mathbf{k}_\perp,\omega) = b^{rad}_{\alpha,\gamma}(\mathbf{k}_\perp,\omega) + b^{t-e}_{\alpha,\gamma}(\mathbf{k}_\perp,\omega) \quad (400)$$

And since the second part does not contribute to the the heat flux, we finally obtain :

$$\mathrm{H_F}(T_1, T_2, a) = \frac{2c^2}{4\pi}\left[\sum_{\mathbf{k}_\perp < \omega \geq 0} \frac{\gamma' k_z}{\omega}\delta_{\gamma,\gamma'}\langle b^{rad}_{\alpha,\gamma}(\mathbf{k}_\perp,\omega) b^{rad,\dagger}_{\alpha,\gamma'}(\mathbf{k}_\perp,\omega)\rangle + \sum_{\mathbf{k}_\perp > \omega \geq 0} \frac{\gamma' k_z}{i\omega}\delta_{\gamma,-\gamma'}\langle b^{rad}_{\alpha,\gamma}(\mathbf{k}_\perp,\omega) b^{rad,\dagger}_{\alpha,\gamma'}(\mathbf{k}_\perp,\omega)\rangle\right] \quad (401)$$

Whereas the expression of the Casimir force was based on the statistical average of the $xy-$integral of the zz components of the Maxwell stress-tensor T_{ij} through equation (369), the radiative heat transfer is given by the statistical average of the $xy-$integral of the z components of the Poynting vector P_i within the cavity. So we can rewrite equation (401) by using the statistical average of $\overline{\chi}$ derived in equation (368), and determine the power of radiative heat transfer W between the plates. If we write :

$$\chi^{(KK')}[P_z] = \frac{c^2 k_z}{4\pi\omega}(-1)^K\left(\delta_{KK'}\Pi^{\mathrm{pw}} + \delta_{KJ(K')}\Pi^{\mathrm{ew}}\right) \quad (402)$$

and replace this expression in equation (368), we find :

$$W = \sum_{\omega>0} \Big[F(\omega, T_1) H(S^{(1)}, S^{(2)}) - F(\omega, T_2) H(S^{(2)}, S^{(1)}) \Big] \tag{403}$$

for

$$H(S^A, S^B) \equiv \mathrm{Tr}_\alpha [\quad U^{AB} \left(\Sigma_{-1}^{\mathrm{pw}} - S^A \Sigma_{-1}^{\mathrm{pw}} S^{A\dagger} + S^A \Sigma_{-1}^{\mathrm{ew}} - \Sigma_{-1}^{\mathrm{ew}} S^{A\dagger} \right) \tag{404}$$

$$\cdot \quad U^{AB\dagger} \left(\Sigma_1^{\mathrm{pw}} - S^{B\dagger} \Sigma_1^{\mathrm{pw}} S^B + S^{B\dagger} \Sigma_1^{\mathrm{ew}} - \Sigma_1^{\mathrm{ew}} S^B \right)] \tag{405}$$

After some lengthy algebra, one can verify the symmetry :

$$H(S^{(1)}, S^{(2)}) = H(S^{(2)}, S^{(1)}) \tag{406}$$

Therefore we can rewrite equation (403) for the radiative heat transfer between the plates :

$$W = \hbar \sum_{\omega>0} \omega \left[\overline{n}(\omega, T_1) - \overline{n}(\omega, T_2) \right] H(S^{(1)}, S^{(2)}) \tag{407}$$

where the operator $F(\omega, T)$ is given in equation (320), $\mathbf{U}_{AB}$ in equation (358), and the projection operators $\mathbf{\Sigma}_1^{pw/ew}$ and $\mathbf{\Sigma}_{-1}^{pw/ew}$ in equations (353-354).

Often we would rather work with the *radiative heat transfer coefficient*, which is the radiative heat transfer divided by the temperature gradient :

$$h = \frac{W}{|T_1 - T_2|} \tag{408}$$

This is again an exact formula, which is written through the symmetric operator $H(S^{(1)}, S^{(2)})$ in the form of S-matrices from scattering theory, describing the geometrical properties of the two plates as well as the materials' properties. So we can replace in equation (407) the scattering matrices between gratings that we have already derived in section VI B 1 through the RCWA method, and thus calculate the radiative heat transfer W between gratings, or we can set these S-matrices as diagonal matrices formed by the scalar Fresnel-Stokes amplitudes and hence obtain that same heat transfer for the plane-plane case.

Notice also that it is written for real frequencies. This matters greatly in the numerical computation of the force, because the associated integrand from equation (405) oscillates and is difficult to integrate over the modes components

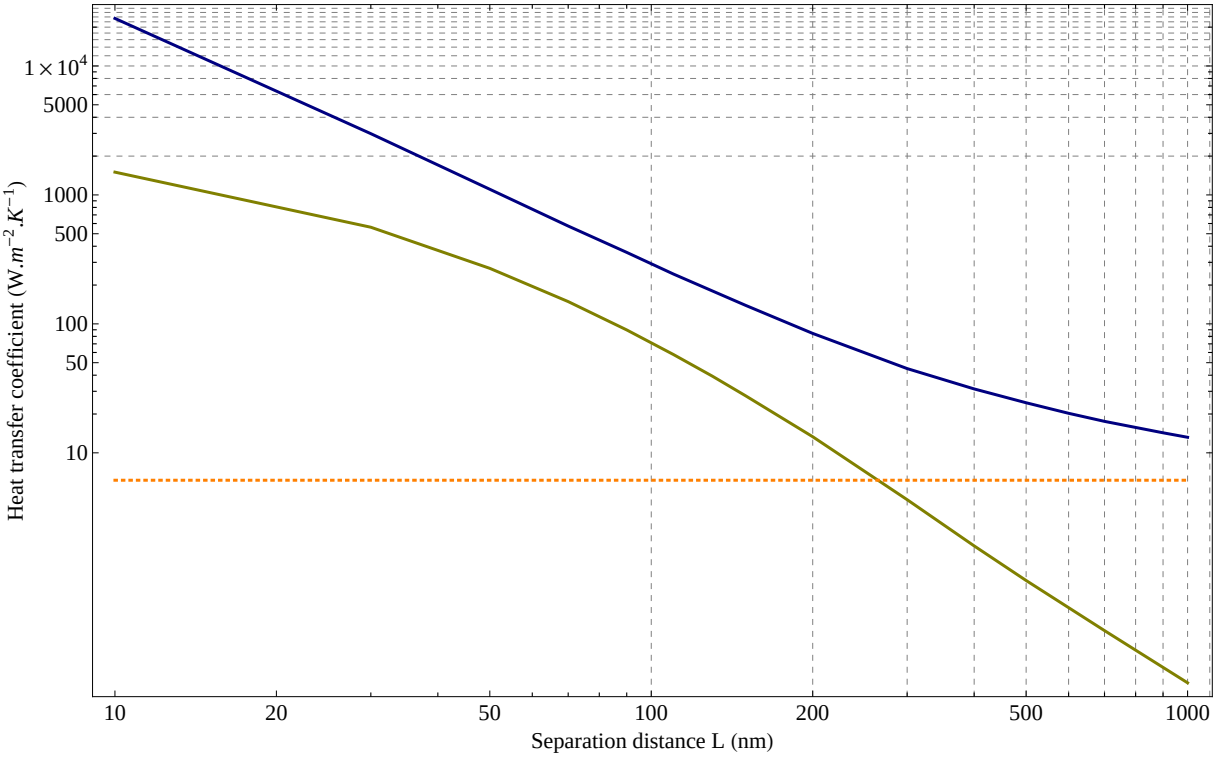

FIG. 37: Heat transfer coefficients between two flat mirrors of SiO_2 (blue curve) and of gold (yellow curve), for separation distances ranging from $L = 10$nm to $L = 1000$nm. The permittivity of SiO_2 comes from optical data in [111], and gold from the Drude model in [70, 114]. The black body limit appears in dashed orange.

k_x, k_z, and ω. One could use again a contour integration and Cauchy's theorem, but the cavity integrand should again obey the analyticity properties explained earlier in section VI A 5, which is not trivial.

In FIG. 37 we show the radiative heat transfer coefficients for planes of different materials, as a function of the separation distance. We also show the black body limit from Stefan-Boltzmann's law in σT^4 from equation (2), now written between the two plates :

$$W = \epsilon\sigma\left(T_1^4 - T_2^4\right) \tag{409}$$

for ϵ the emissivities of the plates. Now this is correct only for a material with emissivity ϵ facing another material with emissivity 1. For two materials with emissivity ϵ, we find $\epsilon/(2-\epsilon)$ due to multiple reflections. Furthermore, the integrated form yielding the T^4 dependence is only valid for non-dispersive materials, which is not the case for gratings.

VII. NUMERICAL EVALUATION : CASIMIR FOR ZERO TEMPERATURES

A. Casimir energy between planar surfaces

We start our study of the Casimir effect with the simplest case of two planar surfaces. In FIG. 38 and 39 we show the variation of the Casimir energy and the Casimir force respectively, as functions of the separation distance L between the plates, in the range $L = 50$ nm to 10μm. This is done for several dielectrics (intrinsic silicon Si and silicon carbide SiC) and several metals (gold Au, aluminum Al, copper Cu, and tungsten W).

The purpose of these two plots is mainly to show that as expected the Casimir energy variation with distance L is proportional to a factor $\sim 1/L^3$, and that the Casimir force variation with distance L is proportional to a factor $\sim 1/L^4$. This is a powerful empirical result, because it allows one to compute fairly accurately the Casimir energy or force at any distance if its value is known at one given separation distance L.

Another interest of these two plots is that one can use them to manually compute the Proximity Approximation to Casimir energy or force between gratings.

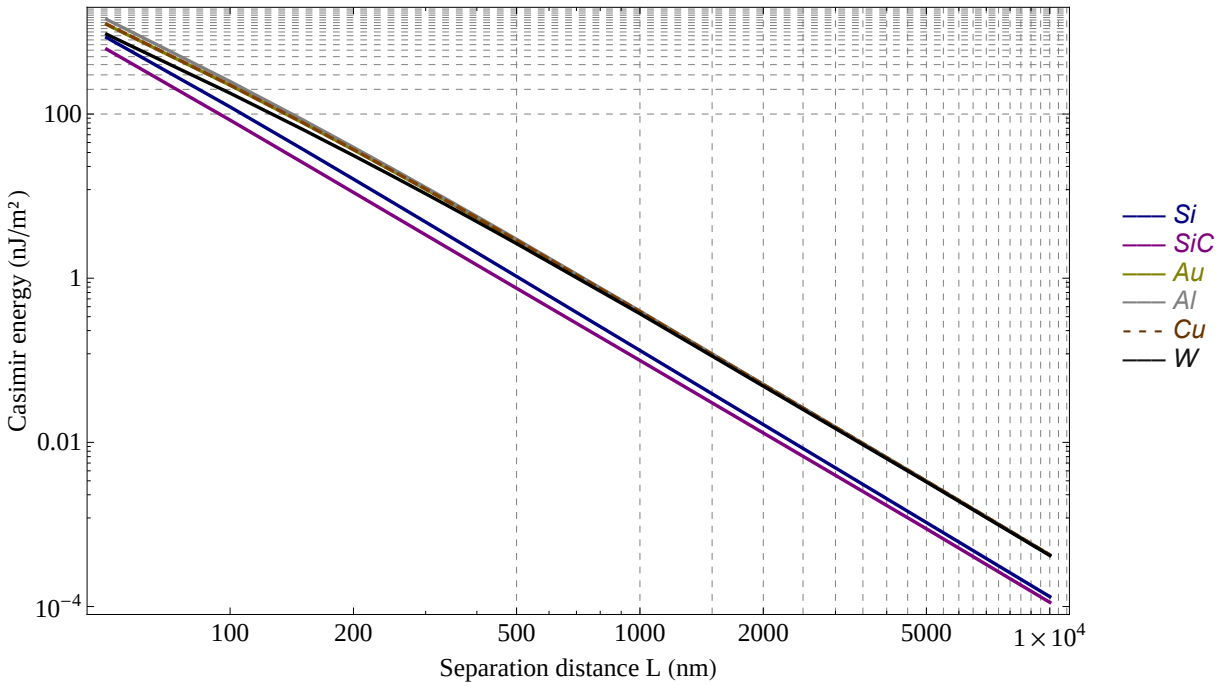

FIG. 38: Log-log dependence of the Casimir energy with the separation distance L, for two planes of different materials. Intrinsic silicon appears in blue, and is described by the Drude-Lorentz model [27, 117, 150] given in equation (137). SiC appears in purple, and is described by the Drude-Lorentz model [65] given in equation (140). Gold appears in yellow, aluminum in gray, copper in dashed orange, and tungsten in black. These four metals are described by a Drude model [70] given by equation (135) and FIG. 11.

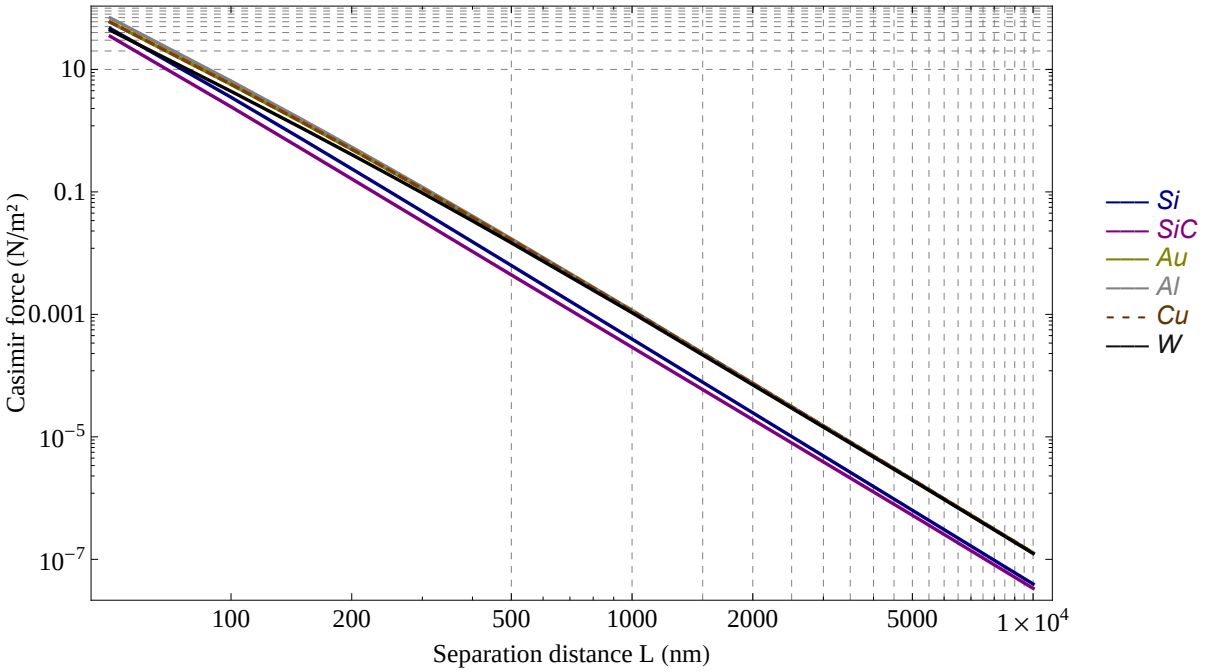

FIG. 39: Log-log dependence of the Casimir force with the separation distance L, for two planes of different materials. Intrinsic silicon appears in blue, and is described by the Drude-Lorentz model [27, 117, 150] given in equation (137). SiC appears in purple, and is described by the Drude-Lorentz model [65] given in equation (140). Gold appears in yellow, aluminum in gray, copper in dashed orange, and tungsten in black. These four metals are described by a Drude model [70] given by equation (135) and FIG. 11.

B. Casimir energy between corrugated gratings

We now present systematic computations of the Casimir energy for different configurations of grating geometries and materials. We vary the geometrical parameters along separation distance L, corrugation period d, filling factor p, and corrugation depth a. We probe different materials : dielectrics first, with intrinsic silicon (Si) and silicon carbide (SiC), and then metals : gold (Au), aluminum (Al), copper (Cu), and tungsten (W).

The reason for exploring the Casimir energy through these parameters of grating geometry and materials, is that these are the only two given parameters that define the scattering matrices associated with each mirror. In other words, the S-matrix associated with each grating is fully specified through the geometry of the corrugations and the materials involved. The results shown here are based on the scattering theory described in Section II.2.1, with the Casimir energy expressed by equation (296).

For application purposes, we will compare these exact results with the Proximity Approximation. This is motivated by the fact that if one wants to obtain exact results for gratings (such as those presented here below through a

scattering formalism), both the computation time and complexity are very involving for practical applications : an approximation method such as the Proximity Approximation is therefore a natural choice for experimentalists and the industry, and its domain of validity is therefore an interesting question. However one should keep in mind that the main focus and results we present here are the scattering results : as exact computations, they provide valuable sets of data for both experimental and other theoretical approaches to compare.

1. Casimir energy between corrugated gratings as a function of the separation distance L

In FIG. 40-43, we show the Casimir energy as a function of separation distance L between gratings of Si, SiC, Au, and W, each with period $d = 200$ nm, filling factor $p = 50\%$, and groove depth $a = 100$ nm. The results for these different materials are compared with one another in FIG. 44, and with Al and Cu.

So based on the results of FIG. 40-44, we can make the following remarks :

- There is a clear correlation in FIG. 44 between the energy values of the different dielectrics, and between the energy values of the different metals. Most notably, the Casimir energies for gold and copper are almost equal.
- This convergence between the Casimir energies of metals increases with larger distances. This is seen especially in FIG. 44 with the energies of gold and tungsten.
- The Proximity Approximation is in general a good approximation for metals in the whole distance range considered. For dielectrics, the Proximity Approximation gives the correct result only in the distance limit $L > 300$ nm. At short distances, relevant for experiments and nanotechnological applications, the Proximity Approximation overestimates the Casimir energy by up to $\sim 35\%$, as shown on FIG. 40 and 41.

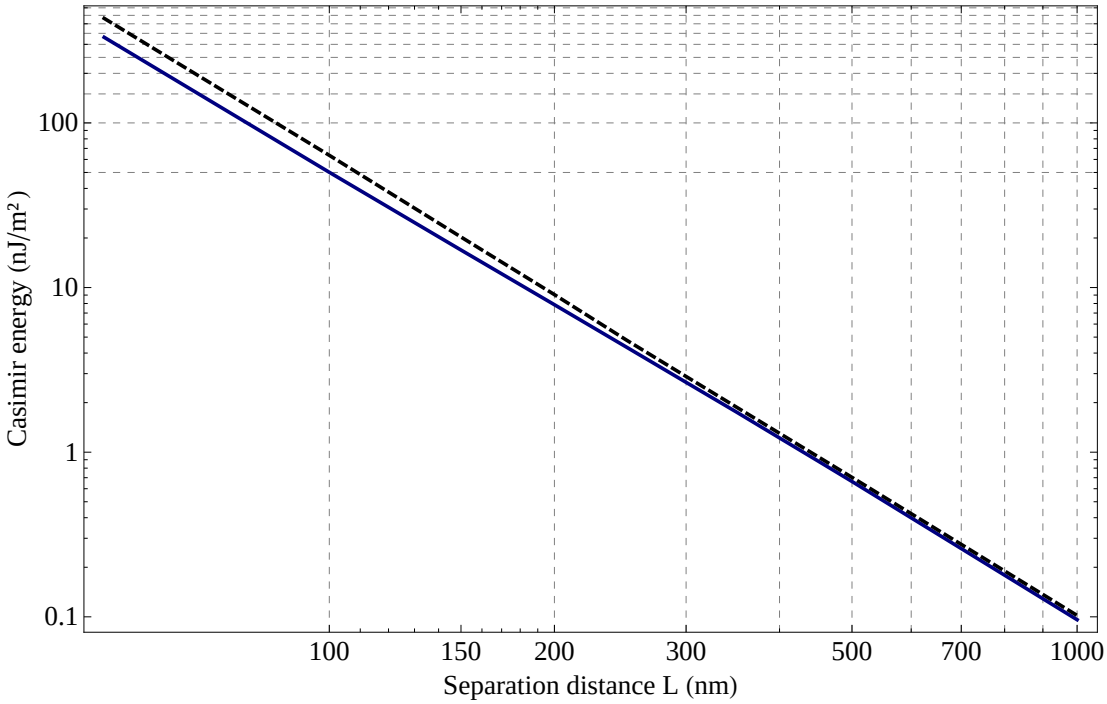

FIG. 40: Log-log dependence of the Casimir energy with the separation distance L, for two gratings of intrinsic silicon described by the Drude-Lorentz model [27, 117, 150] given in equation (137). This is for a grating period $d = 200$ nm, filling factor $p = 50\%$, and groove depth $a = 100$ nm. These scattering results are compared with the Proximity Approximation (dashed line).

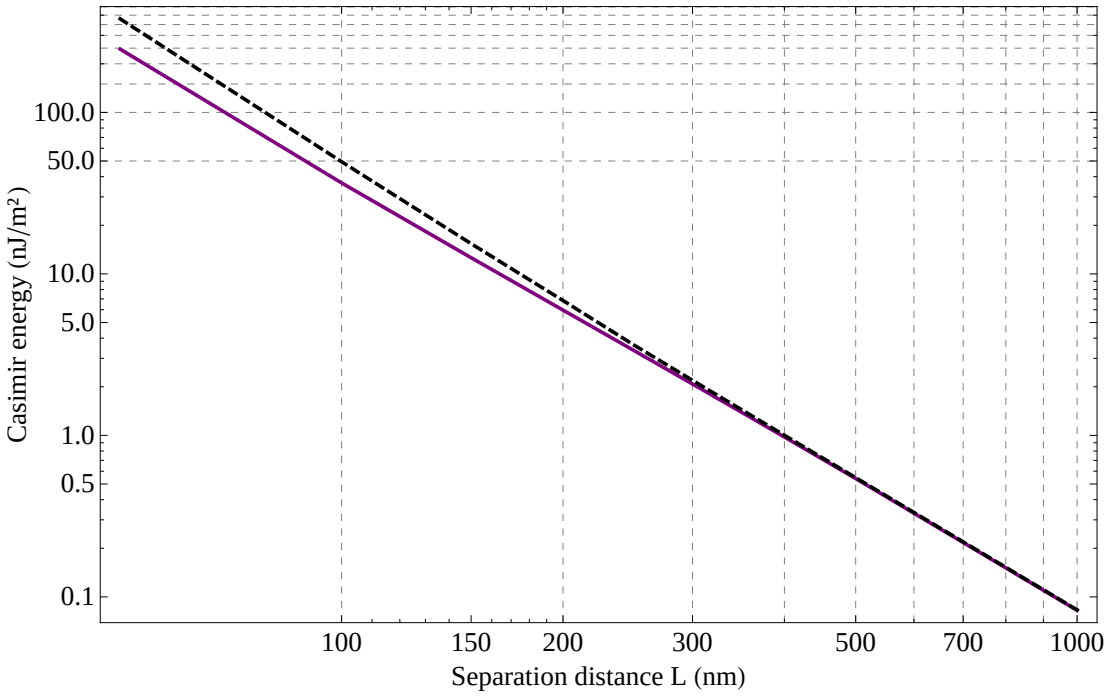

FIG. 41: Log-log dependence of the Casimir energy with the separation distance L, for two gratings of SiC described by the Drude-Lorentz model [65] given in equation (140). This is for a grating period $d = 200$ nm, filling factor $p = 50\%$, and groove depth $a = 100$ nm. These scattering results are compared with the Proximity Approximation (dashed line).

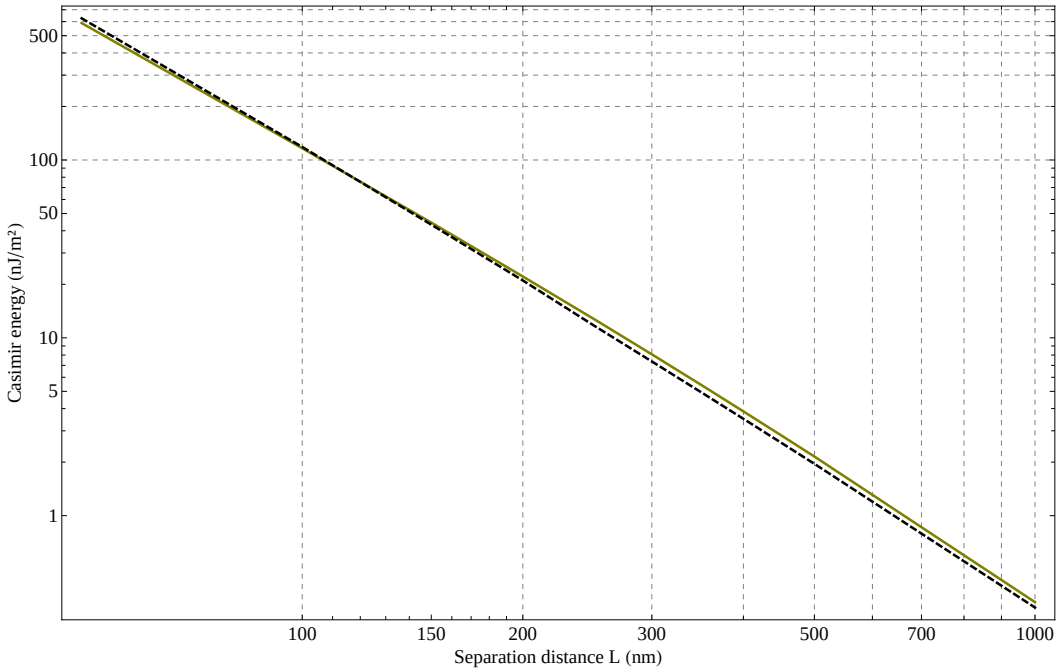

FIG. 42: Log-log dependence of the Casimir energy with the separation distance L, for two gratings of gold described by a Drude model [70] given by equation (135) and FIG. 11. This is for a grating period $d = 200$ nm, filling factor $p = 50\%$, and groove depth $a = 100$ nm. These scattering results are compared with the Proximity Approximation (dashed line).

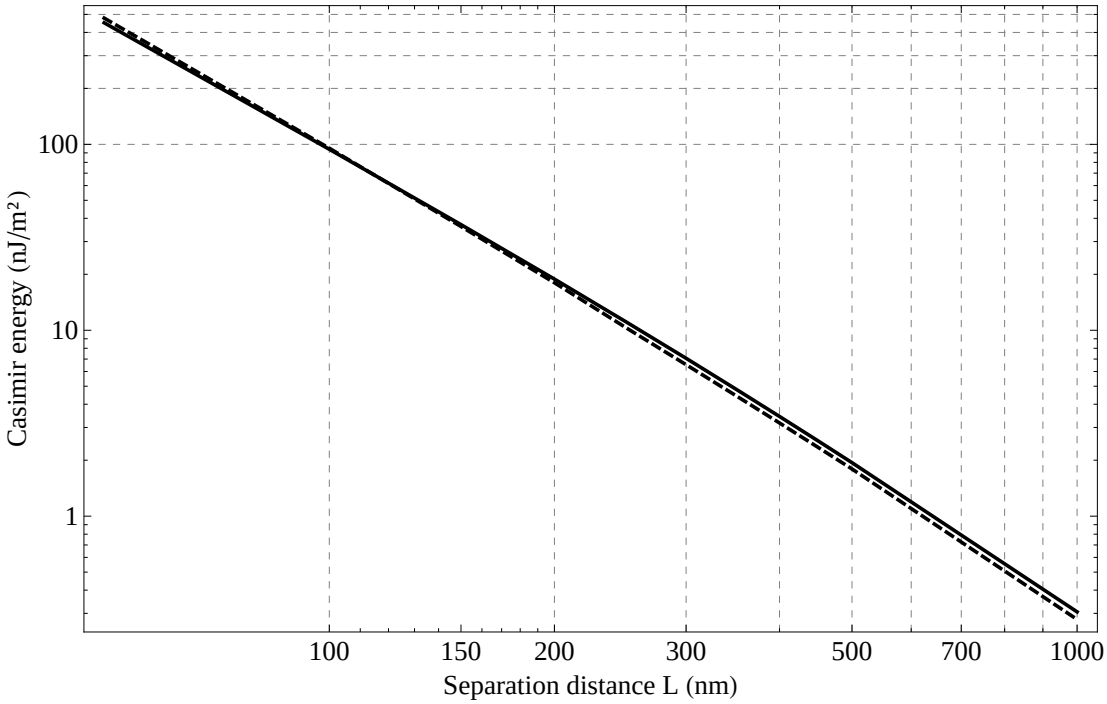

FIG. 43: Log-log dependence of the Casimir energy with the separation distance L, for two gratings of tungsten described by a Drude model [116] given by equation (135) and FIG. 11. This is for a grating period $d = 200$ nm, filling factor $p = 50\%$, and groove depth $a = 100$ nm. These scattering results are compared with the Proximity Approximation (dashed line).

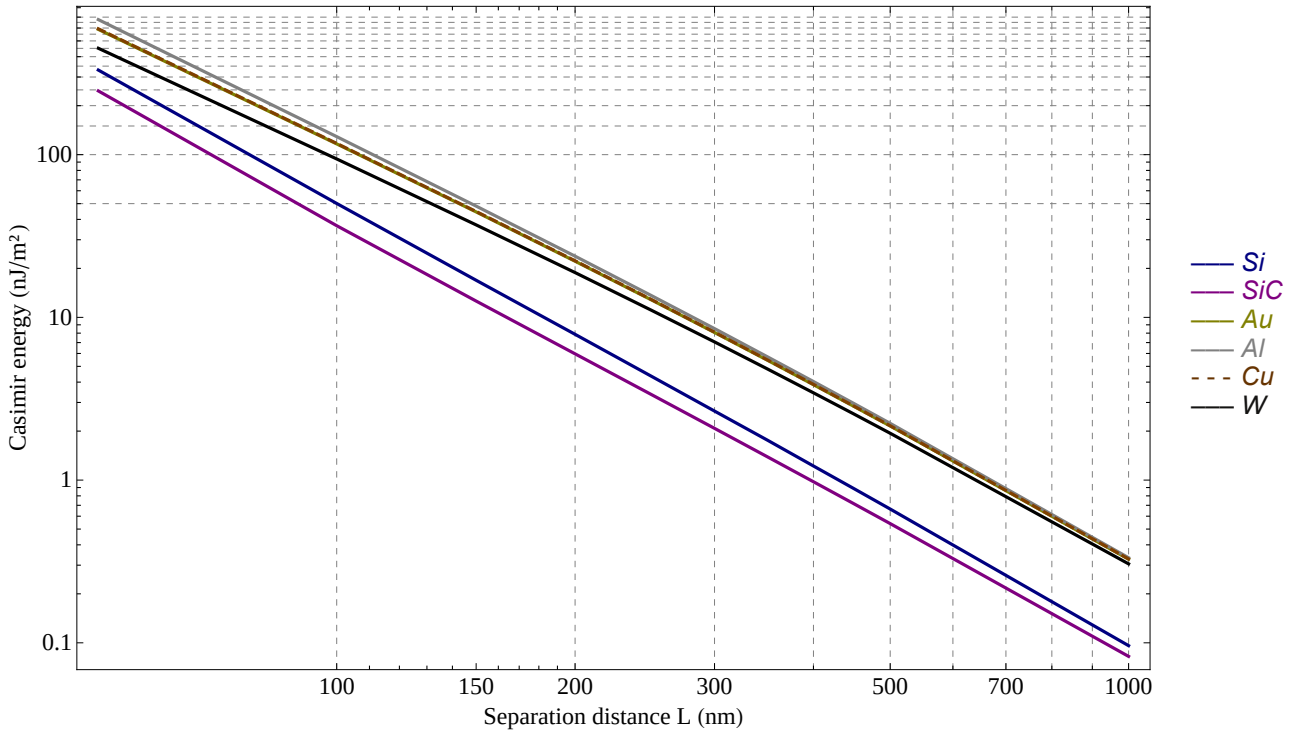

FIG. 44: Log-log dependence of the Casimir energy with the separation distance L, for two gratings of different materials with grating period $d = 200$ nm, filling factor $p = 50\%$, and groove depth $a = 100$ nm. Intrinsic silicon appears in blue, and is described by the Drude-Lorentz model [27, 117, 150] given in equation (137). SiC appears in purple, and is described by the Drude-Lorentz model [65] given in equation (140). Gold appears in yellow, aluminum in gray, copper in dashed orange, and tungsten in black. These four metals are described by a Drude model [70] given by equation (135) and FIG. 11.

2. Casimir energy between corrugated gratings as a function of the grating period d

In FIG. 45-48, we show the Casimir energy as a function of the grating period d between gratings of Si, SiC, Au, Al, Cu, and W, each with filling factor $p = 50\%$, groove depth $a = 100$ nm, and at a separation distance $L = 200$ nm. The results for these different materials are compared in FIG. 48.

Based on the results of FIG. 45-48, we can make the following remarks :

- The Casimir energy decreases abruptly when d varies from 0 to 500 nm, and then the slope varies softly for greater periods.
- This variation of the Casimir energy for greater grating periods changes from dielectrics, where it is increasing, to metals, where it is decreasing.
- Notice the constant values of the Proximity Approximation, due to its expression as the weighted sum of the local planar contributions of the gratings : changing the period and keeping a constant filling factor does not change the weight of each contribution, and hence not the total value of the Proximity Approximation.
- Therefore the Proximity Approximation is not accurate for dielectrics and for metals with period $d < 500$ nm for the geometrical parameters given above. This due to the known domain of validity of the Proximity Approximation, when $L \ll a, d$. Conversely, in the range of periods beyond 500 nm, the Proximity Approximation works well for metals. This is because the fundamental nature of the Proximity Approximation is that its accuracy increases with shorter distances : it is a near-field approximation. So materials such as metals which are more reflective than dielectrics will tend to magnify this near-field dependency (as seen on FIG. 44), and the Proximity Approximation will in general tend to describe the Casimir energy associated to them better than for dielectrics.
- As a side note, the RCWA formalism used here to compute the Casimir energy shows a sign of weakness in the sense that it is accurate up to a convergence of diffraction order n only. This diffraction order is not sensitive for gratings with $a > d$, but becomes predominant in the total value of the energy when $a < d$. This is due to the fact that in these configurations, the modes with larger k_x/k_z ratios begin to contribute strongly.
- Nevertheless, we can gain confidence in the validity of our results by noticing that regardless of the material chosen, the short end of the curve where $d < a = 100$ nm smoothly connects with the rest of the curve where $d > a = 100$ nm.
- The modes that have a wavelengths above the grating period do not enter the corrugations trenches and therefore the problem of diffraction is practically non-existent for the scattering of these modes. The Casimir energy, which is derived as a sum over all the modes within each Brillouin zone, is hence well described by an effective media approximation [151] for $d \to \infty$, and by a plane-plane case at $d \to 0$.

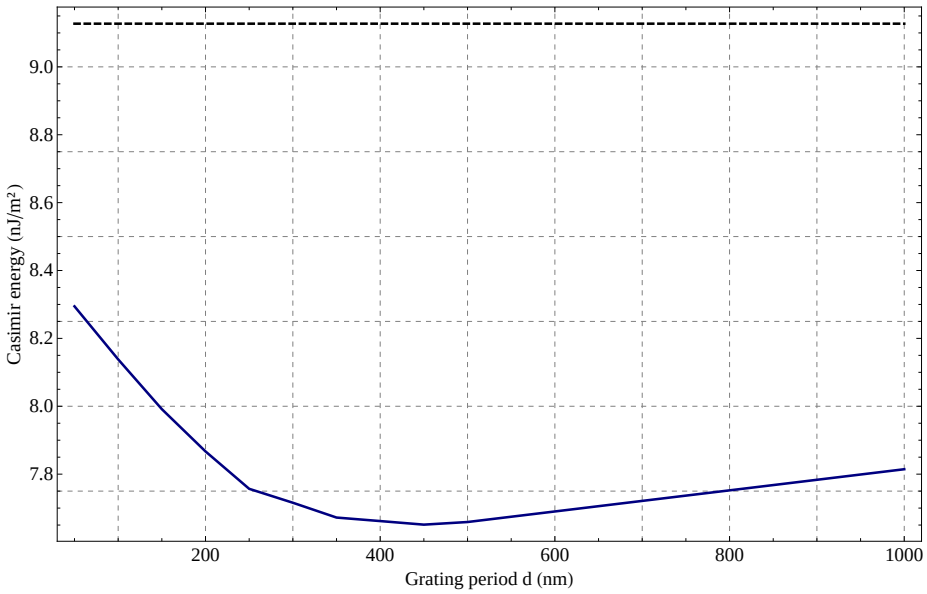

FIG. 45: Casimir energy as a function of the grating period d, for two gratings of intrinsic silicon described by the Drude-Lorentz model [27, 117, 150] given in equation (137). This is for a grating filling factor $p = 50\%$, groove depth $a = 100$ nm, and separation distance $L = 200$ nm. These scattering results are compared with the Proximity Approximation (dashed curve).

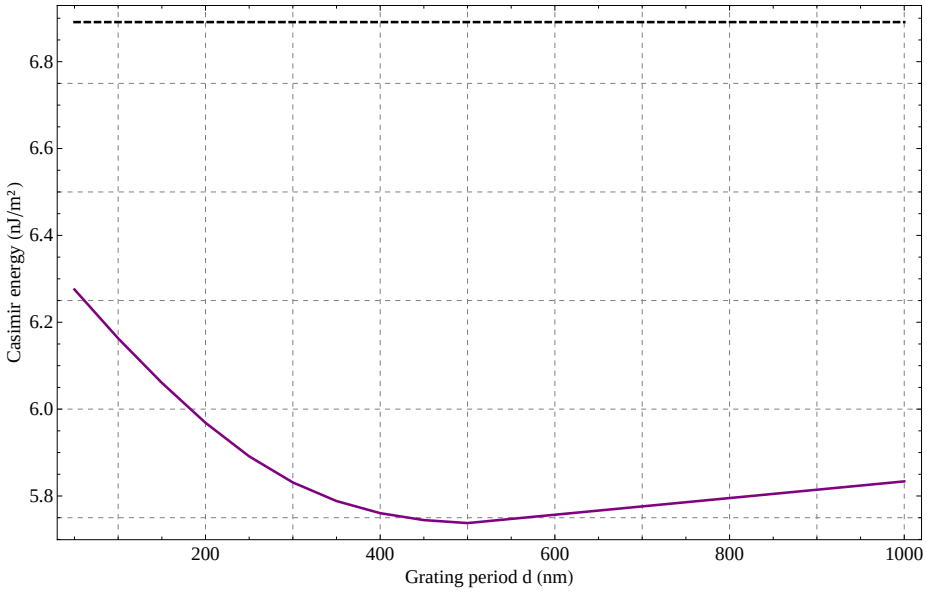

FIG. 46: Casimir energy as a function of the grating period d, for two gratings of SiC described by the Drude-Lorentz model [65] given in equation (140). This is for a grating filling factor $p = 50\%$, groove depth $a = 100$ nm, and separation distance $L = 200$ nm. These scattering results are compared with the Proximity Approximation (dashed curve).

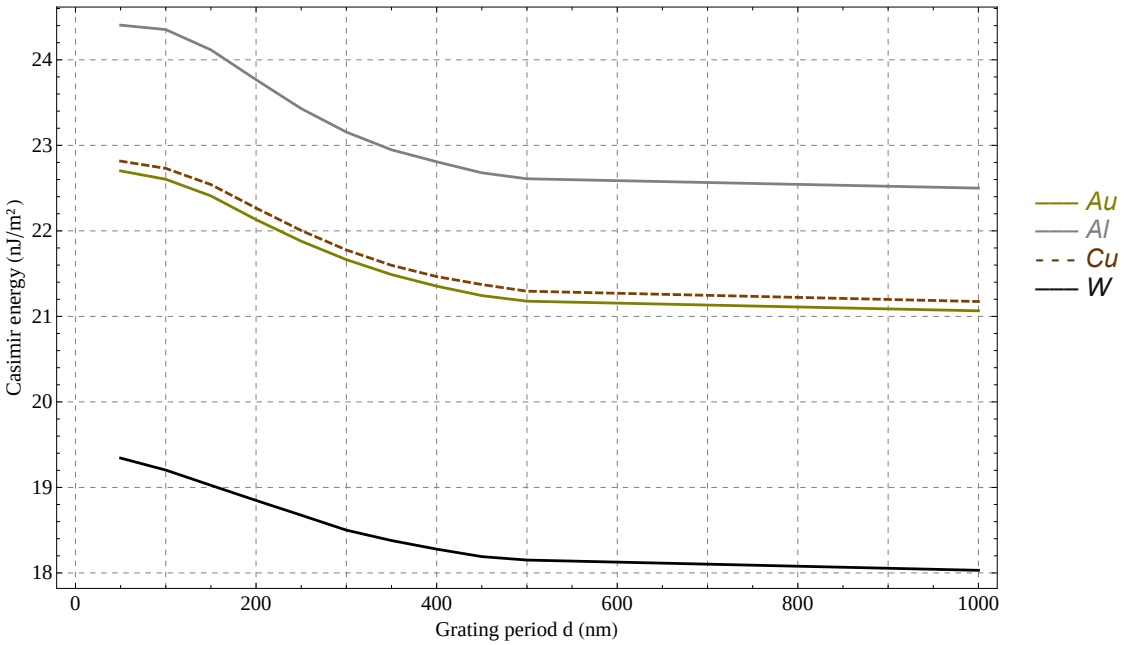

FIG. 47: Log-log dependence of the Casimir energy with the grating period d, for two gratings of different metals with filling factor $p = 50\%$, groove depth $a = 100$ nm, and separation distance $L = 200$ nm. Gold appears in yellow, aluminum in gray, copper in dashed orange, and tungsten in black. These four metals are described by a Drude model [70] given by equation (135) and FIG. 11.

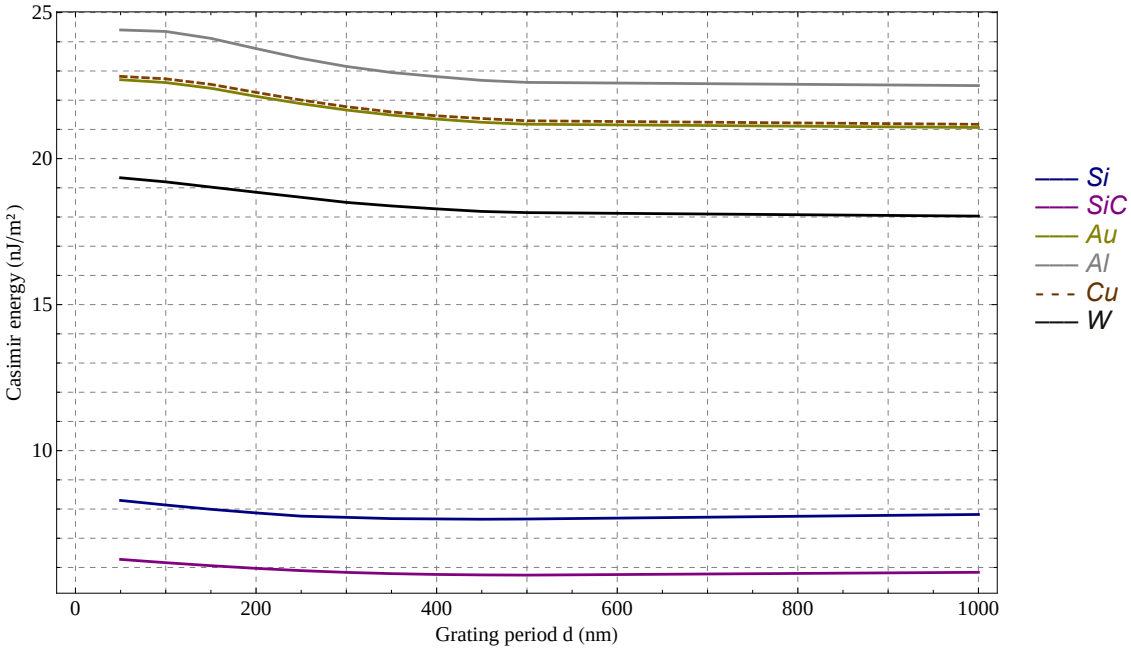

FIG. 48: Log-log dependence of the Casimir energy with the grating period d, for two gratings of different materials with filling factor $p = 50\%$, groove depth $a = 100$ nm, and separation distance $L = 200$ nm. Intrinsic silicon appears in blue, and is described by the Drude-Lorentz model [27, 117, 150] given in equation (137). SiC appears in purple, and is described by the Drude-Lorentz model [65] given in equation (140). Gold appears in yellow, aluminum in gray, copper in dashed orange, and tungsten in black. These four metals are described by a Drude model [70] given by equation (135) and FIG. 11.

3. Casimir energy between corrugated gratings as a function of the filling factor p

In FIG. 49-54, we show the Casimir energy as a function of the grating filling factor p between gratings of Si, SiC, Au, Al, Cu, and W, each with grating period $d = 200$ nm, groove depth $a = 100$ nm, and at a separation distance $L = 200$ nm. The results for these different materials are compared in FIG. 55.

Based on this comparison, we can make the following remarks :

- At both extremities, $p = 0\%$ and $p = 100\%$, we rejoin the case of two flat mirrors of separation distances $L + 2a = 400$ nm and $L = 200$ nm, respectively. This is why the Proximity Approximation and the scattering results are exactly the same at these points, regardless of the material.

- The main result here is that the variation of the filling factor p from 0 to 100% can be approximated, regardless of the material involved, by a straight line joining these two extremities at $p = 0\%$ and $p = 100\%$. This is a useful result because these two points are basically computed from the trivial plane-plane case at the respective separation distances $L + 2a = 400$ nm and $L = 200$ nm. Nevertheless, this is just a rule of thumb, as some filling factors (such as $p = 70\%$ for Si, or $p = 10\%$ for metals) display a $\sim 20\%$ mismatch between the Proximity Approximation and the scattering results.

- Larger filling factors for dielectrics increase the difference in the values of the scattering and Proximity Approximation results —albeit this is clearly less pronounced for the SiC.

- The Proximity Approximation always majors the scattering results of the dielectrics, and minors the scattering results of the metals.

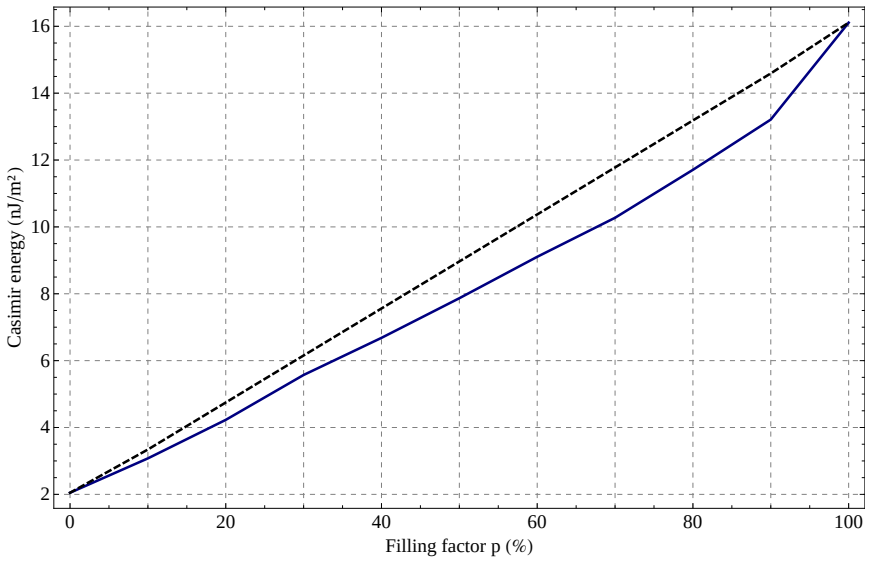

FIG. 49: Casimir energy as a function of the grating filling factor p, for two gratings of intrinsic silicon described by the Drude-Lorentz model [27, 117, 150] given in equation (137). This is for a grating period $d = 200$ nm, groove depth $a = 100$ nm, and separation distance $L = 200$ nm. These scattering results are compared with the Proximity Approximation (dashed curve).

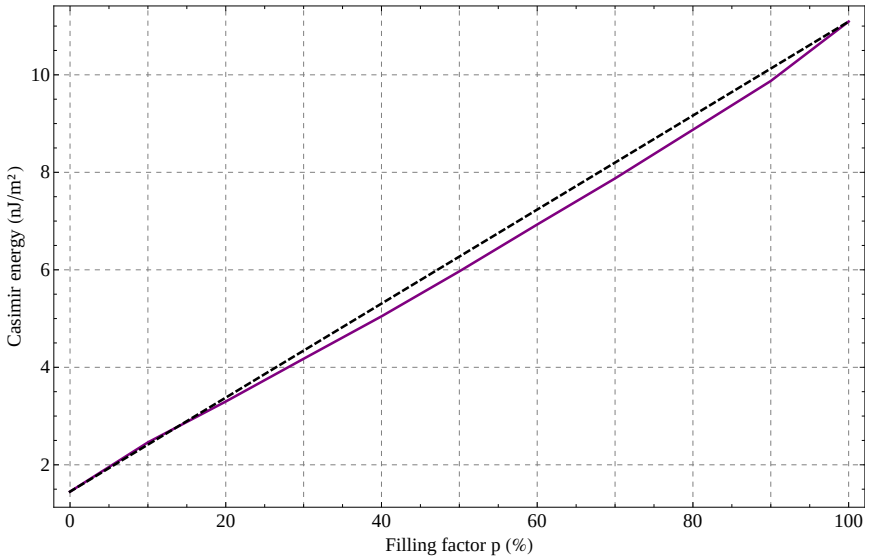

FIG. 50: Casimir energy as a function of the grating filling factor p, for two gratings of SiC described by the Drude-Lorentz model [65] given in equation (140). This is for a grating period $d = 200$ nm, groove depth $a = 100$ nm, and separation distance $L = 200$ nm. These scattering results are compared with the Proximity Approximation (dashed curve).

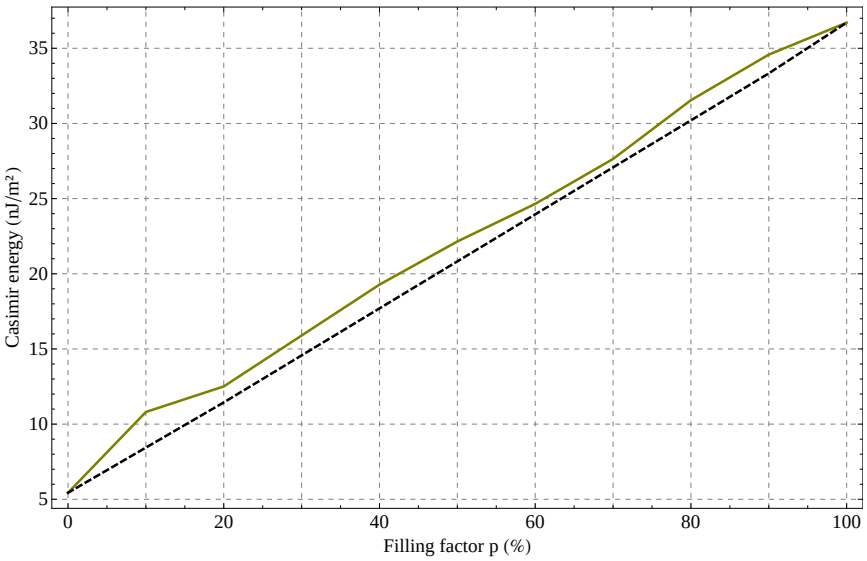

FIG. 51: Casimir energy as a function of the grating filling factor p, for two gratings of gold described by a Drude model [70] given by equation (135) and FIG. 11. This is for a grating period $d = 200$ nm, groove depth $a = 100$ nm, and separation distance $L = 200$ nm. These scattering results are compared with the Proximity Approximation (dashed curve).

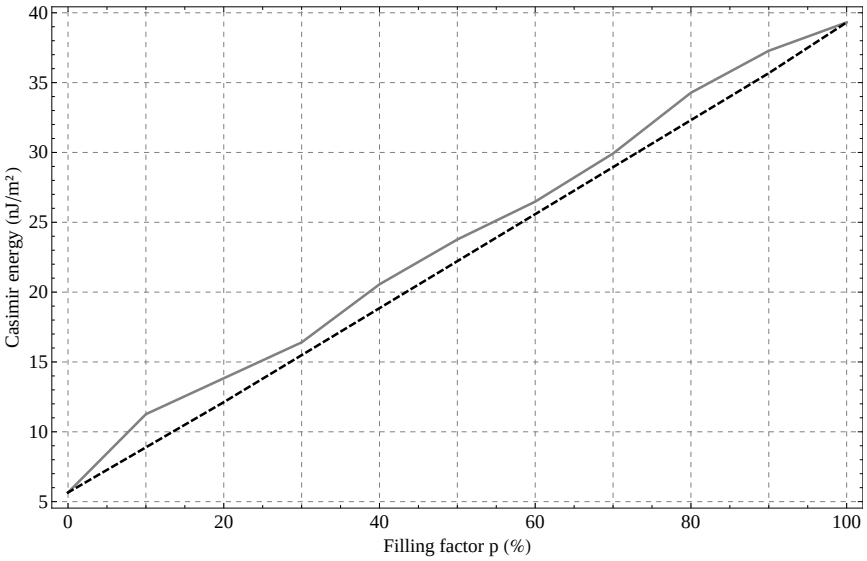

FIG. 52: Casimir energy as a function of the grating filling factor p, for two gratings of aluminum described by a Drude model [152] given by equation (135) and FIG. 11. This is for a grating period $d = 200$ nm, groove depth $a = 100$ nm, and separation distance $L = 200$ nm. These scattering results are compared with the Proximity Approximation (dashed curve).

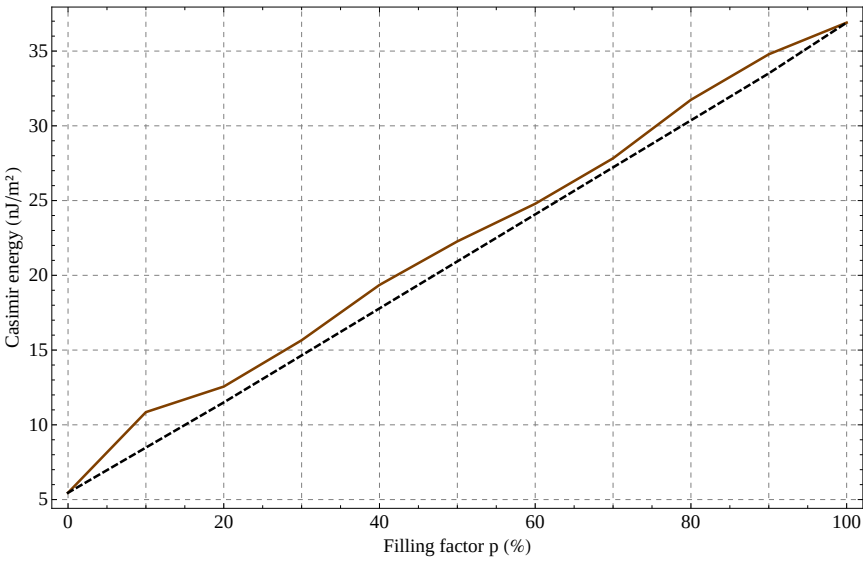

FIG. 53: Casimir energy as a function of the grating filling factor p, for two gratings of copper described by a Drude model [152] given by equation (135) and FIG. 11. This is for a grating period $d = 200$ nm, groove depth $a = 100$ nm, and separation distance $L = 200$ nm. These scattering results are compared with the Proximity Approximation (dashed curve).

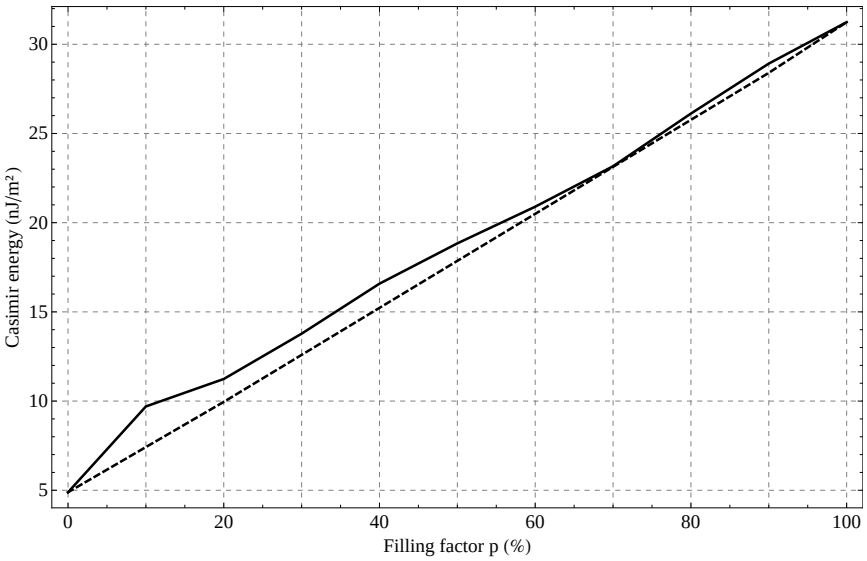

FIG. 54: Casimir energy as a function of the grating filling factor p, for two gratings of tungsten described by a Drude model [116] given by equation (135) and FIG. 11. This is for a grating period $d = 200$ nm, groove depth $a = 100$ nm, and separation distance $L = 200$ nm. These scattering results are compared with the Proximity Approximation (dashed curve).

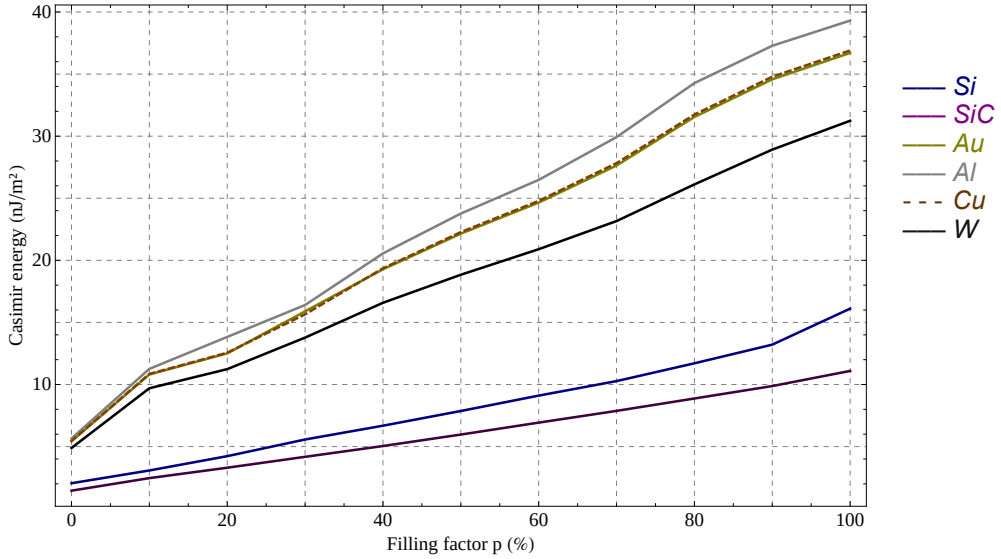

FIG. 55: Log-log dependence of the Casimir energy with the grating filling factor p, for two gratings of different materials with period $d = 200$ nm, groove depth $a = 100$ nm, and separation distance $L = 200$ nm. Intrinsic silicon appears in blue, and is described by the Drude-Lorentz model [27, 117, 150] given in equation (137). SiC appears in purple, and is described by the Drude-Lorentz model [65] given in equation (140). Gold appears in yellow, aluminum in gray, copper in dashed orange, and tungsten in black. These four metals are described by a Drude model [70] given by equation (135) and FIG. 11.

4. Casimir energy between corrugated gratings as a function of the corrugation depth a

In FIG. 56-57, we show the Casimir energy as a function of the grating groove depth a between gratings of Si, and Au, each with grating period $d = 200$ nm, filling factor $p = 50\%$, and at a separation distance $L = 200$ nm. The results for these different materials are compared in FIG. 58 together with SiC, Al, Cu, and W.

By comparing the different figures we may make the following observations :

- There is a convergence of the Casimir energy values to a constant for deeper grooves. This is due to the fact that the bottom of each groove becomes increasingly distant from the other grating with increasing groove depth a, and hence contributes less in a measure following the $1/L^3$ law seen in FIG. 44.
- In the range of depths here considered, we observe an increasing divergence between the scattering and Proximity Approximation values of the deeper grooves for dielectrics, but a an increasing convergence between the two for metals. Nevertheless it may be logical for much deeper trenches to recover a convergence between scattering and Proximity Approximation results, since most of the energy contribution should come from near-field by the top of the corrugation ridges.
- At $a = 0$ nm, we recover the plane-plane values of separation distances $L = 200$ nm. This explains the accuracy of the Proximity Approximation in the neighborhood of this point.
- Since the Proximity Approximation considers the normal modes only, its divergence from the scattering results in the range $50 < a < 250$ nm for metals is an indicator of the importance of the contribution of the lateral modes in this region. Notice how this range of groove depths is correlated with the ratio a/d.

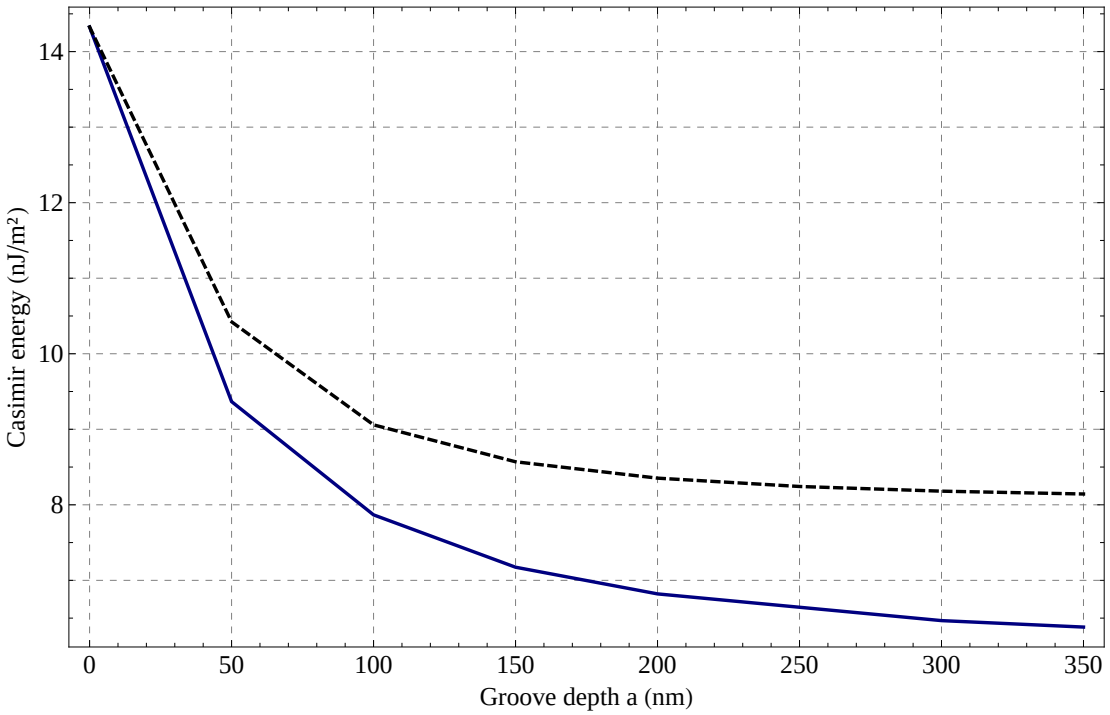

FIG. 56: Casimir energy as a function of the grating groove depth a, for two gratings of intrinsic silicon described by the Drude-Lorentz model [27, 117, 150] given in equation (137). This is for a grating period $d = 200$ nm, filling factor $p = 50\%$, and separation distance $L = 200$ nm. These scattering results are compared with the Proximity Approximation (dashed curve).

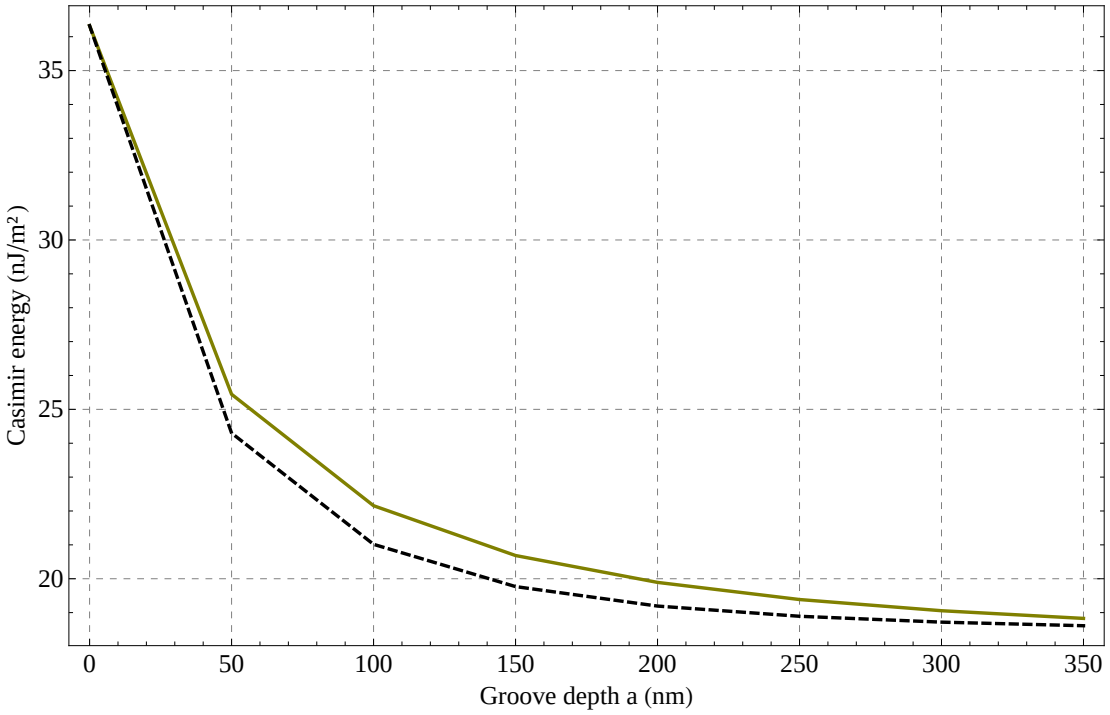

FIG. 57: Casimir energy as a function of the grating groove depth a, for two gratings of gold described by a Drude model [70] given by equation (135) and FIG. 11. This is for a grating period $d = 200$ nm, filling factor $p = 50\%$, and separation distance $L = 200$ nm. These scattering results are compared with the Proximity Approximation (dashed curve).

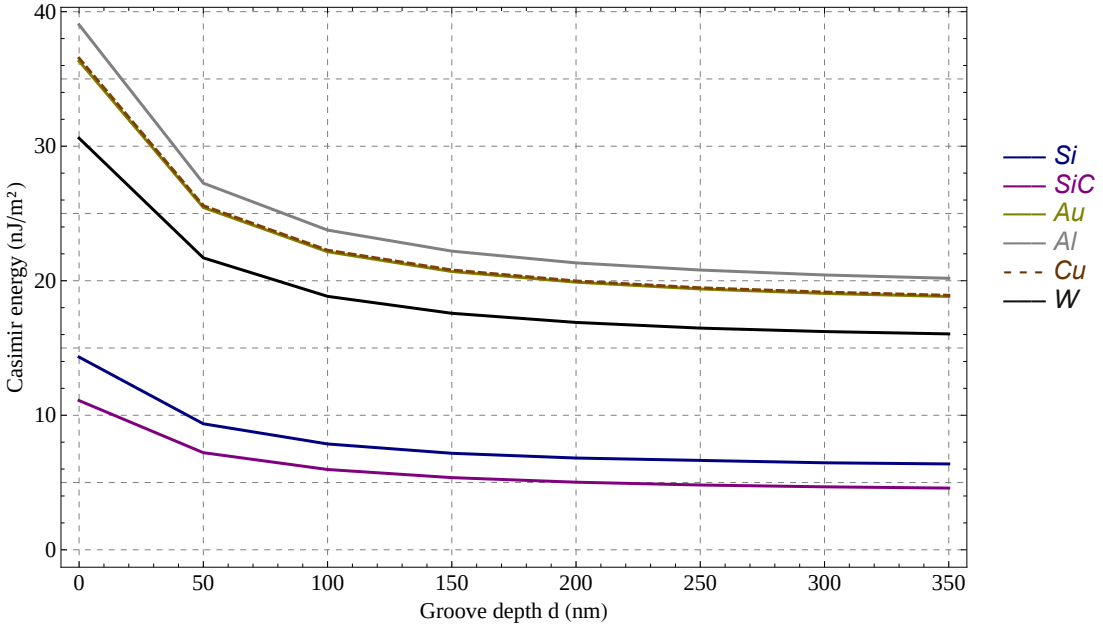

FIG. 58: Dependence of the Casimir energy with the grating groove depth a, for two gratings of different materials with grating period $d = 200$ nm, filling factor $p = 50\%$, and separation distance $L = 200$ nm. Intrinsic silicon appears in blue, and is described by the Drude-Lorentz model [27, 117, 150] given in equation (137). SiC appears in purple, and is described by the Drude-Lorentz model [65] given in equation (140). Gold appears in yellow, aluminum in gray, copper in dashed orange, and tungsten in black. These four metals are described by a Drude model [70] given by equation (135) and FIG. 11.

5. Casimir energy between corrugated gratings as a function of the lateral displacement δ

In FIG. 59-60, we show the Casimir energy as a function of the lateral displacement δ/d between gratings of SiC, and W, each with a grating period $d = 200$ nm, filling factor $p = 50\%$, corrugation depth $a = 100$ nm, and at a separation distance $L = 200$ nm. We interpolated with nearly perfect accuracy the results with a well-parametrized sinusoid reflecting the periodic nature of the energy variation with lateral shift along the $x-$axis. On FIG. 61, we compared these results together with profiles of Si, Au, Al, and Cu.

Based on the results of FIG. 59-61, we can make the following remarks :

- The variations of the Casimir energy with the shift δ are confined within an extremely narrow band. The width of this band does not exceed $\sim 0.2\%$ of the energy, regardless of the material considered. Nevertheless we could expect the width of this band to increase for larger ratios of a/L.

- At this separation distance of $L = 200$ nm, the results are very well interpolated by a sinusoid. This is a useful result because one can hence well approximate in this range the energy variation with lateral shift if only the values at $\delta = 0$ and $\delta = 50\%$ are known.

- An important result concerning the Proximity Approximation here is that it does not well describe at all the variations of energy with lateral shift δ. To show this, we display in FIG. 62 and 63 the Proximity Approximation results compared to the scattering results for W and SiC, respectively. Not only is the variation with δ way out of the scattering narrow band for the Proximity Approximation, but its value do not even cross that band in the case of W. A reason for this mismatch is the importance played by the contribution of the lateral modes at $\delta = 50\%$. These lateral modes are not taken into account by the Proximity Approximation.

It is a known fact that this variation of Casimir energy $E(\delta)$ with lateral shift over periodic grating gives rise to a lateral Casimir force along the $x-$axis. We will study in section VII D the value of this lateral force for the results calculated above, but can already expect the lateral Casimir force to be of very small magnitude in this regime of geometrical parameters.

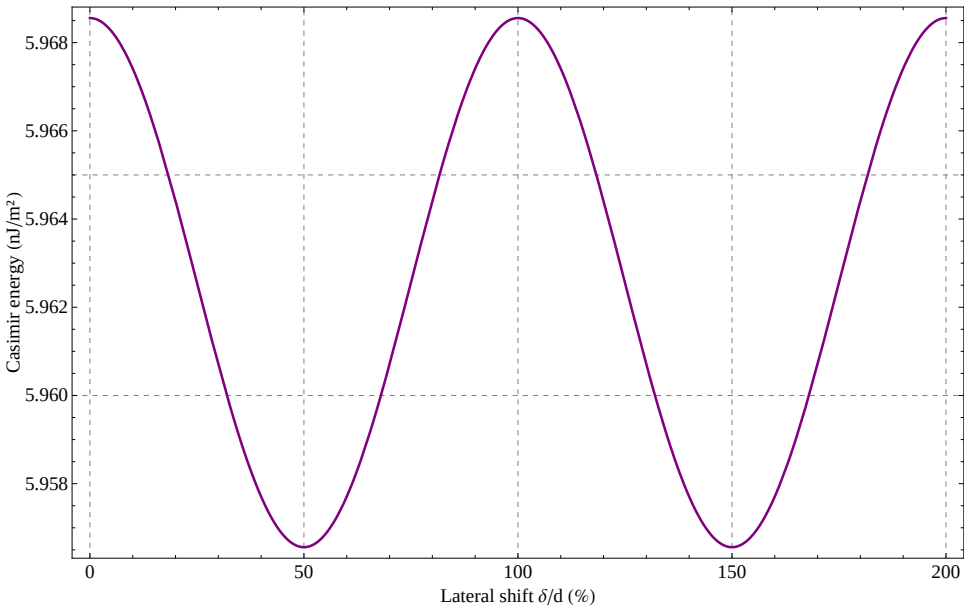

FIG. 59: Casimir energy as a function of the lateral displacement δ/d, for two gratings of SiC described by the Drude-Lorentz model [65] given in equation (140). This is for a grating period $d = 200$ nm, filling factor $p = 50\%$, groove depth $a = 100$ nm, and separation distance $L = 200$ nm.

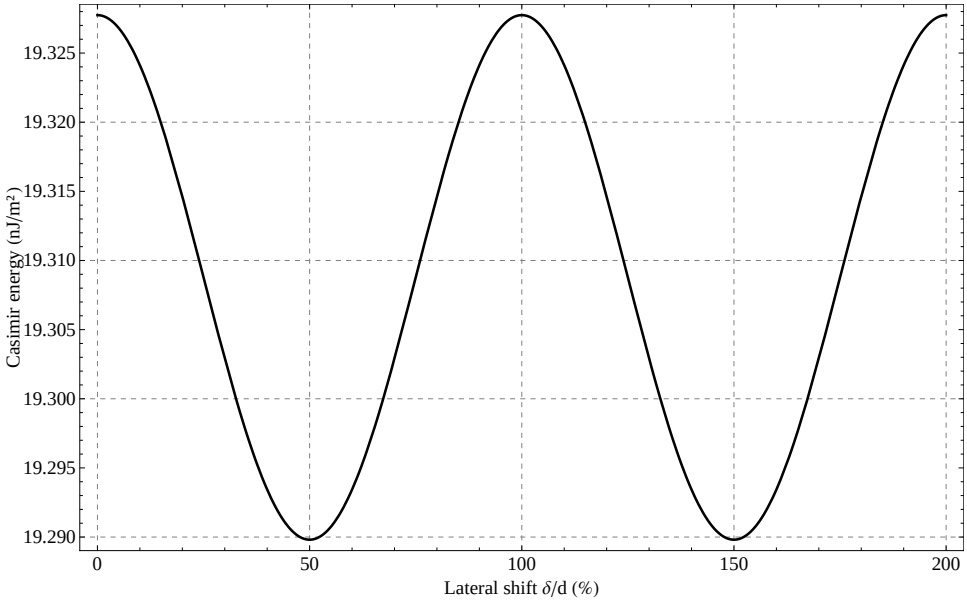

FIG. 60: Casimir energy as a function of the lateral displacement δ/d, for two gratings of tungsten described by a Drude model [116] given by equation (135) and FIG. 11. This is for a grating period $d = 200$ nm, filling factor $p = 50\%$, groove depth $a = 100$ nm, and separation distance $L = 200$ nm.

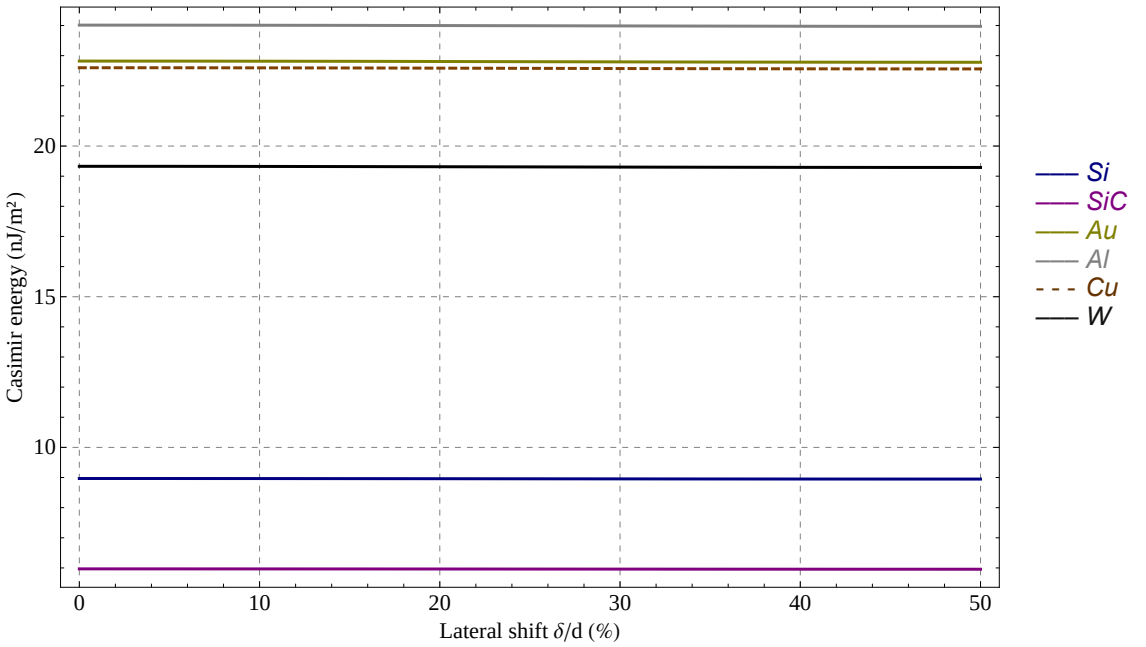

FIG. 61: Casimir energy as a function of the lateral displacement δ/d, for two gratings of different materials with grating period $d = 200$ nm, filling factor $p = 50\%$, groove depth $a = 100$ nm, and separation distance $L = 200$ nm. Intrinsic silicon appears in blue, and is described by the Drude-Lorentz model [27, 117, 150] given in equation (137). SiC appears in purple, and is described by the Drude-Lorentz model [65] given in equation (140). Gold appears in yellow, aluminum in gray, copper in dashed orange, and tungsten in black. These four metals are described by a Drude model [70] given by equation (135) and FIG. 11.

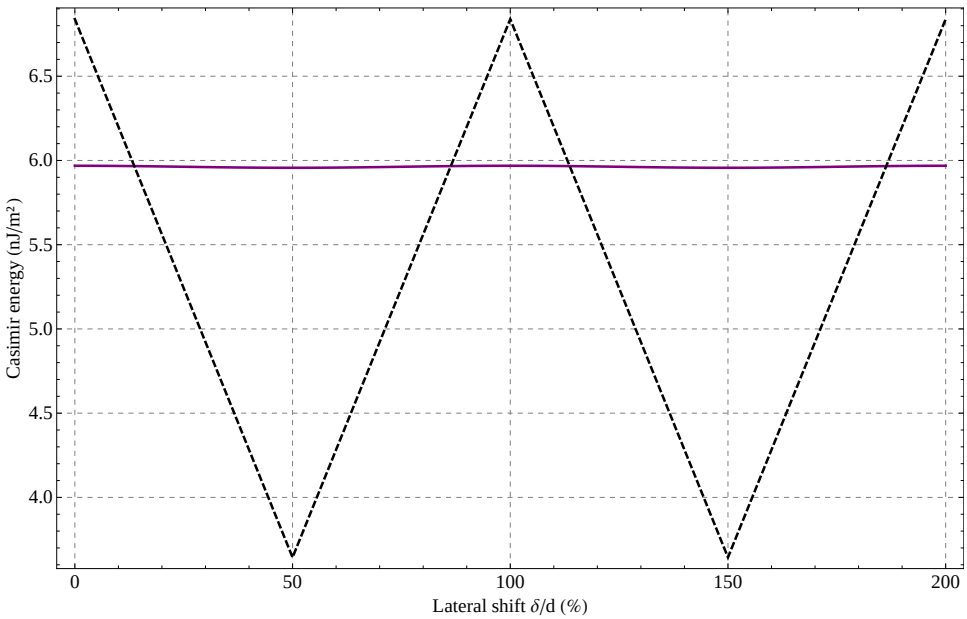

FIG. 62: Casimir energy as a function of the lateral displacement δ/d, for two gratings of SiC described by the Drude-Lorentz model [65] given in equation (140). This is for a grating period $d = 200$ nm, filling factor $p = 50\%$, groove depth $a = 100$ nm, and separation distance $L = 200$ nm. These scattering results are compared with the Proximity Approximation (dashed curve).

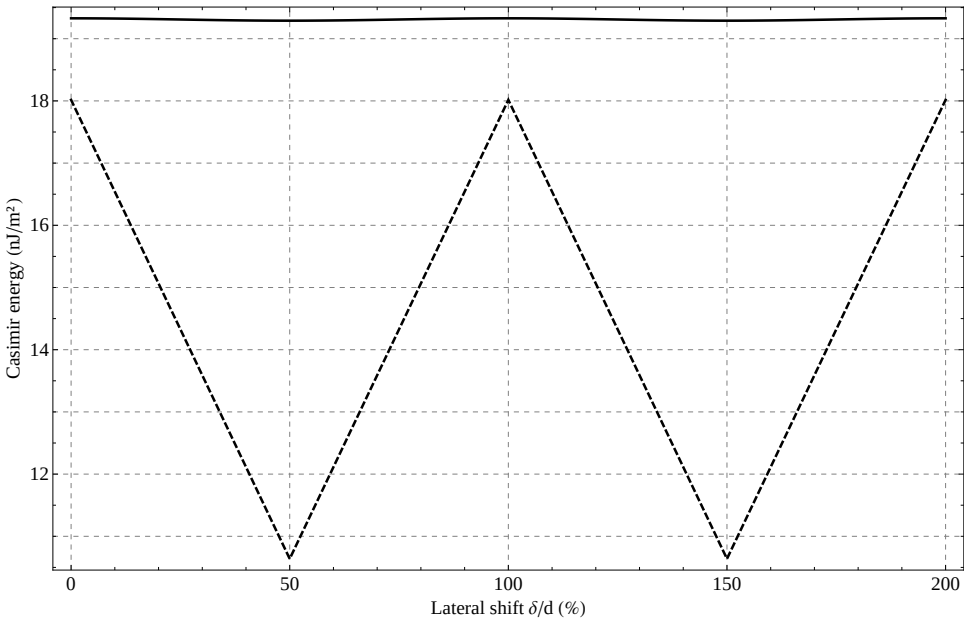

FIG. 63: Casimir energy as a function of the lateral displacement δ/d, for two gratings of tungsten described by a Drude model [116] given by equation (135) and FIG. 11. This is for a grating period $d = 200$ nm, filling factor $p = 50\%$, groove depth $a = 100$ nm, and separation distance $L = 200$ nm. These scattering results are compared with the Proximity Approximation (dashed curve).

C. Casimir force between corrugated gratings

In FIG. 64-65, we show the Casimir force as a function of separation distance L, period d, filling factor p, and groove depth a. This is done for gratings of Si, SiC, Au, Al, Cu, and W, each with period $d = 200$ nm, filling factor $p = 50\%$, groove depth $a = 100$ nm, and separation distance $L = 200$ nm —unless of course these parameters are explicit variables. The results for these different materials are compared with one another in these figures.

The qualitative changes in the Casimir force as a function of separation distance L, filling factor p, and groove depth a nm are exactly the same as the Casimir energy. The most important results hence lay here in the quantitative values of the Casimir force, which for these geometrical parameters $L = d = 2p = 2a = 200$ nm are of the order of a fraction of a N/m^2, regardless of the considered material (Si, SiC, Au, Al, Cu, and W).

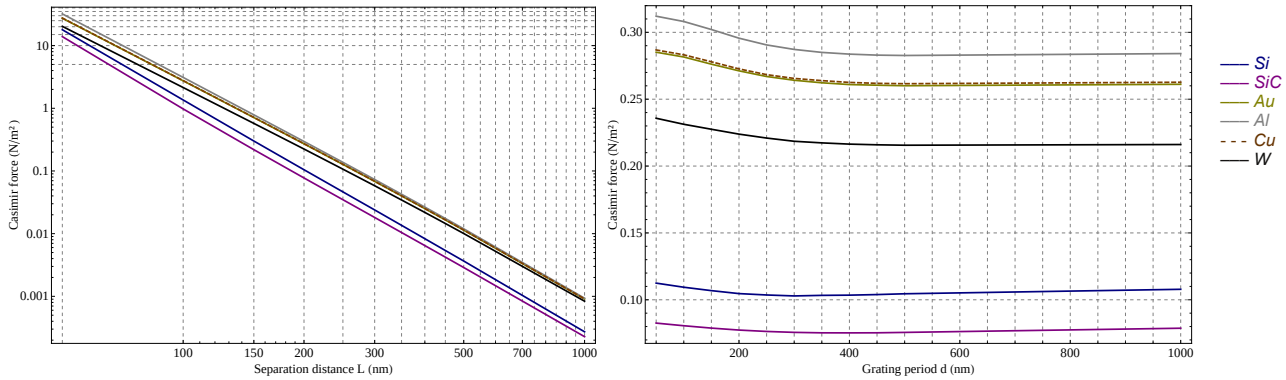

FIG. 64: Log-log dependence of the Casimir force with the separation distance L (left) and grating period d (right), for two gratings of different materials with period $d = 200$ nm (for left-hand plot), filling factor $p = 50\%$, groove depth $a = 100$ nm, and separation distance $L = 200$ nm (for right-hand plot). Intrinsic silicon appears in blue, and is described by the Drude-Lorentz model [27, 117, 150] given in equation (137). SiC appears in purple, and is described by the Drude-Lorentz model [65] given in equation (140). Gold appears in yellow, aluminum in gray, copper in dashed orange, and tungsten in black. These four metals are described by a Drude model [70] given by equation (135) and FIG. 11.

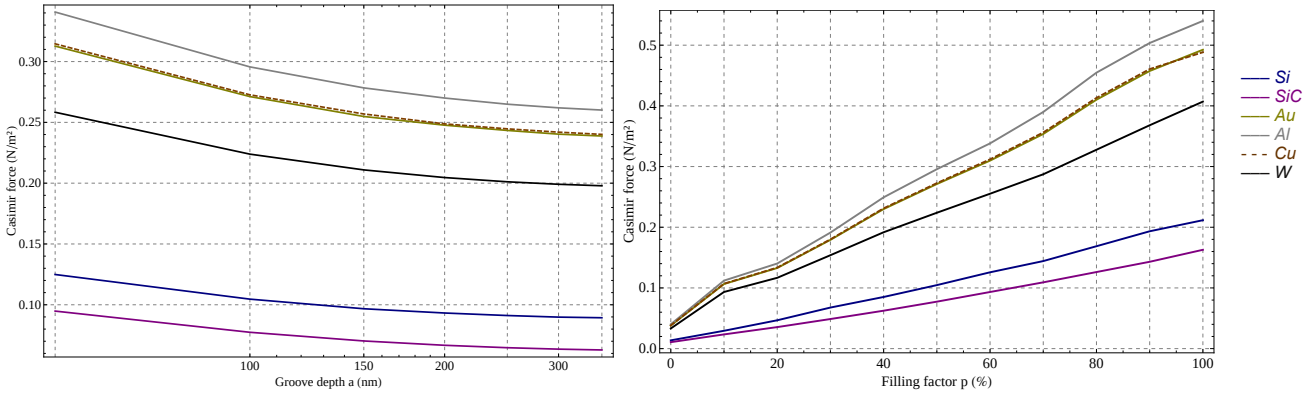

FIG. 65: Dependence of the Casimir force with the groove depth a (right) and filling factor p (right), for two gratings of different materials with grating period $d = 200$ nm, filling factor $p = 50\%$ (for left-hand plot), groove depth $a = 100$ nm (for right-hand plot), and separation distance $L = 200$ nm. Intrinsic silicon appears in blue, and is described by the Drude-Lorentz model [27, 117, 150] given in equation (137). SiC appears in purple, and is described by the Drude-Lorentz model [65] given in equation (140). Gold appears in yellow, aluminum in gray, copper in dashed orange, and tungsten in black. These four metals are described by a Drude model [70] given by equation (135) and FIG. 11.

D. Lateral Casimir force between corrugated gratings

In section VII B 5 we have seen the dependence of the Casimir energy E with lateral shift δ. We now compute the Casimir force F as a function of this same lateral shift δ for SiC on FIG. 66, W on FIG. 67, and comparing different materials on FIG. 68, in order to show the infinitesimal albeit continuous sinusoidal variation of the force with lateral displacement.

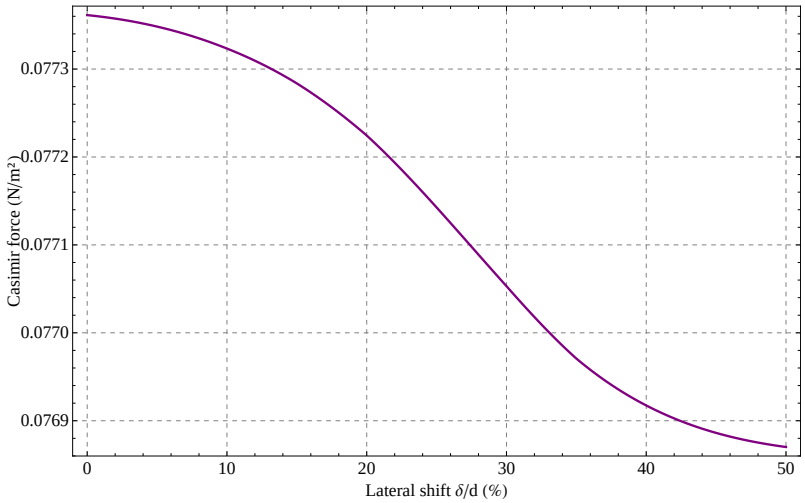

FIG. 66: Casimir force as a function of the lateral displacement δ/d, for two gratings of SiC described by the Drude-Lorentz model [65] given in equation (140). This is for a grating period $d = 200$ nm, filling factor $p = 50\%$, groove depth $a = 100$ nm, and separation distance $L = 200$ nm.

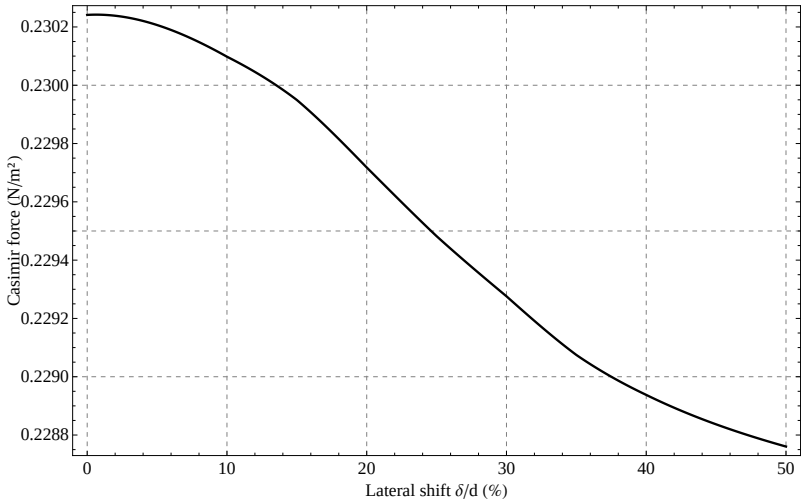

FIG. 67: Casimir force as a function of the lateral displacement δ/d, for two gratings of tungsten described by a Drude model [116] given by equation (135) and FIG. 11. This is for a grating period $d = 200$ nm, filling factor $p = 50\%$, groove depth $a = 100$ nm, and separation distance $L = 200$ nm.

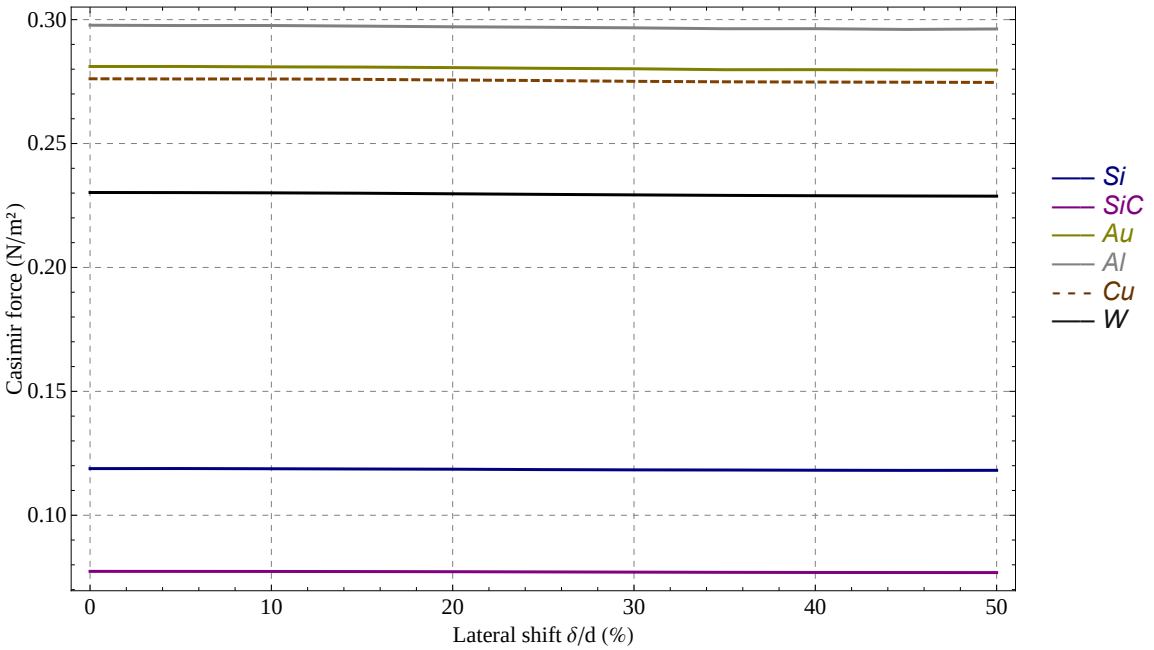

FIG. 68: Dependence of the Casimir force with the lateral shift δ, for two gratings of different materials with grating period $d = 200$ nm, filling factor $p = 50\%$, groove depth $a = 100$ nm, and separation distance $L = 200$ nm. Intrinsic silicon appears in blue, and is described by the Drude-Lorentz model [27, 117, 150] given in equation (137). SiC appears in purple, and is described by the Drude-Lorentz model [65] given in equation (140). Gold appears in yellow, aluminum in gray, copper in dashed orange, and tungsten in black. These four metals are described by a Drude model [70] given by equation (135) and FIG. 11.

The variation of the Casimir *energy* over periodic gratings gives rise to a lateral Casimir force [153] along the $x-$axis given by :

$$E^{(\mathrm{lat})}(\delta) = \frac{\partial E(\delta)}{\partial \delta} \tag{410}$$

Notice that since we derive E with respect to the $x-$axis, the units of the Casimir lateral force are in $\mathrm{N.m}^{-2}$ just like the normal Casimir force.

In most experimental precision measurements of the Casimir force, the requirement of parallelism between the two mirrors is circumvented by one of the two gratings being replaced by a large sphere of radius R compared to the separation distance L. Certain experimental protocols even use a corrugated sphere in front of a corrugated plane in order to measure the Casimir energy in the grating-grating configuration [154]. In this case, one can still compute the lateral Casimir force between two corrugated planes through this corrugated sphere-corrugated plane geometry in the following way : the force in the plane-sphere configuration F_{PS} is derived from a Proximity Approximation approach through the energy in the plane-plane geometry E_{PP} :

$$F_{PS} = 2\pi R E_{PP} \tag{411}$$

We then integrate this force over an infinitesimal length dL in order to recover the energy E_{PS} in the plane-sphere configuration :

$$E_{PS} = 2\pi R \int E_{PP} dL \tag{412}$$

for which an approximation such as a trapezoidal integration method can be used for each value of $L \pm \epsilon$, representing dL with $\epsilon \to 0$. Finally, we can recover the lateral force $F_{PS}^{(\mathrm{lat})}$ in the plane-sphere geometry by deriving with respect to the lateral displacement δ according to equation 410.

On FIG. 69, we compare the lateral Casimir force as a function of the lateral displacement δ for different gratings of Si, SiC, Au, Al, Cu, and W :

- We recover a sinusoidal variation with lateral shift δ, as for the variation of the normal Casimir force or energy with δ. However here the oscillations are centered around zero, and the lateral force switches sign every half-period.
- The magnitude of the lateral Casimir force for dielectrics is much smaller (by a factor two for Si) than for metals.
- Whereas the values of the lateral Casimir force for the different metals are very close to each other, this is not so for the dielectrics : the lateral force for Si is about $\sim 30\%$ larger than for SiC.
- Even though the separation distance for the grating-corrugated sphere configuration is much smaller ($L = 125$ nm) than for the grating-grating case above ($L = 200$ nm), we see in FIG. 70 that the Casimir lateral force is much smaller in the former —of the order of piconewtons per square meter. This is due to the chosen period $d = 400$ nm, as was previously found in FIG. 48.
- We can observe a slight skewness of the curve due to the sphere geometry on FIG. 70, and this is confirmed by experiment in the grating-corrugated sphere configuration [154].

On FIG. 70, we show the lateral Casimir force as a function of the lateral displacement δ/d, with grating period $d = 400$ nm, filling factor $p = 50\%$, groove depth $a = 100$ nm, and separation distance $L = 125$ nm. One of the two gratings is not represented by a corrugated plate but by a corrugated sphere of radius $R = 100\mu$m according to the formalism above.

Finally, we shall mention that the Casimir lateral force between gratings gives rise to a *torque* between the plates [155, 156].

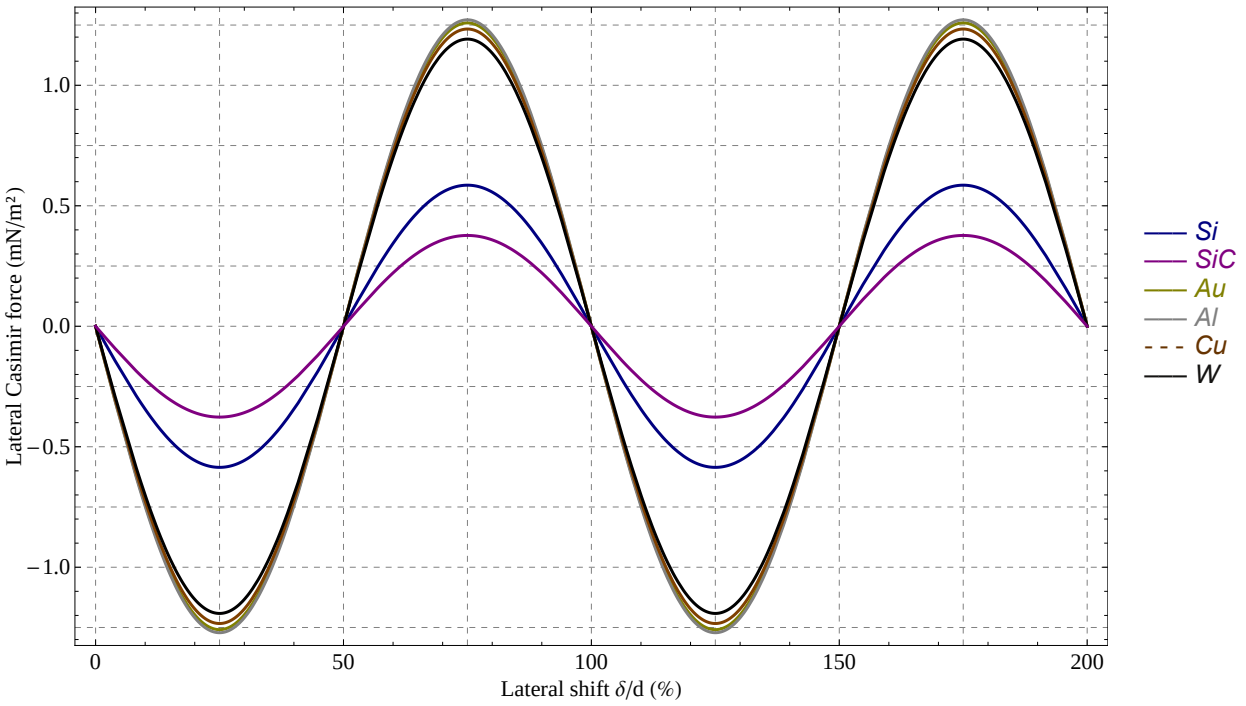

FIG. 69: Casimir lateral force as a function of the lateral displacement δ/d, for two gratings of different materials with grating period $d = 200$ nm, filling factor $p = 50\%$, groove depth $a = 100$ nm, and separation distance $L = 200$ nm. Intrinsic silicon appears in blue, and is described by the Drude-Lorentz model [27, 117, 150] given in equation (137). SiC appears in purple, and is described by the Drude-Lorentz model [65] given in equation (140). Gold appears in yellow, aluminum in gray, copper in dashed orange, and tungsten in black. These four metals are described by a Drude model [70] given by equation (135) and FIG. 11.

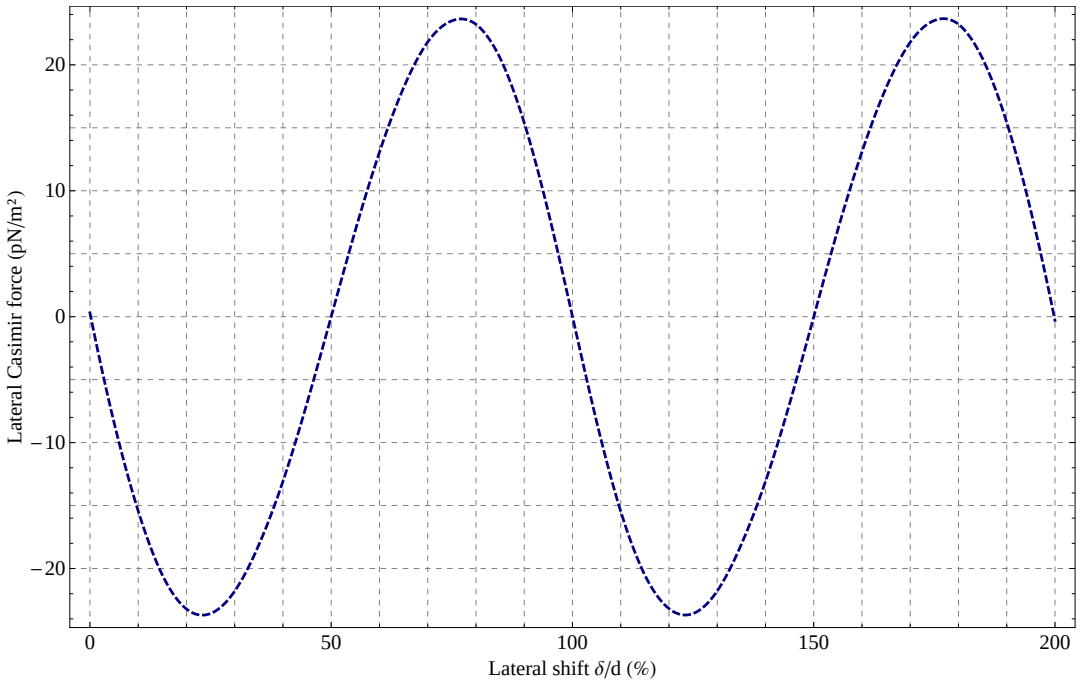

FIG. 70: Lateral Casimir force as a function of the lateral displacement δ/d, for two gratings of intrinsic silicon with grating period $d = 400$ nm, filling factor $p = 50\%$, groove depth $a = 100$ nm, and separation distance $L = 125$ nm. One of the two gratings is not represented by a corrugated plate but by a corrugated sphere of radius $R = 100\mu$m according to equations (411-412). Intrinsic silicon is described by the Drude-Lorentz model [27, 117, 150] given in equation (137).

E. Casimir energy between arbitrary periodic gratings

1. *Casimir energy between periodic profiles shaped as sawteeth*

Based on the scattering formalism developed in section VI B 3, where arbitrary periodic profiles are modeled as stacks of slices, we now consider several types of arbitrary profiles and review the dependence of the Casimir energy as a function of the two mirrors' lateral shift δ. As for the rest of this section, the material chosen for our profiles is intrinsic silicon Si, as described by the Drude-Lorentz model [27, 117, 150] given in equation (137).

We first consider gratings shaped as *sawtooth* of various shapes, the geometries and scale of which are represented in FIG. 72 and 73. If we define d_h as the distance between the corrugations at $y = 0$, and d_l as the distance between corrugations at $y = a$ according to FIG. 71 (or FIG. 35), we can then parametrize *sawtooth* profiles by the function :

$$d_1(y) = \frac{d_l - d_h}{a} y + d_h \tag{413}$$

where we keep d_h fixed and keep $d_l = d$. Now if we increase d_l by constant steps, we can smoothly change from a *sawtooth* profile to a *rectangular* corrugated profile —this is what is represented in FIG. 72.

On FIG. 74, we show the dependence of the Casimir energy wih the lateral shift δ for these profiles. The gratings have a separation distance $L = 100$ nm, period $d = 400$ nm, corrugation depth $a = 50$ nm, length between grating ridges at $y = 0$ given by $d_h = 200$ nm, and a number of slices $K = 20$. The five profiles are parametrized by $d_l = 400$ nm, $d_l = 350$ nm, $d_l = 300$ nm, $d_l = 250$ nm, and $d_l = 200$ nm, so that we indeed progressively shift d_l from a *sawtooth* grating at ($d_l = 400$ nm) to a rectangular corrugated grating at ($d_l = 200$ nm, shown in 3D on FIG. 75), by constant steps of 50 nm :

- If we consider two *rectangular* gratings with given period and groove depth, then the Casimir energy for two *sawtooth* gratings with same period and groove depth will be about half of the Casimir energy of the *rectangular* gratings.
- Shifting from the *sawtooth* grating with $d_l = 400$ nm to the *rectangular* grating with $d_l = 200$ nm by four steps of 50 nm causes the Casimir energy to increase by steps of 7, 8, 8.5, and 9 nJ/m^2 for each of these four profiles at $\delta = 0$. In other words, the increment in Casimir energy is not constant. This is due to the dependence of the Casimir energy in $\propto 1/L^3$: the added surface in near-field increases the energy non-linearly.
- This non-linear increment in Casimir energy is magnified at $\delta = d/2$: the Casimir energy increases by steps of 4, 5, 6, and 8 nJ/m^2 for each of these four profiles. This is due to the fact that at $\delta = d/2$, the lateral modes

with larger wave-vector components along the $x-$axis have a greater contribution than at $\delta = 0$, and that this contribution especially increases as the profiles are progressively shifted from *sawtooth* to *rectangular*.

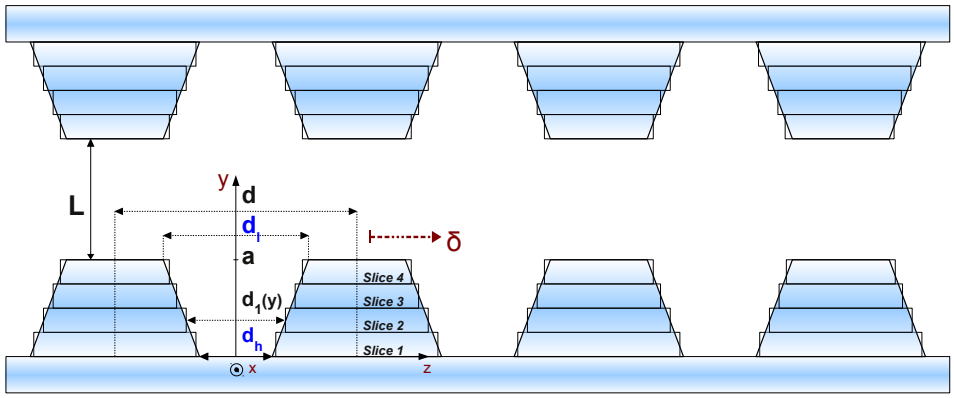

FIG. 71: Arbitrary gratings geometry and parameters in the approximation of vertical stacks of rectangular slices (here for $K = 4$). Notice the important parameters of d_h , which is the distance between the corrugation at $y = 0$, and d_l which is the distance between the corrugation at $y = a$.

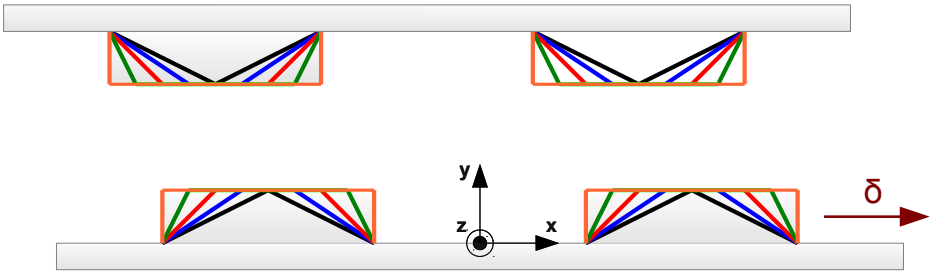

FIG. 72: Two-dimensional perspective on the *sawtooth* gratings used in FIG. 74, with same color code.

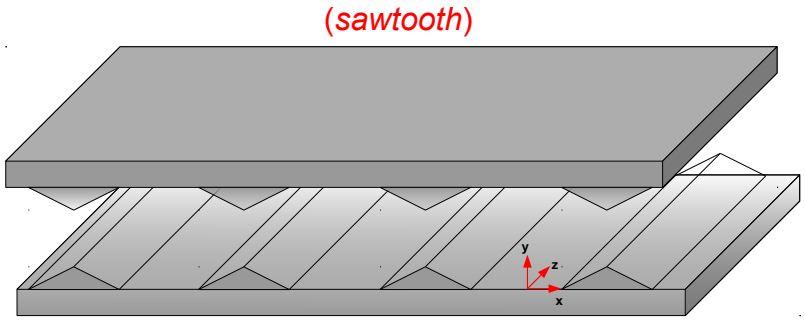

FIG. 73: Three-dimensional perspective on the *sawtooth* gratings.

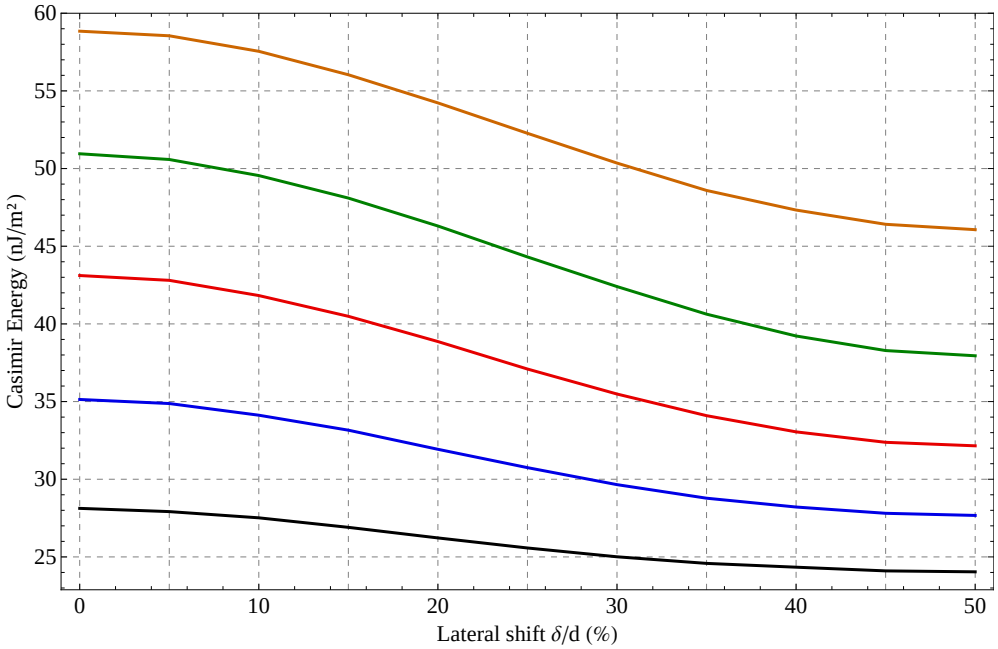

FIG. 74: Casimir energy as a function of the lateral shift δ/d, for arbitrary periodic gratings of intrinsic silicon with separation distance $L = 100$ nm, period $d = 400$ nm, corrugation depth $a = 50$ nm, and number of slices $K = 20$. *Sawtooth* grating with $d_1 = 4y + 200$ appear in black, with $d_1 = 3y + 200$ in blue, with $d_1 = 2y + 200$ in red, and with $d_1 = y + 200$ in green. This is compared with similar size rectangular corrugations $d_1 = 200$ in orange.

2. *Casimir energy between periodic profiles shaped as barbed wires*

We now consider *barbed wired* profiles, as represented in FIG. 76 and 77. These profiles are generated by specifying the length between corrugations $d_1(y)$ according to equation (413), but in such a way that $d_h > d_l$. In FIG. 78, we show the dependence of the Casimir energy with the lateral shift δ for these *barbed wire* periodic profiles, with a separation distance $L = 20$ nm, constant grating period $d = 100$ nm, corrugation depth $a = 50$ nm, and number of slices $K = 20$.

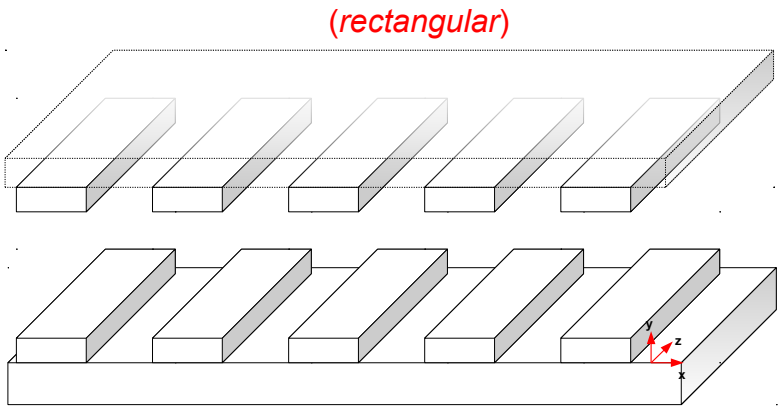

FIG. 75: Three-dimensional perspective (to scale) on the *rectangular* gratings used in FIG. 74.

We study four *barbed wire* profiles parametrized by $d_1 = -0.5y + 85$, $d_1 = -0.5y + 65$, $d_1 = -0.5y + 45$, and $d_1 = -0.5y + 25$. For all these $d_1(y)$, the grating period d is kept constant, so that these four *barbed wire* profiles just differ in their respective width. This is thus a different case than the variation from *sawtooth* to *rectangular* gratings in the previous section, where the width of the *sawtooth* was kept constant. Furthermore the first *barbed wire* profile with $d_1 = -0.5y + 85$ is compared with a *rectangular* corrugated grating that *includes it* ($d_1 = d_l = 85$), and another rectangular corrugated grating that *is included in it* ($d_1 = d_h = 65$).

- The Casimir energy of two *barbed wire* gratings on FIG. 78 with given period and groove depth is about three times larger than the Casimir energy of two *rectangular* gratings that are included within the *barbed wire* profiles (and hence parametrized by $d_1(y) = d_h$). However, the *rectangular* gratings that *include* the *barbed wire* profiles (and are hence parametrized by $d_1(y) = d_l$) have about the same Casimir energy as the latter *barbed wire* profiles. This is due to the fact that the surface in near-field for these latter *rectangular* gratings is the same as the *barbed wire* profiles.

- At $\delta = 0$, the Casimir energy increases by a constant step of about ~ 1.4 nJ/m^2 from grating to grating. This is due to the fact that at a constant local separation distance, the exposed surface in near-field varies constantly from grating to grating. To the contrary, at $\delta = d/2$ the Casimir energy increases by non-constant steps of about 1.9, 2.2, and 2.1 nJ/m^2 from grating to grating. So it means that the difference between these four profiles is maximized when the gratings are laterally shifted. This is because at $\delta/p = 50\%$, the grating surface that is most exposed in near-field is not only the top of the ridges (which is the case for $\delta/p = 0\%$) but also the lower parts of the trenches, which are an area of highly non-trivial diffraction scatterings of the modes, at the local neighborhood of the bottom of the *barbed wire* profiles especially.

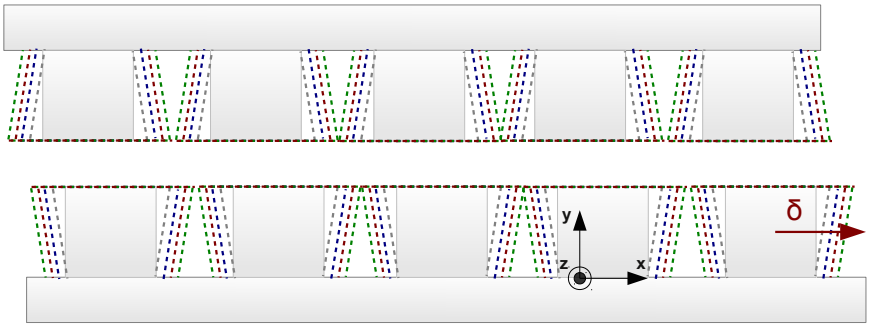

FIG. 76: Two-dimensional perspective on the *barbed wire* gratings used in FIG. 78, with same color code.

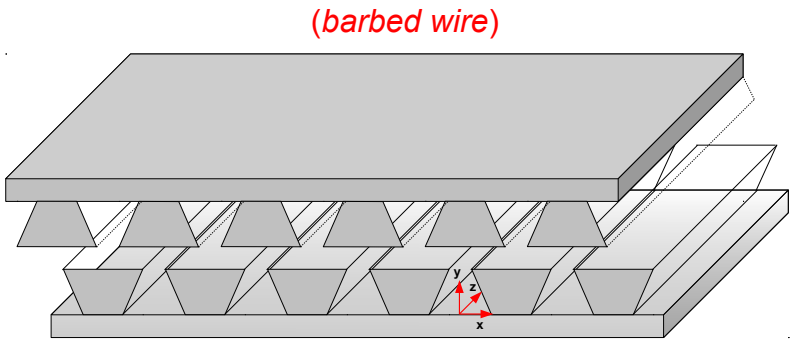

FIG. 77: Three-dimensional perspective on *barbed wire* gratings.

3. *Casimir energy between periodic profiles shaped as a sinusoid*

We now consider *sinusoidal* profiles, as represented in FIG. 79 and 80. These profiles are generated by specifying the length between corrugations $d_1(y)$ according to :

$$d_1(y) = \frac{d}{\pi} \arccos\left(1 - \frac{2y}{a}\right) \tag{414}$$

In FIG. 81, we show the dependence of the Casimir energy with the lateral shift δ for these *sinusoidal* periodic profiles, with a separation distance $L = 100$ nm, constant grating period $d = 400$ nm, corrugation depth $a = 50$ nm, and number of slices $K = 20$. These parameters together with equation (414) give a profile parametrized by $d_1(y) = (400/\pi)\arccos[1 - (y/25)]$.

- At $\delta = 0$, the Casimir energy for these *sinusoidal* gratings is approximatively the same as the Casimir energy of the *sawtooth* gratings parametrized by $d_1 = 2y + 200$ (red curve on FIG. 74). Notice that these two profiles have

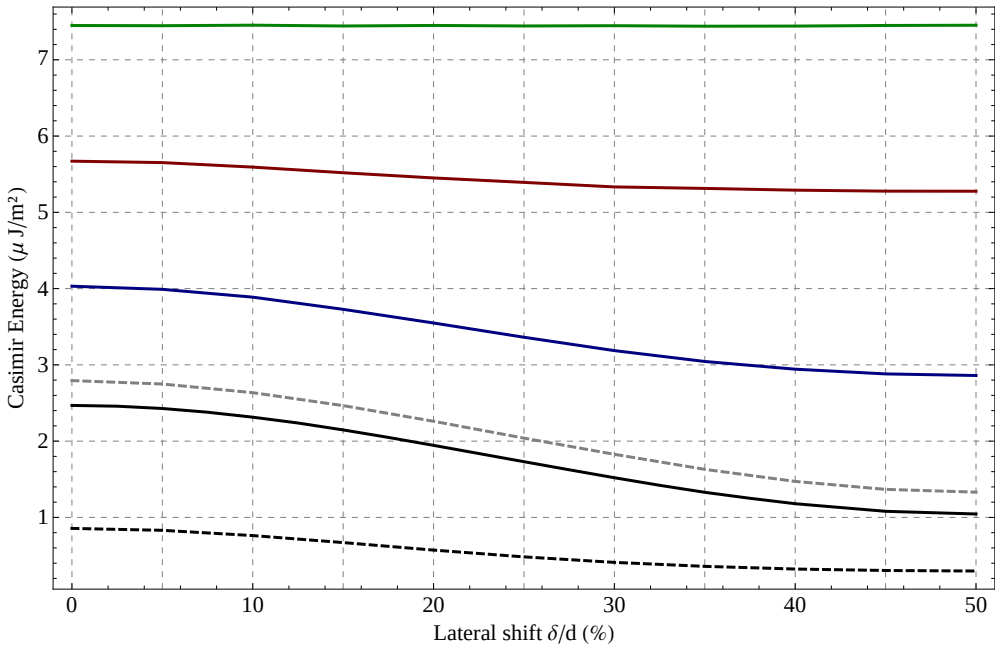

FIG. 78: Dependence of the Casimir energy with the lateral shift δ for two *barbed wire* periodic profiles of intrinsic silicon, with a separation distance $L = 20$ nm, constant grating period $d = 100$ nm, corrugation depth $a = 50$ nm, and number of slices $K = 20$. *Barbed wire* profiles with $d_1 = -0.5y + 85$ appear in black, with $d_1 = -0.5y + 65$ in blue, with $d_1 = -0.5y + 45$ in red, and with $d_1 = -0.5y + 25$ in green. This is compared with two rectangular corrugated profiles with $d_1 = 85$ nm (dashed black curve), and with $d_1 = 60$ nm (dashed gray curve). Notice that while we varied the spacing between the corrugations $d_1(y)$, the grating period d was kept constant, so that these four *barbed wire* profiles just differ in their respective grating width.

same period d, groove depth a, and separation length L. At $\delta = d/2$, the Casimir energy for these *sinusoidal* gratings is exactly the same as the Casimir energy of the *sawtooth* gratings parametrized by $d_1 = y + 200$ (green curve on FIG. 74).

- Compared to these two *sawtooth* gratings, and even more so compared with *rectangular* gratings, the variation in Casimir energy between $\delta = 0$ and $\delta = d/2$ for *sinusoidal* gratings is much smaller.

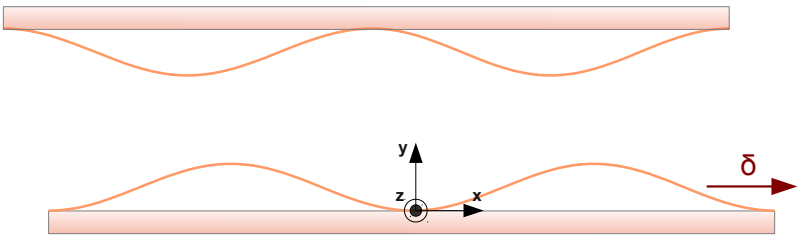

FIG. 79: Two-dimensional perspective on the *sinusoidal* gratings used in FIG. 81.

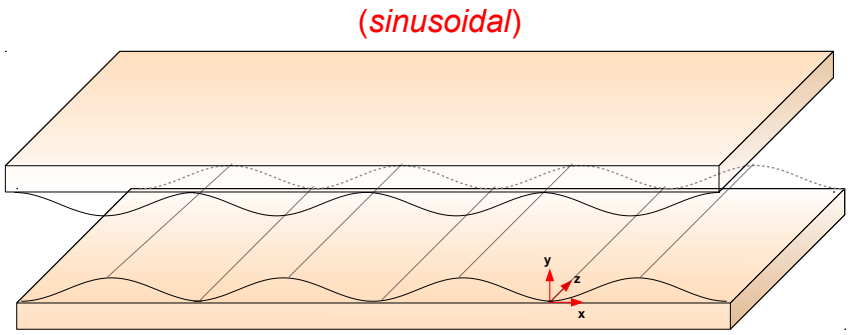

FIG. 80: Three-dimensional perspective on *sinusoidal* gratings.

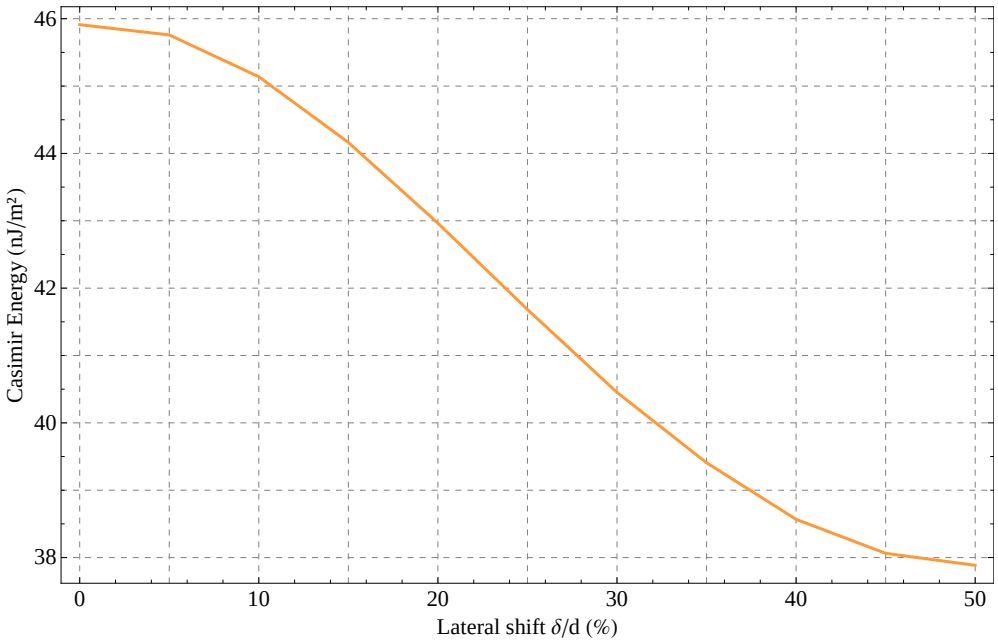

FIG. 81: Dependence of the Casimir energy with the lateral shift δ for two *sinusoidal* periodic profiles of intrinsic silicon, with a separation distance $L = 100$ nm, constant grating period $d = 400$ nm, corrugation depth $a = 50$ nm, and number of slices $K = 20$. The *sinusoidal* profiles are parametrized by equation (414), such that $d_1(y) = (400/\pi)\arccos[1 - (y/25)]$.

4. Casimir energy between periodic profiles shaped as ellipsoids

We now consider *circular* and *ellipsoid* profiles, as represented in FIG. 82 and 83. *Ellipsoid* profiles with a major axis parallel to the $x-$axis are generated by specifying the length between corrugations $d_1(y)$ according to :

$$d_1(y) = d - \frac{2R}{r}\sqrt{r^2 - (y-Y)^2} \tag{415}$$

and *ellipsoid* profiles with a major axis perpendicular to the $x-$axis are generated by :

$$d_1(y) = d - \frac{2r}{R}\sqrt{R^2 - (y-Y)^2} \tag{416}$$

for R and r being the major and minor axes of the ellipse respectively, and Y being the value of y of the ellipse center. *Circular* periodic profiles are also generated by any of these two expressions by setting $R = r$ as the radius. Notice from FIG. 83 that what we call "circular" periodic profiles look more like parallel tubes in the three-dimensional picture.

In FIG. 84, we show the dependence of the Casimir energy with the lateral shift δ for two *circular* and *ellipsoid* profiles, with a separation distance $L = 100$ nm, constant grating period $d = 400$ nm, corrugation depth $a = 50$ nm, and number of slices $K = 15$. These parameters together with equation (415) give a grating parametrized by $d_1 = 400 - 4\sqrt{50y - y^2}$ for horizontal *ellipsoid* profiles (that have $r = Y = 25$ nm and $R = 50$ nm), and $d_1 = 400 - 2\sqrt{50y - y^2}$ for *circular* profiles (that have $R = r = Y = 25$ nm). Again, these two profiles are illustrated in FIG. 82, to scale.

- The variation in Casimir energy between $\delta = 0$ and $\delta = d/2$ for the *circular* gratings is of the order of $\sim 12\%$, and of $\sim 24\%$ for the *ellipsoid* gratings. This is again due to the dependence of the Casimir energy in $\propto 1/L^3$, so that the greater surface of the grating exposed in near-field (such as horizontal *ellipsoid* gratings compared to *circular* gratings), the greater the variation when the gratings are laterally shifted.

- Both at $\delta = 0$ and $\delta = d/2$, the Casimir energy of the *ellipsoid* gratings is exactly the same as the Casimir energy of the *sawtooth* gratings parametrized by $d_1 = 4y + 200$ (black curve on FIG. 74). Notice that these two profiles have same period d, groove depth a, and separation length L, but *not* similar $d_1(y)$.

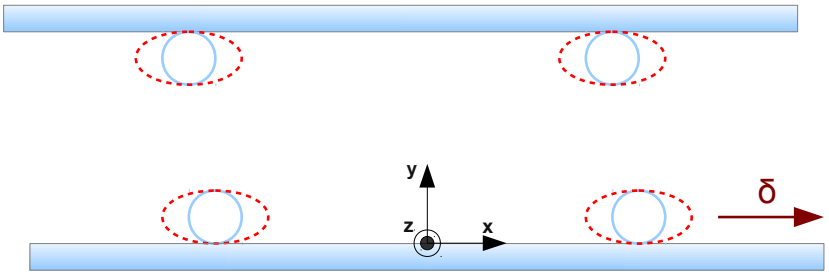

FIG. 82: Two-dimensional perspective on the *ellipsoid* gratings (in dashed red) and *circular* gratings (in blue) used in FIG. 84, with same color code.

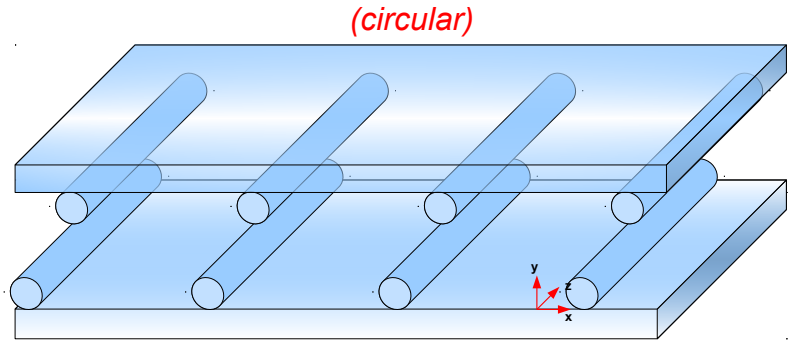

FIG. 83: Three-dimensional perspective on *circular* gratings.

5. *Casimir energy for different compared arbitrary profiles*

In this section we will summarize and compare the different profiles. To this effect we will consider :

- The *rectangular* profiles of section VII E 1, parametrized by $d_1(y) = 200$.
- The *sinusoidal* profiles of section VII E 3, parametrized by $d_1(y) = (400/\pi)\arccos[1 - (y/25)]$.
- The *sawtooth* profiles of section VII E 1, parametrized by $d_1(y) = 4y + 200$.
- The *circular* profiles of section VII E 4, parametrized by $d_1(y) = 400 - 2\sqrt{50y - y^2}$.

We show in FIG. 85 the dependence of the Casimir energy with the lateral shift δ for these four profiles. Furthermore we compare the obtained scattering results with the Proximity Approximation.

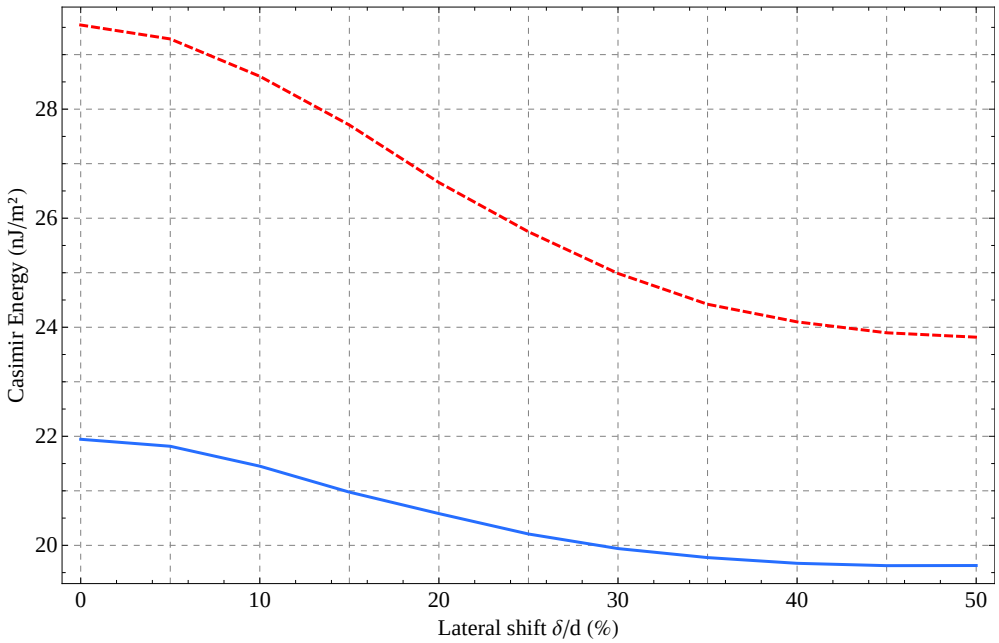

FIG. 84: Dependence of the Casimir energy with the lateral shift δ for two *ellipsoid* and *circular* periodic profiles of intrinsic silicon, with a separation distance $L = 100$ nm, constant grating period $d = 400$ nm, corrugation depth $a = 50$ nm, and number of slices $K = 15$. These two profiles are parametrized by equation (415), such that $d_1 = 400 - 2\sqrt{50y - y^2}$ for *circles* in blue (with $R = r = Y = 25$ nm), and $d_1 = 400 - 4\sqrt{50y - y^2}$ for *ellipses* in dashed red (with $r = Y = 25$ nm and $R = 50$ nm).

- At same grating period d, groove depth a, and separation length L, the Casimir energy is always larger for *rectangular*, *sinusoidal*, *sawtooth*, and *circular* profiles, in this order.

- At same grating period d, groove depth a, and separation length L, the *rectangular* and *sinusoidal* profiles share narrower Casimir energy values, and likewise for *sawtooth* and *circular* profiles.

- An important result is that for non-rectangular corrugated gratings, the Proximity Approximation is rather accurate at $\delta = d/2$ and less when δ tends to 0. To the contrary, and as already seen in section VII B 5, it is almost always a poor approximation for *rectangular* profiles. In the case of arbitrary gratings, the Proximity Approximation can be used in the neighborhood of $\delta = d/2$.

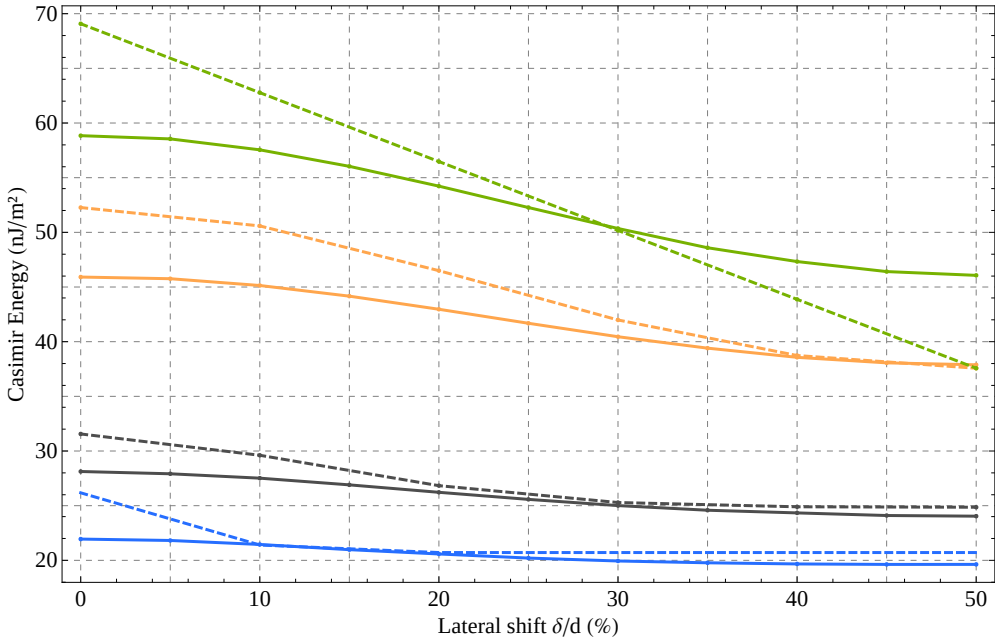

FIG. 85: Dependence of the Casimir energy with the lateral shift δ for four different arbitrary periodic profiles of intrinsic silicon, all with separation distance $L = 100$ nm, grating period $d = 400$ nm, corrugation depth $a = 50$ nm. *Rectangular* profiles are parametrized by $d_1 = 200$ (solid green curve), *sinusoidal* profiles are parametrized by $d_1(y) = (400/\pi)\arccos[1 - (y/25)]$ (solid orange curve), *sawtooth* profiles are parametrized by $d_1 = 4y + 200$ (solid black curve), and *circular* profiles are parametrized by $d_1 = 400 - 2\sqrt{50y - y^2}$ (solid blue curve). These four scattering results are compared with the Proximity Approximation results (respective dashed curves).

VIII. NUMERICAL EVALUATION : CASIMIR FOR NON-ZERO TEMPERATURES

A. Casimir at thermal equilibrium

1. *Casimir energy as a function of the separation distance for $T = 0$ K and $T = 300$ K*

We now study the Casimir energy in the case of non-zero temperatures [21, 127, 157–159], based on the Casimir force given in equation (233) and the thermal equilibrium formalism developed in section VI A 7. Alternatively, we could as well use the Casimir force from equation (381) and the non-equilibrium formalism developed in section VI C 1 (taken with equal grating temperatures $T_1 = T_2$). We will here systematically consider dielectric gratings (intrinsic silicon Si) and metallic gratings (gold Au).

We first compare the Casimir energy as a function of separation distance L for two types of Fabry-Pérot cavities: the first at zero temperature, and the second at 300 K. In FIG. 86 we show the results for two plates of intrinsic silicon Si, and in FIG. 87 for two plates of gold. Then in FIG. 88 and 89, we perform the same calculations for gratings with period $d = 200$ nm, filling factor $p = 50\%$, and groove depth $a = 100$ nm.

Based on the results of FIG. 86-89, we can make the following remarks :

- Regardless of the chosen material, a non-zero temperature increases the value of the Casimir energy at long separation distances.
- Whereas for Si, the Casimir energy increases with temperature at short separation distances also, this is not the case for gold : below the range $L = 3\mu$m, the Casimir energy for zero temperatures is larger than for $T = 300$ K. This is because the temperature contribution to the Casimir energy depends on the plasma wavelength, which for gold is ~ 137.8 nm (determined by $\lambda_p = 2\pi c/\omega_p$ in the Drude model equation (135)).
- Switching from the plane-plane to the grating configuration can be seen as digging corrugation trenches. In this sense, it is natural that the Casimir energy is larger for the planar case than for the grating case. This is seen when comparing FIG. 86 with 88, and FIG. 87 with 89 : the grating geometry does not bring about surprisingly new effects when non-zero temperatures are considered. In other words, a qualitative understanding of the effect of non-zero temperatures on the Casimir energy can be obtained by simply considering the plane-plane case in the range of the geometrical parameters that are here used. This property will also be seen in the next section.

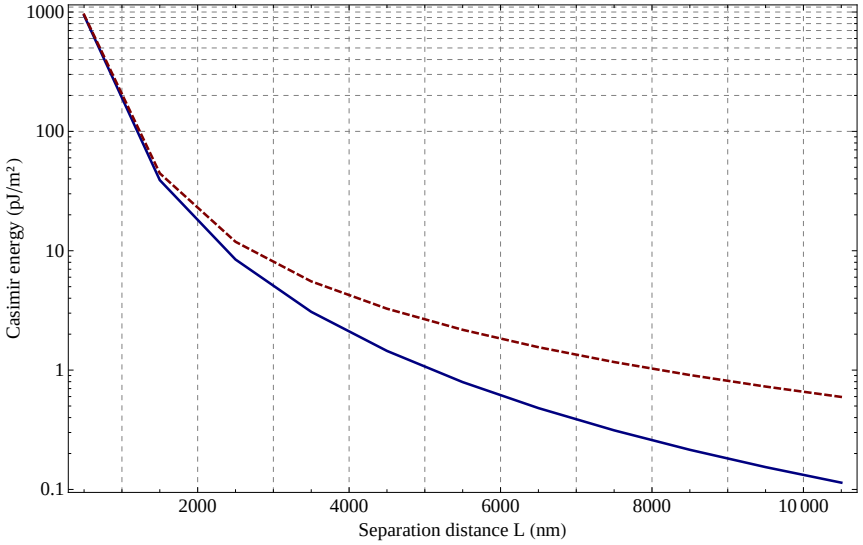

FIG. 86: Casimir energy as a function of the separation distance, for two planes of intrinsic silicon at temperature $T = 0$ K (solid blue curve) and at $T = 300$ K (dashed red curve). The material is described by the Drude-Lorentz model [27, 117, 150] given in equation (137).

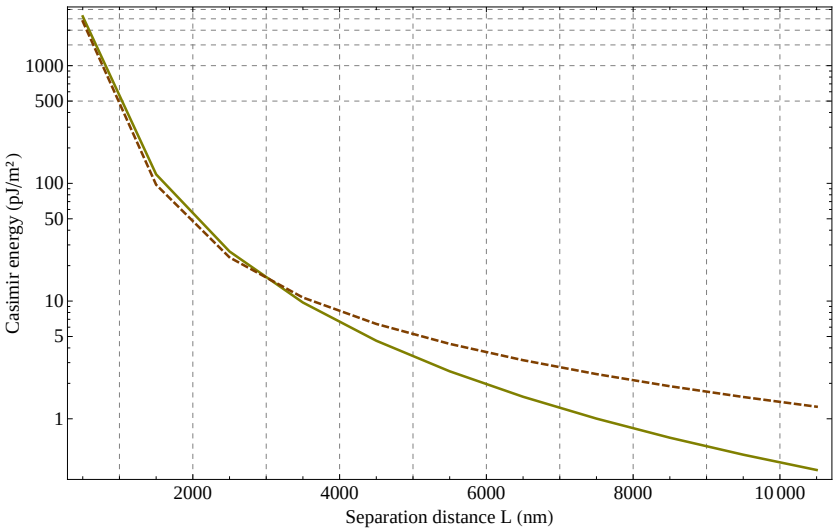

FIG. 87: Casimir energy as a function of the separation distance, for two planes of gold at temperature $T = 0$ K (solid blue curve) and at $T = 300$ K (dashed red curve). The material is described by a Drude model [70] given by equation (135) and FIG. 11.

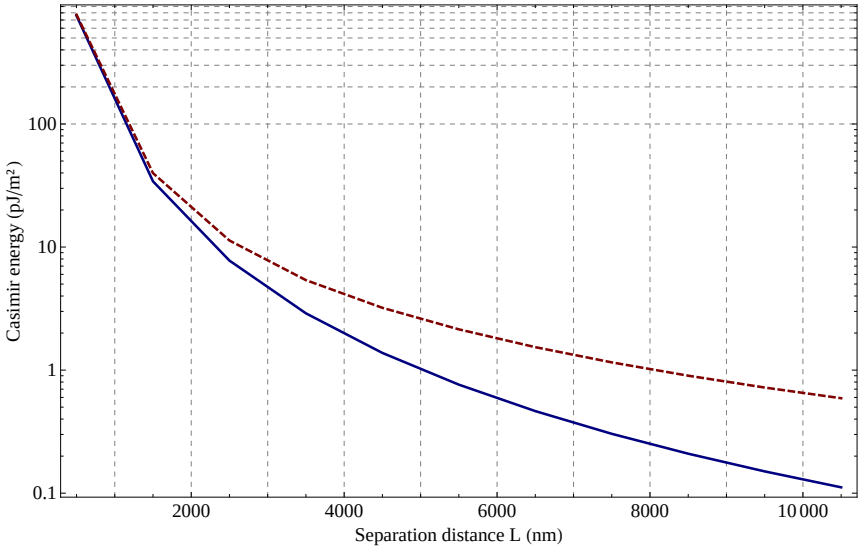

FIG. 88: Casimir energy as a function of the separation distance, for two gratings of intrinsic silicon at temperature $T = 0$ K (solid blue curve) and at $T = 300$ K (dashed red curve). This is for a grating period $d = 200$ nm, filling factor $p = 50\%$, and groove depth $a = 100$ nm. The material is described by the Drude-Lorentz model [27, 117, 150] given in equation (137).

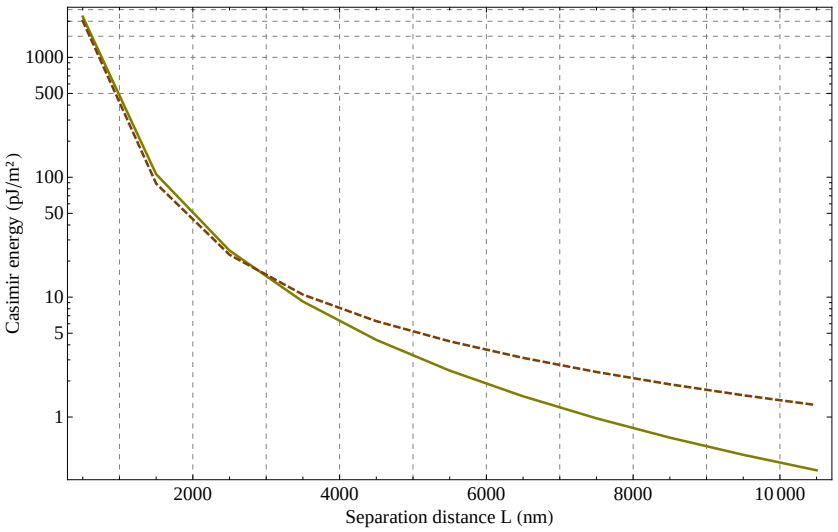

FIG. 89: Casimir energy as a function of the separation distance, for two gratings of gold at temperature $T = 0$ K (solid blue curve) and at $T = 300$ K (dashed red curve). This is for a grating period $d = 200$ nm, filling factor $p = 50\%$, and groove depth $a = 100$ nm. The material is described by a Drude model [70] given by equation (135) and FIG. 11.

2. Casimir energy as a function of the temperature for $L = 100$ nm, 500 nm, 1μm, and 10μm

We now study the variation of the Casimir energy as a function of the temperature itself for several separation distance $L = 100$ nm, 500 nm, 1μm, and 10μm, so as to fully grasp the relation between temperature T and separation distance L. We systematically compare the plane-plane configuration with the grating geometry for each of these results, and perform these computations first for intrinsic silicon Si (in FIG. 90-94) and then for gold Au (in FIG. 95-99). The gratings all have a period $d = 200$ nm, filling factor $p = 50\%$, and groove depth $a = 100$ nm.

FIG. 90 shows the variation of the Casimir energy for two planes of Si at $L = 100$ nm, and FIG. 91 shows the same for gratings. Then FIG. 92, 93, 94 show the variation of the Casimir energy for two planes and two gratings of Si at $L = 500$ nm, $L = 1\mu$m, and $L = 10\mu$m, respectively.

FIG. 95 shows the variation of the Casimir energy for two planes of Au at $L = 100$ nm, and FIG. 96 shows the same for gratings. Then FIG. 97, 98, 99 show the variation of the Casimir energy for two planes and two gratings of Au at $L = 500$ nm, $L = 1\mu$m, and $L = 10\mu$m, respectively.

- At a close separation distance $L = 100$ nm, the gradual increase of temperature from 0 to 500 K has but a small effect on the Casimir energy. This is true for both planes and gratings, and regardless of the material chosen —albeit gold is less affected by this rule than intrinsic silicon. Conversely, at large distances L the contribution of non-zero temperatures to the Casimir energy is large : we see in FIG. 94 and 99 that the Casimir energy at $T = 500$ K is about five times larger than the energy at $T = 0$ K. This is due to the contribution of the thermal wavelength modes $\lambda_T/2 > 100$ nm.

- Regardless of separation distance L, the Casimir energy increases with temperature T. But for gold the opposite happens for $L \geqslant 1000$ nm and for temperatures above 300 K, as seen on FIG. 98. There is a temperature T_r at which the Casimir energy shifts from decreasing to increasing with larger temperatures is $T_r \sim 425$ K for gratings and beyond $T_r > 500$ K for planes at $L = 1000$ nm, as seen on FIG. 98. And it is $T_r \sim 50$ K for both planes and gratings at $L = 10\mu$m, as seen on FIG. 99. Now following an *effective medium approximation* [151, 160], we can consider the grating case as a plane-plane case with greater separation distance L, where L is majored by the grating groove depth a. In this approach, the grating of FIG. 98 can be seen as a plane with separation distance comprised between $L = 200$ nm and $L + 2a = 400$ nm.

- From this and the last section, we can draw two conclusions : increasing the separation distance L implies that the reversal temperature T_r becomes smaller, and likewise switching from a plane-plane configuration to gratings implies that T_r becomes smaller proportionally with deeper corrugation trenches a.

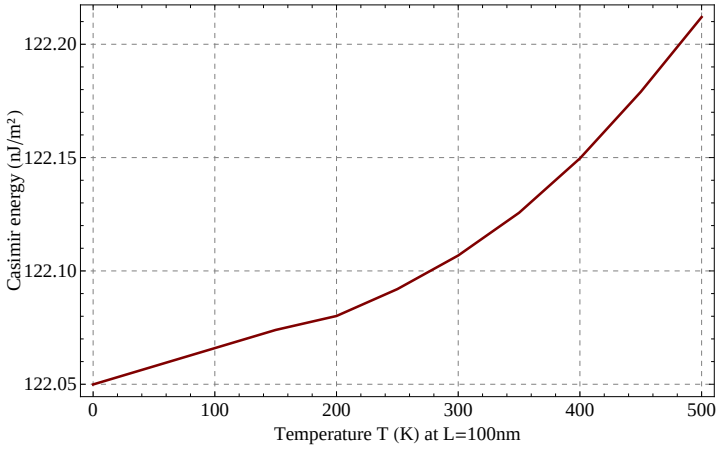

FIG. 90: Casimir energy as a function of the temperature T, for two planes of intrinsic silicon at a separation distance $L = 100$ nm. The material is described by the Drude-Lorentz model [27, 117, 150] given in equation (137).

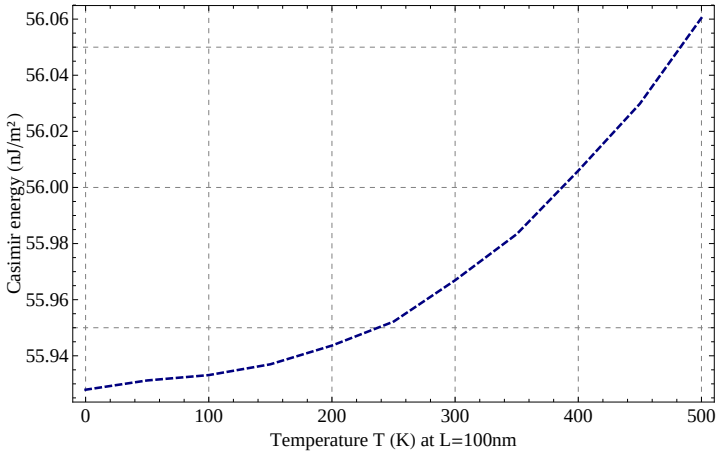

FIG. 91: Casimir energy as a function of the temperature T, for two gratings of intrinsic silicon at a separation distance $L = 100$ nm. This is for a grating period $d = 200$ nm, filling factor $p = 50\%$, and groove depth $a = 100$ nm. The material is described by the Drude-Lorentz model [27, 117, 150] given in equation (137).

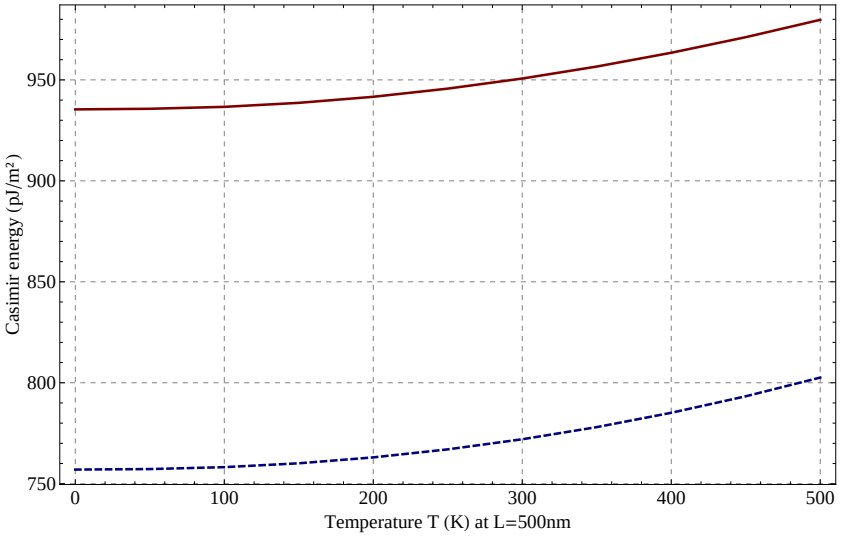

FIG. 92: Casimir energy as a function of the temperature T, for two planes (red solid curve) and two gratings (blue dashed curve) of intrinsic silicon at a separation distance $L = 500$ nm. The gratings have a period $d = 200$ nm, filling factor $p = 50\%$, and groove depth $a = 100$ nm. The material is described by the Drude-Lorentz model [27, 117, 150] given in equation (137).

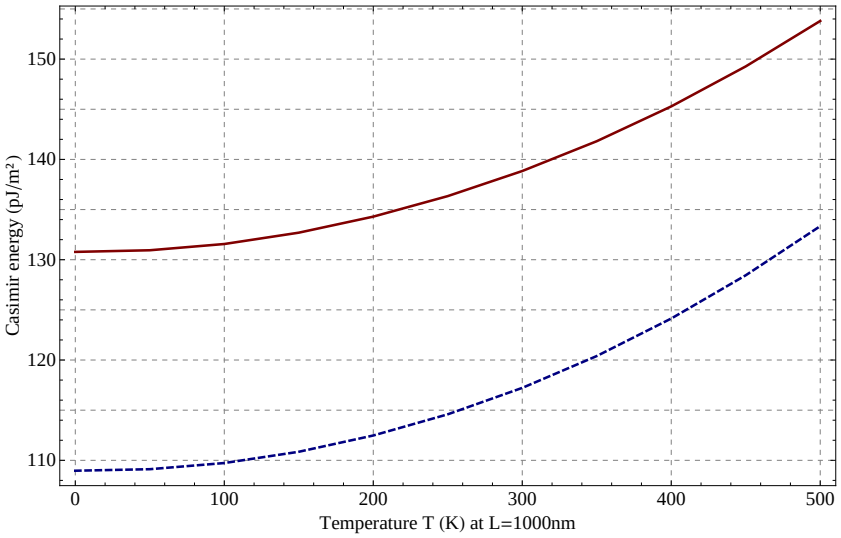

FIG. 93: Casimir energy as a function of the temperature T, for two planes (red solid curve) and two gratings (blue dashed curve) of intrinsic silicon at a separation distance $L = 1000$ nm. The gratings have a period $d = 200$ nm, filling factor $p = 50\%$, and groove depth $a = 100$ nm. The material is described by the Drude-Lorentz model [27, 117, 150] given in equation (137).

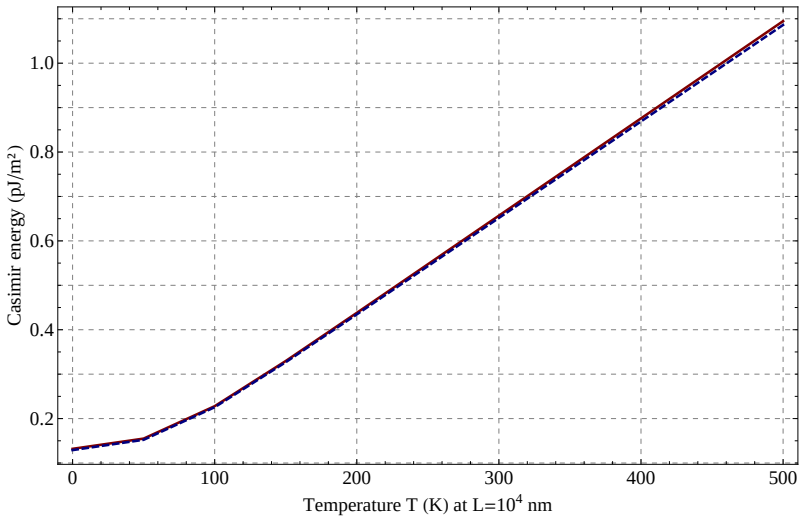

FIG. 94: Casimir energy as a function of the temperature T, for two planes (red solid curve) and two gratings (blue dashed curve) of intrinsic silicon at a separation distance $L = 1\mu$m. The gratings have a period $d = 200$ nm, filling factor $p = 50\%$, and groove depth $a = 100$ nm. The material is described by the Drude-Lorentz model [27, 117, 150] given in equation (137).

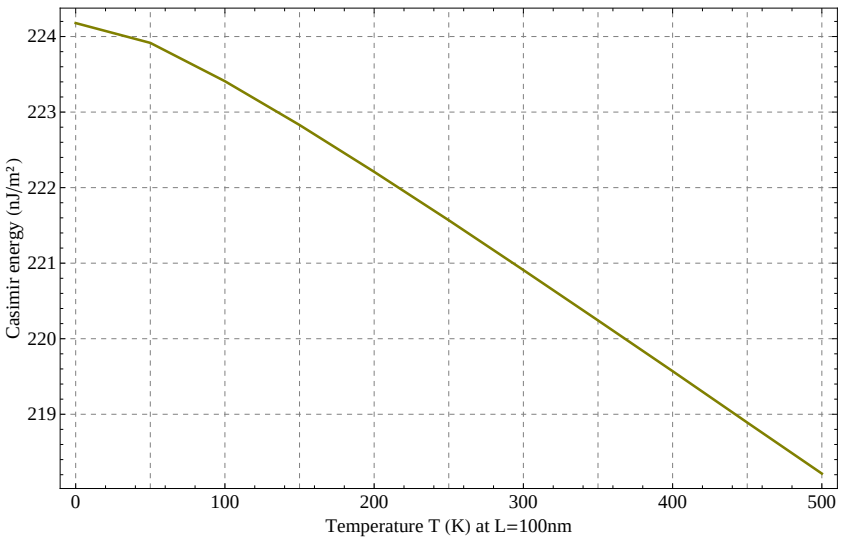

FIG. 95: Casimir energy as a function of the temperature T, for two planes of gold at a separation distance $L = 100$ nm. The material is described by a Drude model [70] given by equation (135) and FIG. 11.

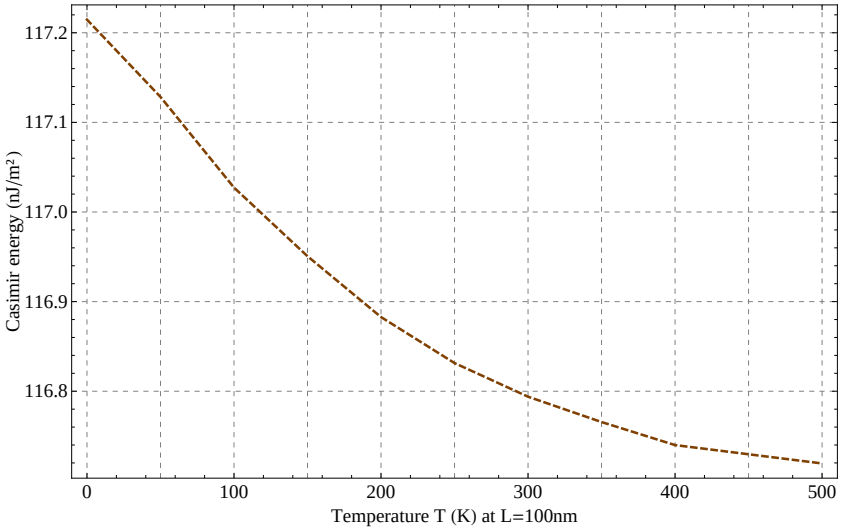

FIG. 96: Casimir energy as a function of the temperature T, for two gratings of gold at a separation distance $L = 100$ nm. This is for a grating period $d = 200$ nm, filling factor $p = 50\%$, and groove depth $a = 100$ nm. The material is described by a Drude model [70] given by equation (135) and FIG. 11.

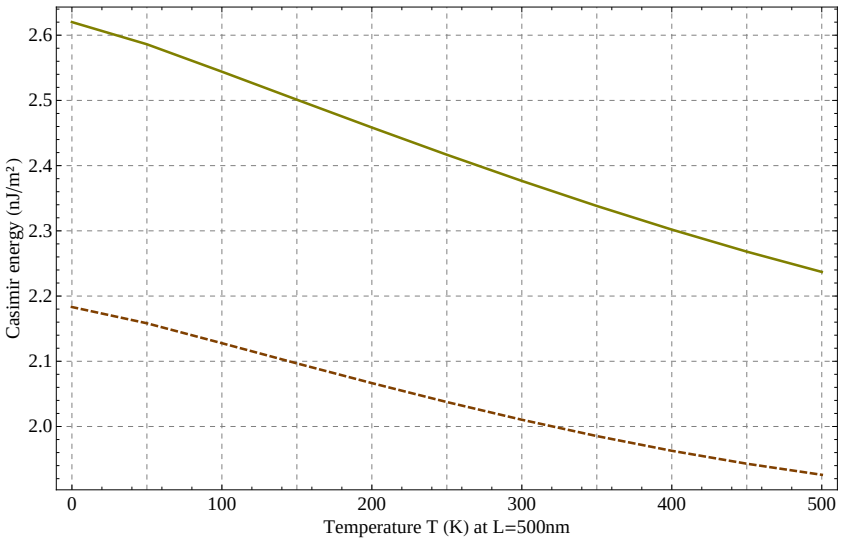

FIG. 97: Casimir energy as a function of the temperature T, for two planes (red solid curve) and two gratings (blue dashed curve) of gold at a separation distance $L = 500$ nm. The gratings have a period $d = 200$ nm, filling factor $p = 50\%$, and groove depth $a = 100$ nm. The material is described by a Drude model [70] given by equation (135) and FIG. 11.

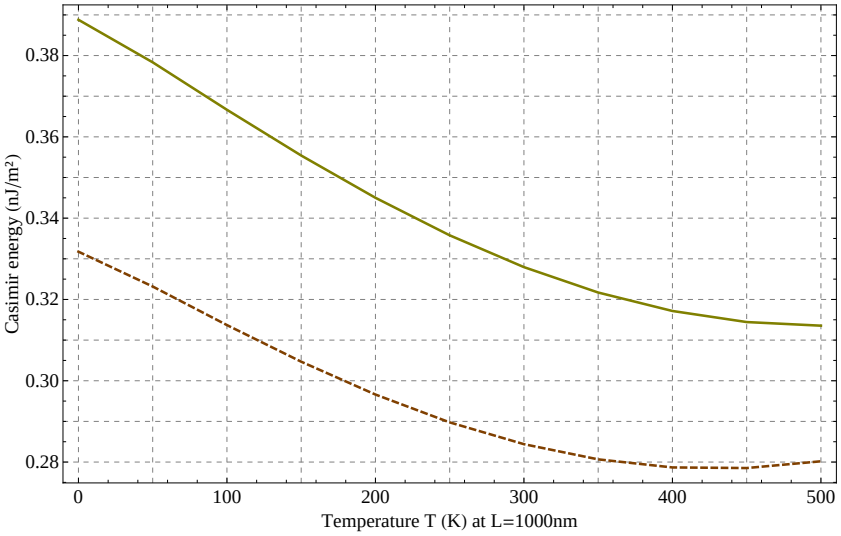

FIG. 98: Casimir energy as a function of the temperature T, for two planes (red solid curve) and two gratings (blue dashed curve) of gold at a separation distance $L = 1000$ nm. The gratings have a period $d = 200$ nm, filling factor $p = 50\%$, and groove depth $a = 100$ nm. The material is described by a Drude model [70] given by equation (135) and FIG. 11.

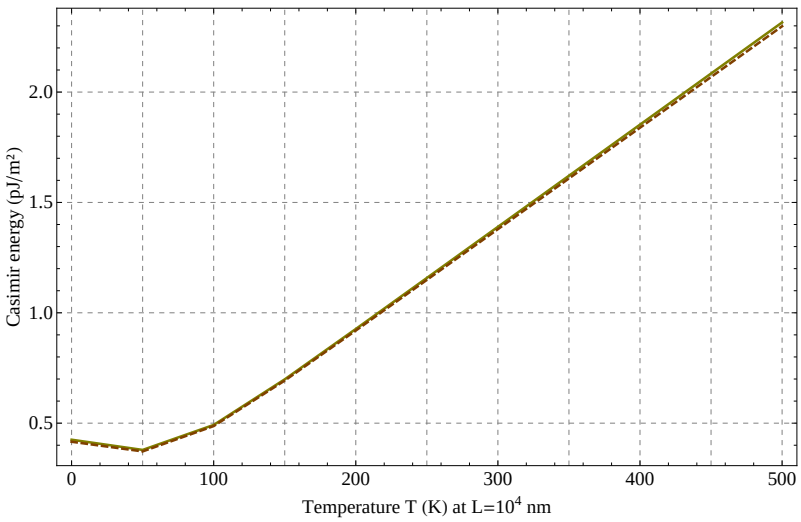

FIG. 99: Casimir energy as a function of the temperature T, for two planes (red solid curve) and two gratings (blue dashed curve) of gold at a separation distance $L = 1\mu$m. The gratings have a period $d = 200$ nm, filling factor $p = 50\%$, and groove depth $a = 100$ nm. The material is described by a Drude model [70] given by equation (135) and FIG. 11.

B. Casimir out-of-thermal equilibrium

1. Comparison between equilibrium and out-of-equilibrium situations

We now study the Casimir energy in the case where each plate has a different temperature T_1 and T_2, based on the out-of-thermal equilibrium formalism developed in section VI C 1. It is known that at thermal equilibrium and at zero temperatures, the Casimir force can be repulsive for certain Fabry-Pérot cavities formed by two different materials of specific impedances [161]. But this is met for instance in the case of magnetic media, or when the gap between the plates is filled by a medium other than vacuum. This situation can also happen in the case where the plates are out-of-thermal equilibrium [162–165] for certain ranges of temperatures T_1, T_2. This is the case that will interest here, knowing that it is possible to find regimes where the non-equilibrium contribution is large enough compared to the equilibrium contribution that it changes the sign of the total Casimir force.

Based on equations (376), (379), and (381), and section VI C 1, this is explained by a negative non-equilibrium contribution $\Delta F_z^{(\mathrm{neq})}(T_1,T_2)$ which counter-balances the equilibrium contribution $(F_z^{(\mathrm{eq})}(T_1)+F_z^{(\mathrm{eq})}(T_2))/2$, so that the total Casimir force $F_z^{(\mathrm{neq})}(T_1,T_2)$ switches sign. In the following, we study the variation of this non-equilibrium part $\Delta F_z^{(\mathrm{neq})}(T_1,T_2)$ so as to probe the weight of its contribution to the total Casimir force compared to the equilibrium part $(F_z^{(\mathrm{eq})}(T_1)+F_z^{(\mathrm{eq})}(T_2))/2$, and in which regimes of parameters it becomes negative.

The motivation for studying these two aspects lays in practical applications (such as tailoring the Casimir force, or canceling its effect with a specific control of temperatures), and in experimental setups (where the difference between an equilibrium and an out-of-equilibrium measurement protocol will depend on a sufficiently large non-equilibrium contribution to the total force).

On FIG. 100 we show the non-equilibrium contribution $\Delta F_z^{(\mathrm{neq})}(T_1,T_2)$ as a function of the separation distance L, for a Fabry-Pérot cavity formed by a plane of silicon dioxide SiO_2 at temperature $T_1 = 250$ K, and a plane of silicon carbide SiC at temperature $T_2 = 350$ K. We vary the distance from $L = 10$ nm to 1μm. On FIG. 101 we then show the total Casimir force $F_z^{(\mathrm{neq})}(T_1,T_2)$ together with the equilibrium contribution $(F_z^{(\mathrm{eq})}(T_1)+F_z^{(\mathrm{eq})}(T_2))/2$ as a function of the separation distance L, for that same cavity.

Based on the results of FIG. 100-101, we can make the following remarks :

- Both the non-equilibrium and equilibrium contributions (and hence the total Casimir force) follow a power law, proportional to $1/L^3$.
- The non-equilibrium part is smaller than the equilibrium part by about three orders of magnitudes, regardless of the separation distance L in the range 10 nm to 1μm.

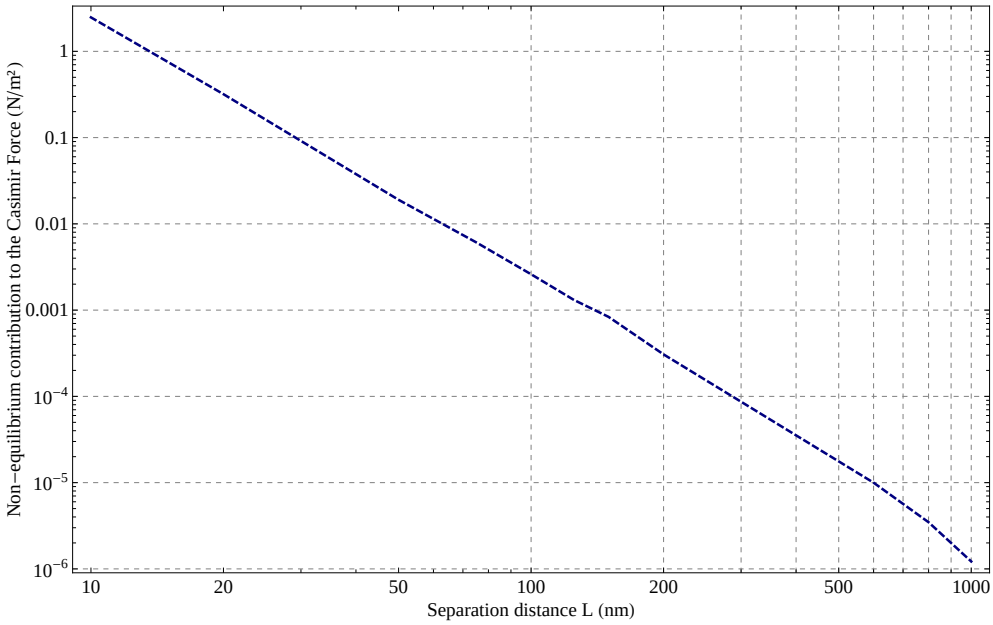

FIG. 100: Non-equilibrium contribution to the Casimir force $\Delta F_z^{(\mathrm{neq})}(T_1, T_2)$ from equation (376) as a log-log function of the separation distance L, for a Fabry-Pérot cavity formed by a plane of silicon dioxide SiO_2 at temperature $T_1 = 250$ K, and a plane of silicon carbide SiC at temperature $T_2 = 350$ K. The permittivity of SiO_2 is extrapolated from optical data [111, 112] and SiC is described by the Drude-Lorentz model [65] given in equation (140).

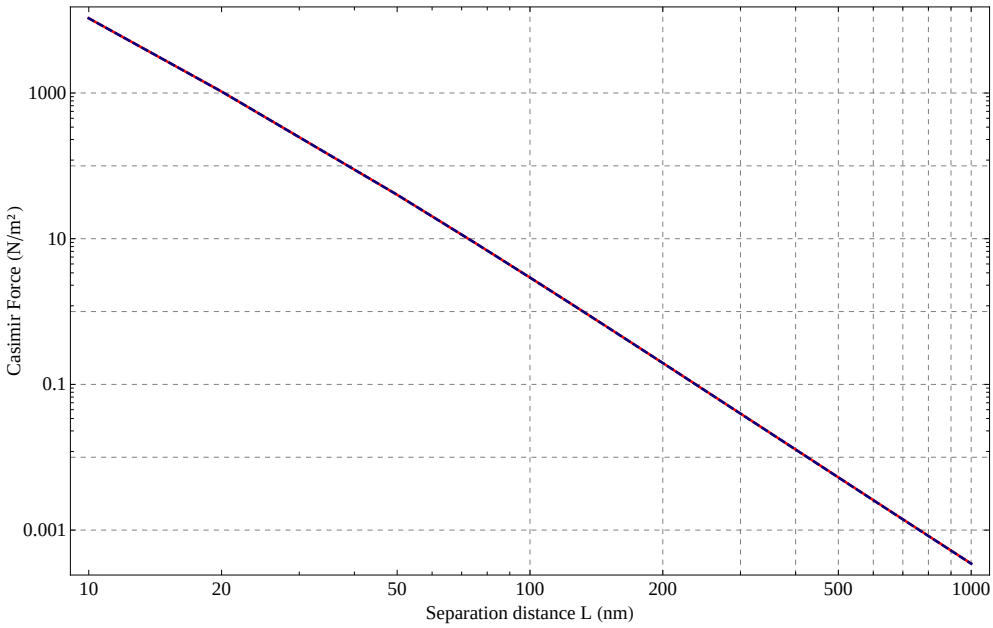

FIG. 101: Log-log dependence on the separation distance L of the total Casimir force $F_z^{(\mathrm{neq})}(T_1, T_2)$ from equation (381) (red curve), which is formed as the sum of the equilibrium contribution $(F_z^{(\mathrm{eq})}(T_1) + F_z^{(\mathrm{eq})}(T_2))/2$ from equation (379) (blue dashed curve) and of the non-equilibrium contribution $\Delta F_z^{(\mathrm{neq})}(T_1, T_2)$ from equation (376) seen on FIG. 100. This is for a Fabry-Pérot cavity formed by a plane of silicon dioxide SiO_2 at temperature $T_1 = 250$ K, and a plane of silicon carbide SiC at temperature $T_2 = 350$ K. The permittivity of SiO_2 is extrapolated from a Sellmeier model [119] given in equation (142) and SiC is described by the Drude-Lorentz model [65] given in equation (140).

Based on these results, we conclude that the non-equilibrium contribution is so small compared to the equilibrium part, that practical applications and experimental measurements of the out-of-equilibrium Casimir force may be challenging. However we explore further geometrical parameters than the separation distance L. In FIG. 102 and 103 we respectively show the non-equilibrium contribution $\Delta F_z^{(\mathrm{neq})}(T_1, T_2)$ and the equilibrium contribution $(F_z^{(\mathrm{eq})}(T_1) + F_z^{(\mathrm{eq})}(T_2))/2$ together with the total Casimir force $F_z^{(\mathrm{neq})}(T_1, T_2)$, as a function of the grating groove depth a. This is done for gratings separated by a distance $L = 100$ nm, with period $d = 500$ nm, and filling factor $p = 50\%$. The first grating is made of silicon dioxide SiO_2 and is at a temperature $T_1 = 250$ K, and the second grating is made of silicon carbide SiC and is at a temperature $T_2 = 350$ K.

- The non-equilibrium part does not decrease continuously with larger corrugation depths a unlike the equilibrium part. Over the range $a = 50$ nm to 1000 nm, it reaches a minimum at $a = 300$ nm.
- The non-equilibrium part is smaller than the equilibrium part by less than three orders of magnitudes, and this is especially true for smaller values of a.
- We can expect the total Casimir force to converge with larger a's beyond a groove depth of $a \sim 500$ nm.

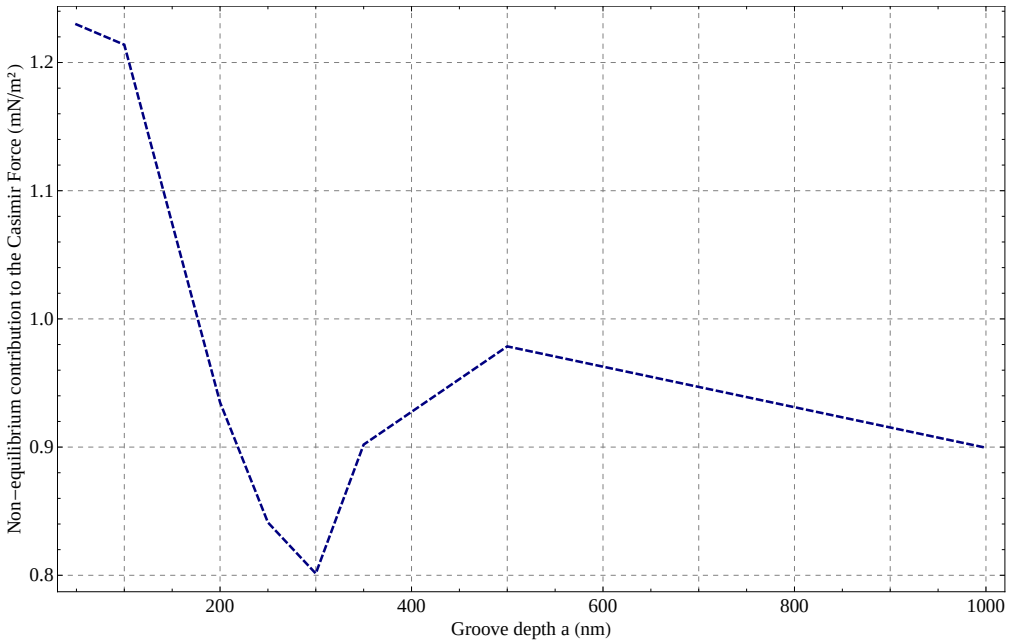

FIG. 102: Non-equilibrium contribution to the Casimir force $\Delta F_z^{(\mathrm{neq})}(T_1, T_2)$ from equation (376) as a function of the grating groove depth a. This is for a Fabry-Pérot cavity formed by a grating of silicon dioxide SiO_2 at temperature $T_1 = 250$ K, and a grating of silicon carbide SiC at temperature $T_2 = 350$ K. Both gratings are separated by a distance $L = 100$ nm, and have the same grating period $d = 500$ nm and filling factor $p = 50\%$. The permittivity of SiO_2 is extrapolated from optical data [111, 112] and SiC is described by the Drude-Lorentz model [65] given in equation (140).

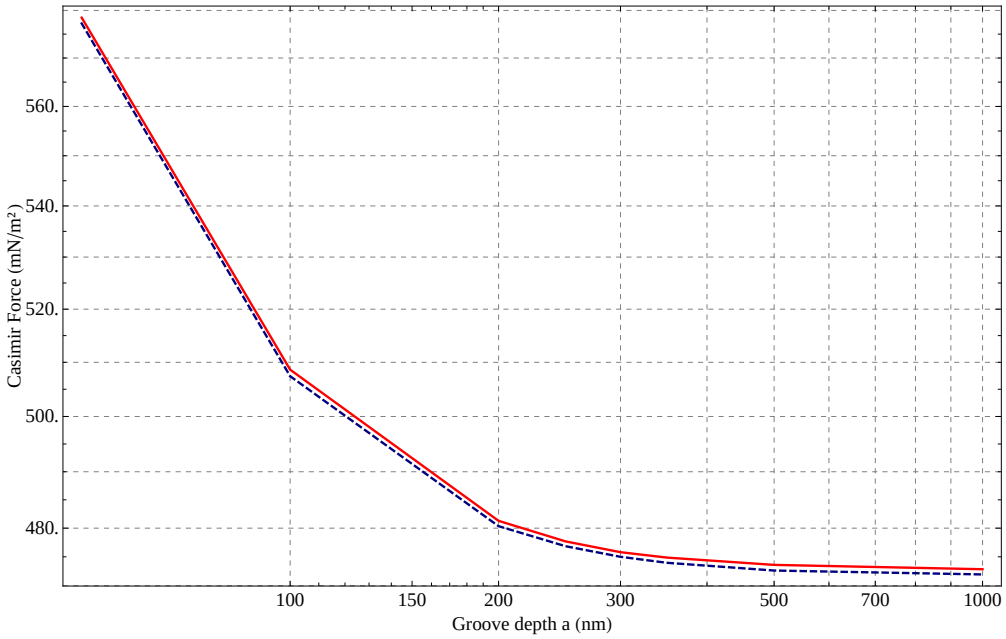

FIG. 103: Log-log dependence on the grating groove depth a of the total Casimir force $F_z^{(\mathrm{neq})}(T_1,T_2)$ from equation (381) (solid red curve), which is formed as the sum of the equilibrium contribution $(F_z^{(\mathrm{eq})}(T_1)+F_z^{(\mathrm{eq})}(T_2))/2$ from equation (379) (blue dashed curve) and of the non-equilibrium contribution $\Delta F_z^{(\mathrm{neq})}(T_1,T_2)$ from equation (376) seen on FIG. 102. Thplot corresponds to a Fabry-Pérot cavity formed by a grating of silicon dioxide SiO_2 at temperature $T_1 = 250$ K, and a grating of silicon carbide SiC at temperature $T_2 = 350$ K. Both gratings are separated by a distance $L = 100$ nm, and have the same grating period $d = 500$ nm and filling factor $p = 50\%$. The permittivity of SiO_2 is extrapolated from a Sellmeier model [119] given in equation (142) and SiC is described by the Drude-Lorentz model [65] given in equation (140).

2. Dependence on the temperature gradient and temperature average

From the former discussion we see that regardless of both the separation distance L in FIG. 100-101 for planes, and the grating groove depth a in FIG. 102-103, the contribution of the non-equilibrium part to the total Casimir force is very small. From now on, we study only the non-equilibrium contribution, in particular its dependence with both temperatures T_1, T_2 and distance L.

In FIG. 104, we show the non-equilibrium contribution $\Delta F_z^{(\mathrm{neq})}(T_1,T_2)$ for two planes as a function of the temperature gradient $\Delta T = T_1 - T_2$ when the temperature average of the two plates $\langle T\rangle = (T_1+T_2)/2$ is kept constant at 300 K. And in FIG. 105, we show the temperature average $\langle T\rangle = (T_1+T_2)/2$ when the temperature gradient of the two plates $\Delta T = T_1 - T_2$ is kept constant at 100 K.

- We see that the non-equilibrium contribution increases linearly in $\propto \Delta T$ when the average $\langle T\rangle = 300$ K is kept constant. In the range of temperature gradient $\Delta T = 20$ K to 520 K, we see that the non-equilibrium contribution varies from about $500\mu\mathrm{N.m}^{-2}$ to about $0.01\ \mathrm{N.m}^{-2}$.

- The non-equilibrium contribution converges beyond a temperature average of $\langle T\rangle \sim 900$ K when the temperature gradient $\Delta T = 100$ K is kept constant. The fusion of silica being reached around $T \sim 2700$ K, we kept the range

bound by a maximum temperature of $\langle T \rangle = 1200$ K.

- Below $\langle T \rangle \sim 215$ K, the non-equilibrium contribution is negative. This doesn't necessarily mean that the whole Casimir force becomes repulsive, but that there is a counter-balance of the equilibrium contribution by the non-equilibrium part for certain regimes of temperatures T_1 and T_2. We explore this interplay between T_1, T_2 and repulsivity in the next section.

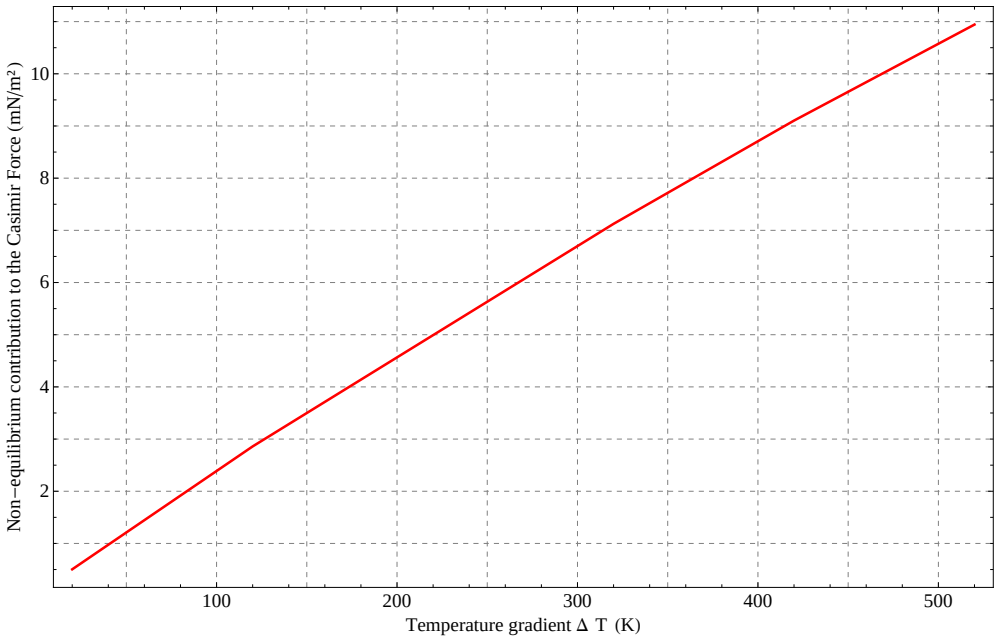

FIG. 104: Non-equilibrium contribution to the Casimir force $\Delta F_z^{(\mathrm{neq})}(T_1, T_2)$ from equation (376) as a function of temperature gradient $\Delta T = T_1 - T_2$, when the temperature average of the two plates $\langle T \rangle = (T_1 + T_2)/2$ is kept constant at 300 K and at a separation distance $L = 100$ nm. This is for a Fabry-Pérot cavity formed by a plane of silicon dioxide SiO_2 at temperature $T_1 = 300 - \Delta T/2$ K, and a plane of silicon carbide SiC at temperature $T_2 = 300 + \Delta T/2$ K. The permittivity of SiO_2 is extrapolated from optical data [111, 112] and SiC is described by the Drude-Lorentz model [65] given in equation (140).

3. Repulsivity and contribution of the non-equilibrium term

Finally we combine these results, and study the non-equilibrium contribution to the Casimir force $\Delta F_z^{(\mathrm{neq})}(T_1, T_2)$ between two planes as a function of separation distance L for different temperature gradients ($\Delta T = 200$ K, 150 K, 100 K, and 50 K) when the temperature average is kept constant at $\langle T \rangle = 350$ K in FIG. 106, and for different temperature averages ($\langle T \rangle = 350$ K, 250 K, and 150 K) when the temperature gradient is kept constant at $\Delta T = 200$ K in FIG. 107. In FIG. 108, we then show the non-equilibrium contribution as a percentage of the equilibrium contribution at a separation distance $L = 3000$ nm for the different gradients and averages of temperatures used in FIG. 106-107.

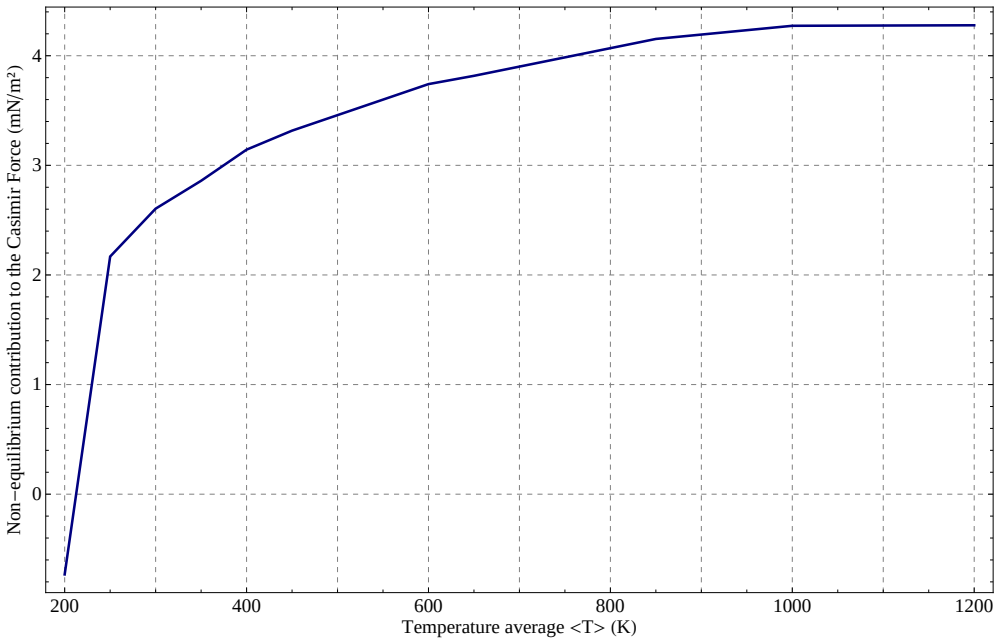

FIG. 105: Non-equilibrium contribution to the Casimir force $\Delta F_z^{(\mathrm{neq})}(T_1, T_2)$ from equation (376) as a function of temperature average $\langle T\rangle = (T_1 + T_2)/2$, when the temperature gradient of the two plates $\Delta T = T_1 - T_2$ is kept constant at 100 K and at a separation distance $L = 100$ nm. This is for a Fabry-Pérot cavity formed by a plane of silicon dioxide SiO_2 at temperature $T_1 = \langle T\rangle - 50$ K, and a plane of silicon carbide SiC at temperature $T_2 = \langle T\rangle + 50$ K. The permittivity of SiO_2 is extrapolated from optical data [111, 112] and SiC is described by the Drude-Lorentz model [65] given in equation (140).

- Whether the temperature average $\langle T\rangle = 350$ K is kept constant and we vary the temperature gradient $\Delta T = 200$ K, 150 K, 100 K, and 50 K as in FIG. 106, or the temperature gradient $\Delta T = 200$ K is kept constant and we vary the temperature average $\langle T\rangle = 350$ K, 250 K, and 150 K as in FIG. 107, there exists a *separation distance* L_s where all the profiles have the same non-equilibrium contribution. This lesser separation distance is equal to $L_s = 1275$ nm and $L_s = 1300$ nm for these two figures, respectively.

- In the first case shown on FIG. 106, this separation distance L_s coincides with the shift from a positive to a negative non-equilibrium contribution. It is beyond this separation distance L_s that the total Casimir force is expected to be negative, due to the non-equilibrium contribution, and hence repulsive [162].

- At a constant temperature gradient $\Delta T = 200$ K, it is possible to reach smaller values of L_s by decreasing the temperature average $\langle T\rangle$: we find $L_s = 1.270\mu$m for $\langle T\rangle = 350$ K, $L_s = 1.245\mu$m for $\langle T\rangle = 250$ K, and $L_s = 1.170\mu$m for $\langle T\rangle = 150$ K, as seen on FIG. 107.

- However even if L_s decreases when the temperature average is lowered, and hence the smallest distance at which the total Casimir force is partly counter-balanced by its non-equilibrium contribution and potentially shifted towards a repulsive regime, we see on FIG. 108 that the ratio of the non-equilibrium to the equilibrium part decreases likewise.

- We thus found an optimal range of parameters of separation distance $L = 3000$ nm, temperature gradient $\Delta T = 200$ K, and temperature average $\langle T\rangle = 350$, where the non-equilibrium contribution represents more than

22% of the equilibrium contribution, and is thus large enough to be measured by experimental protocols.

These elements should also give future prospects of research with a further study of the tailoring of the Casimir force *via* temperature control of the two plates. The problem of stiction [59, 139, 140] which impairs NEMS and MEMS as well as other applications of nanotechnology could be explored with the variations of this non-equilibrium contribution to cancel the whole Casimir force at certain temperatures [162].

A key understanding for this study is the domain of L_s, as the issue of stiction happens within ranges of L at which the total Casimir force is strong, that is below the micrometer range. To the contrary of [162], we do not consider here a third temperature T_3 in the gap between the plates, and do not find a repulsive regime for planes of SiO_2/SiC. But as already said, we find a non-equilibrium contribution of more than 22% of the equilibrium contribution, which is large enough for experimental interests.

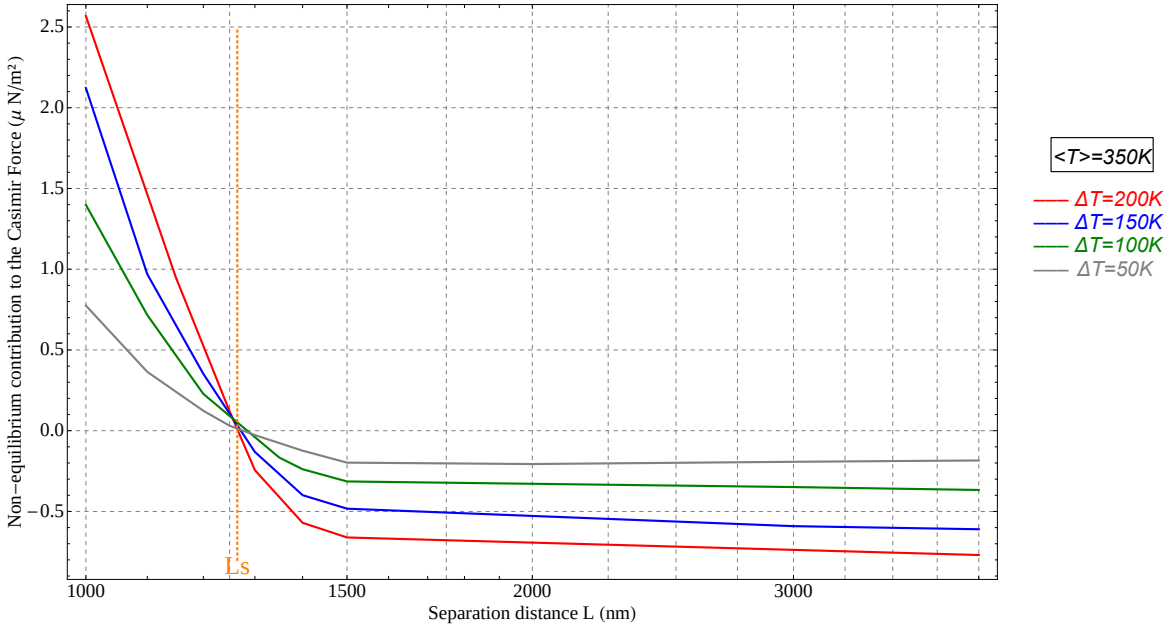

FIG. 106: Log-linear non-equilibrium contribution to the Casimir force $\Delta F_z^{(\mathrm{neq})}(T_1, T_2)$ from equation (376) as a function of the separation distance L, when the temperature average $\langle T \rangle = 350$ K is kept constant and for different temperature gradients : $\Delta T = 200$ K (red curve), $\Delta T = 150$ K (blue curve), $\Delta T = 100$ K (green curve), and $\Delta T = 50$ K (gray curve). This is for a Fabry-Pérot cavity formed by a plane of silicon dioxide SiO_2 at temperature $T_1 = 350 - \Delta T/2$ K, and a plane of silicon carbide SiC at temperature $T_2 = 350 + \Delta T/2$ K. The permittivity of SiO_2 is extrapolated from optical data [111, 112] and SiC is described by the Drude-Lorentz model [65] given in equation (140).

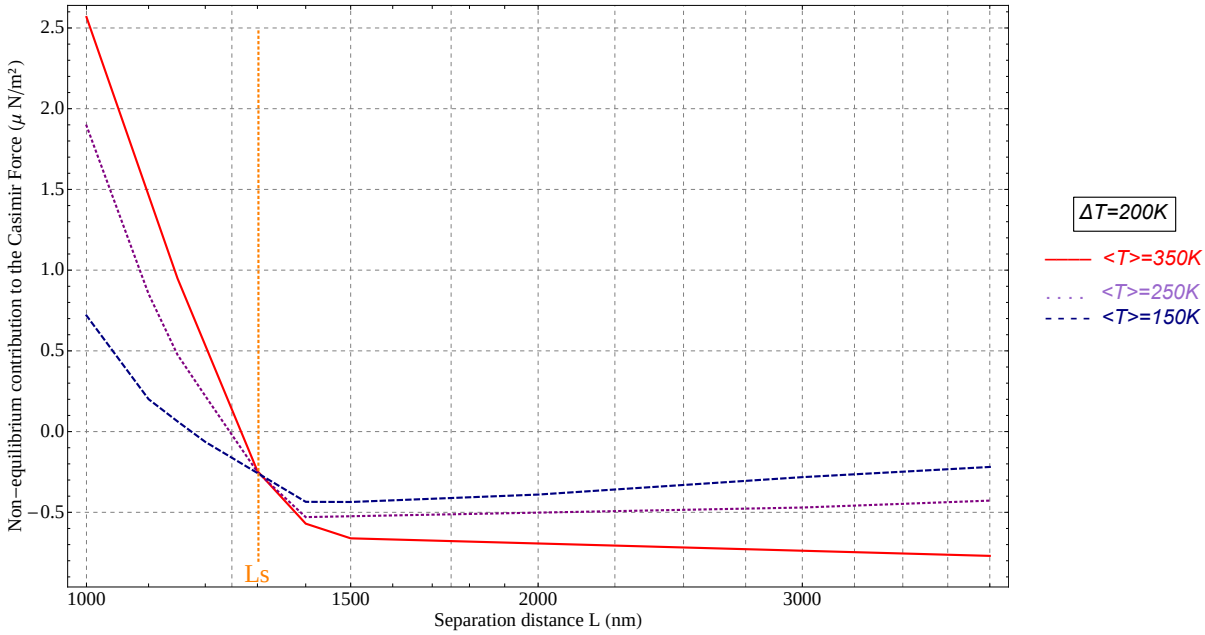

FIG. 107: Log-linear non-equilibrium contribution to the Casimir force $\Delta F_z^{(\mathrm{neq})}(T_1, T_2)$ from equation (376) as a function of the separation distance L, when the temperature gradient $\Delta T = 200$ K is kept constant and for different temperature averages : $\langle T \rangle = 350$ K (red curve), $\langle T \rangle = 250$ K (purple dotted curve), and $\langle T \rangle = 150$ K (blue dashed curve). This is for a Fabry-Pérot cavity formed by a plane of silicon dioxide SiO_2 at temperature $T_1 = \langle T \rangle - 100$ K, and a plane of silicon carbide SiC at temperature $T_2 = \langle T \rangle + 100$ K. The permittivity of SiO_2 is extrapolated from optical data [111, 112] and SiC is described by the Drude-Lorentz model [65] given in equation (140).

$\langle \mathbf{T} \rangle$	$\mathbf{\Delta T}$	$\mathbf{T_1}$	$\mathbf{T_2}$	$\mathbf{\Delta F^{(neq)}/F^{(eq)}}$
350	**200**	**450**	**250**	**22.12%**
350	**150**	**425**	**275**	**18.11%**
350	**100**	**400**	**300**	**10.78%**
350	**50**	**375**	**325**	**5.98%**
350	**200**	**450**	**250**	**22.12%**
250	**200**	**350**	**150**	**16.89%**
150	**200**	**250**	**50**	**11.50%**

FIG. 108: Ratios of the non-equilibrium part to the equilibrium part for the different temperatures shown on FIG. 106 and 107 (with same color code) at the separation distance $L = 3000$ nm.

IX. NUMERICAL EVALUATION : RADIATIVE HEAT TRANSFER IN NEAR-FIELD

A. Radiative heat transfer between planes

The studies of near-field heat transfer are in general of great interest to both NEMS and MEMS designs, since these systems are naturally affected by the side-effects of heat exchange at the nanoscale. Other important applications lie in the fields of nanotechnology, photonic crystals [66], metamaterials [67, 166], thermalphotovoltaics [69, 167], multilayered structures [168], improved resolution in nano-structure imaging, and new nano-fabrication techniques.

We now use the results of the scattering formalism developed in section VI C 2, and perform numerical calculations of the heat transfer coefficients h between two plates of silicon dioxide SiO_2 at temperatures T_1 and T_2, as given by equations (407) and (408). We already saw that radiative heat transfer for distances shorter than the average thermal wavelength becomes much larger than the black body limit, which is understood as an effect arising from the contribution of the evanescent waves.

In FIG. 109 we show the radiative heat transfer coefficient h as a function of the separation distance L, for two planes of silicon dioxide SiO_2 at temperatures $T_1 = 310$ K and $T_2 = 290$ K (these temperatures will be taken for T_1 and T_2 for the remainder of this section IX). We can see that beyond a distance $L \sim 3.7\mu$m, the flux becomes smaller than the black body limit, which is about ~ 6.13 W.m^2.K^{-1} for this temperature gradient $\Delta T = 20$ K.

Furthermore, one can see from the slope of the curve that the variation of the heat flux h with distance can be categorized in approximatively three domains of separation distances : A corresponding to the *extreme near-field* below 200 nm, B corresponding to the *near-field* from 200 nm to 10μm, and C corresponding to the domain of *Stefan-Boltzmann's law* beyond 10μm.

Along those ranges, the strongest contributions physically come from the dipole-dipole interaction for domain A, from surface phonon-polaritons for domain B, and from the classical radiative heat transfer for domain C. The surface phonon-polaritons supported by silicon dioxide SiO_2 thus enhance the heat flux. This is practically shown in the field modulus map of FIG. 110 for two gratings of SiO_2 at a separation distance $L = 25$nm, with period $d = 1500$nm, filling factor $p = 20\%$, and groove depth $a = 500$nm.

The contribution in the first domain A of FIG. 109 hence corresponds to the localized heat transfer seen in the upper-left map of FIG. 110, whereas the main contribution in the second domain B corresponds to the delocalized heat transfer mediated by the surface wave seen on the right maps of FIG. 110.

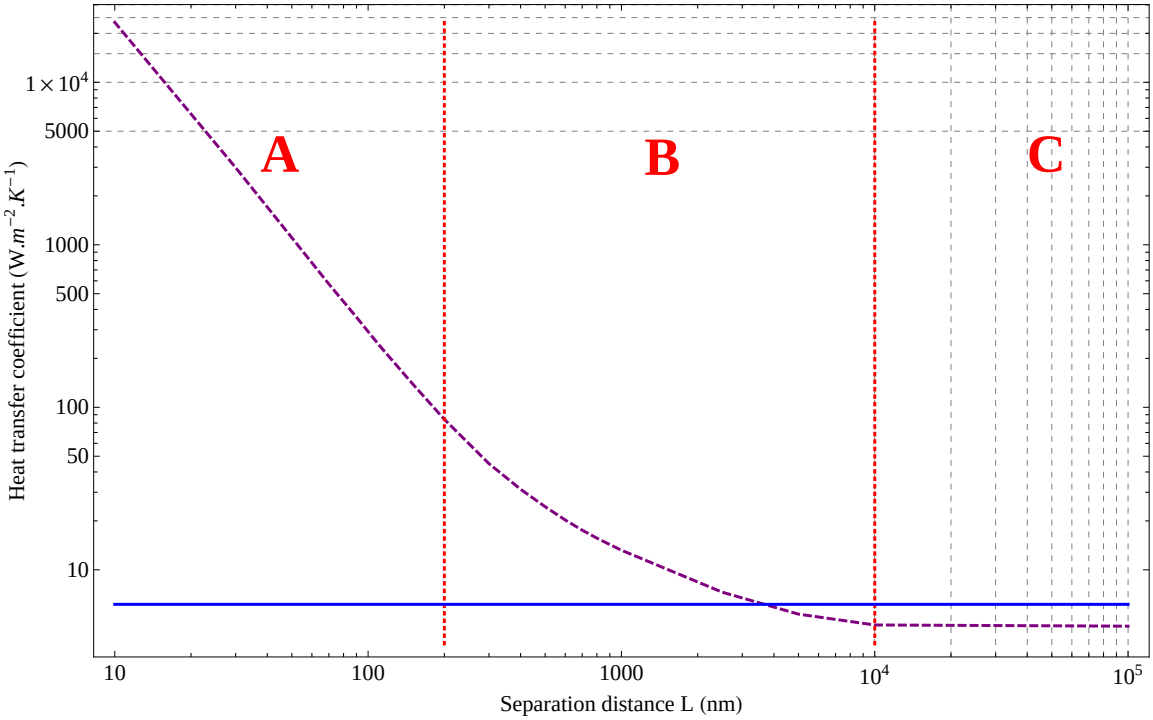

FIG. 109: Radiative heat transfer coefficient as a function of the separation distance L, for two planes of silicon dioxide SiO_2 at temperatures $T_1 = 310$ K and $T_2 = 290$ K (dashed purple curve), and compared with the black body limit (solid blue line). One can divide the separation distance L in three domains A, B, and C, respectively corresponding to the extreme near-field below 200 nm, to the near-field from 200 nm to 10μm, and to the domain of Stefan-Boltzmann's law beyond 10μm. This can be seen by a change of the slope of the curve along these three ranges. The permittivity of SiO_2 is extrapolated from optical data [111, 112].

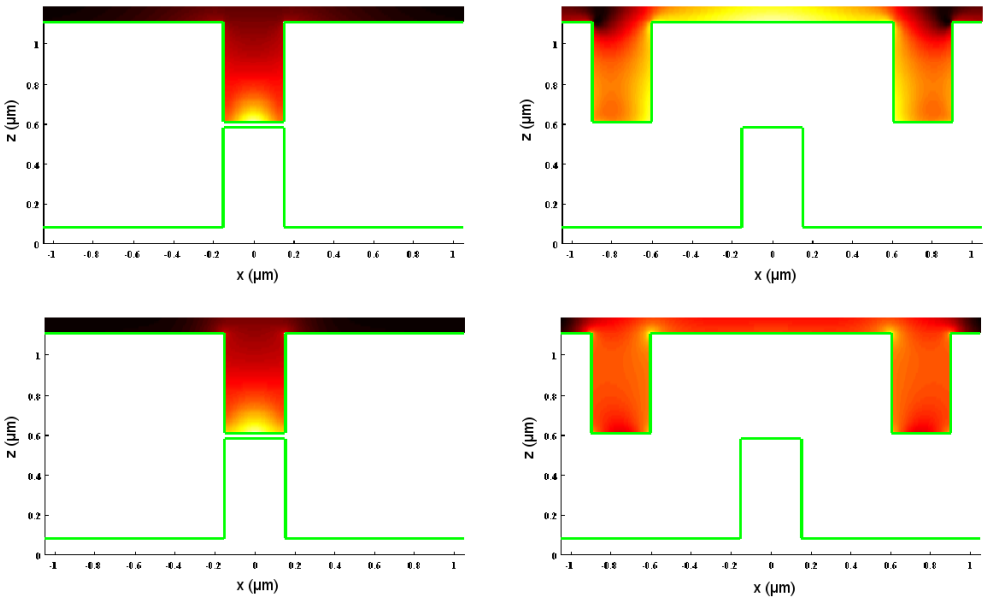

FIG. 110: Field modulus map of a given source dipole placed in the middle of a corrugation and right under the surface. The field is here represented only in the upper grating, so as to highlight where the absorption takes place. This is for gratings at a separation distance $L = 25$nm. The two figures on the left display the profiles in the $xz-$plane (in green) when they are aligned ($\delta = 0$), and the two figures on the right when they are laterally displaced by half-a-period ($\delta = d/2$), both for two different wavelengths $\lambda = 8.75\mu$m (top) and 9.15μm (down).

The intensity or square modulus of the electric field represented in FIG. 110 appears only in the upper grating so as to highlight the place of absorption. Two different wavelengths $\lambda = 8.75\mu$m and $\lambda = 9.15\mu$m are considered, based on the fact that SiO_2 has two resonance frequencies at $\lambda = 8.75\mu$m and $\lambda = 21\mu$m, as was shown on FIG. 12 of section VI A 1.

In the case where $\delta/p = 0\%$ and $\lambda = 8.75\mu$m, we see that the field is clearly both intense and confined. As 8.75μm corresponds to the horizontal asymptote of the surface phonon dispersion relation, a large number of modes with different values of the wave vector are excited. This leads to a highly localized subwavelength hot spot. At 9.15μm, the spot is broader as expected : this is similar to the loss of resolution of surperlens away from the resonance. On the right column of the figure, we show the intensity for $\delta/d = 50\%$. As already said, these results can also be understood through the data of FIG. 109, when considering the flux in the domains A and B.

In FIG. 111 we show the radiative heat transfer coefficient h as a function of the separation distance L, for two planes at temperatures $T_1 = 310$ K and $T_2 = 290$ K. This is done for different materials : silicon dioxide SiO_2, as well as gold Au, aluminum Al, copper Cu, and tungsten W [69]. We see that the heat flux associated with the profiles of SiO_2 has a *convex* dependence on the separation distance L, whereas the flux associated with all four metals display a *concave* dependence on L. As a result, the black body limit ~ 6.13 W.m^2.K^{-1} is reached much faster for metals with increasing separation distance L : we find this distance to be approximatively equal to 250 nm, 260 nm, 275 nm, and 340 nm for copper, gold, aluminum, and tungsten, respectively. This is to be compared with SiO_2 where the black body limit was seen on FIG. 109 to be reached around $\sim 3.7\mu$m.

One should note that in near-field, the heat flux is highly dependant on the properties of the materials permittivity. We use here in this context silicon dioxide which is known to have surface polaritons, but in the case of two metallic gratings such as gold for instance [73], the property of shallow skin depth for gold compared to dielectrics together with the presence of surface plasmons may present non-trivial effects on the flux.

Unlike for the Casimir force, the power laws here for the radiative heat transfer as a function of separation distance depend on which domain of separation range A, B, or C on FIG. 109 is considered. However one could imagine that gradually increasing the electrical conductivity of a given dielectric would progressivley shift its curve in the plot of FIG. 111 from having a convex shape to a concave shape, thus approximating in between a straight line and hence a power law for at a given conductivity over the whole separation range. For instance this could be done with silicon for different levels of doping or charge carrier densities [117], or for materials such as UV-treated indium tin oxide (ITO) [169].

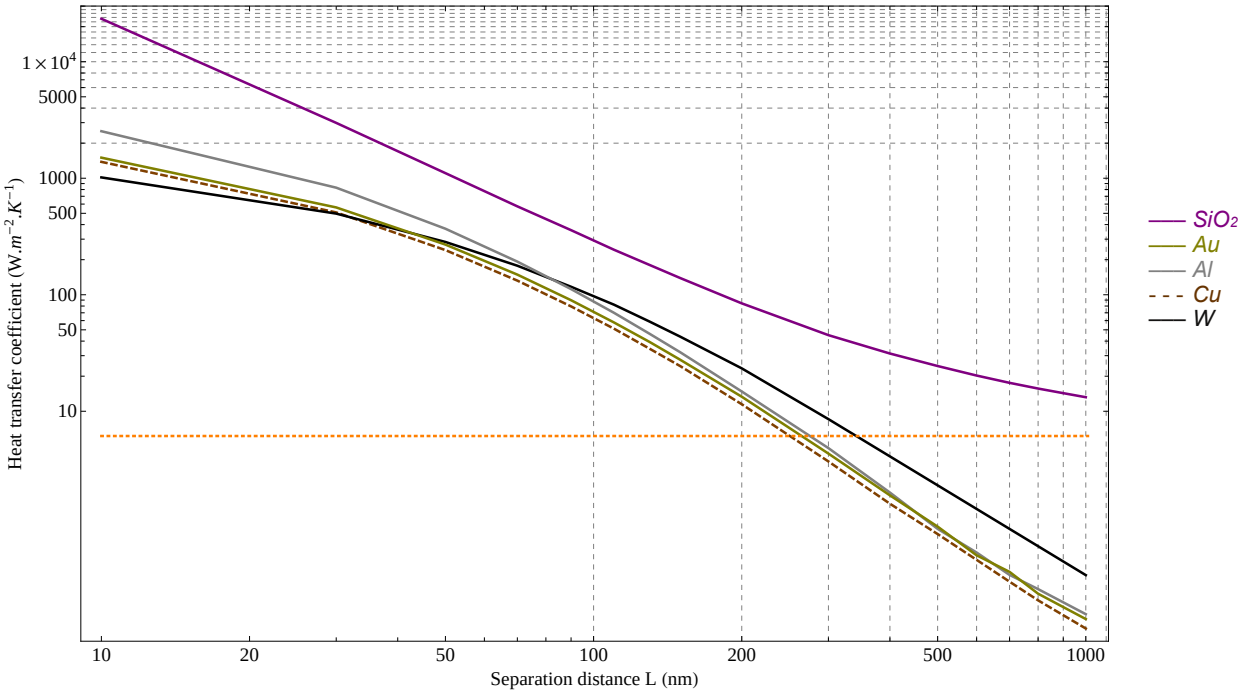

FIG. 111: Radiative heat transfer coefficient as a function of the separation distance L, for two planes of different materials at temperatures $T_1 = 310$ K and $T_2 = 290$ K. Silicon dioxide SiO_2 appears in purple, and its permittivity is extrapolated from optical data [111, 112]. Gold appears in yellow, aluminum in gray, copper in dashed orange, and tungsten in black. These four metals are described by a Drude model [70] given by equation (135) and FIG. 11.

B. Radiative heat transfer between gratings

We from now on consider two dielectric gratings of silicon dioxide SiO_2 at temperatures $T_1 = 310$ K and $T_2 = 290$ K, and explore the variations of the heat transfer coefficient h when the gratings are not laterally shifted ($\delta/d = 0\%$), and when they are by half-a-period ($\delta/d = 50\%$), as shown on FIG. 112. This is done for several geometrical parameters specifying the grating and cavity profiles : for the separation distance L in FIG. 113, for the grating period d in FIG. 114, for the filling factor p in FIG. 115, and for the grating groove depth a in FIG. 116.

Furthermore on FIG. 117, we study the heat transfer coefficient h as a function of a continuous lateral shift δ. For each of these numerical computations, the scattering results coming from the formalism developed in section VI C 2 are compared with Derjaguin's Proximity Approximation [131]. Notice that for all these plots, we are in the extreme near-field ranges of separation distances.

We can make some remarks on the results of FIG. 113-117 :

- We recover for gratings at $\delta/d = 50\%$ the plane-plane case of a variation of the flux with separation distance following a convex shape on the log-log plots of FIG. 113, as compared to FIG. 109.
- At long separation ranges the gratings at $\delta/d = 0\%$ and $\delta/d = 50\%$ converge to the same value (FIG. 113). This is because the lateral modes contribution, which accounts for the difference between these two lateral shifts do not play a major role anymore at large distances L.
- Regardless of the distance on FIG. 113, the Proximity Approximation for the heat transfer coefficient works well at $\delta = 0$, but not at $\delta = d/2$. At $L = 25$nm, the error of the Proximity Approximation is of $\sim 3\%$ for $\delta = 0$, and of $\sim 35\%$ for $\delta = d/2$. The reason for this is illustrated in FIG. 110, especially on the right column of the figure, showing the intensity for $\delta = d/2$. There we can see that the heated region is delocalized, which explains why the Proximity Approximation is clearly not valid. In this regime, the heat transfer is no longer due to a dipole-dipole interaction through the gap. Instead, a dipole excites modes of the structures. In turn, these spatially extended modes produce dissipation in the walls. This discussion indicates that the Proximity Approximation is valid if the gap width does not vary significantly on a length scale approximatively given by the spatial extension of the modes.
- In FIG. 114, we see that the heat transfer coefficients at $\delta = 0$ do not vary much with a change of period d and this is a further confirmation of the validity of the Proximity Approximation in this configuration. At $\delta = d/2$, however the scattering and Proximity Approximation results radically differ for small periods, but tend to agree for large periods. The reason for this is that when $d \to \infty$, the ratio a/d tends to zero and we expect the heat transfer to be well approximated by the plane-plane case, and hence the Proximity Approximation.

- As we saw for the dependence of the Casimir energy on the filling factor, we see again on FIG. 115 a linear variation of the heat flux with p when the gratings are not laterally shifted. In this case, the Proximity Approximation thus fits the scattering results very well. However in the case where the gratings are shifted by half-a-period, we find this linear variation appearing only beyond $p \sim 40\%$, and the Proximity Approximation results progressively rejoin the scattering values of the flux beyond a filling factor of 50%.

- The dependence of the heat flux on corrugation groove depth a shown in FIG. 116 confirms this difference between the shifted and non-shifted gratings. For trenches with $a > 150$ nm, we see that the curves corresponding to the scattering results for these two cases are almost perfectly parallel. This is again a consequence of the heat flux being exponentially dependent on separation distance, which is expressed here through a deepening of the grating grooves, so that the bottom of the grooves contributes less and less with increasing a.

- However because of the slope of the curves beyond $a = 150$ nm, this doesn't mean that the ratio of the $\delta/p = 50\%$ case over the non-shifted case remains constant —we see a slow decrease of this ratio along this range, from 95% at $a = 150$ nm to 40% at $a = 1\mu$m.

- Notice also that the Proximity Approximation increases in accuracy with deeper trenches for the non-shifted gratings, and decreases in accuracy with deeper trenches for the shifted gratings. Both the scattering and Proximity Approximation results converge perfectly as $a \to 0$, since the profiles recover the shape of two planes separated by a distance L.

- FIG. 117 gives a precious information on the dependence of the flux with lateral shift δ within the two boundaries $\delta/p = 0\%$ and $\delta/p = 50\%$ considered in the previous plots. As already seen for the Casimir energy in section VII B 5, the scattering results can be well fitted by a sinusoid, and the Proximity Approximation does not describe well the variation of the flux with a continuous lateral shift δ. The change in slope of the Proximity Approximation at $\delta/p = 30\%$ is directly related to the value of the filling factor $p = 30\%$ beyond which the local separation distance shifts along with δ from a situation where the grating surface exposed at L decreases and the surface exposed at $L + a$ increases, to a situation where suddenly no grating surface is exposed at L but only at $L + a$.

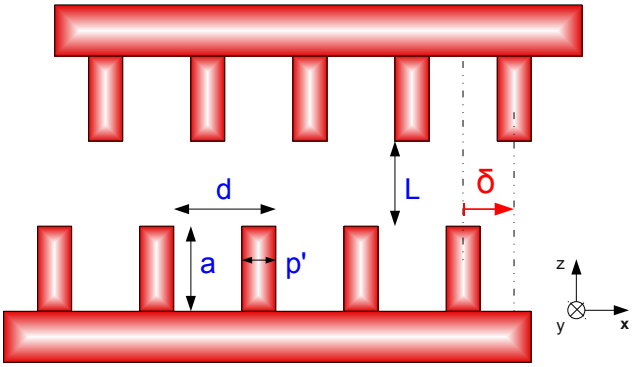

FIG. 112: Two identical gratings facing each other at a distance L and relatively shifted by a lateral displacement δ. The corrugations have a period d, height a and thickness p'. The filling factor $p = p'/d$ is given as a percentage of the period d.

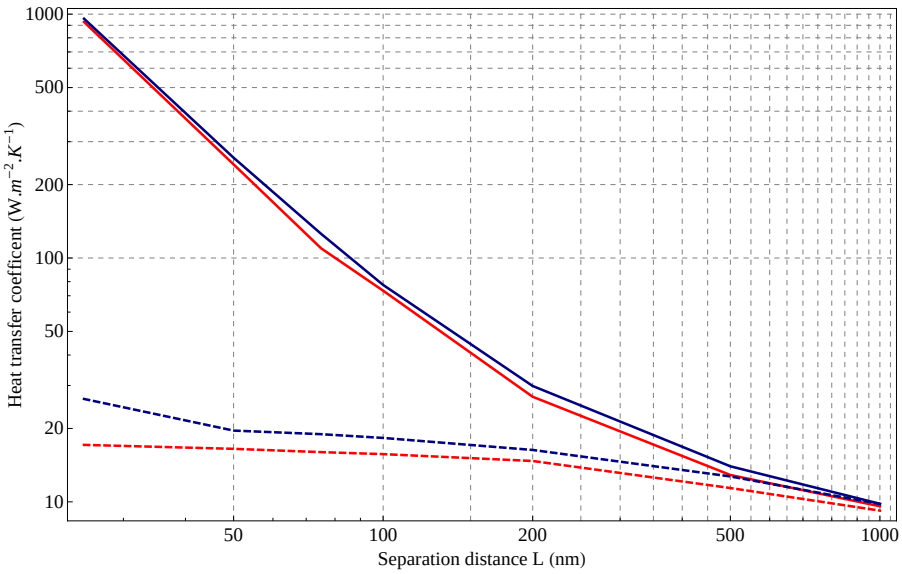

FIG. 113: Radiative heat transfer coefficient as a function of the separation distance L, for two gratings of silicon dioxide SiO_2 at temperatures $T_1 = 310$ K and $T_2 = 290$ K, for a lateral shift $\delta/d = 0\%$ (blue curve) and $\delta/d = 50\%$ (dashed blue curve). These two scattering results are compared with the Proximity Approximation (respective red curves). The gratings have a period $d = 1500$ nm, filling factor $p = 20\%$, and groove depth $a = 500$ nm. The permittivity of SiO_2 is extrapolated from optical data [111, 112].

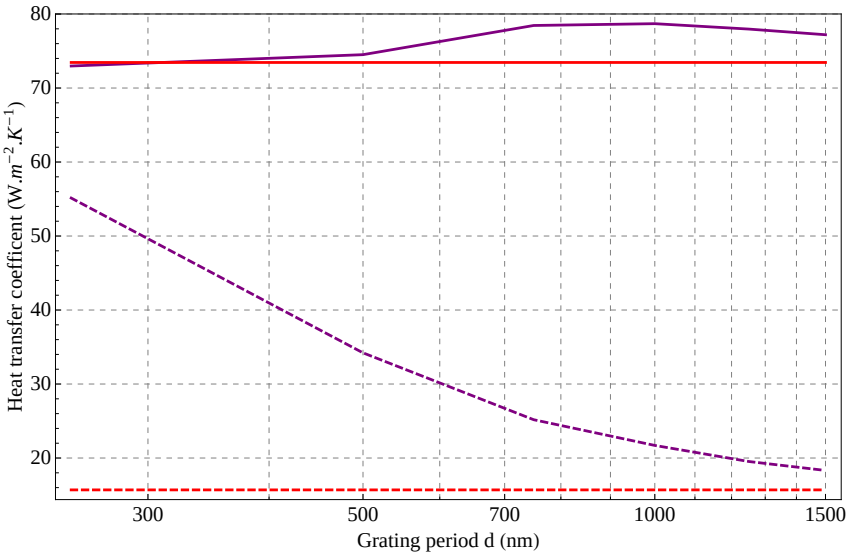

FIG. 114: Radiative heat transfer coefficient as a function of the grating period d, for two gratings of silicon dioxide SiO_2 at temperatures $T_1 = 310$ K and $T_2 = 290$ K, for a lateral shift $\delta/d = 0\%$ (purple curve) and $\delta/d = 50\%$ (dashed purple curve). These two scattering results are compared with the Proximity Approximation (respective red curves). The gratings are at a separation distance $L = 100$ nm, filling factor $p = 20\%$, and groove depth $a = 500$ nm. The permittivity of SiO_2 is extrapolated from optical data [111, 112].

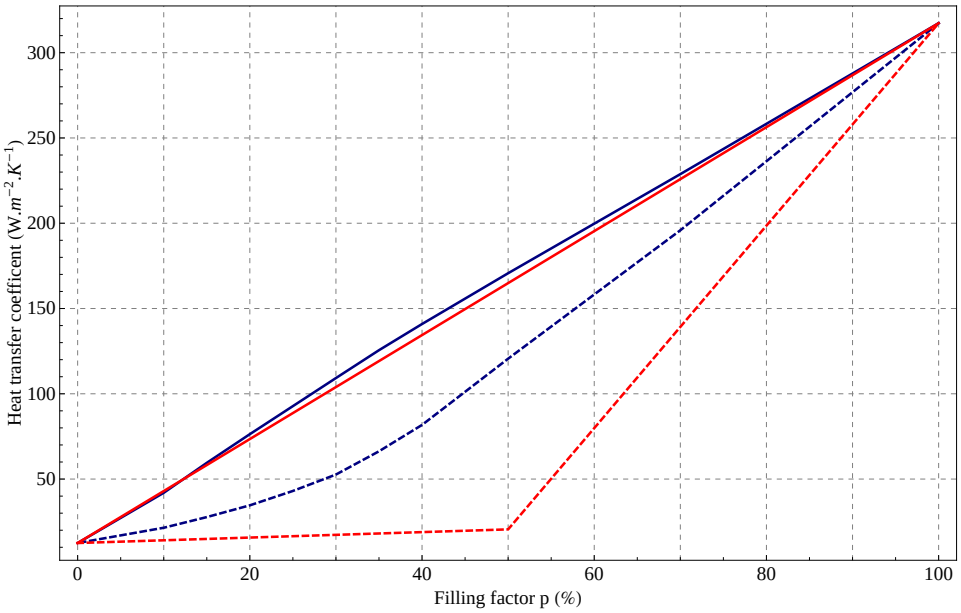

FIG. 115: Radiative heat transfer coefficient as a function of the filling factor p, for two gratings of silicon dioxide SiO_2 at temperatures $T_1 = 310$ K and $T_2 = 290$ K, for a lateral shift $\delta/d = 0\%$ (blue curve) and $\delta/d = 50\%$ (dashed blue curve). These two scattering results are compared with the Proximity Approximation (respective red curves). The gratings have a period $d = 500$ nm, separation distance $L = 100$ nm, and groove depth $a = 500$ nm. The permittivity of SiO_2 is extrapolated from optical data [111, 112].

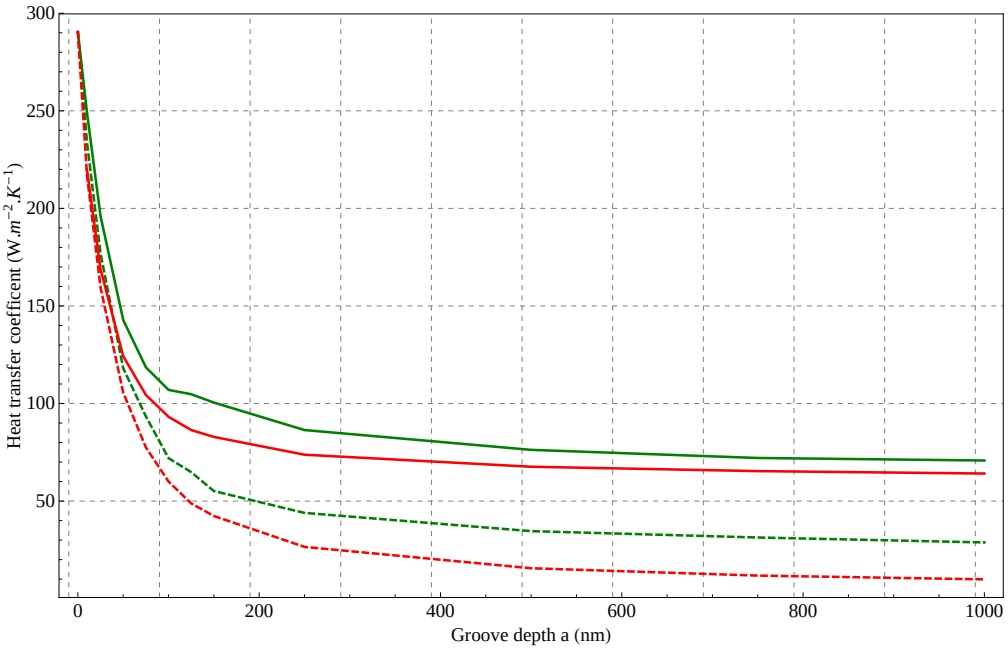

FIG. 116: Radiative heat transfer coefficient as a function of the grating groove depth a, for two gratings of silicon dioxide SiO_2 at temperatures $T_1 = 310$ K and $T_2 = 290$ K, for a lateral shift $\delta/d = 0\%$ (green curve) and $\delta/d = 50\%$ (dashed green curve). These two scattering results are compared with the Proximity Approximation (respective red curves). The gratings have a period $d = 500$ nm, filling factor $p = 20\%$, and separation distance $L = 100$ nm. The permittivity of SiO_2 is extrapolated from optical data [111, 112].

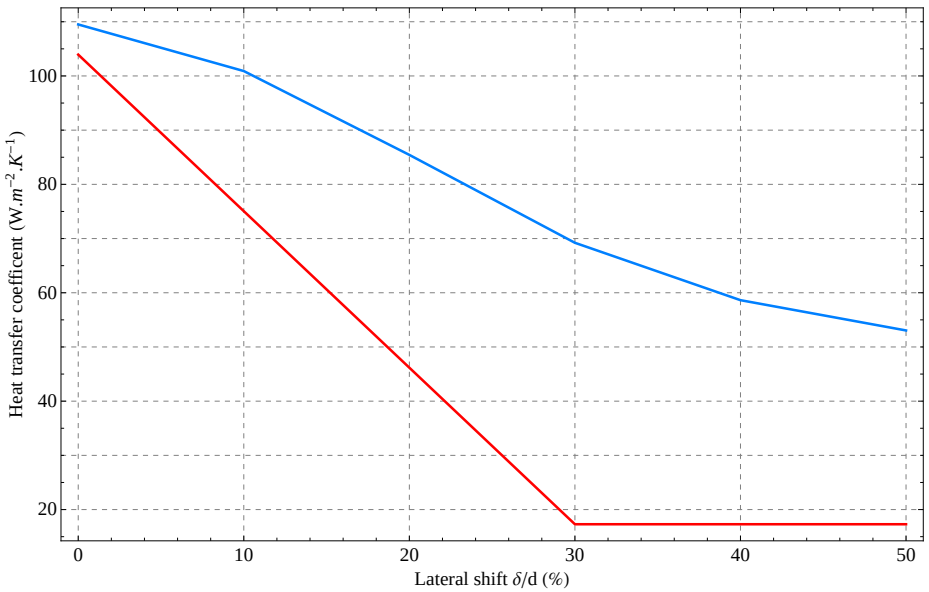

FIG. 117: Radiative heat transfer coefficient as a function of the lateral shift δ, for two gratings of silicon dioxide SiO_2 at temperatures $T_1 = 310$ K and $T_2 = 290$ K (blue curve). These scattering results are compared with the Proximity Approximation (red curve). The gratings have a period $d = 500$ nm, filling factor $p = 30\%$, groove depth $a = 500$ nm, and separation distance $L = 100$ nm. The permittivity of SiO_2 is extrapolated from optical data [111, 112].

C. A thermal modulator device for nanosystems

In the previous section we have seen that, an important contribution to the total value of the flux can come from the surface polaritons present in certain materials [80]. Here we focus on the interplay between the surface waves excitation and the surface profile, as already shown on FIG. 112 and see how this modulates the flux. We already saw in section IX B that for certain geometrical parameters, the radiative heat transfer varied strongly between the case where the gratings were not laterally shifted ($\delta/p = 0\%$) and the case where they were by half-a-period ($\delta/p = 50\%$).

This modulation of the flux with lateral shift δ could easily find a practical nanotechnological application in the form of a *thermal modulator* device for nanosystems. Although such a thermal modulator could also be based on a variation of the separation distance L [72, 76] according to the results shown in FIG. 109 and 111, modulating the flux through the lateral shift δ is much more stable in its implementation. Other thermal modulator devices could be based on a rotation of the two plates with respect to one another along the z-axis [64]. Unfortunately no exact method of calculation presently exists to estimate the efficiency of such devices yet.

Furthermore, radiative heat transfer is now being studied over a broad range of materials [68], such as different alloys combining the polaritons of certain dielectrics and the near-field properties of metals. The issue of heat transfer in near-field in the case of coatings [168], phase change materials [68, 70], metamaterials [166, 170], and graphene-covered dielectrics [62] are also being explored. The practical applications of thermal modulators could therefore be numerous and diverse.

In FIG. 118-121, we vary the different geometrical grating parameters in order to optimize the modulation of the flux between $\delta/p = 0\%$ and $\delta/p = 50\%$, and potentially specify an optimized thermal modulator. As mentioned before, silicon dioxide SiO_2 is a good choice of material for such a device, as it supports surface phonon-polaritons, which are known to enhance the flux. This was practically shown in the field modulus map of FIG. 110, and the plots of FIG. 109 and 111.

- We find an optimized value of the filling factor at $p = 20\%$, as seen on FIG. 118, for corrugated profiles with period $d = 500$ nm and at a distance $L = 100$ nm.
- The main result is that we have shown the possibility to modulate the heat flux by simply varying the gratings laterally along δ by a modulation factor $W_{\delta/d=0\%}/W_{\delta/d=50\%}$ of more than 36. This is shown on FIG. 119 in extreme near-field at a separation distance $L = 25$ nm, for gratings with corrugation period $d = 1500$ nm, filling factor $p = 20\%$, and groove depth $a = 500$ nm. It is important to choose a filling factor $p \neq 50\%$ to optimize the modulation enhancement, as this avoids the lateral modes contribution present at $\delta/d = 50\%$, as already shown on the field modulus map of FIG. 110.

- From the plots shown in FIG. 119-121, we can draw general rules of modulation enhancement by a convenient choice of the grating geometrical parameters : one should design a thermal modulator based on gratings with a separation distance L kept as small as possible, a grating period d as large as possible, a filling factor p kept at around a fifth of the period, and for corrugation trenches as deep as possible.

- Based on our study of the previous section, these geometrical parameters should be determined through an exact method such as scattering theory, not the Proximity Approximation which is used in metrology experiments and nanotechnological applications. Had we used the Proximity Approximation to calculate the modulation factor at $L = 25$ nm for the gratings of FIG. 119, we would have found a value of more than 54, thereby overestimating the exact value of the modulation by more than 50%.

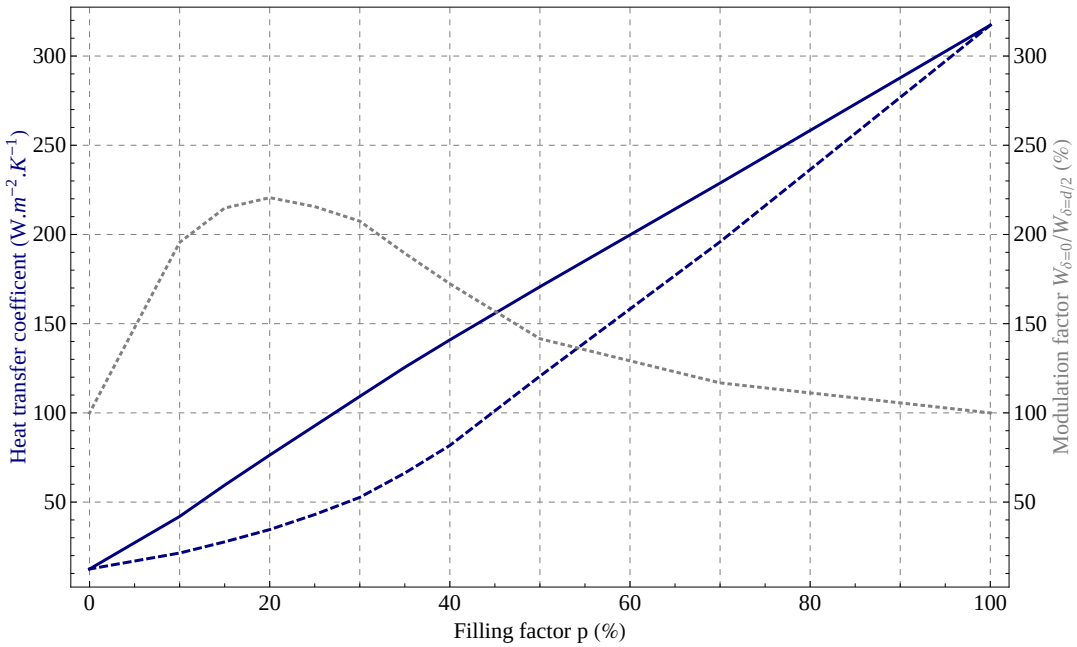

FIG. 118: Radiative heat transfer coefficient as a function of the filling factor p, for two gratings of silicon dioxide SiO_2 at temperatures $T_1 = 310$ K and $T_2 = 290$ K, for a lateral shift $\delta/d = 0\%$ (blue curve) and $\delta/d = 50\%$ (dashed blue curve). The results are plotted together with the percentage of modulation factor $W_{\delta/d=0\%}/W_{\delta/d=50\%}$ (dotted gray line). The gratings have a period $d = 500$ nm, separation distance $L = 100$ nm, and groove depth $a = 500$ nm. The permittivity of SiO_2 is extrapolated from optical data [111, 112].

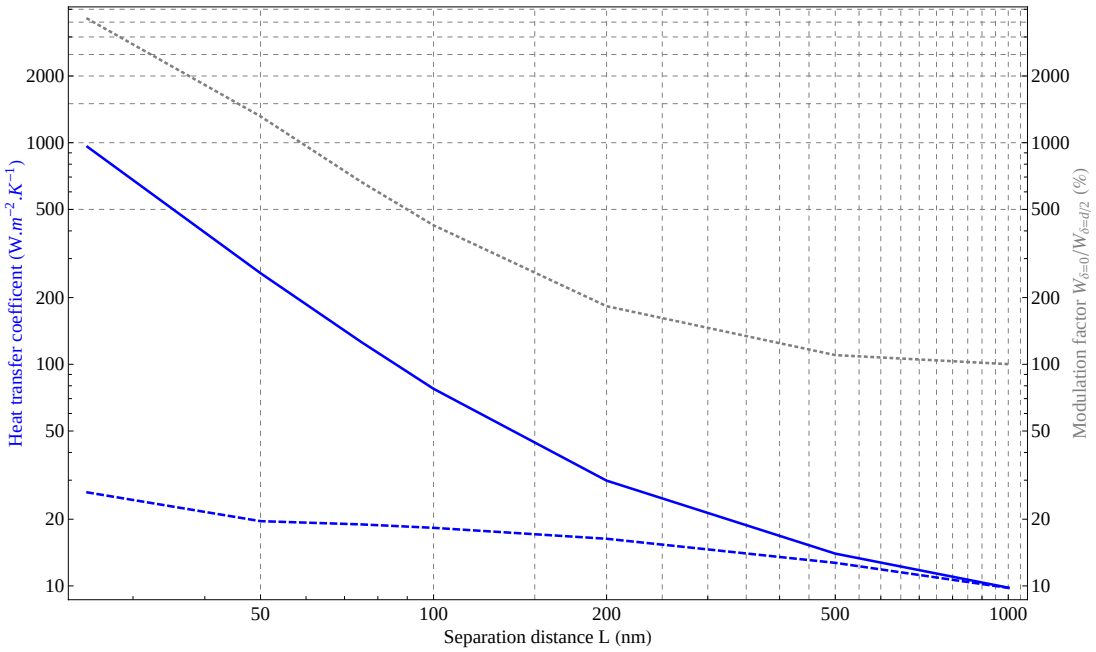

FIG. 119: Radiative heat transfer coefficient as a function of the separation distance L, for two gratings of silicon dioxide SiO_2 at temperatures $T_1 = 310$ K and $T_2 = 290$ K, for a lateral shift $\delta/d = 0\%$ (blue curve) and $\delta/d = 50\%$ (dashed blue curve). The results are plotted together with the percentage of modulation factor $W_{\delta/d=0\%}/W_{\delta/d=50\%}$ (dotted gray line). The gratings have a period $d = 1500$ nm, filling factor $p = 20\%$, and groove depth $a = 500$ nm. The permittivity of SiO_2 is extrapolated from optical data [111, 112].

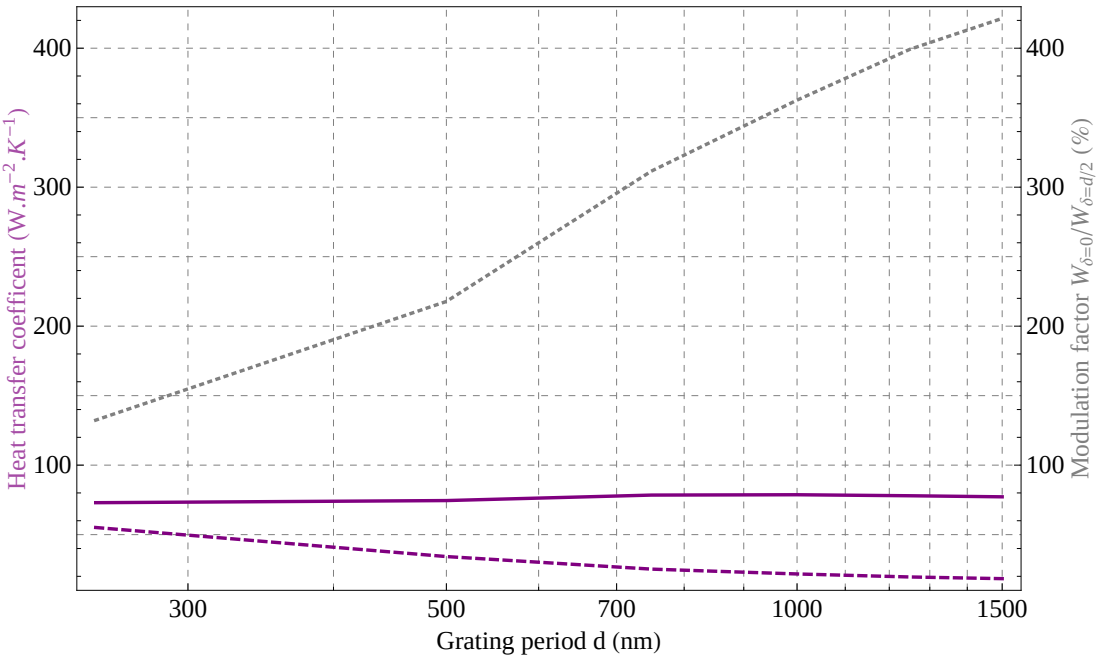

FIG. 120: Radiative heat transfer coefficient as a function of the grating period d, for two gratings of silicon dioxide SiO_2 at temperatures $T_1 = 310$ K and $T_2 = 290$ K, for a lateral shift $\delta/d = 0\%$ (purple curve) and $\delta/d = 50\%$ (dashed purple curve). The results are plotted together with the percentage of modulation factor $W_{\delta/d=0\%}/W_{\delta/d=50\%}$ (dotted gray line). The gratings are at a separation distance $L = 100$ nm, filling factor $p = 20\%$, and groove depth $a = 500$ nm. The permittivity of SiO_2 is extrapolated from optical data [111, 112].

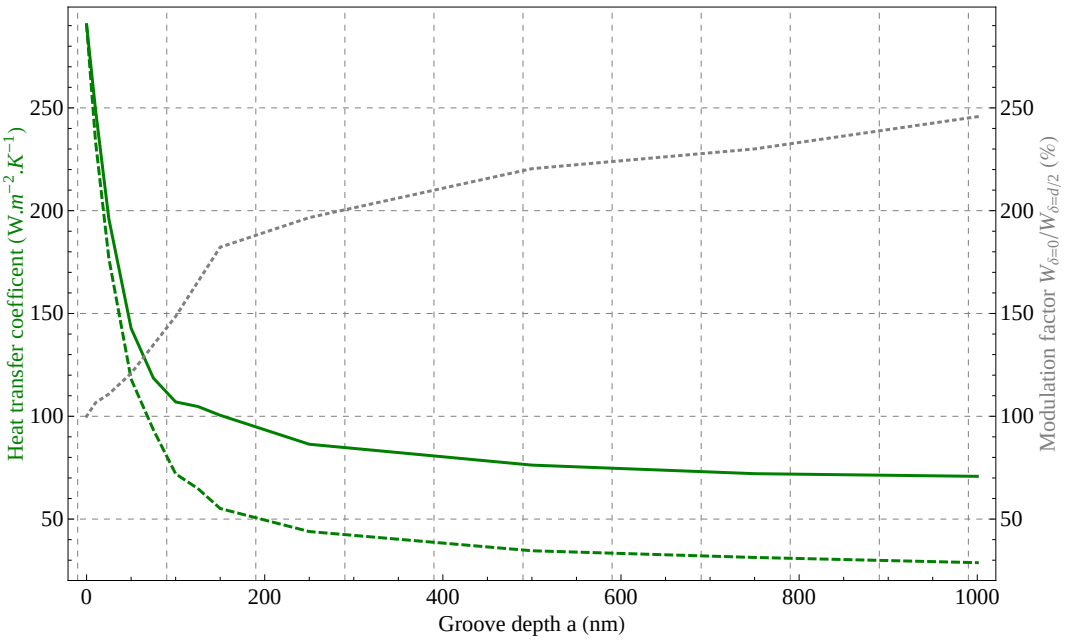

FIG. 121: Radiative heat transfer coefficient as a function of the grating groove depth a, for two gratings of silicon dioxide SiO_2 at temperatures $T_1 = 310$ K and $T_2 = 290$ K, for a lateral shift $\delta/d = 0\%$ (green curve) and $\delta/d = 50\%$ (dashed green curve). The results are plotted together with the percentage of modulation factor $W_{\delta/d=0\%}/W_{\delta/d=50\%}$ (dotted gray line). The gratings have a period $d = 500$ nm, filling factor $p = 20\%$, and separation distance $L = 100$ nm. The permittivity of SiO_2 is extrapolated from optical data [111, 112].

X. DISCUSSION OF THE RESULTS AND CONCLUSION

As discussed in the introduction, the Casimir energy and near-field radiative heat transfer are both theoretically and experimentally well known between planar surfaces. But the real world of nanoengineering rarely deals with such simples surfaces. In this thesis we have studied periodic nanogratings, which present a whole new level of complexity in the calculation of both the Casimir force and the heat flux due to their associated diffraction of the electromagnetic modes present in vacuum.

After briefly reviewing some main aspects of the quantum theory and thermodynamics in section V, we gave the ensuing derivation of the Casimir energy and heat flux between nanogratings through a scattering formalism in section VI. This was done for a Casimir force at thermal equilibrium in section VI B, and out-of-thermal equilibrium in section VI C.

Then we presented numerical calculations by computing the Casimir energy at zero temperature for all kinds of gratings in section VII, at non-zero temperatures for gratings in section VIII A, and out-of thermal equilibrium for gratings in section VIII B. We finished our study by calculating radiative heat transfer between gratings in section IX, and the narrowing of several geometric and permittivity parameters for the design of a potential thermal modulator for nanosystems. Let us now recall our most important results.

First concerning our results of sections VII-VIII on the Casimir effect :

- The variation of the Casimir energy with filling factor can be well approximated, regardless of the material, by a straight line joining the two extremities $p = 0\%$ and $p = 100\%$. This is a useful result because these two points are basically computed from the trivial plane-plane case at the respective separation distances L and $L + 2a$.
- The variations of the Casimir energy with the lateral shift are confined within an extremely narrow band, regardless of the considered material. The results can be very well interpolated by a sinusoid, which is again a useful result because one can well approximate the Casimir energy over different lateral shifts if only the values at $\delta = 0$ and $\delta = 50\%$ are known. The Proximity Approximation does not well describe at all the variations of energy with lateral shift.
- The magnitude of the lateral Casimir force is very small compared to the magnitudes of the normal Casimir force. The lateral Casimir force for dielectrics is smaller than for metals by up to a factor two.
- The Proximity Approximation is in general a precise approximation when compared to the Casimir energy as a function of separation distance for metallic gratings, but not for dielectrics.
- We then considered arbitrary periodic gratings. At a given distance, the Casimir energy for *sawtooth* gratings

with specific period and groove depth is about half of the Casimir energy for rectangular gratings with same period and groove depth.

- The Casimir energy of two *barbed wire* gratings with given period and groove depth is about three times larger than the Casimir energy of rectangular gratings that are included within them. However, the rectangular gratings that include *barbed wire* profiles have about the same Casimir energy as them.

- Rectangular and *sinusoidal* profiles share narrower Casimir energy values, and likewise for *sawtooth* and *circular* profiles. An important result is that in the case of these arbitrary gratings, the Proximity Approximation can be used in the neighborhood of $\delta = d/2$.

- We then studied the Casimir energy at thermal equilibrium for non-zero temperatures. Regardless of the chosen material, a non-zero temperature increases the value of the Casimir energy at long separation distances. But for gold below the range of approximatively three microns, the Casimir energy at zero temperature is larger than at 300 K.

- At a close separation distance, the gradual increase of temperature has but a small effect on the Casimir energy, both for planes and gratings and regardless of the material. Conversely, at large distances the contribution of non-zero temperatures to the Casimir energy is large.

- Concerning our results on the Casimir force out-of-thermal equilibrium, we conclude that both the non-equilibrium and equilibrium contributions to the total Casimir force for two planes at temperatures 290 K and 310 K follow a power law when plotted as a function of separation distance in $1/L^3$.

- When plotted as a function of corrugation groove depth for two gratings of silicon with same temperatures 290 K and 310 K, the non-equilibrium part does not decrease continuously with larger corrugation depths but reaches a minimum at $a = 300$ nm. As in the plane-plane case, the non-equilibrium contribution is smaller than the equilibrium part by almost three orders of magnitudes.

- We studied the interplay between temperature gradient, temperature average, and separation distance so as to both explore the domain where the non-equilibrium contribution is negative, and to see when its proportion to the total Casimir force becomes large enough to become interesting to experimental measurements and practical applications. We found that for certain values of these variables, there exists a separation distance beyond which the non-equilibrium part becomes negative, and it is possible to optimize those variables so that this separation distance is decreased. Since the equilibrium part decreases with distance as well, the proportion of the non-equilibrium part was found at three microns to reach almost a fourth of the equilibrium part. Since these are recent results, the physical explanation of these effects is not ye fully clear.

Let us now recall our main results of section VIII on radiative heat transfer :

- In the plane-plane case, the heat flux associated with the profiles of SiO_2 has a convex dependence on the separation distance, whereas the flux associated with metals display a concave shape on a logarithmic plot. As a result, the black body limit is reached much faster for metals with increasing distance than silicon dioxide. The heat flux associated with SiO_2 can be divided into three domains, each displaying a local power law with distance associated with the contributions of distinct physical phenomena.
- At long separation ranges the heat flux associated with gratings that are laterally shifted or not is approximatively the same, but in extreme near-field this difference can be very large. At a separation distance of 25 nm, we found it is thus possible to modulate the heat flux by simply shifting the gratings laterally with a modulation factor of more than 36.
- At a separation distance of 25 nm, we found that the error of the Proximity Approximation is of 3% for the non-shifted considered gratings, and of 35% when shifted.
- For silicon dioxide, the heat flux decreases with deeper corrugation grooves. This is in opposition to gratings of gold [73], where digging the grooves may unintendedly create waveguides so that the flux is enhanced by surface plasmons travelling into the trenches.
- There is a linear variation of the heat flux with increasing filling factor when the gratings are not laterally shifted. When the gratings are shifted by half-a-period, we find this linear variation appearing only beyond a filling factor of 40%.
- As for the Casimir energy, the heat flux as a function of lateral shift is well fitted by a sinusoid. However, the variations reached by the flux over this shift are important.
- Our study allows us to draw general rules of thermal modulation enhancement by a convenient choice of the grating geometrical parameters : smaller separation distance, larger grating periods, deeper corrugations grooves, and a filling factor kept at around a fifth of the period.

Throughout these numerical calculations, we have systematically compared exact results from scattering theory with Derjaguin's Proximity Approximation [131]. The reason for this is not to exagerate the importance of this approximation. Rather, it is used as a tool in the framework of scattering theory, which considers the sum of all the diffracted modes at the interface : the contribution of the lateral modes to the total force or flux can then be compared with the contribution of the normal modes through the Proximity Approximation results. Furthermore this approximation is used in measurement experiments and nanoengineering [171], where the exact computation of the force or flux faces an obvious challenge of time and complexity[1] that can be only met by a systematic study like the one presented here.

---

[1] It was not uncommon that the numerical computation of just one point of the plots of section VIII B on the out-of-thermal equilibrium force, or of section IX on the heat flux, would take several weeks on a workstation.

Based on all these results, we can say that the field of research in Casimir physics and especially near-field heat transfer has a strong potential. Future developments based on our work could lead to an in-depth study of the repulsive regime of the Casimir force through out-of-thermal equilibrium conditions. From an application perspective [172, 173], these could lead practically to a mechanical modulation of the Casimir force through temperature control of each plate.

Also from an application perspective, the heat flux for *arbitrary* periodic gratings such as those seen in section VII E for the Casimir energy, could also be evaluated. This could open the way to potentially greater factors of modulation through lateral displacement. The issue of new materials that are of interest to heat transfer enhancement should also be explored [68], as well as coatings [62, 168, 174] and metamaterials [166, 170].

Finally, the computations presented here are the first exact numerical calculations of the Casimir force out-of-thermal equilibrium between gratings, and of the heat flux between dielectric gratings. From an experimental point of view, our results are waiting for confirmation by precision measurements and should hence be a valuable information to experimentalists.

Appendix A : The Wave-Vector-Space Method Applied to Nonplanar Surfaces

We use the wave-vector-space method described in[175], and try to apply it to different nonplanar surfaces. In order to do this, we will seek to Fourier-transform the wave equation of the field so that it is written in wave-vector-space. We will do that for the case of a corrugated surface, and any surface bounded by an analytical function. We show that this method is not particularly adapted to these nonplanar surfaces.

I. The polynomial theorem

Our first concern here will be to clearly outline the conditions of validity of an important theorem which is used in the **k**-space method, which we shall call the *polynomial theorem* for further reference. We consider a one-dimensional approach here only, but this will be done in view of an ultimate application in a two-dimensional environnement. Generalization of this framework to a function of the vector variable **k** should be trivial.

- First let's consider an analytical function $f(k)$ where k is a component of the vector **k**, such as k_x, k_y, or k_z.
- By Liouville's theorem we know that $f(k)$ must either be constant, or have poles. Disregarding the case where it is constant, let's write it as the sum of two parts $f(k) = f^{(+)}(k) + f^{(-)}(k)$, such that $f^{(+)}(k)$ (resp. $f^{-)}(k)$) is the part of $f(k)$ with all the poles in the upper half (resp. lower half) complex k-plane.
- The poles must not be lying on the real axis. Assume we have M (resp. N) poles in the upper half (resp. lower half) complex k-plane, and with the u-th (resp. l-th) pole at k_u (resp. k_l) and of order n_u (resp. n_l). Then if we define $p_u(k)$ (resp. $p_l(k)$) a given polynomial in k, we can express $f^{(+)}(k)$ and $f^{-)}(k)$ as :

$$f^{(+)}(k) = \sum_{u=1}^{M} \frac{p_u(k)}{(k-k_u)^{n_u}}$$

$$f^{(-)}(k) = \sum_{l=1}^{N} \frac{p_l(k)}{(k-k_l)^{n_l}}$$

- Now since for infinite k, $f(k)$ tends to 0 at least as fast as $1/k$, we can deduce that the degree of the polynomial $p_u(k)$ (resp. $p_l(k)$) must be below $n_u - 1$ (resp. $n_l - 1$).
- Now under these conditions we can express the polynomial theorem, for an infinitesimal positive quantity η :

$$\frac{1}{2\pi i} \int_{-\infty}^{+\infty} \frac{f(k')dk'}{k - k' - i\eta} = f^{(+)}(k)$$

Proof : Let's prove this equation above by considering the series expressing $f^{(+)}(k)$:

$$\frac{1}{2\pi i}\int_{-\infty}^{+\infty}\frac{1}{k-k'-i\eta}\sum_{u=1}^{M}\frac{p_u(k')}{(k'-k_u)^{n_u}}dk'$$

Now all poles $k'=k_u$ are in the upper half-plane, and the other pole of the integrand is in the lower half-plane, at $k'=k-i\eta$.

This can be simplified by a contour integration over the perimeter of a semi-circle with the real axis forming the straight side, and the semicircular arc extending into the lower half-plane.

Now the real integral is equal to the residue at pole $k'=k-i\eta$, because the contribution along the semi-circular arc vanishes as its radius becomes infinite (for the integrand approaches zero at least as fast as $1/k^2$ when $k\to\infty$).

So we have, for $\eta\to 0$:

$$\frac{1}{2\pi i}\int_{-\infty}^{+\infty}\frac{f^{(+)}(k')dk'}{k-k'-i\eta}=\sum_{u=1}^{M}\frac{p_u(k-i\eta)}{(k-k_u-i\eta)^{n_u}}=f^{(+)}(k)$$

.

As for $f^{(-)}(k)$, the method follows a similar philosophy of contour integration, so that the real integral vanishes :

$$\frac{1}{2\pi i}\int_{-\infty}^{+\infty}\frac{f^{(-)}(k')dk'}{k-k'-i\eta}=0$$

Then this equation together with the previous one proves our theorem.

II. The k-space method step by step

The wave-vector-space method works without boundary conditions, and thus differs from the real-space method. In a nutshell, it works by Fourier-transforming the wave equation of the electric field, simplifying it in **k**-space so that the poles of the field are determined and the electric field can be written as a function of the r and t amplitudes of the S-matrix ; then in selected and specific conditions, these may be derived by re-inserting the electric field expressions into the wave equation.

Following the example of the article, let's proceed further and detail the step by step procedure :

1. Wisely choose a step function that will separate the vacuum $\theta(z)=0$ from the medium $\theta(z)=1$ (see [175] equation 4). The boundary of z defines the geometry of the medium's surface. Here we set it as equal to 0 because we consider a planar surface, but as we will see, we could have defined it as any analytical function of $z=\gamma(x)$:

$$\theta(z) = \begin{cases} 1 & \text{if } z > 0 \\ 0 & \text{if } z < 0 \end{cases}$$

2. Fourier-transform it along with the whole wave equation describing the electric field in real-space (see [175] equation 2), so as to have it expressed in wave-vector-space (see [175] equation 8) :

$$\nabla \times [\nabla \times \mathbf{E}(\mathbf{x},\omega)] - \frac{\omega^2}{c^2}[1 + \theta(z)\chi(\omega)]\mathbf{E}(\mathbf{x},\omega) = 0$$

$$\downarrow$$

$$\int \{\mathbf{k} \times [\mathbf{k} \times \mathbf{E}(\mathbf{k})] + \frac{\omega^2}{c^2}\mathbf{E}(\mathbf{k})\} e^{i\mathbf{k}.\mathbf{x}} \mathbf{dk}$$

$$+\frac{\omega^2}{c^2}\chi \iint \frac{\delta(k'_x)\delta(k'_y)}{2\pi i(k'_z - i\eta)} \mathbf{E}(\mathbf{k}'') e^{i(\mathbf{k}'+\mathbf{k}'').\mathbf{x}} \mathbf{dk}'\mathbf{dk}'' = 0$$

3. Write the electric field as a sum of two parts : one corresponding to the field in the medium $\mathbf{E}^{(+)}(\mathbf{k})$ with poles in the upper-half of the complex $\mathbf{k}$-plane, and the other corresponding to the field in the vacuum $\mathbf{E}^{(-)}(\mathbf{k})$ with poles in the lower-half of the complex $\mathbf{k}$-plane. And through the use of the polynomial theorem (see [175] equation 11) :

$$\frac{1}{2\pi i} \int \frac{\mathbf{E}(k_x, k_y, k'_z)}{k_z - k'_z - i\eta} dk'_z = \mathbf{E}^{(+)}(\mathbf{k})$$

simplify the wave equation above in $\mathbf{k}$-space (see [175] equation 13) :

$$\mathbf{k}.\mathbf{E}^{(-)}(\mathbf{k}) + \kappa \mathbf{k}.\mathbf{E}^{(+)}(\mathbf{k}) = 0$$

4. Determine the poles of $\mathbf{E}^{(+)}(\mathbf{k})$ and $\mathbf{E}^{(-)}(\mathbf{k})$ through that simplified wave equation (see [175] equation 15,17).

$$\begin{cases} k_V \equiv [k_0^2 - k_x^2 - k_y^2]^{\frac{1}{2}} \\ k_M \equiv [\kappa k_0^2 - k_x^2 - k_y^2]^{\frac{1}{2}} \end{cases} \tag{417}$$

5. Write the electric fields $\mathbf{E}^{(+)}(\mathbf{k})$ and $\mathbf{E}^{(-)}(\mathbf{k})$ in terms of these poles, and in terms of yet undetermined functions : $\mathbf{t}^{(-)}(k_x, k_y)$, $\mathbf{r}^{(-)}(k_x, k_y)$, $\mathbf{t}^{(+)}(k_x, k_y)$, and $\mathbf{r}^{(+)}(k_x, k_y)$ which we will later associate with the transmission and reflection amplitudes of the electric fields, both for the medium and the vacuum (see [175] equation 18).

$$\begin{cases} \mathbf{E}^{(+)}(\mathbf{k}) = \frac{1}{2\pi i}[\frac{\mathbf{t}^{(+)}(k_x,k_y)}{k_z - k_M - i\eta} + \frac{\mathbf{r}^{(+)}(k_x,k_y)}{k_z + k_M - i\eta}] \\ \mathbf{E}^{(-)}(\mathbf{k}) = \frac{1}{2\pi i}[-\frac{\mathbf{t}^{(-)}(k_x,k_y)}{k_z - k_V + i\eta} - \frac{\mathbf{r}^{(-)}(k_x,k_y)}{k_z + k_V + i\eta}] \end{cases} \tag{418}$$

6. Choose certain oblique incidences so as to specify these amplitudes (see [175] equation 19), and then recast them into the expressions of the electric fields found in the previous step.

$$\begin{cases} \mathbf{t}^{(-)}(k_x,k_y) = E_0\mathbf{e_1}\delta(k_x - k_0 sin\theta_i)\delta(k_y) \\ \mathbf{r}^{(-)}(k_x,k_y) = E_0 r\mathbf{e_2}\delta(k_x - k_0 sin\theta_r)\delta(k_y) \\ \mathbf{t}^{(+)}(k_x,k_y) = E_0 t\mathbf{e_3}\delta(k_x - k_0 n sin\theta_\phi)\delta(k_y) \\ \mathbf{r}^{(+)}(k_x,k_y) = 0 \end{cases} \tag{419}$$

7. Now replace these electric fields in the simplified wave equation from step 4 so as to now clearly specify their poles (see [175] equation 23,24) :

$$\begin{cases} k_V = k_0 cos\theta \\ k_M = k_0 n cos\phi \end{cases} \tag{420}$$

8. Substitute these poles in that obtained equation (see [175] equation 25).

$$-[(k_0^2 - k^2)\mathbf{e_1} + \mathbf{k}(\mathbf{k}.\mathbf{e_1})]\frac{1}{k_z - k_0 cos\theta}$$

$$-[(k_0^2 - k^2)\mathbf{e_2} + \mathbf{k}(\mathbf{k}.\mathbf{e_2})]\frac{r}{k_z + k_0 cos\theta}$$

$$+[(\kappa k_0^2 - k^2)\mathbf{e_3} + \mathbf{k}(\mathbf{k}.\mathbf{e_3})]\frac{t}{k_z - k_0 n cos\phi} = 0$$

9. Finally choose a given s- or p-polarization (resp. TE or TM) in order to simplify the expressions of the unit vectors $\mathbf{e_1}$, $\mathbf{e_2}$, and $\mathbf{e_3}$, and solve the equation, finding the corresponding amplitudes, and thus the S-matrix.

III. Application to different surfaces

We will now try to apply this wave-vector-space method, but now for different types of surfaces. As explained earlier, the shape of the mirror's surface appears as the boundary of z in the step-function θ. We will thus use a

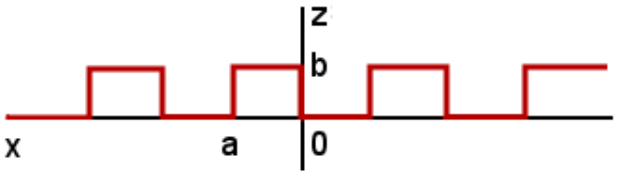

FIG. 122: Two-dimensional illustration of corrugated gratings.

step-function separating vacuum and medium, with a geometry corresponding to a corrugated surface and then to any surface represented by an analytical $z = \gamma(x)$ function in the x-z plane.

III.1 Corrugated surfaces

Let's define a two-dimensional step function $\theta(x, z)$ describing a corrugated surface, $\forall n \in Z$ defining the step of the corrugation :

$$\theta(x,z) = \begin{cases} 1 & \text{if } (z > b \text{ and } 2na < x < [2n+1]a) \text{ or } (z > 0 \text{ and } [2n+1]a < x < [2n+2]a) \\ 0 & \text{if } (z < b \text{ and } 2na < x < [2n+1]a) \text{ or } (z < 0 \text{ and } [2n+1]a < x < [2n+2]a) \end{cases}$$

Now this can be written $\forall n \in Z$ as :

$$\theta(x,z) = \theta_1(z)\theta_1(x) + \theta_2(z)\theta_2(x)$$

by defining the following smaller step functions :

$$\theta_1(z) = \begin{cases} 1 & \text{if } z > b \\ 0 & \text{if } z < b \end{cases}$$

$$\theta_2(z) = \begin{cases} 1 & \text{if } z > 0 \\ 0 & \text{if } z < 0 \end{cases}$$

$$\theta_1(x) = \begin{cases} 1 & \text{if } 2na < x < (2n+1)a \\ 0 & \text{if } (2n+1)a < x < (2n+2)a \end{cases}$$

$$\theta_2(x) = \begin{cases} 1 & \text{if } (2n+1)a < x < (2n+2)a \\ 0 & \text{if } 2na < x < (2n+1)a \end{cases}$$

Now we can work out the Fourier transform of this product of simpler step-functions according to (see [175] equation 5) :

$$\theta(\mathbf{k}) = \theta(k_x, k_y, k_z) = \frac{1}{(2\pi)^3} \iiint [\theta_1(z)\theta_1(x) + \theta_2(z)\theta_2(x)] e^{-i(k_x x + k_y y + k_z z)} dxdydz$$

The term in y is Fourier-transformed as $2\pi\delta(k_y)$, and so we are left with a sum of two double-integrals on x and z :

$$\theta(\mathbf{k}) = \frac{\delta(k_y)}{(2\pi)^2} \iint \theta_1(z)\theta_1(x) e^{-ik_x x} e^{-ik_z z} dxdz + \frac{\delta(k_y)}{(2\pi)^2} \iint \theta_2(z)\theta_2(x) e^{-ik_x x} e^{-ik_z z} dxdz$$

Now already at this early stage we can see that we will face difficulties in the application of the polynomial theorem for this Fourier transform. Even if we fortunately came to a most simple form, such as :

$$\Im\{\theta(x,z)\} = \theta(\mathbf{k}) = \Im\{\theta_1(z)\}\Im\{\theta_1(x)\} + \Im\{\theta_2(z)\}\Im\{\theta_2(x)\}$$

we would already see that the requirement of step 3 in the **k**-space method will not be met. This requirement stressed that the polynomial theorem as applied to the step function in **k**-space allows one to write it as $\mathbf{E}^{(+)}$, hence greatly simplifying the wave equation. And since this is crucial to find the poles of these electric fields, which themselves are to specify the r and t amplitudes later on, it seems we are confined to step 3 at least for now. Hence in our case, even in the most optimistic scenario of a total Fourier transform $\theta(\mathbf{k_x}, \mathbf{k_z})$ becoming a sum of products of individual Fourier-transformed simpler step functions as, we couldn't hope to recover the theorem in any trivial way.

Sidenote : We can already intuitively sense from this case of a corrugated surface, that both x- and z-components will be appearing in the electric field wave equation, and hence deduce that the field coming from the vacuum and interfering with the medium at a certain angle will likely be dispersed and not simply reflected.

III.2 Surfaces bounded by an analytical function $z = \gamma(x)$

Now let's assume any given analytical function $z = \gamma(x)$ describing the surface geometry of our mirror. For reasons that will become clear later on, let's also assume it is vanishing outside of the interval $-l < x < l$. Since we saw in our previous section that the case of a corrugated surface doesn't allow one to use the wave-vector-space method in any trivial way beyond step 3, our methodology here will be to go as far as possible in the derivation of $z = \gamma(x)$, and then to see which of its analytical properties may simplify its Fourier-transform to the point where one could use the polynomial theorem successfully. More specifically, one should keep in mind that the reason that the polynomial

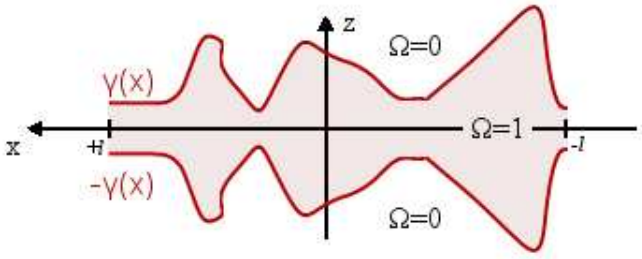

FIG. 123: Arbitrary gratings parametrized by an analytical function $z = \gamma(x)$.

theorem is used is that it allows one to conveniently write the electric field into two parts, $\mathbf{E}^{(+)}(\mathbf{k})$ and $\mathbf{E}^{(-)}(\mathbf{k})$, and hence simplify the wave equation in $\mathbf{k}$-space to the point where it is easily solvable.

Let's define the following step function :

$$\Omega(x, y = 0, z) = \Omega(x, z) = \begin{cases} 1 & \text{if } \mid z \mid < \gamma(x) \\ 0 & \text{if } \mid z \mid > \gamma(x) \end{cases}$$

To switch from real-space to wave-vector-space, let's find its Fourier transform $\Im\{\Omega(x, y = 0, z)\} = \Im\{\Omega(x, z)\} = \Omega(k_x, k_y, k_z) = \Omega(\mathbf{k})$:

$$\begin{aligned}
\Omega(\mathbf{k}) &= \tfrac{1}{(2\pi)^3} \iiint \Omega(x, z) e^{-i(k_x x + k_y .0 + k_z z)} dz dy dx \\
&= \tfrac{1}{(2\pi)^3} \iint [\int_{-\gamma(x)}^{+\gamma(x)} 1.e^{-ik_x x} e^{-ik_z z} dz \\
&\quad + \int_{-\infty}^{-\gamma(x)} 0.e^{-ik_x x} e^{-ik_z z} dz \\
&\quad + \int_{+\gamma(x)}^{+\infty} 0.e^{-ik_x x} e^{-ik_z z} dz] dy dx \\
&= \tfrac{1}{(2\pi)^3} \int [\int [\tfrac{e^{-i(k_x x + k_z z)}}{-ik_z}]_{-\gamma(x)}^{+\gamma(x)} dy] dx \\
&= \tfrac{\delta(k_y)}{4\pi^2 ik_z} \int_{-l}^{+l} [e^{-ik_x x + ik_z \gamma(x)} - e^{-ik_x x - ik_z \gamma(x)}] dx \\
&= \tfrac{\delta(k_y)}{4\pi^2 ik_z} \{ [\tfrac{e^{-ik_x x - ik_z \gamma(x)}}{ik_x + ik_z \gamma'(x)}]_{-l}^{+l} + [\tfrac{e^{-ik_x x + ik_z \gamma(x)}}{-ik_x + ik_z \gamma'(x)}]_{-l}^{+l} \}
\end{aligned}$$

Where, following the article, we Fourier-transformed the term in y as $2\pi\delta(k_y)$. Now, we can expand this expression, but the result is so complex that it is nowhere near useful for the rest of our calculus in $\mathbf{k}$-space. Nevertheless we can operate some cuts on $\gamma(x)$ and narrow its analytical properties in such a way that the expression of $\Omega(\mathbf{k})$ becomes much simpler, allowing us hopefully to go on with the wave-vector-space method. So let's choose $\gamma(x)$ in such a way

that :

$$\begin{cases} \gamma(l) = \gamma(-l) \\ \gamma'(l) = \gamma'(-l) = 0 \end{cases} \tag{421}$$

Eventually, we come to the much simpler form :

$$\Omega(\mathbf{k}) = \frac{\delta(k_y)}{\pi^2 k_x k_z} \sin[k_x l] \sin[k_z \gamma(l)]$$

This is an interesting result in view of the later task of finding the poles, since the sine functions are always comprised between -1 and $+1$.
We must now replace this result into the electric field wave equation, and make the inverse Fourier-transform of it :

$$\int \{\mathbf{k} \times [\mathbf{k} \times \mathbf{E}(\mathbf{k})] + \frac{\omega^2}{c^2} \mathbf{E}(\mathbf{k})\} e^{i\mathbf{k}.\mathbf{x}} d\mathbf{k} + \frac{\omega^2}{c^2} \chi . \Im\{\Omega(x,z).\mathbf{E}(\mathbf{x},\omega)\} = 0$$

Notice the *nabla* operators from real-space have become wave-vectors $\mathbf{k}$, and that we used again $\chi(\omega)$ as the susceptibility. Then all we need, in order to simplify this equation is to find $\Im\{\Omega(x,z).\mathbf{E}(\mathbf{x},\omega)\}$:

$$\begin{aligned} \Im\{\Omega(x,z).\mathbf{E}(\mathbf{x},\omega)\} &= \int_{\{\mathbf{k}'\}} \int_{\{\mathbf{k}''\}} \Omega(\mathbf{k}') \mathbf{E}(\mathbf{k}'') e^{i(\mathbf{k}'\mathbf{x} + \mathbf{k}''\mathbf{x})} d\mathbf{k}' d\mathbf{k}'' \\ &= \frac{1}{\pi^2} \int_{\{\mathbf{k}'\}} \int_{\{\mathbf{k}''\}} \frac{\sin[k'_x l]}{k'_x} \delta(k'_y) \frac{\sin[k'_z \gamma(l)]}{k'_z} \\ &\quad \cdot e^{i(k'_x x + k'_y y + k'_z z)} e^{i(k''_x x + k''_y y + k''_z z)} \mathbf{E}(k''_x, k''_y, k''_z) d\mathbf{k}' d\mathbf{k}'' \end{aligned}$$

Where in the second equation we expanded $\mathbf{k}'$ and $\mathbf{k}''$ in the integrand over their components (k'_x, k'_y, k'_z) and (k''_x, k''_y, k''_z) respectively. Following [equ.9], we should now substitute $\mathbf{k} = \mathbf{k}' + \mathbf{k}''$ and carry the k'_y integration. The result should manifest a two-dimensional version of the polynomial theorem, which would simplify to a trivial function of $\mathbf{E}^{(+)}(\mathbf{k})$.

IV. Discussion

At this stage, we need to find a proper derivation of the polynomial theorem for our two-dimensional case, so that the $\mathbf{k}$-space version of the wave equation may simplify (in view of finding the poles of the electric field). The article implies that the generalization of its proof to any function $f(\mathbf{k})$ is straightforward. But the result we found

for $\Im\{\Omega(x,z)\mathbf{E}(\mathbf{x},\omega)\}$ suggests that, at least for the cases of corrugated surfaces or for analytical functions $\gamma(x)$ such as we specified them, this will not be an easy task. And much less, when we will consider a Fabry-Pérot cavity later on.

However, we can already forsee the main analytical properties that an analytical function describing the surface of a mirror will have to bear, so as to simplify $\Im\{\Omega(x,z)\}$ and hence be usable. Among these properties, we may say that :

- Any trigonometrical function, even written in exponential form, does not simplify $\Omega(\mathbf{k})$ particularly. This is due to the fact that we Fourier-transform a step function, not $\gamma(x)$: our $\gamma(x)$ function only appears in the exponent of the exponential term, since it is the boundary of the medium and hence of the step-function when integrated. Now we are not interested in having an exponential of an exponential.

- The interest of working in Fourier-space is that it is in general well-suited to the study of periodic signals. Nevertheless, since we are Fourier-transforming a step-function and not a function describing the (periodic) shape of our mirror, the property of periodicity is not of particular advantage to us.

- We could try to define $\gamma(x)$ in such a way that it cancels this exponential term. However this is not an easy task, because for example even if we could find nano-objects whose surface is described satisfactorily by logarithmic functions ($\gamma(x) = \ln x$), the logarithm term in the exponent wouldn't simplify the exponential, since we are not dealing with $e^{\ln x}$ but with $e^{-ik_z \ln x}$.

- Last but not least, we used a medium that is bounded by **two** functions $+\gamma(x)$ and $-\gamma(x)$. So we are not in the case of a medium whose surface's shape is described by an analytical function, and that has the rest of its frame spreading towards infinity. Also, we took our mirror surface to be delimited by $x = \pm l$. And finally, remember we required that $\gamma(l) = \gamma(-l)$ and $\gamma'(l) = \gamma'(-l) = 0$. A simple way to sum up all these conditions is to visualize a nano-mirror whose shape in the x-z plane is that of a vase, with its center being the origin, and its extremities consisting of two discs of arbitrary thickness. Notice that if we had described a trigonometrical or corrugated surface with an analytical function, we could have used our result here for $\Omega(\mathbf{k})$. Also, it still has to be shown whether or not all these analytical requirements make $\gamma(x)$ to describe potentially interesting nano-surfaces.

CONFERENCES AND SEMINARS ATTENDED

- "Ecole de Physique des Houches - Casimir, van der Waals and nanoscale interactions", Les Houches, France, on 11-16 April 2010.

- "Journées de prospective du Laboratoire Kastler Brossel" in Paris, France on 6 and 7 June 2011.

- "Eurotherm seminar 91 - Microscale heat transfer III", Poitiers, France, on August 29-31, 2011.

- "QFEXT Proceedings - Quantum field theory under the influence of external conditions" Benasque, Spain, on 18 - 24 September 2011.

- "Journée inaugurale du club Nanométrologie et d'essais" Paris, France on 6 October 2011.

- "Casimir Physics Workshop 2012" Lorentz Center, Leiden, Netherlands, on 11-16 March 2012

- "Wilhelm und Else Heraeus-Seminar - Highlights of Quantum Optics", Physikzentrum Bad Honnef, Germany on 6 - 11 May 2012.

- "13e Journées de la Matière Condensée" Montpellier, France on 27 - 31 August 2012.

[1] H. Casimir, Proc. Kon. Ned. Akad. We. **51**, 793 (1948).
[2] G. Bressi, G. Carugno, R. Onofrio, and G. Ruoso, Phys. Rev. Lett. **88**, 041804 (2002).
[3] W. R. Tinga, W. A. G. Voss, and D. F. Blossey, Phys. Rev. Lett. **81**, 4549 (1998).
[4] S. K. Lamoreaux, Phys. Rev. Lett. **78**, 5 (1997).
[5] S. K. Lamoreaux, Phys. Rev. Lett. **81**, 5475 (1998).
[6] L. S. Brown and G. J. Maclay, Phys. Rev. **184**, 1272 (1969).
[7] B. W. Harris, F. Chen, and U. Mohideen, Phys. Rev. A **62**, 052109 (2000).
[8] R. S. Decca, D. Lopez, E. Fischbach, and D. E. Krause, Phys. Rev. Lett. **91**, 050402 (2003).
[9] T. Ederth, Phys. Rev. A **62**, 062104 (2000).
[10] R. S. Decca, E. Fischbach, G. L. Klimchitskaya, D. E. Krause, D. Lopez, and V. M. Mostepanenko, Phys. Rev. D **68**, 116003 (2003).
[11] R. S. Decca, D. Lopez, E. Fischbach, G. L. Klimchitskaya, D. E. Krause, and V. M. Mostepanenko, Phys. Rev. D **75**, 077101 (2007).
[12] H. B. Chan, Y. Bao, J. Zou, R. A. Cirelli, F. Klemens, W. M. Mansfield, and C. S. Pai, Phys. Rev. Lett. **101**, 030401 (2008).
[13] D. Garcia-Sanchez, K. Y. Fong, H. Bhaskaran, S. Lamoreaux, and H. X. Tang, Phys. Rev. Lett. **109**, 027202 (2012).
[14] A. Lambrecht, C. Genet, F. Intravaia, and S. Reynaud, J. Phys. IV France **119**, 43 (2004).
[15] Genet, C., Lambrecht, A., and Reynaud, S., Eur. Phys. J. Special Topics **160**, 183 (2008).
[16] A. Lambrecht and S. Reynaud, Phys. Rev. Lett. **84**, 5672 (2000).
[17] A. Canaguier-Durand, G.-L. Ingold, M.-T. Jaekel, A. Lambrecht, P. A. M. Neto, and S. Reynaud, Phys. Rev. A **85**, 052501 (2012).
[18] A. Canaguier-Durand, A. Gérardin, R. Guérout, P. A. M. Neto, V. V. Nesvizhevsky, A. Y. Voronin, A. Lambrecht, and S. Reynaud, Phys. Rev. A **83**, 032508 (2011).
[19] L. Rosa and A. Lambrecht, Phys. Rev. D **82**, 065025 (2010).
[20] A. Canaguier-Durand, P. A. M. Neto, A. Lambrecht, and S. Reynaud, Phys. Rev. A **82**, 012511 (2010).
[21] A. Canaguier-Durand, P. A. M. Neto, A. Lambrecht, and S. Reynaud, Phys. Rev. Lett. **104**, 040403 (2010).
[22] I. Pirozhenko and A. Lambrecht, Phys. Rev. A **80**, 042510 (2009).
[23] A. Lambrecht and I. G. Pirozhenko, Phys. Rev. A **78**, 062102 (2008).
[24] I. Pirozhenko and A. Lambrecht, Phys. Rev. A **77**, 013811 (2008).
[25] P. A. M. Neto, A. Lambrecht, and S. Reynaud, Phys. Rev. A **72**, 012115 (2005).
[26] A. Lambrecht and S. Reynaud, Eur. Phys. J. D. **8**, 309 (2000).
[27] A. Lambrecht, I. Pirozhenko, L. Duraffourg, and P. Andreucci, Eur. Phys. Lett. **77**, 44006 (2007).
[28] A. Lambrecht and V. Marachevsky, Phys. Rev Lett. **101**, 160403 (2008).
[29] C. Genet, A. Lambrecht, and S. Reynaud, Phys. Rev. A **67**, 043811 (2003).
[30] T. Emig, A. Hanke, R. Golestanian, and M. Kardar, Phys. Rev. Lett. **87**, 260402 (2001).
[31] T. Emig, N. Graham, R. Jaffe, and M. Kardar, Phys. Rev. Lett. **99**, 170403 (2007).
[32] T. Emig, A. Hanke, R. Golestanian, and M. Kardar, Phys. Rev. A **67**, 022114 (2003).
[33] J. S. H. I. Brevik, J. B. Aarseth and K. A. Milton, Phys. Rev. E **71**, 056101 (2005).
[34] L. H. Ford, Phys. Rev. D **38**, 528 (1988).
[35] R. L. Jaffe, Phys. Rev. D **72**, 021301 (2005).
[36] A. Rodriguez, M. Ibanescu, D. Iannuzzi, F. Capasso, J. D. Joannopoulos, and S. G. Johnson, Phys. Rev. Lett. **99**, 080401 (2007).
[37] H. Gies and K. Klingmüller, Phys. Rev. Lett. **96**, 220401 (2006).
[38] M. P. Hertzberg, R. L. Jaffe, M. Kardar, and A. Scardicchio, Phys. Rev. Lett. **95**, 250402 (2005).
[39] R. Büscher and T. Emig, Phys. Rev. Lett. **94**, 133901 (2005).
[40] T. Emig, Europhys. Lett. **62**, 466 (2003).
[41] P. W. Milonni, R. J. Cook, and M. E. Goggin, Phys. Rev. A **38**, 1621 (1988).
[42] M. Kardar and R. Golestanian, Rev. Mod. Phys. **71**, 1233 (1999).
[43] O. Kenneth, I. Klich, A. Mann, and M. Revzen, Phys. Rev. Lett. **89**, 033001 (2002).
[44] P. J. van Zwol and G. Palasantzas, Phys. Rev. A **81**, 062502 (2010).
[45] A. G. Grushin and A. Cortijo, Phys. Rev. Lett. **106**, 020403 (2011).
[46] M. Levin, A. P. McCauley, A. W. Rodriguez, M. T. H. Reid, and S. G. Johnson, Phys. Rev. Lett. **105**, 090403 (2010).
[47] V. Yannopapas and N. V. Vitanov, Phys. Rev. Lett. **103**, 120401 (2009).
[48] R. Zhao, J. Zhou, T. Koschny, E. N. Economou, and C. M. Soukoulis, Phys. Rev. Lett. **103**, 103602 (2009).
[49] F. M. Schmidt and H. W. Diehl, Phys. Rev. Lett. **101**, 100601 (2008).
[50] C. Henkel and K. Joulain, Europhys. Lett. **72**, 929 (2005).
[51] C.-G. Shao, D.-L. Zheng, and J. Luo, Phys. Rev. A **74**, 012103 (2006).
[52] J. N. Munday and F. Capasso, Phys. Rev. A **75**, 060102 (2007).

[53] A. Gambassi, A. Maciolek, C. Hertlein, U. Nellen, L. Helden, C. Bechinger, and S. Dietrich, Phys. Rev. E **80**, 061143 (2009).
[54] A. Ashourvan, M. Miri, and R. Golestanian, Phys. Rev. Lett. **98**, 140801 (2007).
[55] A. Ashourvan, M. Miri, and R. Golestanian, Phys. Rev. E **75**, 040103 (2007).
[56] H. B. Chan, V. A. Aksyuk, R. N. Kleiman, D. J. Bishop, , and F. Capasso, Phys. Rev. Lett. **87**, 211801 (2001).
[57] D. Zhabinskaya and E. J. Mele, Phys. Rev. B **80**, 155405 (2009).
[58] T. Emig, Phys. Rev. Lett. **98**, 160801 (2007).
[59] E. Buks and M. L. Roukes, Phys. Rev. B **63**, 033402 (2001).
[60] M. Krüger, T. Emig, and M. Kardar, Phys. Rev. Lett. **106**, 210404 (2011).
[61] G. Bimonte, Phys. Rev. A **80**, 042102 (2009).
[62] V. B. Svetovoy, P. J. van Zwol, and J. Chevrier, arXiv:1201.1824v1 (2012).
[63] K. Joulain, J.-P. Mulet, F. Marquier, R. Carminati, and J.-J. Greffet, *Surface Science Reports*, vol. 57 (Elsevier, Issue 3-4, 2005).
[64] S.-A. Biehs, F. S. S. Rosa, and P. Ben-Abdallah, Appl. Phys. Lett. **98**, 243102 (2011).
[65] A. V. Shchegrov, K. Joulain, R. Carminati, and J.-J. Greffet, Phys. Rev. Lett. **85**, 1548 (2000).
[66] P. Ben-Abdallah, K. Joulain, and A. Pryamikov, Appl. Phys. Lett. **96**, 143117 (2010).
[67] K. Joulain, P. Ben-Abdallah, and J. Drevillon, Phys. Rev. B **81**, 165119 (2010).
[68] P. J. van Zwol, K. Joulain, P. Ben-Abdallah, and J. Chevrier, Phys. Rev. B **84**, 161413(R) (2011).
[69] M. Laroche, R. Carminati, and J. Greffet, J. of Quant. Spec. and Rad. Trans. **100**, 063704 (2006).
[70] P. J. van Zwol, K. Joulain, P. B. Abdallah, J. J. Greffet, and J. Chevrier, Phys. Rev. B **83**, 201404(R) (2011).
[71] M. Antezza, L. Pitaevskii, S. Stringari, and V. Svetovoy, Phys. Rev. A **77**, 022901 (2008).
[72] A. Narayanaswamy and G. Chen, Phys. Rev. B **77**, 075125 (2008).
[73] R. Guérout, J. Lussange, F. Rosa, J.-P. Hugonin, D. Dalvit, J.-J. Greffet, A. Lambrecht, and S. Reynaud, Phys. Rev. B **85**, 180301(R) (2012).
[74] S.-A. Biehs and J.-J. Greffet, Phys. Rev. B **82**, 245410 (2010).
[75] O. Huth, F. Rüting, S.-A. Biehs, and M. Holthaus, Eur. Phys. J. Appl. Phys. **50**, 10603 (2010).
[76] E. Rousseau, M. Laroche, and J.-J. Greffet, J. of Quant. Spec. and Rad. Transf. **111**, 1005 (2010).
[77] G. Domingues, S. Volz, K. Joulain, and J.-J. Greffet, Phys. Rev. Lett. **94**, 085901 (2005).
[78] Y. Sherkunov, Phys. Rev. A **79**, 032101 (2009).
[79] P.-O. Chapuis, M. Laroche, S. Volz, and J.-J. Greffet, Phys. Rev. B **77**, 125402 (2008).
[80] J.-P. Mulet, K. Joulain, R. Carminati, and J.-J. Greffet, Appl. Phys. Lett. **78**, 2931 (2001).
[81] A. Kittel, W. Müller-Hirsch, J. Parisi, S.-A. Biehs, D. Reddig, and M. Holthaus, Phys. Rev. Lett. **95**, 224301 (2005).
[82] W. Broer, G. Palasantzas, J. Knoester, and V. B. Svetovoy, Phys. Rev. B **85**, 155410 (2012).
[83] P. J. van Zwol, G. Palasantzas, and J. T. M. D. Hosson, Phys. Rev. B **77**, 075412 (2008).
[84] P. A. Maia Neto, A. Lambrecht, and S. Reynaud, Europhys. Lett. **69**, 924 (2005).
[85] M. G. Moharam, E. B. Grann, D. A. Pommet, and T. K. Gaylord, J. Opt. Soc. Am. A **12**, 1068 (1995).
[86] M. Planck, Annalen der Physik **309(3)**, 553–63 (1901).
[87] A. Einstein, Annalen der Physik **17**, 132–148 (1905).
[88] R. Clausius, Annalen der Physik und Chemie (Poggendorff, Leipzig) **155 (3)**, 373 (1850).
[89] S. Carnot, *Reflections on the Motive Power of Fire* (J. Wiley and Sons, 1890).
[90] W. Nernst, *Begründung der Theoretischen Chemie : Neun Abhandlungen* (Verlag Harri Deutsch, 1889–1921).
[91] L. Onsager, Phys. Rev. **37**, 405–426 (1931).
[92] L. Onsager, Phys. Rev. **38**, 2265–2279 (1931).
[93] S. Y. Buhmann, S. Scheel, and D. Butcher, *Quantum electrodynamics and Casimir–Polder interactions : Towards the full magneto-electric picture* (Powerpoint presentation - Casimir Worshop Leiden, 2012).
[94] S. Chandrasekhar, *Radiative Transfer* (Dover Publications, 1960).
[95] Y. Cengel and A. Ghajar, *Heat and Mass Transfer, 3rd Edition* (McGraw Hill, 2006).
[96] G. Kirchhoff, Annalen der Physik und Chemie **109**, 275–301 (1860).
[97] M. Peskin and D. Schroeder, *An Introduction to Quantum Field Theory* (Addison-Wesley Advanced Book Program, 1995).
[98] D. B. Melrose and R. C. McPhedran, *Electromagnetic Processes in Dispersive Media - A Treatment Based on the Dielectric Tensor* (Cambridge University Press, 1991).
[99] D. Tong, *Quantum Field Theory Part III lecture notes* (University of Cambridge, 2006-2007).
[100] P. Dirac, Proceedings of the Royal Society of London A **114 (767)**, 243265 (1927).
[101] R. Feynman, *QED : The Strange Theory of Light and Matter* (Princeton University Press, 1985).
[102] M. O. Scully and M. S. Zubairy, *Quantum Optics* (Cambridge University Press, 2001).
[103] C. Cohen-Tannoudji, B. Diu, and F. Laloë, *Mécanique Quantique Vol. I and II* (Hermann, 1997).
[104] L. Landau and E. Lifchitz, *Quantum Mechanics - Course of Theoretical Physics Vol. III* (Pergamon Press, 1991).
[105] S. Weinberg, *The Quantum Theory Of Fields Vol. I* (Cambridge University Press, 1995).
[106] F. Intravaia and A. Lambrecht, Phys. Rev. Lett. **94**, 110404 (2005).
[107] K. Joulain, C. Henkel, and J.-J. Greffet, J. Phys. IV France **135**, 113 (2006).
[108] F. Intravaia, A. Lambrecht, and S. Reynaud, J. Phys. IV France **119**, 199 (2004).
[109] Lambrecht, A., Pirozhenko, I., Duraffourg, L., and Andreucci, Ph., EPL **81**, 19901 (2008).
[110] Torricelli, G., Pirozhenko, I., Thornton, S., Lambrecht, A., and Binns, C., EPL **93**, 51001 (2011).
[111] E. Palik, *Handbook of optical constants of solids* (Elsevier, 1998).

[112] D. L. Windt, Computers in Physics **12**, 360 (1998).
[113] G. Palasantzas, V. B. Svetovoy, and P. J. van Zwol, Phys. Rev. B **79**, 235434 (2009).
[114] V. B. Svetovoy, P. J. van Zwol, G. Palasantzas, and J. T. M. D. Hosson, Phys. Rev. B **77**, 035439 (2008).
[115] R. Guérout, *Permittivités - notes* (February 2012).
[116] M. Diem, T. Koschny, and C. M. Soukoulis, Phys. Rev. B **79**, 033101 (2009).
[117] Y. Bao, R. Guérout, J. Lussange, A. Lambrecht, R. A. Cirelli, F. Klemens, W. M. Mansfield, C. S. Pai, and H. B. Chan, Phys. Rev Lett. **105**, 250402 (2010).
[118] A. Lambrecht and S. Reynaud, The European Physical Journal D - Atomic, Molecular, Optical and Plasma Physics **8**, 309 (2000), ISSN 1434-6060, 10.1007/s100530050041.
[119] URL `http://refractiveindex.info`.
[120] S. Reynaud, *The Casimir force and the quantum theory of optical networks* (Lectures given at Ecole Doctorale de Physique, 2002).
[121] K. Joulain, *Transferts aux petites échelles : application au rayonnement thermique, aux forces de Casimir et à la conduction thermique* (Mémoire pour l'obtention du diplôme d'Habilitation à Diriger des Recherches - École Nationale Supérieure de Mécanique et d'Aérotechnique, 2008).
[122] S. Reynaud, A. Lambrecht, C. Genet, and M.-T. Jaekel, in *Comptes Rendus de l'Académie des Sciences - Series IV - Physics*, edited by Elsevier (2001), vol. 2 of *9*, p. 1287–1298.
[123] M. Jaekel and S. Reynaud, J. Phys. I France **2**, 149 (1991).
[124] A. Lambrecht, M. Jaekel, and S. Reynaud, Phys. Rev. Lett. **78**, 2267–2267 (1997).
[125] L. Landau and E. Lifchitz, *Electrodynamics in continuous media - Course of Theoretical Physics Vol. III* (Pergamon Press, 1984), §82.
[126] M. Boström and B. E. Sernelius, Phys. Rev. Lett. **84**, 4757 (2000).
[127] C. Genet, A. Lambrecht, and S. Reynaud, Phys. Rev. A **62**, 012110 (2000).
[128] C. Genet, A. Lambrecht, and S. Reynaud, J. Phys. IV France **12**, 143 (2002).
[129] C. Genet, Ph.D. thesis, Université Pierre et Marie Curie (2002).
[130] E. Lifchitz and L. Pitaevskii, *Satistical Physics part 2 - Course of Theoretical Physics Vol. IX* (Pergamon Press, 1981).
[131] B. V. Derjaguin, Kolloid-Z **69**, 155 (1934).
[132] J. Błocki, J. Randrup, W. J. Świątecki, and C. F. Tsang, Ann. Phys. **105**, 427 (1977).
[133] M. Bordag, G. Klimchitskaya, and V. Mostapanenko, Phys. Lett. A **200**, 95 (1995).
[134] V. Bezerra, G. Klimchitskaya, and C. Romero, Mod. Phys. Lett. A **12**, 2613 (1997).
[135] P. Y. Yu and M. Cardona, *Fundamentals of Semiconductors : Physics and Materials Properties (4th ed.)* (Springer, 2010).
[136] T. W. Ebbesen, C. Genet, and S. I. Bozhevolnyi, Physics Today pp. 44–50 (May 2008).
[137] W. Barnes, A. Dereux, and T. W. Ebbesen, Nature **424**, 824 (2003).
[138] F. Marquier, R. Carminati, K. Joulain, and J.-J. Greffet, J. Phys. IV France **119**, 229 (2004).
[139] R. Esquivel-Sirvent, L. Reyes, and J. Bárcenas, New J. Phys. **8**, 241 (2006).
[140] *Roughness correction to the Casimir force and the stability of MEMS, Casimir Workshop Leiden NL by W. Broer* (2012).
[141] A. Canaguier-Durand, Ph.D. thesis, Université Pierre et Marie Curie (2011).
[142] *Presentation at Casimir Workshop in Leiden NL by S. Scheer* (2012).
[143] Yolcu, C., Rothstein, I. Z., and Deserno, M., EPL **96**, 20003 (2011).
[144] Rodriguez-Lopez, P., Brito, R., and Soto, R., EPL **96**, 50008 (2011).
[145] F. Rosa, *Bimonte's Approach to Near-Field Heat Transfer - notes* (March 2011).
[146] S. M. Rytov, *Theory of electrical fluctuations and thermal radiation* (Publishing House, Academy of Sciences, USSR, 1953).
[147] K. A. Milton and J. Wagner, J. Phys. A : Math. Theor. **41**, 155402 (2008).
[148] P. A. M. Neto, A. Lambrecht, and S. Reynaud, Phys. Rev. A **72**, 012115 (2005).
[149] W. Eckhardt, Phys. Rev. A **29**, 1991 (1984).
[150] L. Bergström, Adv. Colloid Interface Sci. **70**, 125 (1997).
[151] W. R. Tinga, W. A. G. Voss, and D. F. Blossey, J. Appl. Phys. **44(9)**, 3897 (1973).
[152] S.-A. Biehs, O. Huth, and F. Rüting, Phys. Rev. B **78**, 085414 (2008).
[153] R. B. Rodrigues, P. A. M. Neto, A. Lambrecht, and S. Reynaud, Phys. Rev. Lett. **96**, 100402 (2006).
[154] H.-C. Chiu, G. L. Klimchitskaya, V. N. Marachevsky, V. M. Mostepanenko, and U. Mohideen, Phys. Lett. B **81**, 115417 (2010).
[155] R. B. Rodrigues, P. A. M. Neto, A. Lambrecht, and S. Reynaud, Phys. Rev. A **75**, 062108 (2007).
[156] Rodrigues, R. B., Maia Neto, P. A., Lambrecht, A., and Reynaud, S., Europhys. Lett. **76**, 822 (2006).
[157] A. Canaguier-Durand, P. A. Maia Neto, A. Lambrecht, and S. Reynaud, Phys. Rev. A **83**, 039905 (2011).
[158] V. A. Yampol'skii, S. Savel'ev, Z. A. Mayselis, S. S. Apostolov, and F. Nori, Phys. Rev. Lett. **101**, 096803 (2008).
[159] F. Chen, G. L. Klimchitskaya, U. Mohideen, and V. M. Mostepanenko, Phys. Rev. Lett. **90**, 160404 (2003).
[160] A. P. McCauley, F. S. S. Rosa, A. W. Rodriguez, J. D. Joannopoulos, D. A. R. Dalvit, and S. G. Johnson, Phys. Rev. A **83**, 052503 (2011).
[161] L. Rosa and A. Lambrecht, Phys. Rev. D **82**, 065025 (2010).
[162] R. Messina and M. Antezza, Phys. Rev. A **84**, 042102 (2011).
[163] M. Antezza, L. P. Pitaevskii, S. Stringari, and V. B. Svetovoy, Phys. Rev. Lett. **97**, 223203 (2006).
[164] Messina, R. and Antezza, M., EPL **95**, 61002 (2011).

[165] Krüger, M., Emig, T., Bimonte, G., and Kardar, M., EPL **95**, 21002 (2011).
[166] M. Francoeur, S. Basu, and S. Petersen, Optics Exp. **19(20)**, 18774 (2011).
[167] K. Park, S. Basu, W. P. King, and Z. M. Zhang, J. of Quant. Spec. and Rad. Trans. **109**, 305 (2008).
[168] S.-A. Biehs, The European Physical Journal B - Condensed Matter and Complex Systems **58**, 423 (2007), ISSN 1434-6028, 10.1140/epjb/e2007-00254-8.
[169] A. A. Banishev, C.-C. Chang, R. Castillo-Garza, G. L. Klimchitskaya, V. M. Mostepanenko, and U. Mohideen, Phys. Rev. B **85**, 045436 (2012).
[170] S. Basu, Z. Zhang, and C. Fu, Int. J. Energy Res. **33**, 1203 (2009).
[171] Bimonte, G., Emig, T., Jaffe, R. L., and Kardar, M., EPL **97**, 50001 (2012).
[172] G. Torricelli, P. J. van Zwol, O. Shpak, C. Binns, G. Palasantzas, B. J. Kooi, V. B. Svetovoy, and M. Wuttig, Phys. Rev. A **82**, 010101 (2010).
[173] A. W. Rodriguez, D. Woolf, A. P. McCauley, F. Capasso, J. D. Joannopoulos, and S. G. Johnson, Phys. Rev. Lett. **105**, 060401 (2010).
[174] S.-A. Biehs, D. Reddig, and M. Holthaus, The European Physical Journal B - Condensed Matter and Complex Systems **55**, 237 (2007), ISSN 1434-6028, 10.1140/epjb/e2007-00053-3.
[175] B. Chen and D. F. Nelson, Phys. Rev. B **48**, 15365 (1993).

Résumé de la thèse “Energie de Casimir et transfert thermique radiatif entre surfaces nanostructurées”, J. Lussange

Nous étudions dans cette thèse le cas d'une cavité formée par des plaques parallèles nanostructurées séparées par du vide, lorsque les deux plaques sont à l'équilibre thermique et lorsqu'elles sont hors-équilibre thermique. Par une méthode exacte basée sur l'approche de diffusion, nous évaluons d'abord de façon numérique dans le premier cas la force de Casimir pour une température nulle puis pour une température non nulle, et ensuite dans le deuxième cas nous nous intéressons à la force de Casimir hors-équilibre puis au transfert thermique radiatif.

I. PROFILS À L'ÉQUILIBRE THERMIQUE

A. Température nulle

1. L'effet Casimir entre des surfaces planes

A la fin des années 1940, un jeune Hollandais du nom de Hendrik Casimir travaillait aux Laboratoires de Recherche chez Philips aux Pays-Bas sur le sujet des *solutions colloidales*. Les solutions colloidales sont des solutions visqueuses, soit gazeuses soit liquides, qui contiennent des particules de dimensions micromètriques en suspension —comme de l'argile mélangée à de l'eau, du lait, de l'encre, ou encore de la fumée. Theodor Overbeek, qui était un collègue de Casimir, se rendit compte que la théorie qui était utilisée jusqu'alors pour décrire les *forces de van der Waals* entre ces particules en suspension était en contradiction avec les observations expérimentales. Il demanda à Casimir d'étudier ce problème. Travaillant avec Dirk Polder, et après plusieurs suggestions émanant de Niels Bohr, Casimir eut l'intuition que l'interaction de van der Waals entre des molécules neutres devait être correctement interprétée en termes de *fluctuations du vide*. A partir de là, Casimir orienta son travail de recherche de la configuration particule-particule vers le cas de deux mirroirs plans parallèles. En 1948 il fit ainsi la prédiction d'une attraction mécanique d'origine quantique entre deux plaques conductrices plongées dans le vide. Cette force est aujourd'hui appelée *force de Casimir* [1] et a depuis été fort bien étudiée dans son domaine de validité, aussi bien au niveau expérimental [2–13] que théorique [14–19].

La force de Casimir vient d'une compréhension quantique du vide [20, 21]. At tout moment, l'énergie des champs présents dans le vide oscille autour d'une valeur moyenne constante dite d'*énergie de point zéro*, ou *énergie du vide*. Celle-ci est donnée par la quantification de l'oscillateur harmonique associé à chaque mode, sachant que l'énergie la plus basse de chaque oscillateur est égale à la moitié de l'énergie du photon, à laquelle s'ajoute une fonction de densité du nombre de photons $\overline{n}(\omega, T)$ en présence d'un champ thermique :

$$E(\omega, T) = \hbar\omega \left(\frac{1}{2} + \overline{n}(\omega, T) \right) = \frac{1}{2} \hbar\omega \coth \frac{\hbar\omega}{2k_B T} \qquad \text{avec} \qquad \overline{n}(\omega, T) = \frac{1}{e^{\hbar\omega / k_B T} - 1} \tag{1}$$

Dans un espace non-confiné, les longueurs d'onde du spectre des champs ont toutes la même importance. En revanche, dans une cavité formée par les deux mirroirs plans parallèles imaginés par Casimir, les fluctuations du vide

de ces champs sont amplifiées à une résonance dite *de cavité*, qui apparait lorsque la distance de séparation des deux mirroirs est égale à la moitié de la longueur d'onde des champs, multipliée par un entier. Reciproquement, le champ est supprimé à toutes les autres longueurs d'onde. Ceci est dû aux multiples phénomènes d'interférence à l'intérieur de la cavité.

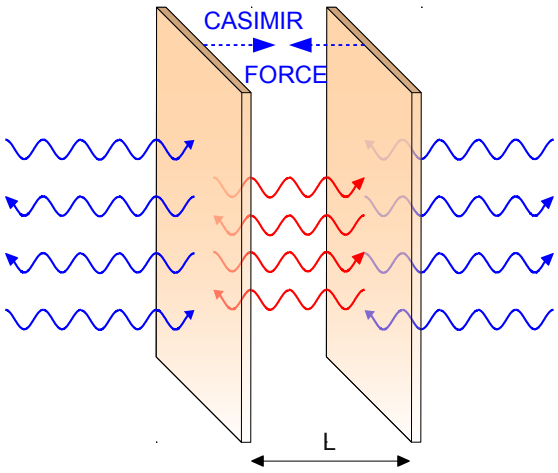

FIG. 1: Cavité de Fabry-Pérot formée par deux plaques parallèles de surface $\mathcal{A}$, et séparées par une distance L dans le vide.

L'énergie du vide associée à ces champs à l'intérieur et à l'extérieur de la cavité est à l'origine d'une *pression de radiation des champs*. A la résonance de cavité, la pression de radiation à l'intérieur de la cavité est plus grande que celle qui est à l'extérieur si bien que les deux mirroirs sont repoussés l'un de l'autre. En revanche dans le cas hors-résonance de cavité, la pression de radiation à l'intérieur de la cavité est plus petite que celle à l'extérieur et les mirroirs sont poussés l'un vers l'autre. La force de Casimir est construite à partir de la somme de toutes les fréquences des modes et apparaît donc comme une force attractive entre les deux mirroirs.

Entre deux plaques de surface A séparées par une distance L à température nulle, la force de Casimir peut être écrite comme la somme sur tous les modes du champ, spécifiés par leur polarisation p, composantes de vecteur d'onde $\mathbf{k} = (k_x, k_y)$, et fréquence $\xi(= -i\omega)$:

$$F = \frac{A\hbar c}{8\pi^3} \sum_p \int_{k_x \in \mathbb{R}} dk_x \int_{k_y \in \mathbb{R}} dk_y \int_0^\infty d\xi \kappa \frac{r^p_{\mathbf{k},1}(i\xi) e^{-\kappa L} r^p_{\mathbf{k},2}(i\xi) e^{-\kappa L}}{1 - r^p_{\mathbf{k},1}(i\xi) e^{-\kappa L} r^p_{\mathbf{k},2}(i\xi) e^{-\kappa L}}$$

où les coefficients scalaires $r^p_{\mathbf{k},1}$ et $r^p_{\mathbf{k},2}$ sont les amplitudes de Fresnel-Stokes correspondant aux réflections spéculaires sur les profils. Nous avons utilisé ici les conventions suivantes :

$$\frac{\omega^2}{c^2} = k_x^2 + k_y^2 + k_z^2 = \mathbf{k} + k_z^2 \qquad \text{avec} \qquad \kappa = \sqrt{\frac{\xi^2}{c^2} + \mathbf{k}^2} = ik_z$$

Sur la FIG. 1, on peut voir une telle cavité dite de *Fabry-Pérot*, consistant en deux plaques parallèles séparées par du vide. Dans la limite de miroirs parfaitement réfléchissants cette expression se réduit à la formule de Casimir :

$$\frac{A\hbar c\pi^3}{240L^4} \tag{2}$$

On peut voir dans l'équation précédente que la force de Casimir est donnée par une loi de puissance inverse avec la distance de séparation entre les plaques. C'est la raison pour laquelle la force de Casimir devient si grande en champ très proche —en général en dessous de quelques microns. A 100 nm, la force de Casimir à température nulle est approximativement égale à 1 N.m^{-2} pour deux plaques de carbure de silicium SiC, et à 3 N.m^{-2} pour deux plaques d'or Au. A 1μm, la force de Casimir décroît à environ 230 μN.m^{-2} et à 900 μN.m^{-2} dans ces deux cas, respectivement.

La propriété de dependence en champ extrêmement proche ainsi que la magnitude proportionnellement élevée de la force de Casimir pourrait avoir de nombreuses applications pratiques au niveau nanotechnologique [22–26]. Notons également le problème récurrent d'adhérence des sous-composants de systèmes nano- ou micro-électromécaniques (NEMS et MEMS) à cause de la force de Casimir, à l'origine de toutes sortes de malfonctionnements [27]. A cause de cela, le calcul précis et exact de la force de Casimir est un enjeu théorique et numérique important, ainsi qu'un défi récurrent pour la recherche fondamentale.

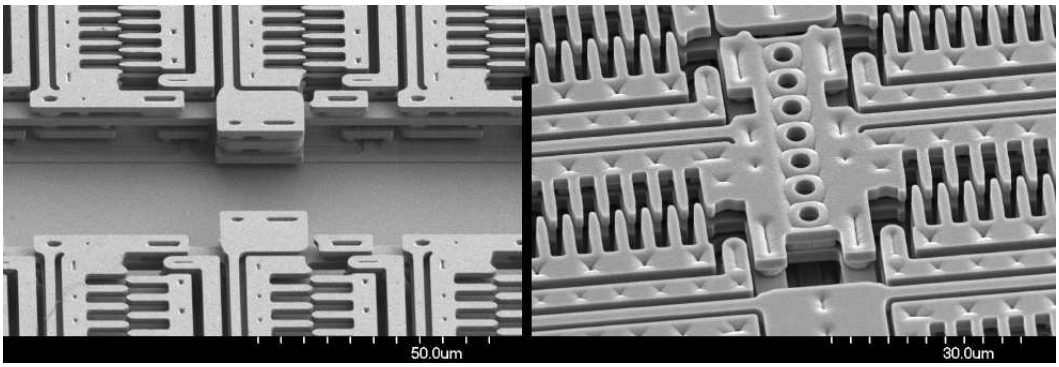

FIG. 2: Mirco-actionneurs de force électrostatique (MEMS).

2. Casimir entre des surfaces corruguées

Comme le montre la FIG. 2, les applications nanotechnologiques réelles ont une architecture considérablement plus complexe que le cas simplifié de deux mirroirs plans parallèles formant une cavité de Fabry-Pérot. Dans cette thèse,

nous nous intéresserons particulièrement au cas de surfaces *nanostructurées* ou de *réseaux périodiques corrugués*, comme illustrés sur la FIG. 3. La réflexion d'un mode par une surface plane obéit à une simple loi de Snell-Descartes, mais ici les modes présents dans la cavité sont diffractés à incidence selon une diffusion complexe à cause des corrugations.

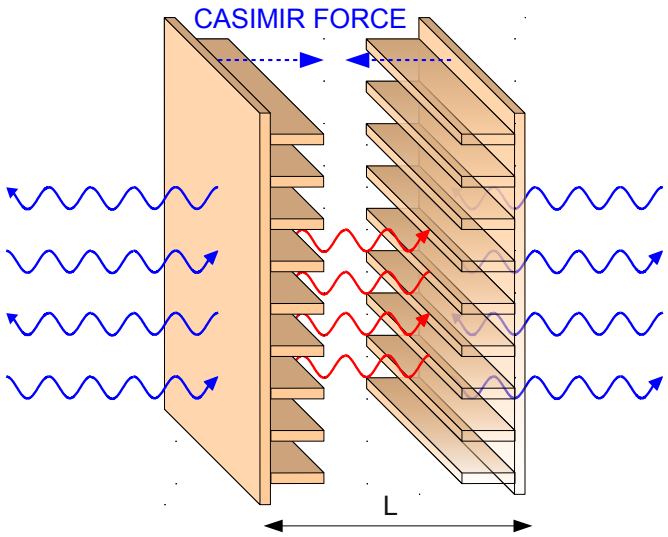

FIG. 3: Cavité de Fabry-Pérot formée par deux profils en réseaux corrugués séparés par une distance L dans le vide.

La première étape de nos calculs numériques de la force de Casimir (et du transfert thermique radiatif) entre de tels profils nanostructurés va dépendre de l'obtention des matrices S de chaque profil. Ces matrices S contiennent toutes les amplitudes de Fresnel-Stokes pour la réflexion et la transmission des modes à l'interface des plaques avec le vide. Les deux ensembles de paramètres spécifiant complètement un réseau donné sont contenus dans la matrice S associée : ceux définissant sa géométrie (d, a, p sur la FIG. 4), et ceux définissant le matériau de ce réseau (fonction de permittivité). On peut donc dire que la matrice S est utilisée pour définir le profil nanostructuré choisi, ainsi que la façon dont les modes issus de la cavité sont diffractés à sa surface.

La base du formalisme mathématique que nous utiliserons pour calculer ces matrices S associées à chaque profil corrugué repose sur la méthode *'Rigorous Coupled-Wave Analysis'* (RCWA), de la théorie de diffusion [28]. Considérons des réseaux périodiques unidimensionnels et infiniment longs, séparés par le vide comme le montre la FIG. 4. Par unidimensionnel nous entendons que les réseaux sont périodiques dans la direction des x et constants dans la direction des y. Leur température est supposée égale à zéro. De plus, nous considérons ces profils comme étant

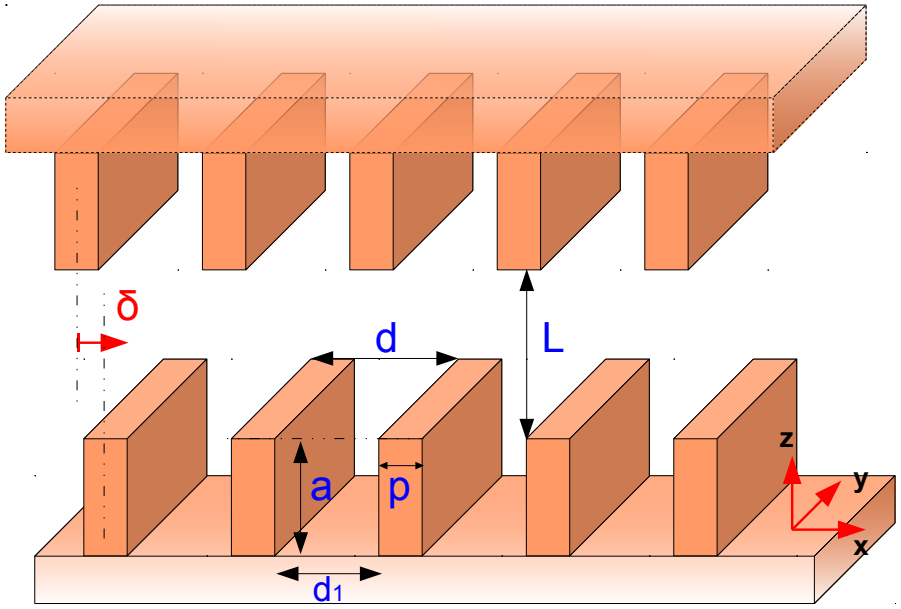

FIG. 4: Principaux paramètres géométriques de plaques corruguées formant une cavité de Fabry-Pérot : on note d la période des corrugations, p le facteur de remplissage (souvent exprimé comme un pourcentage de la période), a la profondeur des corrugations, d_1 l'espace entre les corrugations, L la distance de séparation entre les têtes des corrugations des deux plaques, et δ le déplacement latéral selon l'axe des x. Les plaques ont une surface infinie dans les directions de x et y.

infiniment épais dans la direction z.

Les paramètres géométriques des réseaux sont la période des corrugations d, le facteur de remplissage p, la profondeur des corrugations a, l'espacement des corrugations d_1, la distance de séparation entre les profils L, et le déplacement latéral δ selon l'axe des x.

On sait de la théorie de diffusion qu'au dessus et en dessous des corrugations, la solution du champ électromagnétique est donnée par une *expansion de Rayleigh*. Il y a $2N + 1$ modes couplés, ce qui représente le nombre de coefficients présents dans une expansion de Rayleigh pour une onde monochromatique incidente, lorsque les composantes longitudinales du champs au dessus des réseaux sont écrites sous la forme d'une telle expansion. Suivant une méthode détaillée dans [29], nous dérivons à présent la matrice S de chaque réseau de facçon similaire à la méthode RCWA originellement expliquée dans [28].

En utilisant l'invariance du problème selon y et t, on peut considérer les champs électriques et magnétiques selon les directions x et z seulement :

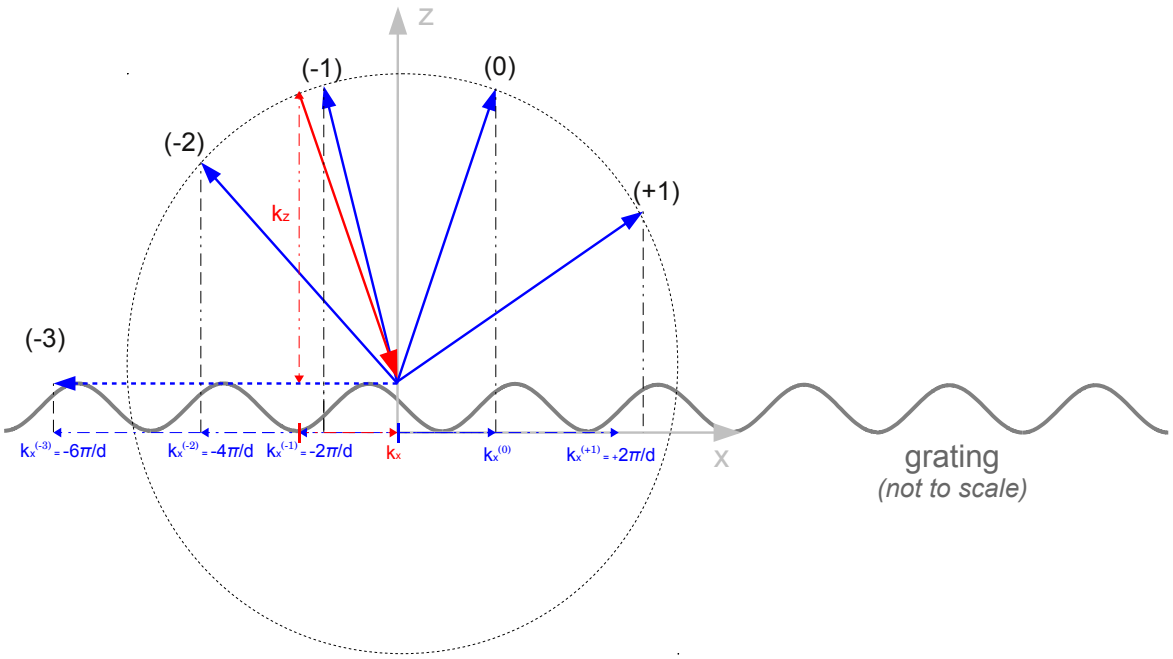

FIG. 5: Processus de diffusion d'un mode sur des réseaux. Après avoir fixé un ordre de diffraction N de telle manière que $p, n \in [-N, ..., -2, -1, 0, +1, +2, ..., +N]$, on considère pour chaque mode incident p son nombre de modes diffractés n associé. Chaque mode diffracté n est généré selon une orientation spécifique donnée par sa composante latérale $k_x^{(n)} = 2\pi n/d$ appartenant à la zone de Brillouin associée, et par son amplitude fixée à $|\mathbf{k}| = \omega/c$. Cette amplitude apparaît comme le rayon du cercle en pointillé sur la figure, dans lequel chaque mode diffracté a une amplitude $|\mathbf{k}| < \omega/c$, et est donc propagatif. Lorsque les modes diffractés dépassent cette limite $|\mathbf{k}| > \omega/c$, ils appartiennent alors au secteur evanescent. Ceci est illustré par le mode en pointillé, qui correspond à $n = (-3)$. Notons qu'une *réflexion speculaire* peut apparaître lorsque le mode incident a un angle d'incidence égal à l'*angle de Bragg*, dans quel cas le premier mode diffracté $n = (0)$ est réfléchi dans la même direction que le mode incident. L'énergie de Casimir entre des réseaux est dérivée d'une intégration sur toutes les composantes des modes k_x, k_z, ω, à l'intérieur de chaque zone de Brillouin $k_x \in [0, 2\pi/d]$.

$$E_i(x, y, z, t) = E_i(x, z)e^{i(k_y y - \omega t)} \tag{3}$$

$$H_i(x, y, z, t) = H_i(x, z)e^{i(k_y y - \omega t)} \tag{4}$$

L'avantage mathématique de considérer des nanoréseaux *périodiques* est que l'on peut se réstreindre dans notre dérivation mathématique de la force de Casimir à seulement une période donnée en tant que *première zone de Brillouin*. Ainsi l'on considère le vecteur d'onde comme étant confiné dans $0 < k_x < 2\pi/d$. Nous avons seulement besoin de trouver les composantes longitudinales en dehors de la région corruguée ($z > a$), et en-dessous de la région corruguée ($z \leqslant 0$).

Pour $z > a$:

$$E_y(x,z) = I_p^{(e)} e^{i(\alpha_p x - \beta_p^{(1)} z)} + \sum_{n=-\infty}^{+\infty} R_{np}^{(e)} e^{i(\alpha_n x + \beta_n^{(1)} z)} \tag{5}$$

$$H_y(x,z) = I_p^{(h)} e^{i(\alpha_p x - \beta_p^{(1)} z)} + \sum_{n=-\infty}^{+\infty} R_{np}^{(h)} e^{i(\alpha_n x + \beta_n^{(1)} z)} \tag{6}$$

$$\alpha_p = k_x + \frac{2\pi p}{d} \quad \text{and} \quad \alpha_n = k_x + \frac{2\pi n}{d} \tag{7}$$

$$\beta_p^{(1)2} = \omega^2 - k_y^2 - \alpha_p^2 \quad \text{and} \quad \beta_n^{(1)2} = \omega^2 - k_y^2 - \alpha_n^2 \tag{8}$$

$$\beta_n^{(2)2} = \omega^2 \epsilon\mu - k_z^2 - \alpha_n^2 \tag{9}$$

où p est un entier. Pour chaque mode incident p on considère $n \in \{2N+1\}$ modes diffractés, où $2N+1$ est le nombre de coefficients de Rayleigh, comme le montre la FIG. 5. Pour $n = 0$, une réflexion spéculaire est retrouvée.

Pour $z \leqslant 0$:

$$E_y(x,z) = \sum_{n=-\infty}^{+\infty} T_{np}^{(e)} e^{i(\alpha_n x - \beta_n^{(2)} z)} \tag{10}$$

$$H_y(x,z) = \sum_{n=-\infty}^{+\infty} T_{np}^{(h)} e^{i(\alpha_n x - \beta_n^{(2)} z)} \tag{11}$$

où I_p, R_{np}, T_{np} sont les matrices d'incidence, de réflexion, et de transmission respectivement, toutes de dimension $2N+1$.

Les sommes sont effectuées sur tous les entiers n. Par symétrie, les autres composantes des champs électriques et magnétiques peuvent être exprimées en fonction des composantes selon z des *deux* champs. Nous devons à présent calculer les coefficients de réflexion R_{np} associés à ces réseaux corrugués. D'abord il faut ré-écrire les équations de Maxwell à l'intérieur de la région corruguée $0 < z < a$ au moyen d'un ensemble d'équations différentielles du premier ordre :

$$\partial_z \mathbf{F} = \mathbf{M}\mathbf{F} \tag{12}$$

avec $\mathbf{F}^\top = (E_y, E_x, H_y, H_x)$, et $\mathbf{M}$ étant une matrice carrée constante de dimension $8N+4$. La solution des champs s'écrit donc sous la forme :

$$\mathbf{F}(z) = e^{\mathbf{M}z}\mathbf{F}(0) \tag{13}$$

A partir de là, la méthode générale consiste à écrire les champs à l'intérieur des réseaux sous cette forme, et à les réunir sous forme de relations de continuité pour chaque E_y, H_y, E_x, H_x avec les équations aux limites précédentes: celles à la limite $z = a$ pour les champs dans $z > a$, et celles à la limite $z = 0$ pour les champs dans $z \leqslant 0$. Eventuellement on peut trouver après quelques calculs les solutions écrites en fonction des matrices de transmission T_{np}, que l'on ré-écrit elles-mêmes en fonction des matrices de réflexion recherchées R_{np} au travers des relations de continuité à $z = a$.

On trouve finalement que la force de Casimir à température nulle entre deux réseaux corrugués peut être écrite [29]:

$$F = \frac{A\hbar c}{8\pi^3} \int_{k_x=-\pi/d}^{+\pi/d} dk_x \int_{k_y\in\mathbb{R}} dk_y \int_0^\infty d\xi \mathrm{Tr}\left[\mathbf{Z}_1\mathbf{Z}_2\right]$$

avec :

$$\mathbf{Z}_1 = \left[I - \mathbf{R}_1(i\xi)\mathbf{K}(i\xi)\mathbf{R}_2(i\xi)\mathbf{K}(i\xi)\right]^{-1}$$

$$\mathbf{Z}_2 = \mathbf{R}_1(i\xi)\mathrm{diag}(\kappa)\mathbf{K}(i\xi)\mathbf{R}_2(i\xi)\mathbf{K}(i\xi) + \mathbf{R}_1(i\xi)\mathbf{K}(i\xi)\mathbf{R}_2(i\xi)\mathrm{diag}(\kappa)\mathbf{K}(i\xi)$$

$$K(i\xi) = \mathrm{diag}\left[\exp\left(-L\sqrt{\xi^2 + k_y^2 + [k_x + (2n\pi/d)]^2}\right)\right] \quad \text{et} \quad n = -N, \ldots, +N$$

Donc dans le cas de réseaux les réflexions spéculaires couplent les modes de polarisation et vecteurs d'onde transverse différents. Les matrices de réflexion peuvent alors être écrites en terme de matrices par blocs $\mathbf{r}_{01}$ prenant en compte ce couplage des polarisations :

$$\mathbf{R}_1(i\xi) = \begin{pmatrix} \mathbf{r}_{01}^{\mathrm{TE/TE}} & \mathbf{r}_{01}^{\mathrm{TE/TM}} \\ \mathbf{r}_{01}^{\mathrm{TM/TE}} & \mathbf{r}_{01}^{\mathrm{TM/TM}} \end{pmatrix}$$

Tous les résultats touchant à la force de Casimir entre des réseaux à température nulle sont présentés dans les sections VII.B-D du manuscrit.

3. L'effet Casimir entre des surfaces corruguées arbitraires

On peut utiliser le formalisme RCWA décrit ci-dessus pour décrire n'importe quels réseaux périodiques de formes arbitraires, si on les modèle comme étant composés d'un empilement de fines tranches rectangulaires (cf. FIG. 6). La

différence principale avec le calcul présenté auparavant repose dans une équation différentielle similaire à l'équation (12) qui peut être résolue pour chaque tranche rectangulaire (i) afin de relier les champs à $z = ia/K$ et $z = (i+1)a/K$, de telle sorte qu'éventuellement le champ à $z = a$ est relié au champ à $z = 0$ via la relation :

$$\mathbf{F}(a) = \left[\prod_{i=K}^{1} e^{\mathbf{M}(i)a/K}\right] \mathbf{F}(0) \tag{14}$$

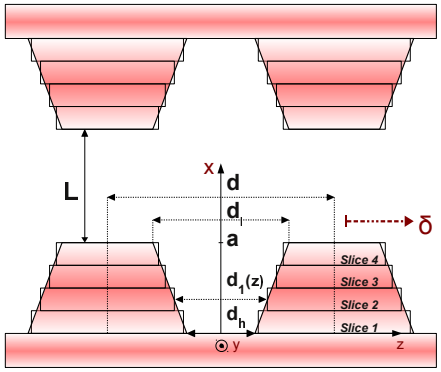

FIG. 6: Géométrie de réseaux arbitraires, avec paramètres associés dans l'approximation des réseaux par un empilement vertical de K fines tranches rectangulaires (ici avec $K = 4$).

Ainsi nous pouvons définir toutes sortes de réseaux arbitraires, tels que ceux en forme de *dents de scie*, de *fil barbelé*, de *sinusoïde*, ou d'*ellipsoïdes* (voir FIG. 7).

La FIG. 8 montre la dépendence de l'énergie de Casimir avec le déplacement latéral δ pour quatre réseaux périodiques arbitraires de silicium intrinsèque. Les profils rectangulaires et *sinusoïdaux* ont en commun des valeurs voisines de l'énergie de Casimir, et de même, les profils en *dents de scie* et *circulaires* ont également des valeurs voisines, mais beaucoup plus faibles. Un résultat important est que dans le cas de ces réseaux arbitraires, l'Approximation de Proximité peut être utilisée au voisinage de $\delta = d/2$.

Une étude systématique de la force de Casimir entre des réseaux périodiques arbitraires est présentée dans la section VII.E du manuscrit.

B. Température non-nulle

Il est possible de dériver le formalisme précédent pour la force de Casimir entre des réseaux lorsque les plaques sont toutes à une même température non-nulle $T \neq 0$. On doit maintenant prendre en compte la contribution du champ thermique à la densité d'énergie du vide $E(\omega, T)$ de l'équation (1). Celle-ci apparaît comme un facteur coth

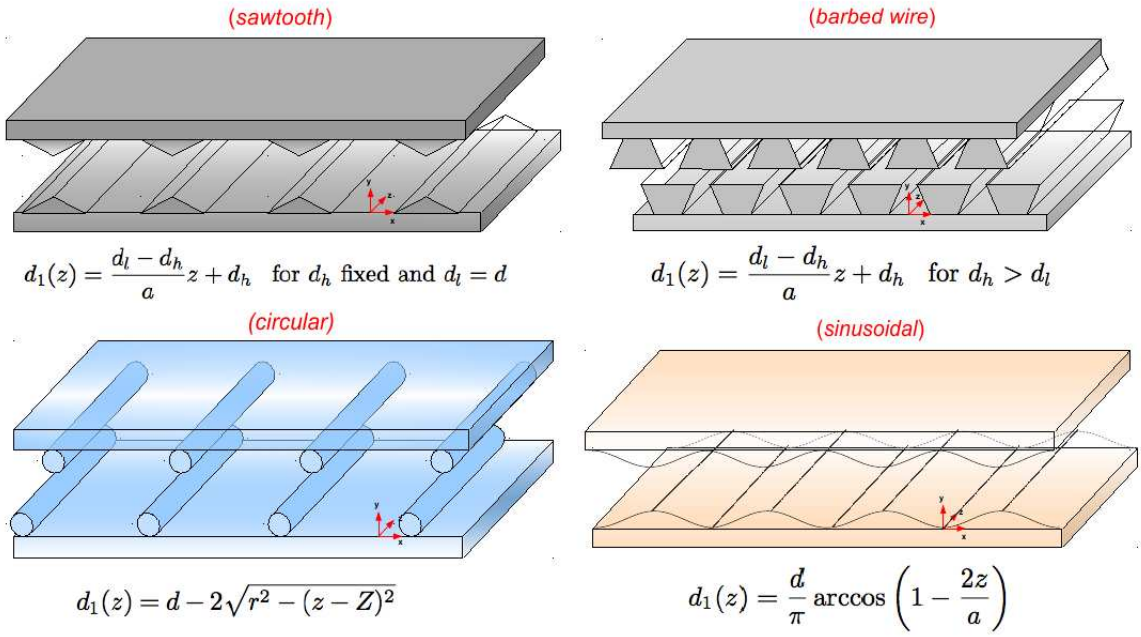

FIG. 7: Différentes géométries de réseaux arbitraires avec spécification associée de la fonction d'espacement entre les corrugations $d_1(z)$.

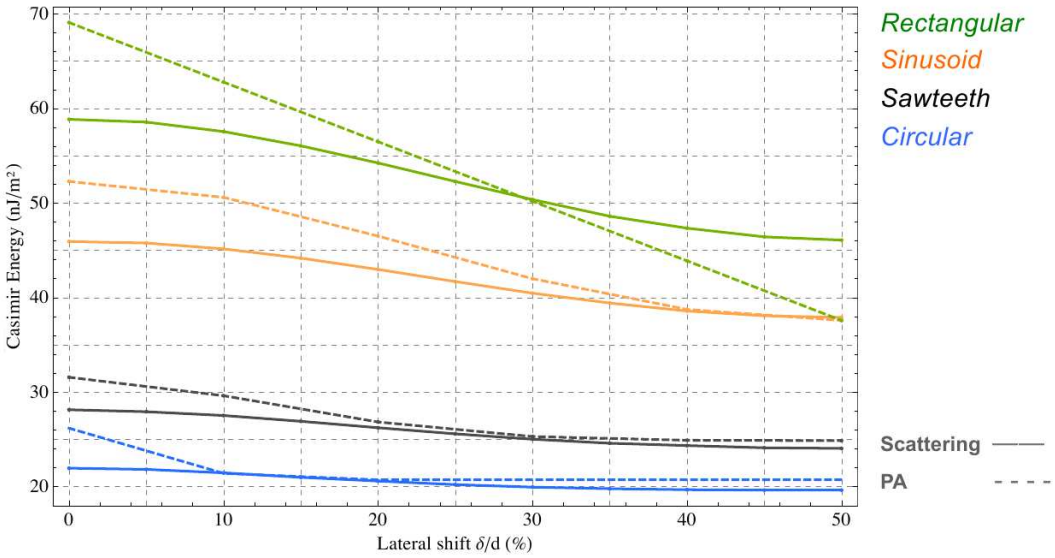

FIG. 8: Dépendance de l'énergie de Casimir en fonction du déplacement latéral δ pour quatre types de réseaux arbitraires de silicium intrinsèque, pour une distance de séparation $L = 100$ nm, une période $d = 400$ nm, et une profondeur de corrugation $a = 50$ nm. Les profils *rectangulaires* sont paramétrés par $d_1 = 200$ (courbe verte), les profils *sinusoïdaux* par $d_1(z) = (400/\pi) \arccos[1 - (z/25)]$ (courbe orange), les profils en *dents de scie* par $d_1 = 4z + 200$ (courbe noire), et les profils *circulaires* par $d_1 = 400 - 2\sqrt{50z - z^2}$ (courbe bleue). Ces quatre ensembles de résultats exacts provenant de la théorie de diffusion (courbes continues) sont comparés avec les résultats obtenus par l'Approximation de Proximité (courbes en pointillés de couleur respectives).

dans l'intégrande de l'expression de la force de Casimir, avec des pôles apparaissant sous la formes de *fréquences de Matsubara*:

$$F = \frac{A}{4\pi^2} k_B T \sum_{m=0}^{'} \int_{k_x=-\pi/d}^{+\pi/d} dk_x \int_{k_y \in \mathbb{R}} dk_y \mathrm{Tr}\left[\mathbf{Z}_1 \mathbf{Z}_2\right]$$

les fréquences de Matsubara étant données par :

$$\omega_m = i\xi_m = im\frac{2\pi k_B T}{\hbar} \to 0$$

On retrouve la limite de température nulle lorsque :

$$\omega_T = \frac{2\pi k_B T}{\hbar} \to 0 \qquad \text{avec} \qquad \lambda_T = \frac{\hbar c}{k_B T} = \frac{2\pi c}{\omega_T}$$

Pour des distances au-delà de la valeur de $\lambda_T/2$, les contributions thermiques à la force de Casimir sont importantes. Ceci apparaît clairement sur la FIG. 9, qui montre l'énergie de Casimir en fonction de la distance de séparation L pour deux réseaux de silicium intrinsèque (à gauche) et d'or (à droite), à des températures $T = 0$ K et 300 K.

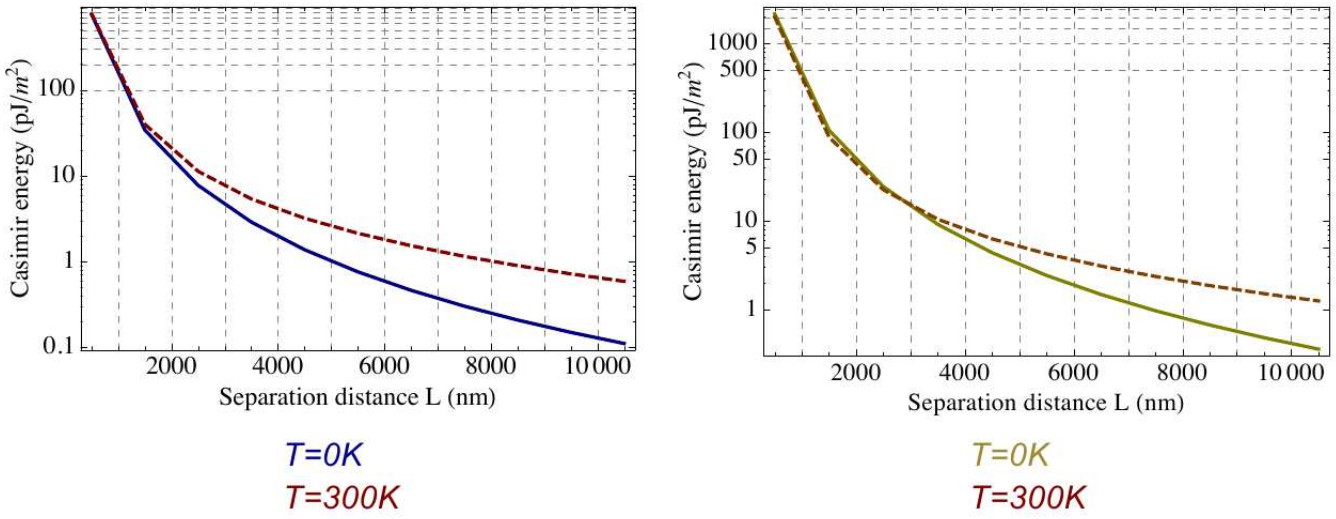

FIG. 9: Energie de Casimir en fonction de la distance de séparation, pour deux réseaux de silicium intrinsèque (à gauche) et d'or (à droite), à des températures $T = 0$ K et 300 K. Les réseaux ont une période $d = 200$ nm, un facteur de remplissage $p = 50\%$, et une profondeur de corrugation $a = 100$ nm.

On voit que l'énergie de Casimir augmente avec la température. Ceci est particulièrement vrai pour de grandes distances de séparation à cause de la contribution associée à des longueurs d'onde plus grandes que la longueur d'onde thermique λ_T.

Les résultats pour la force de Casimir à l'équilibre thermique pour des températures non-nulles sont présentés dans la section VIII.A du manuscrit.

II. PROFILS HORS-ÉQUILIBRE THERMIQUE

A. Force de Casimir hors-équilibre

On peut également utiliser la méthode RCWA pour extraire les matrices de réflection de chaque profil et par approche de diffusion calculer la force de Casimir hors-equilibre [30, 31]. Prenons les conventions suivantes :

$$k_z = \sqrt{\omega^2/c^2 - \mathbf{k}_\perp^2} \qquad \text{avec} \qquad -\frac{\pi}{2} \leqslant \arg k_z \leqslant \frac{\pi}{2}$$

avec les projecteurs sur les secteurs propagatifs et evanescents :

$$\Sigma_n^{\mathrm{pw}} = k_z^n \Pi^{\mathrm{pw}} \qquad \text{pour} \qquad \Pi_{\rho\rho'}^{\mathrm{pw}} = \delta_{\rho\rho'} \frac{1+s_\alpha}{2}$$

$$\Sigma_n^{\mathrm{ew}} = k_z^n \Pi^{\mathrm{ew}} \qquad \text{pour} \qquad \Pi_{\rho\rho'}^{\mathrm{ew}} = \delta_{\rho\rho'} \frac{1-s_\alpha}{2}$$

et $s_\alpha \equiv \mathrm{sgn}\left(\omega^2/c^2 - \mathbf{k}_\perp^2\right)$. On peut alors écrire l'expression de la force de Casimir hors-équilibre comme étant la somme d'une partie à l'équilibre thermique et d'une partie non-équilibre [32] :

$$F_z^{(\mathrm{neq})}(T_1, T_2) = \frac{1}{2} F_z^{(\mathrm{eq})}(T_1) + \frac{1}{2} F_z^{(\mathrm{eq})}(T_2) + \frac{1}{2} \Delta F_z^{(\mathrm{neq})}(T_1, T_2)$$

avec :

$$F_z^{(\mathrm{eq})}(T) = \frac{1}{8\pi^3} 2\mathrm{Re} \int_{\omega>0} \frac{F(\omega,T)}{\omega} \int_{k_x=-\pi/d}^{+\pi/d} \int_{k_y\in\mathbb{R}} \mathrm{Tr}\left[k_z \left(\mathbf{U}^{12}\mathbf{S}^1\mathbf{S}^2 + \mathbf{U}^{21}\mathbf{S}^2\mathbf{S}^1\right)\right] dk_y dk_x d\omega$$

$$\Delta F_z^{(\mathrm{neq})}(T_1, T_2) = \frac{1}{8\pi^3} \int_{\omega>0} \frac{F(\omega,T_1) - F(\omega,T_2)}{\omega} \int_{k_x=-\pi/d}^{+\pi/d} \int_{k_y\in\mathbb{R}} \mathrm{Tr}\left[\mathbf{J}^{12} - \mathbf{J}^{21}\right] dk_y dk_x d\omega$$

$$\mathbf{U}^{12} = \left[1 - S^1 S^2\right]^{-1}$$

$$\mathbf{J}^{12} = \mathbf{U}^{12}\left(\mathbf{\Sigma}_{-1}^{\mathrm{pw}} - \mathbf{S}^1\mathbf{\Sigma}_{-1}^{\mathrm{pw}}\mathbf{S}^{1\dagger} + \mathbf{S}^1\mathbf{\Sigma}_{-1}^{\mathrm{ew}} - \mathbf{\Sigma}_{-1}^{\mathrm{ew}}\mathbf{S}^{1\dagger}\right) \times \mathbf{U}^{12\dagger}\left(\mathbf{\Sigma}_2^{\mathrm{pw}} + \mathbf{S}^{2\dagger}\mathbf{\Sigma}_2^{\mathrm{pw}}\mathbf{S}^2 + \mathbf{S}^{2\dagger}\mathbf{\Sigma}_2^{\mathrm{ew}} + \mathbf{\Sigma}_2^{\mathrm{ew}}\mathbf{S}^2\right)$$

et avec $\mathbf{S}_1 = \mathbf{R}_1(\omega)$ et $\mathbf{S}_2 = e^{ik_z L}\mathbf{R}_2(\omega)e^{ik_z L}$. Comme le montre la FIG. 10, on peut utiliser ce résultat pour calculer la force de Casimir en fonction de la profondeur des corrugations pour des profils corrugués de SiO_2 à $T_1 = 250$ K

et de SiC à $T_2 = 350$ K. Les profils sont séparés par une distance $L = 100$nm, et ont la même période $d = 500$nm et facteur de remplissage $p = 50\%$.

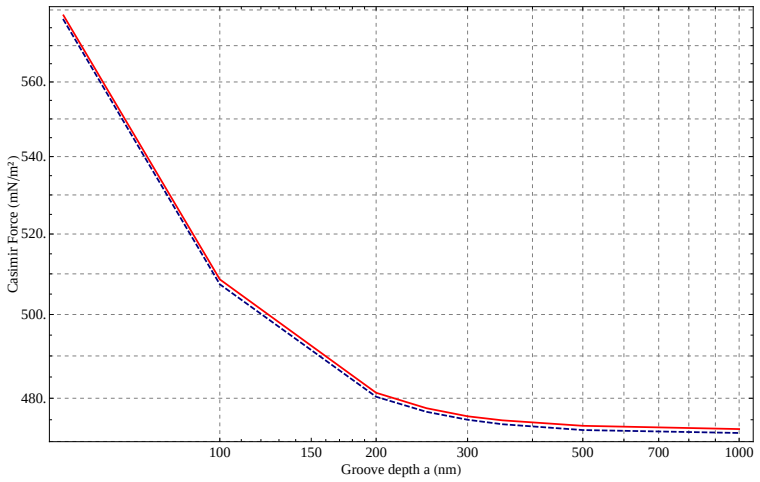

FIG. 10: Dépendance logarithmique de la force de Casimir totale $F_z^{(\mathrm{neq})}(T_1, T_2)$ en fonction de la profondeur des corrugations a (courbe rouge continue), qui est égale à la somme de la contribution à l'équilibre $(F_z^{(\mathrm{eq})}(T_1) + F_z^{(\mathrm{eq})}(T_2))/2$ (courbe bleue en pointillée) et de la contribution non-équilibre $\Delta F_z^{(\mathrm{neq})}(T_1, T_2)$. Un profil en réseaux de dioxyde de silicium SiO_2 à une température $T_1 = 250$ K, se trouve en face d'un autre profil en réseaux de carbure de silicium SiC à température $T_2 = 350$ K. Les deux réseaux sont séparés par une distance $L = 100$ nm, et ont la même période $d = 500$ nm et le même facteur de remplissage $p = 50\%$.

La comparaison entre la force totale (courbe rouge) et la partie équilibre $(F_z^{(\mathrm{eq})}(T_1) + F_z^{(\mathrm{eq})}(T_2))/2$ (courbe bleue) révèle que la partie non-équilibre $\Delta F_z^{(\mathrm{neq})}(T_1, T_2)$ est considérablement plus petite –de presque trois ordres de grandeur. Au vu de cette faible contribution, la question se pose naturellement de savoir s'il est possible d'augmenter la partie non-équilibre par rapport à la force totale pour certaines configurations géométriques.

Cette thèse contient une étude qui prouve qu'à une distance de 3μm entre deux plans parallèles de SiO_2 à $T_1 = 450$ K et de SiC à $T_2 = 250$ K, on peut atteindre un régime où le ratio $\Delta F^{(\mathrm{neq})}/F^{(\mathrm{eq})}$ dépasse les 22%. Les résultats pour la force de Casimir hors-équilibre thermique sont présentés en détail dans la section VIII.B du manuscrit.

B. Transfert thermique radiatif

On peut également utiliser la méthode RCWA pour extraire les matrices S de chaque profil et par l'approche de diffusion calculer le transfert thermique radiatif [30, 31] entre deux profils nanostructurés. On sait que le transfert thermique radiatif entre deux plans parallèles est beaucoup plus grand en champ proche que l'émissivité du corps noir [33, 34]. Avec les conventions précédentes, l'expression du coefficient de transfert thermique radiatif entre des profils corrugués est donnée par :

$$h = \frac{1}{8\pi^3|T_1 - T_2|} \int_{\omega>0} (F(\omega, T_1) - F(\omega, T_2)) \int_{k_x=-\pi/d}^{+\pi/d} \int_{k_y\in\mathbb{R}} \mathrm{Tr}\left[\mathbf{H}^{12}\right] dk_y dk_x d\omega$$

avec :

$$\mathbf{H}^{12} = \left[\mathbf{U}^{12}\left(\mathbf{\Sigma}_{-1}^{\mathrm{pw}} - \mathbf{S}^1\mathbf{\Sigma}_{-1}^{\mathrm{pw}}\mathbf{S}^{1\dagger} + \mathbf{S}^1\mathbf{\Sigma}_{-1}^{\mathrm{ew}} - \mathbf{\Sigma}_{-1}^{\mathrm{ew}}\mathbf{S}^{1\dagger}\right) \times \mathbf{U}^{12\dagger}\left(\mathbf{\Sigma}_1^{\mathrm{pw}} - \mathbf{S}^{2\dagger}\mathbf{\Sigma}_1^{\mathrm{pw}}\mathbf{S}^2 + \mathbf{S}^{2\dagger}\mathbf{\Sigma}_1^{\mathrm{ew}} - \mathbf{\Sigma}_1^{\mathrm{ew}}\mathbf{S}^2\right)\right]$$

On peut utiliser cette expression pour calculer le flux en fonction de la distance de séparation L (FIG. 11) pour deux profils corrugués [35] de SiO_2 avec les paramètres suivants : $d = 1500$nm, $p = 20\%$, $a = 500$nm, $T_1 = 290$ K, et $T_2 = 310$ K. On calcule le flux lorsque les corrugations de chaque profils sont en face les unes des autres (courbe continue), et lorsque les profils sont latéralement décalés d'une demi-période (courbe en traits discontinus). On obtient ainsi une forte modulation entre les deux cas (courbe pointillée). En particulier, à très courte distance $L = 25$ nm ce facteur de modulation dépasse 35. Basé sur ces résultats, nous proposons ainsi dans la thèse un concept nouveau d'application de *modulateur thermique*.

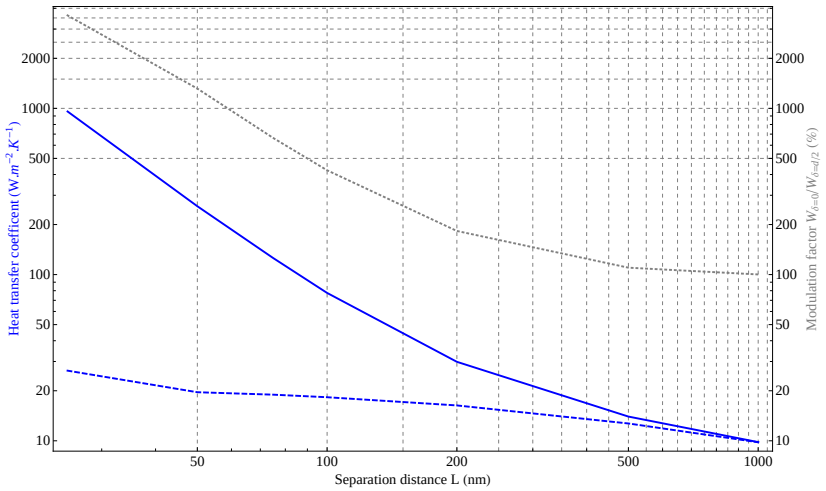

FIG. 11: Coefficient de transfert thermique radiatif en fonction de la distance de séparation L pour deux réseaux de dioxyde de silicium SiO_2 à des températures réspectives $T_1 = 310$ K et $T_2 = 290$ K, pour un déplacement latéral $\delta/d = 0\%$ (courbe bleue continue) et $\delta/d = 50\%$ (courbe bleue pointillée). Les résultats sont comparés avec le facteur de modulation $W_{\delta/d=0\%}/W_{\delta/d=50\%}$ (courbe grise pointillée). Les réseaux ont une période $d = 1500$ nm, un facteur de remplissage $p = 20\%$, et une profondeur de corrugations $a = 500$ nm.

On peut également calculer le flux en fonction de la profondeur des corrugations (FIG. 12) pour deux profils corrugués d'or [36] avec les paramètres suivants : $L = 1\mu$m, $p = 50\%$, $T_1 = 290$ K, $T_2 = 310$ K. On considère des profils de période de corrugation variées : $d = 1\mu$m (en bleu), $d = 2.5\mu$m (en rouge), $d = 10\mu$m (en vert), et l'on compare ces résultats exacts avec l'approximation de proximité (courbe noire pointillée). Il apparaît que le flux est

exalté lorsque l'on creuse les corrugations. Ceci s'explique par le fait que l'on créé ainsi des guides d'ondes qui donnent naissance à un couplage des modes thermiques dans l'infra-rouge, tout en gardant la contribution en champ proche des têtes des corrugations avec celles du profil opposé.

Tous les résultats du transfert thermique radiatif sont présentés dans la section IX du manuscrit.

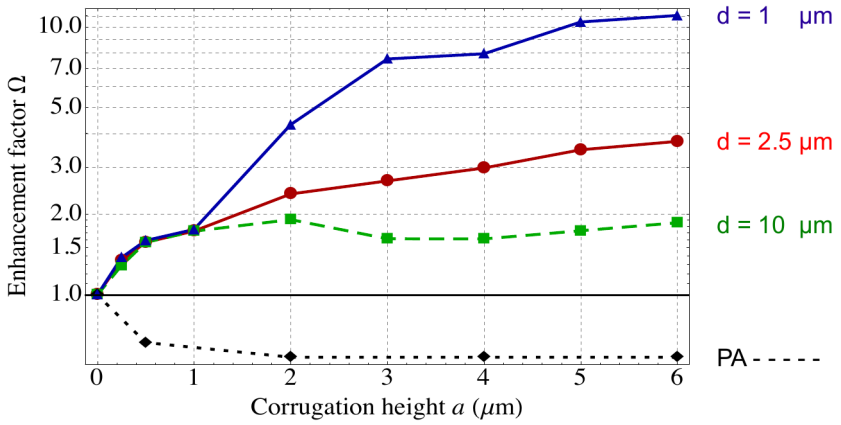

FIG. 12: Coefficient de transfert thermique radiatif en fonction de la profondeur des corrugations a pour différents réseaux d'or à des températures $T_1 = 310$ K et $T_2 = 290$ K. Ces résultats exacts provenant de la méthode de diffusion sont comparés à ceux de l'Approximation de Proximité (courbe noire pointillée). Les réseaux sont à une distance de séparation $L = 1000$ nm, et ont un facteur de remplissage $p = 50\%$.

III. CONCLUSION

Nous rappelons ici les principaux résultats présentés dans la thèse. En dérivant la matrice S d'un profil donné grâce à la méthode RCWA, nous avons effectué en utilisant la théorie de diffusion les premiers calculs numériques exacts de la force de Casimir hors-équilibre et du transfert thermique radiatif entre des profils nanostructurés. Nos résultats ouvrent des champs de recherche nouveaux, avec des découvertes potentielles liées aux domaines suivants :

- La force de Casimir entre des réseaux arbitraires, avec des applications directes de nano-ingénierie.
- La force de Casimir entre des réseaux hors-équilibre thermique, avec la présentation des premiers calculs exacts déstinés aux expérimentateurs.
- Le flux de chaleur entre des réseaux, avec de vastes modulations dans le cas d'un déplacement latéral des profils.

En conclusion, ce travail théorique amène des applications potentielles directes :

- La modulation éventuelle de la force de Casimir et donc la possibilité de réduire les problèmes de malfonctionnement dans les NEMS et les MEMS au travers d'un contrôle de la température des réseaux.

- Beaucoup de systèmes électromécaniques doivent être mis à la masse, souvent par le biais de revêtements d'or. Rappelons la présence d'échanges de flux de chaleur tout-à-fait non-triviaux dans le cas de réseaux d'or.

- Le flux de chaleur entre des réseaux, avec la conception potentielle d'un modulateur thermique de facteur 35.

---

[1] H. Casimir, Proc. Kon. Ned. Akad. We. **51**, 793 (1948).
[2] G. Bressi, G. Carugno, R. Onofrio, and G. Ruoso, Phys. Rev. Lett. **88**, 041804 (2002).
[3] W. R. Tinga, W. A. G. Voss, and D. F. Blossey, Phys. Rev. Lett. **81**, 4549 (1998).
[4] S. K. Lamoreaux, Phys. Rev. Lett. **78**, 5 (1997).
[5] S. K. Lamoreaux, Phys. Rev. Lett. **81**, 5475 (1998).
[6] L. S. Brown and G. J. Maclay, Phys. Rev. **184**, 1272 (1969).
[7] B. W. Harris, F. Chen, and U. Mohideen, Phys. Rev. A **62**, 052109 (2000).
[8] R. S. Decca, D. Lopez, E. Fischbach, and D. E. Krause, Phys. Rev. Lett. **91**, 050402 (2003).
[9] T. Ederth, Phys. Rev. A **62**, 062104 (2000).
[10] R. S. Decca, E. Fischbach, G. L. Klimchitskaya, D. E. Krause, D. Lopez, and V. M. Mostepanenko, Phys. Rev. D **68**, 116003 (2003).
[11] R. S. Decca, D. Lopez, E. Fischbach, G. L. Klimchitskaya, D. E. Krause, and V. M. Mostepanenko, Phys. Rev. D **75**, 077101 (2007).
[12] H. B. Chan, Y. Bao, J. Zou, R. A. Cirelli, F. Klemens, W. M. Mansfield, and C. S. Pai, Phys. Rev. Lett. **101**, 030401 (2008).
[13] D. Garcia-Sanchez, K. Y. Fong, H. Bhaskaran, S. Lamoreaux, and H. X. Tang, Phys. Rev. Lett. **109**, 027202 (2012).
[14] A. Lambrecht, C. Genet, F. Intravaia, and S. Reynaud, J. Phys. IV France **119**, 43 (2004).
[15] Genet, C., Lambrecht, A., and Reynaud, S., Eur. Phys. J. Special Topics **160**, 183 (2008).
[16] A. Lambrecht and S. Reynaud, Phys. Rev. Lett. **84**, 5672 (2000).
[17] A. Canaguier-Durand, G.-L. Ingold, M.-T. Jaekel, A. Lambrecht, P. A. M. Neto, and S. Reynaud, Phys. Rev. A **85**, 052501 (2012).
[18] A. Canaguier-Durand, A. Gérardin, R. Guérout, P. A. M. Neto, V. V. Nesvizhevsky, A. Y. Voronin, A. Lambrecht, and S. Reynaud, Phys. Rev. A **83**, 032508 (2011).
[19] L. Rosa and A. Lambrecht, Phys. Rev. D **82**, 065025 (2010).
[20] P. W. Milonni, R. J. Cook, and M. E. Goggin, Phys. Rev. A **38**, 1621 (1988).
[21] M. Kardar and R. Golestanian, Rev. Mod. Phys. **71**, 1233 (1999).
[22] A. Ashourvan, M. Miri, and R. Golestanian, Phys. Rev. Lett. **98**, 140801 (2007).
[23] A. Ashourvan, M. Miri, and R. Golestanian, Phys. Rev. E **75**, 040103 (2007).
[24] H. B. Chan, V. A. Aksyuk, R. N. Kleiman, D. J. Bishop, , and F. Capasso, Phys. Rev. Lett. **87**, 211801 (2001).
[25] D. Zhabinskaya and E. J. Mele, Phys. Rev. B **80**, 155405 (2009).
[26] T. Emig, Phys. Rev. Lett. **98**, 160801 (2007).
[27] E. Buks and M. L. Roukes, Phys. Rev. B **63**, 033402 (2001).
[28] M. G. Moharam, E. B. Grann, D. A. Pommet, and T. K. Gaylord, J. Opt. Soc. Am. A **12**, 1068 (1995).
[29] A. Lambrecht and V. Marachevsky, Phys. Rev Lett. **101**, 160403 (2008).
[30] G. Bimonte, Phys. Rev. A **80**, 042102 (2009).
[31] R. Messina and M. Antezza, Phys. Rev. A **84**, 042102 (2011).
[32] M. Antezza, L. P. Pitaevskii, S. Stringari, and V. B. Svetovoy, Phys. Rev. Lett. **97**, 223203 (2006).
[33] D. Polder and M. V. Hove, Phys. Rev. B **4**, 3303 (1971).
[34] C. M. Hargreaves, Phys. Lett. A **30**, 491 (1969).
[35] J. Lussange, R. Guérout, F. Rosa, J.-J. Greffet, A. Lambrecht, and S. Reynaud, Phys. Rev. B **86**, 085432 (2012).
[36] R. Guérout, J. Lussange, F. Rosa, J.-P. Hugonin, D. Dalvit, J.-J. Greffet, A. Lambrecht, and S. Reynaud, Phys. Rev. B **85**, 180301(R) (2012).

Casimir Force on a Surface with Shallow Nanoscale Corrugations: Geometry and Finite Conductivity Effects

Y. Bao,[1] R. Guérout,[2] J. Lussange,[2] A. Lambrecht,[2] R. A. Cirelli,[3] F. Klemens,[3] W. M. Mansfield,[3] C. S. Pai,[3] and H. B. Chan[4,*]

[1]*Department of Physics, University of Florida, Gainesville, Florida 32611, USA*
[2]*Laboratoire Kastler-Brossel, CNRS, ENS, Université Pierre et Marie Curie case 74, Campus Jussieu, F-75252 Paris Cedex 05, France*
[3]*Bell Laboratories, Alcatel-Lucent, Murray Hill, New Jersey 07974, USA*
[4]*Department of Physics, the Hong Kong University of Science and Technology, Hong Kong, China*

(Received 16 September 2010; revised manuscript received 12 October 2010; published 15 December 2010)

We measure the Casimir force between a gold sphere and a silicon plate with nanoscale, rectangular corrugations with a depth comparable to the separation between the surfaces. In the proximity force approximation (PFA), both the top and bottom surfaces of the corrugations contribute to the force, leading to a distance dependence that is distinct from a flat surface. The measured Casimir force is found to deviate from the PFA by up to 10%, in good agreement with calculations based on scattering theory that includes both geometry effects and the optical properties of the material.

DOI: 10.1103/PhysRevLett.105.250402 PACS numbers: 12.20.Fv, 03.70.+k, 12.20.Ds, 42.50.Lc

The Casimir force between two neutral conductors arises from the change of the zero point energy associated with quantum fluctuation of the electromagnetic field in the presence of boundaries. Between two parallel plates, the Casimir force is attractive and its magnitude increases rapidly as the separation decreases. In recent years, the Casimir force has received significant attention, from fundamental interests to possible applications in micro and nanoelectromechanical systems [1–12]. For instance, fundamental questions on how to account for the temperature corrections to the Casimir force remain a controversial topic [13]. At the same time, there has been much progress in the control of the Casimir force by modifying the optical properties of the interacting surfaces, such as using dissimilar metals [6], replacing one surface with semiconductors with different carrier concentrations [7], and inserting fluid into the gap between the surfaces [11]. In addition, a number of efforts aim at generating repulsive Casimir forces with a vacuum gap using metamaterials [14,15].

Apart from the optical properties of the material, the Casimir force depends on the shape of the interacting objects in nontrivial ways. For small deviations from the planar geometry, the Casimir force can be estimated by the proximity force approximation (PFA) [16]. In the common experimental configuration of a sphere and plate, the PFA works well provided that the separation is much smaller than the radius of the sphere. However, the PFA breaks down for other geometries. Theoretical analysis indicates that for a thin conducting spherical shell [17] or a rectangular box with a certain aspect ratio [18], the Casimir energy has opposite sign to parallel plates, opening the possibility of generating repulsive Casimir forces. Advanced theoretical approaches are now capable of calculating the Casimir force between structures of arbitrary shapes [19–21]. These approaches are not limited to perfectly conducting objects, but can also take into account the optical properties of the material. Experimentally, revealing the strong geometry dependence of the Casimir force involves introducing deformations on a planar surface. The first such attempt was performed by Roy and Mohideen, who measured the Casimir force on surfaces with small sinusoidal corrugations [3]. Subsequently, the lateral Casimir force in similar structures has been demonstrated by the same team to deviate from the PFA [12]. Recently, we measured the Casimir force on a surface with an array of high aspect ratio trenches [8]. A deviation of up to 20% from the PFA is observed. While this experiment provides evidence for the nontrivial boundary dependence of the Casimir force, the measured results are smaller than the predicted values for perfect metallic structures of the same geometry [16]. It becomes apparent that a meaningful comparison of experimental results to theory would require both geometry effects and finite conductivity of the material to be included.

In our previous experiment [8], we considered the Casimir force between a surface with an array of deep rectangular trenches and another flat surface on top. The trench array is assumed to have solid volume fraction equal to p. In the PFA picture, the total interaction is a sum of two contributions: (i) the interaction between a fraction p of the flat surface and the top surface of the trench array separated by distance z; and (ii) the interaction between a fraction of $(1 - p)$ of the flat surface and the bottom of the trench array at distance $z + a$, where a is the depth of the trenches. The second contribution is negligible for such deep trenches because the Casimir force at this separation ($z + a > 1\ \mu$m) is too small to be detected in our measurement setup. Therefore, under the PFA, the force on the trench array is

practically identical to the force between two parallel flat surfaces at separation z multiplied by a constant factor p. In other words, for the deep trenches, the distance dependence of the force under the PFA is the same as a flat surface.

In this Letter, we report measurements of the Casimir force between a gold sphere and a silicon plate with nanoscale, rectangular corrugations with depth comparable to the separation between the surfaces. In the PFA, both the top and bottom surfaces of the corrugations contribute to the force, yielding a distance dependence that is distinct from a flat surface. The measured Casimir force is found to deviate from the PFA by about 10%. We present calculations based on scattering theory that includes the finite conductivity of silicon, yielding good agreement with measurement. Our results demonstrate that for surfaces with nanoscale deformations, the Casimir force depends on a profound interplay between geometry effects and material properties.

Figure 1(a) shows a scanning electron micrograph of the cross section of the trench array with periodicity of 400 nm. We fabricate the trenches by dry etching into a highly p-doped silicon wafer with a lithographically defined silicon oxide pattern as the etch mask. In the reactive ion etching step, an inductively coupled plasma of SF_6 and Ar was used without any passivation gas. The reactant flow rate, pressure and bias were optimized to yield a smooth and flat bottom surface so that its contribution to the PFA can be easily determined. Such a recipe, however, produced a sidewall at 94.6° to the top surface, close to but not exactly vertical. After etching, the oxide mask is removed using hydrofluoric acid (HF). Another sample, consisting of a flat surface with no corrugations, is also prepared. Both samples are fabricated from the same wafer to ensure that the optical properties of the silicon are identical.

Accurate determination of the dimensions of the trench array is crucial in the electrostatic force and the Casimir force calculations. Ten cross section views [similar to Fig. 1(a)] at different positions of the trench array are taken using a scanning electron microscope (SEM). The lengths of the top surface and the bottom surface in one period are measured to be $l_1 = 185.3 \pm 2.4$ nm and $l_2 = 199.1 \pm 4.2$ nm, respectively. An atomic force microscope is used to obtain the depth of the trenches. The average of one set of ten scans of 2 μm square and another set of 1 μm square at different locations gives $t = 97.8 \pm 0.7$ nm. This depth is chosen to be smaller than the typical separation between the two interacting bodies, so that the force from the bottom surface is not negligible if the PFA is assumed to be valid:

$$F_{\mathrm{PFA}} = (1/\lambda)\int_0^{\lambda} F_{\mathrm{flat}}(z(x))dx = p_1 F_{\mathrm{flat}}(z) + p_2 F_{\mathrm{flat}}(z+t) + 2\int_0^{p_3} F_{\mathrm{flat}}(z + tx/p_3)dx, \quad (1)$$

where F_{flat} is the force on a flat surface made of the same material, $p_1 = l_1/\lambda$, $p_2 = l_2/\lambda$ and $p_3 = (1 - p_1 - p_2)/2$. In Eq. (1), the first two terms represent the contributions of the top and bottom surfaces, respectively, accounting for ~97% of the force under the PFA. The third term introduces a small modification originating from the sidewalls that are not perfectly vertical. While deriving the force on such corrugated structures using the PFA is rather straight forward, the actual Casimir force is expected to deviate from the PFA due to its nontrivial dependence on the geometry of the interacting objects. Since such deviations increase with the ratio z/λ [16], the corrugated sample is chosen to have the smallest λ that can be reproducibly fabricated with our lithography and etching tools. Calculations of the Casimir force on this exact geometry using scattering theories will be presented later.

Figure 1(b) shows a schematic (not to scale) of a micromechanical oscillator that measures the force gradient between the corrugated surface and a spherical surface. The oscillator is made of a 3.5 μm thick, 500 μm square heavily doped polysilicon plate suspended by two torsional rods. Underneath the oscillator's top plate, there are two fixed electrodes. Torsional oscillations of the top plate are electrostatically excited when a small ac voltage close to the resonant frequency of the oscillator ($f_0 = 1783$ Hz and quality factor 32 000) is applied to one electrode. Motion of the top plate is detected by the capacitance change between the top plate and the electrodes using additional ac voltages at amplitude of 100 mV and frequency of 102 kHz. Two glass spheres, each with radius $R = 50$ μm, are coated with a layer of gold with thickness of 4000 A. They are stacked and attached onto one side of the top plate using conductive epoxy at a distance of $b = 210$ μm from the rotation axis.

Preparation of the silicon surfaces for force measurement involves a number of important steps. First, the native oxide on the surfaces of the silicon samples was removed by HF. This procedure also passivates the silicon surface so that oxide does not re-form in ambient pressure for a few hours [7]. To eliminate residual water on the corrugations, the silicon chip was baked at 350 °C for 15 min. Afterwards, the silicon sample is positioned face down at a few μm from the top of the spheres. The chamber is then immediately evacuated to a base pressure of 10^{-6} torr by dry pumps.

A closed-loop piezoelectric actuator controls the distance between the silicon sample and the sphere. The

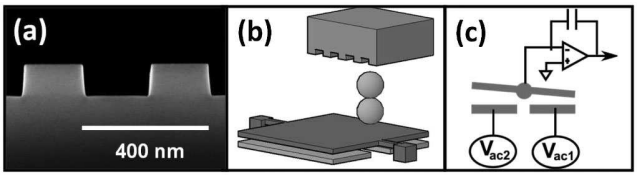

FIG. 1. (a) Scanning electron micrograph of the cross section view of the trench array. (b) Schematic of the experimental setup (not to scale). (c) Measurement scheme with electrical connections. V_{ac1} and V_{ac2} are the excitation voltages applied to the bottom electrodes.

distance z is given by $z = z_0 - z_{\text{piezo}} - b\theta$, where z_0 is the initial gap between two surfaces, z_{piezo} is the piezo extension and $b\theta$ is a correction term to account for the tilting angle θ of the top plate. A phase locked loop is used to track the frequency shift of the oscillator as the sphere approaches the silicon sample. At small oscillations where nonlinear effects can be neglected, the shift in the resonant frequency is proportional to the force gradient

$$\Delta f = C\frac{\partial F}{\partial z}, \tag{2}$$

where $C = -b^2/8\pi^2 I f_0$ and I is the moment of inertia of the top plate together with the two spheres. The oscillation amplitude of the oscillator is reduced as z decreases to avoid the oscillation from becoming nonlinear.

We apply electrostatic forces to calibrate the constant C and the initial distance between the surfaces z_0. The electrostatic force between the grounded gold sphere and the flat plate at voltage V is given by:

$$F_e = 2\pi\epsilon_0(V - V_0)^2 \sum_{n=1}^{\infty} \frac{[\coth(\alpha) - n\coth(n\alpha)]}{\sinh(n\alpha)}, \tag{3}$$

where ϵ_0 is the permittivity of vacuum, $\alpha = \cosh^{-1}(1 + d/R)$ and d is the separation between the sphere and the plate. The residual voltage V_0 is measured to be -0.499 V by finding the voltage at which the frequency shift Δf attains minimum at a fixed distance. V_0 is found to change by less than 3 mV for z ranging from 100 to 600 nm. In Fig. 2, the solid circles represent the measured electrostatic force gradient on the flat silicon sample at $V - V_0 =$ 300 mV and the solid line is a fit using Eqs. (2) and (3) after subtracting the contribution of the Casimir force (the measurement of which is described later). C is determined to be $614 \pm 3\ \text{m N}^{-1}\,\text{s}^{-1}$ by averaging six sets of data with $V - V_0$ between 245 and 300 mV. For the corrugated silicon sample, the calibration procedure is similar. However, since there is no analytic expression for the electrostatic force, it is necessary to solve Poisson's equation in 2D numerically. The boundary conditions, as shown in the inset of Fig. 2, are set by maintaining a fixed potential between the trench array and a flat surface, with periodic boundary conditions applied to one period of the array. Then, the potential distribution is calculated using finite element analysis, with the confined area divided into $N > 10,000$ triangles. Since $R \gg z$, the proximity force approximation $F_{s,\text{grat}} = 2\pi R E_{f,\text{grat}}$ is used to obtain the force $F_{s,\text{grat}}$ between a sphere and a corrugated surface, where $E_{f,\text{grat}}$ is the electrostatic energy per unit area between a flat surface and a corrugated surface. To ensure the convergence of the numerical calculation, we checked that the calculated force varies by less than 0.1% even when N is doubled.

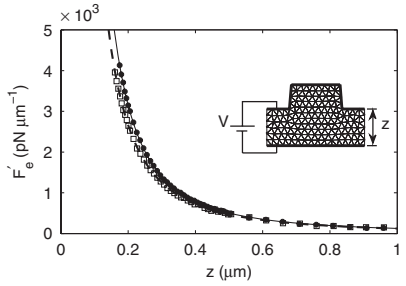

FIG. 2. The electrostatic force gradient as a function of distance for $V = V_0 + 300$ mV on the flat silicon surface (solid circles) and corrugated silicon structure (hollow squares). The solid line is a fit using Eq. (3) for a flat surface and the dash line is a fit using the numerical calculations for the corrugated structure. Inset: Meshing of the gap between the two surfaces to solve the Poisson equation in 2D ($z = 150$ nm). The number of triangles is 40 times larger in the actual calculation.

Next, the Casimir force gradient $F'_{c,\text{flat}}$ on the flat silicon surface is measured by setting V equal to V_0. In Fig. 3(a), the circles are the measured data and the solid line represents the theoretical values. To account for the finite conductivity of the materials, the dielectric functions evaluated at imaginary frequencies $\epsilon(i\omega)$ are used in Lifshitz's formula. For gold, we use tabulated optical data. The low frequency values are extrapolated by the Drude model $\epsilon_g(i\omega) = 1 + \frac{\omega_{p,g}^2}{\omega(\omega+\gamma_g)}$ with a plasma frequency $\omega_{p,g} =$ 9 eV and a relaxation rate $\gamma_g = 35$ meV. For silicon, the Drude-Lorentz model is used: $\epsilon_{si}(i\omega) = \epsilon_i(i\omega) + \frac{\omega_{p,si}^2}{\omega(\omega+\gamma_{si})}$. $\epsilon_i(i\omega)$ is the dielectric function for intrinsic

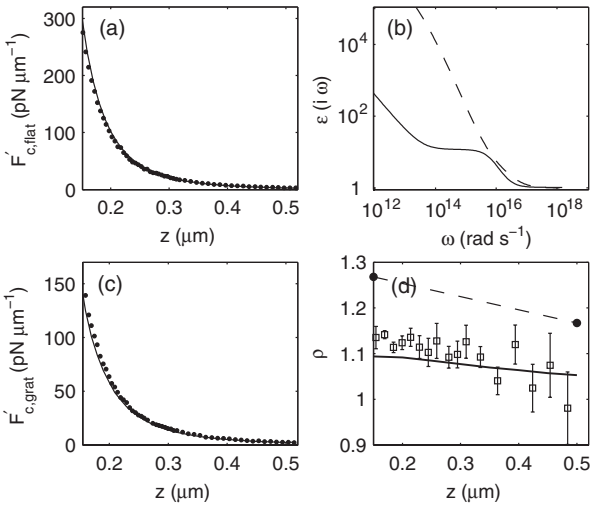

FIG. 3. (a) Measured Casimir force gradient between the gold sphere and the flat silicon surface $F'_{c,\text{flat}}$. The solid line represents the theoretical calculation including finite conductivity and surface roughness corrections. (b) Dielectric functions evaluated at imaginary frequencies for doped silicon (plain line) and gold (dashed line). (c) Measured Casimir force gradient on corrugated silicon structure. The line represents the force gradient expected from the PFA. (d) The squares are the ratio ρ of the measured Casimir force gradient to the force gradient expected from the PFA. The solid line plots the theoretical values including both geometry and finite conductivity effects. The dashed line is a linear interpolation between the two theoretical values (solid circles) assuming perfect conductors.

silicon, taken from Ref. [22]. The plasma frequency $\omega_{p,si}$ (1.36×10^{14} rad s^{-1}) and the relaxation rate γ_{si} (4.75×10^{13} rad s^{-1}) are interpolated from the data in Ref. [23] for a carrier density of 2×10^{18} cm^{-3} determined from the dc conductivity of the wafer. Figure 3(b) shows the dielectric functions used for doped silicon and gold. The force calculated by Lifshitz's formula is further modified by the roughness correction using the geometrical averaging method [24]. The contribution to the roughness correction ($< 1\%$ of the total force) originates mainly from the gold surface (~ 4 nm rms) rather than the silicon wafer (~ 0.6 nm rms).

The Casimir force gradient $F'_{c,\mathrm{grat}}$ between the same gold sphere and the corrugated silicon sample is then measured and plotted as circles in Fig. 3(c). Comparison to the PFA is performed by evaluating Eq. (1) with the measured Casimir force on the flat silicon surface. As described earlier, the force gradient on the corrugations under the PFA, $F'_{c,\mathrm{PFA}}$, is the sum of the force on the top and bottom surfaces, with a small contribution from the slightly slanted sidewalls. The deviations of the measured Casimir force from the PFA arise due to the strong geometry dependence of the Casimir force. For a more quantitative analysis of the deviation, the ratio $\rho = F'_{c,\mathrm{grat}}/F'_{c,\mathrm{PFA}}$ is plotted in Fig. 3(d). The measured $F'_{c,\mathrm{grat}}$ clearly exceeds $F'_{c,\mathrm{PFA}}$, by up to 15%.

We perform exact calculations for the Casimir force $F_{c,\mathrm{grat}}(z)$ per unit area between a flat gold plate and the corrugated silicon surface, taking into account the nonspecular reflections introduced by the grating structure. Then, we use the PFA to relate the sphere-plane and the plane-plane geometries according to $F'_{c,\mathrm{grat}} = 2\pi R F_{c,\mathrm{flat}}$. The theory for calculating the Casimir energy based on scattering theory [19] for structures involving gratings has been presented elsewhere [25] and will be only briefly summarized. The zero temperature Casimir force per unit area between two reflecting objects separated by a distance z is

$$F = -\hbar \iiint \mathrm{tr}((\mathbf{1} - \mathcal{M})^{-1} \partial_z \mathcal{M}) d^2\mathbf{k}_\perp d\xi, \qquad (4)$$

where $\mathbf{k}_\perp$ gathers the components of the wave vector in the plane of the objects and $\xi = i\omega$ is the Wick-rotated imaginary frequency. $\mathcal{M}$ is the open-loop function $\mathcal{M} = \mathbf{R_1}(\xi) e^{-\boldsymbol{\kappa} z} \mathbf{R_2}(\xi) e^{-\boldsymbol{\kappa} z}$ with $\mathbf{R_1}$ and $\mathbf{R_2}$ the reflection operators for the two objects and $\boldsymbol{\kappa} = \sqrt{\xi^2/c^2 + \mathbf{k}_\perp^2}$. For planar objects, the reflection operators are diagonal in the plane wave basis and collect the appropriate Fresnel coefficients. For gratings, this does not hold anymore. The reflection operators are not diagonal as they mix different polarizations and account for nonspecular reflections. Therefore, in general the matrices $\boldsymbol{R}_i$ and $e^{-\boldsymbol{\kappa} z}$ do not commute and we write $-\partial_z \mathcal{M} = \mathbf{R_1}(\xi) \boldsymbol{\kappa} e^{-\boldsymbol{\kappa} z} \mathbf{R_2}(\xi) e^{-\boldsymbol{\kappa} z} + \mathbf{R_1}(\xi) e^{-\boldsymbol{\kappa} z} \mathbf{R_2}(\xi) \boldsymbol{\kappa} e^{-\boldsymbol{\kappa} z}$. The results of the exact calculation, normalized by the PFA, are plotted as the solid line in Fig. 3(d), yielding good agreement with measurements. If the gold and silicon surfaces were replaced by perfect metals, the calculated deviations from the PFA for the corrugated surface becomes considerably larger, exceeding the measured value by about a factor of 2, as shown in the dashed line in Fig. 3(d). Here the ratio ρ is calculated for zero temperature, a valid assumption given that at 300 K, the thermal correcton to the Casimir force on a flat surface at $z < 0.5$ μm is negligible.

Our results demonstrate that the optical properties of the material must be included in predicting the Casimir force between structures of nonconventional shapes, due to the nontrivial interplay with geometry effects. It is possible to both calculate and measure the Casimir force in nanostructured surfaces with high accuracy. The interplay between finite conductivity and geometry effects holds promise as an important tool to control the Casimir force between mechanical components at close proximity.

Y. B. and H. B. C. are supported by DOE Grant No. DE-FG02-05ER46247 and NSF Grant No. DMR-0645448. R. G., J. L., and A. L. are supported by the European Science Foundation (ESF) within the activity "New Trends and Applications of the Casimir Effect" (www.casimir-network.com) and by the French National Research Agency (ANR) through grant No ANR-06-NANO-062-MONACO project.

*hochan@ust.hk

[1] S. K. Lamoreaux, Phys. Rev. Lett. **78**, 5 (1997).
[2] U. Mohideen and A. Roy, Phys. Rev. Lett. **81**, 4549 (1998).
[3] A. Roy and U. Mohideen, Phys. Rev. Lett. **82**, 4380 (1999).
[4] H. B. Chan *et al.*, Science **291**, 1941 (2001).
[5] G. Bressi *et al.*, Phys. Rev. Lett. **88**, 041804 (2002).
[6] R. S. Decca *et al.*, Phys. Rev. Lett. **91**, 050402 (2003).
[7] F. Chen *et al.*, Phys. Rev. Lett. **97**, 170402 (2006).
[8] H. B. Chan *et al.*, Phys. Rev. Lett. **101**, 030401 (2008).
[9] S. de Man *et al.*, Phys. Rev. Lett. **103**, 040402 (2009).
[10] G. Jourdan *et al.*, Europhys. Lett. **85**, 31 001 (2009).
[11] J. N. Munday, F. Capasso, and V. A. Parsegian, Nature (London) **457**, 170 (2009).
[12] H. C. Chiu *et al.*, Phys. Rev. B **81**, 115417 (2010).
[13] G. L. Klimchitskaya, U. Mohideen, and V. M. Mostepanenko, Rev. Mod. Phys. **81**, 1827 (2009).
[14] F. S. S. Rosa, D. A. R. Dalvit, and P. W. Milonni, Phys. Rev. Lett. **100**, 183602 (2008).
[15] R. Zhao *et al.*, Phys. Rev. Lett. **103**, 103602 (2009).
[16] R. Buscher and T. Emig, Phys. Rev. A **69**, 062101 (2004).
[17] T. H. Boyer, Phys. Rev. **174**, 1764 (1968).
[18] G. J. Maclay, Phys. Rev. A **61**, 052110 (2000).
[19] A. Lambrecht, P. A. M. Neto, and S. Reynaud, New J. Phys. **8**, 243 (2006).
[20] S. J. Rahi *et al.*, Phys. Rev. D **80**, 085021 (2009).
[21] M. T. H. Reid *et al.*, Phys. Rev. Lett. **103**, 040401 (2009).
[22] A. Lambrecht *et al.*, Europhys. Lett. **77**, 44 006 (2007).
[23] L. Duraffourg and P. Andreucci, Phys. Lett. A **359**, 406 (2006).
[24] F. Chen *et al.*, Phys. Rev. A **74**, 022103 (2006).
[25] A. Lambrecht and V. N. Marachevsky, Phys. Rev. Lett. **101**, 160403 (2008).

PHYSICAL REVIEW B **85**, 180301(R) (2012)

Enhanced radiative heat transfer between nanostructured gold plates

R. Guérout,[1] J. Lussange,[1] F. S. S. Rosa,[2] J.-P. Hugonin,[2] D. A. R. Dalvit,[3] J.-J. Greffet,[2] A. Lambrecht,[1] and S. Reynaud[1]

[1]*Laboratoire Kastler-Brossel, CNRS, ENS, UPMC, Case 74, F-75252 Paris, France*

[2]*Laboratoire Charles Fabry, Institut d'Optique, CNRS, Université Paris-Sud, Campus Polytechnique, RD128, F-91127 Palaiseau Cedex, France*

[3]*Theoretical Division, Mail Stop B213, Los Alamos National Laboratory, Los Alamos, New Mexico 87545, USA*

(Received 27 January 2012; revised manuscript received 7 March 2012; published 24 May 2012)

We compute the radiative heat transfer between nanostructured gold plates in the framework of the scattering theory. We predict an enhancement of the heat transfer as we increase the depth of the corrugations while keeping the distance of closest approach fixed. We interpret this effect in terms of the evolution of plasmonic and guided modes as a function of the grating's geometry.

DOI: 10.1103/PhysRevB.85.180301 PACS number(s): 44.40.+a, 42.50.−p, 68.35.−p

The far-field radiative heat transfer between good conductive metals is very low at room temperature, since they are very good reflectors at the infrared frequencies of blackbody radiation. The radiative heat transfer is enhanced in the near field, due to the contribution of evanescent surface modes.[1–3] Polar materials such as SiO_2 or SiC are in addition favored by the contribution of surface phonon polaritons whose resonance frequencies lie in the infrared.[4] There is an analogous effect for metals arising from the surface plasmon resonances but those lie in the ultraviolet and do not contribute significantly to the heat transfer.[5]

It has been shown recently that the radiative heat transfer can be controlled by nanostructuring the interfaces periodically. When the period d is much smaller than the wavelength λ and the separation distance L, the system can be treated using an effective refractive index for the equivalent homogeneous medium. It has been shown that the induced anisotropy introduces additional modes[6] and also allows modulating the flux.[7] For periods on the order of the wavelength, a full solution of Maxwell equations is needed. The heat transfer between two periodic slabs has been studied within a two-dimensional approximation for p polarization using a finite difference time domain (FDTD) technique.[8] A flux enhancement attributed to the excitation of the structure's modes was found. While FDTD allows modeling complex shapes easily, dealing with bulk three-dimensional (3D) media and accounting for polarization effects has not been achieved so far, to the best of our knowledge.

In this Rapid Communication, we compute the radiative heat transfer between one-dimensional (1D) gold lamellar gratings in the framework of the scattering theory. We do include all propagation directions (the so-called conical diffraction) and all polarization states, which is of critical importance in order to deal quantitatively with cross-polarization effects.[9] The scattering theory is the most successful technique for treating the Casimir effect between bodies at thermodynamic equilibrium.[10,11] The method determines the electromagnetic field in the space between the two bodies in interaction in order to compute the Casimir force in terms of the reflection amplitudes on the two bodies. When the two bodies are not at the same temperature, there is a net flux of energy transferred from the warm body to the cold one. Recently, this heat transfer problem between two bodies kept at different temperatures has also been formulated in terms of the scattering properties of the bodies.[12–15]

In the following, we use the scattering amplitudes which have already been calculated for studying the Casimir interaction between 1D lamellar gratings[16] and deduce the heat flux when the two bodies are at different temperatures. We show that the heat flux is largely enhanced when the corrugation depth is increased while keeping the distance of closest approach fixed. We attribute the heat flux growth to the excitation of guided modes and surface plasmons whose frequencies change with the corrugation depth.

We consider the cavity formed by two gratings separated by a distance of closest approach L measured so as to vanish at contact (Fig. 1). The gratings are aligned and not displaced laterally. We model the gold permittivity with a Drude model $\epsilon(\omega) = 1 - \frac{\omega_P^2}{\omega(\omega+\imath\gamma)}$ with $\omega_P = 9$ eV and $\gamma = 35$ meV. We write the heat flux q between two bodies at temperatures T_1 and T_2 as[3]

$$q = \iiint \left[e_{T_1}(\omega) - e_{T_2}(\omega)\right]\mathcal{T}_L(\mathbf{k},\omega)\frac{d\omega d^2\mathbf{k}}{(2\pi)^3}, \tag{1}$$

where $e_T(\omega) = \hbar\omega(e^{\hbar\omega/k_BT} - 1)^{-1}$ is the mean energy per mode of frequency ω at temperature T, while $\mathcal{T}_L(\mathbf{k},\omega)$ is the sum (trace) of the transmission factors for all the modes of frequency ω and lateral wave vector $\mathbf{k}$ between the two gratings separated by a distance L.[17,18] The expression of this transmission factor is given by scattering amplitudes

$$\mathcal{T}_L(\mathbf{k},\omega) = \mathrm{tr}(\mathbf{D}\mathbf{W_1}\mathbf{D}^\dagger\mathbf{W_2}), \tag{2a}$$

$$\mathbf{D} = (\mathbf{1} - \mathbf{S_1}\mathbf{S_2})^{-1}, \tag{2b}$$

$$\mathbf{W_1} = \mathbf{\Sigma}_{-1}^{pw} - \mathbf{S_1}\mathbf{\Sigma}_{-1}^{pw}\mathbf{S_1}^\dagger + \mathbf{S_1}\mathbf{\Sigma}_{-1}^{ew} - \mathbf{\Sigma}_{-1}^{ew}\mathbf{S_1}^\dagger, \tag{2c}$$

$$\mathbf{W_2} = \mathbf{\Sigma}_{1}^{pw} - \mathbf{S_2}^\dagger\mathbf{\Sigma}_{1}^{pw}\mathbf{S_2} + \mathbf{S_2}^\dagger\mathbf{\Sigma}_{1}^{ew} - \mathbf{\Sigma}_{1}^{ew}\mathbf{S_2}, \tag{2d}$$

$$\mathbf{S_1} = \mathbf{R_1}(\mathbf{k},\omega), \tag{2e}$$

$$\mathbf{S_2} = e^{\imath k_z L}\mathbf{R_2}(\mathbf{k},\omega)e^{\imath k_z L}. \tag{2f}$$

Mode counting is defined over frequency ω and lateral wave vector $\mathbf{k}$ restricted to the first Brillouin zone, due to the Bloch theorem. $k_z = \sqrt{\omega^2/c^2 - \mathbf{k}^2}$ is the longitudinal wave vector for the Fabry-Pérot cavity, with the principal square root used in its definition $-\frac{\pi}{2} < \arg k_z \leqslant \frac{\pi}{2}$. The operators $\mathbf{\Sigma}_n^{pw/ew} = k_z^n\mathbf{\Pi}^{pw/ew}$ involve the projectors $\mathbf{\Pi}^{pw/ew}$ on the propagative

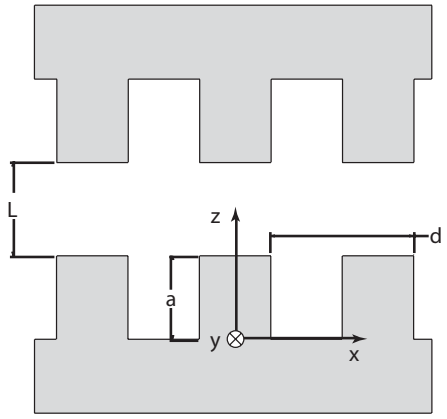

FIG. 1. The conventions used in the present article. The grating period is d, the corrugation depth is a, and the distance of closest approach of the two gratings is L. The lines of the grating are along the y direction, while the Fabry-Pérot cavity between the two gratings is along the z direction.

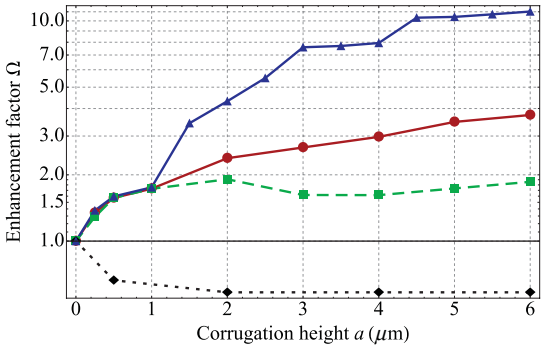

FIG. 2. (Color online) The enhancement factor Ω between two gold gratings as a function of the depth a of the corrugations, with the distance of closest approach kept fixed $L = 1$ μm. Blue solid curve (triangles): period $d = 1$ μm. Red solid curve (circles): period $d = 2.5$ μm. Green dashed curve: period $d = 10$ μm. Black dotted curve: proximity approximation.

or the evanescent sector, respectively. $\mathbf{S_1}$ and $\mathbf{S_2}$ are scattering operators defined from the reflection operators $\mathbf{R_1}(\mathbf{k},\omega)$ and $\mathbf{R_2}(\mathbf{k},\omega)$. $\mathbf{S_i}$ are represented in the basis of the wave vectors $\{\mathbf{k}^{(n)}\}$ coupled by the grating. We define $\mathbf{k}^{(n)} = \mathbf{k} + n\frac{2\pi}{d}\hat{\mathbf{e}}_x$ where d is the grating period, $\hat{\mathbf{e}}_x$ the direction perpendicular to the lines of the grating (see Fig. 1), and n runs from $-N$ to $+N$, where N is the highest diffraction order retained. The operators $\mathbf{S_i}$ are square matrices of dimension $2(2N + 1)$ (Ref. 16) as well as all bold operators appearing in Eqs. (2). All scattering operators appearing in Eqs. (2) are represented in the (s/p) (also denoted TE/TM) polarization basis, well adapted to propagative fields. The reflection operators are calculated following the rigorous coupled-wave analysis (RCWA) method described in Ref. 19: The fields are expressed in terms of a Rayleigh expansion in both homogeneous regions $z < 0$ and $z > a$. In the corrugated region $0 > z > a$, the fields are developed in Fourier components. The Maxwell equations are solved in each region and writing the continuity of each Rayleigh and Fourier components at the boundaries $z = 0$ and $z = a$ leads to the reflection and transmission coefficients for the grating. In the limit of an infinite number of Fourier harmonics, this method solves exactly the diffraction of the fields by the grating. Metallic gratings are known to be difficult to account for using the RCWA method. We incorporate in the RCWA formalism the modifications presented in Ref. 20 which greatly improve the convergence rate for the reflection coefficients of a p-polarized light impinging on a metallic grating, and our calculations are performed with $N = 51$ which shows converged results.

In the following, we apply formula (1) to compute the heat transfer coefficient h defined as $h = \frac{q}{T_1 - T_2}$ for two temperatures T_1 and T_2 close enough to each other, say, for example, $T_1 = 310$ K and $T_2 = 290$ K. We note that $e_{T_1} - e_{T_2}$ acts as a cutoff function for frequencies greater than the thermal frequency $\omega_T = \frac{2\pi c}{\lambda_T} \approx 2.5 \times 10^{14}$ rad s^{-1} ($\lambda_T \approx 7.6$ μm). The transmission factor $\mathcal{T}_L(\mathbf{k},\omega)$ thus exhibits the mode structure for the problem under study (Fig. 1) while (1) integrates the contributions of all these modes to the heat transfer, taking into account the values of their frequencies with respect to ω_T (more discussions below).

For a depth of the corrugation $a = 0$, we recover the heat transfer coefficient $h_0(L) = 0.16$ W m^{-2}K^{-1} between two gold plates separated by a distance $L = 1$ μm. For a non-null depth a, we introduce the factor of enhancement of heat transfer with respect to noncorrugated plates

$$\Omega = \frac{h(L)}{h_0(L)}. \tag{3}$$

We present in Fig. 2 the enhancement factor Ω as a function of the corrugation depth a, with the distance of closest approach $L = 1$ μm and the filling factor $p = 0.5$ kept fixed. The blue solid curve corresponds to a period $d = 1$ μm for the gratings while the red solid curve corresponds to a period $d = 2.5$ μm. The dashed curve corresponds to a period $d = 10$ μm. As the corrugations become deeper, we see a striking increase in the heat transfer coefficient. We note that the enhancement factor is largely independent of the grating period up to a corrugation depth $a \approx 1$ μm. For a period $d = 1$ μm for which the effect is more important, we get an enhancement up to a factor 10 for $a = 6$ μm. For a period $d = 2.5$ μm, the enhancement reaches nearly a factor 4 for $a = 6$ μm. For the largest period $d = 10$ μm, the enhancement still reaches nearly a factor 2 at $a = 6$ μm.

For comparison, we have shown as the dotted line in Fig. 2 the prediction of the proximity approximation (PA) which amounts to adding plane-plane heat transfer contributions, as if they were independent,

$$\Omega^{\mathrm{PA}} = p + (1 - p)\frac{h_0(L + 2a)}{h_0(L)}. \tag{4}$$

As expected, the PA predicts a decrease of Ω when a is increased, in complete contradiction with the exact results shown by the solid and dashed curves.

In the remainder of this Rapid Communication, we analyze the electromagnetic mode structure in order to explain the increase of the heat transfer.[17,18] To this aim, we use the scattering formula (1) and show that, as we increase the corrugation depth, some modes of the system are indeed brought to the infrared frequencies and thus are able to

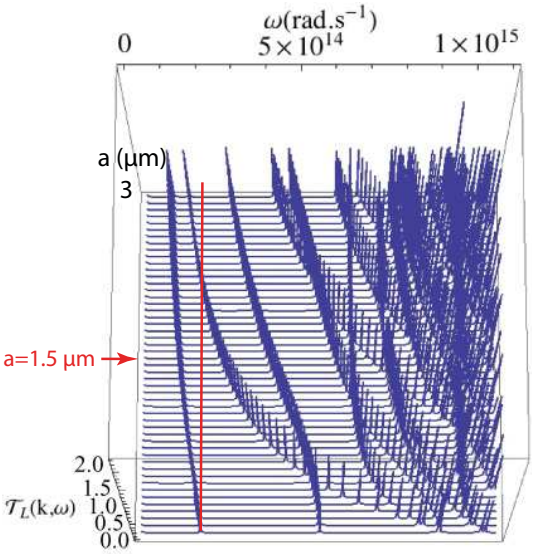

FIG. 3. (Color online) The transmission factor for two gold gratings as a function of the frequency ω and the corrugations depth a. The lower curve is for plane-plane $a = 0$ while the upper one is for a corrugations depth $a = 3$ μm. The vertical red line is the light line. The horizontal arrow at $a = 1.5$ μm shows a cut of this plot represented on Fig. 4.

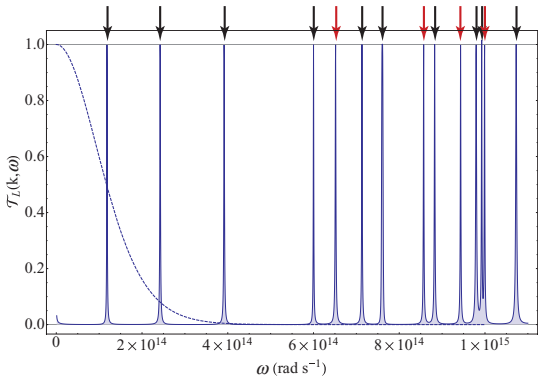

FIG. 4. (Color online) The transmission factor for two gold gratings with corrugation depth $a = 1.5$ μm as a function of frequency ω. The arrows indicate the position of the modes in a direct mode calculation [red (gray) for s polarization and black for p polarization]. The dashed curve is the function $\frac{e_{T_1}-e_{T_2}}{k_B(T_1-T_2)}$.

contribute to the heat transfer. The mode structure is described by the transmission factor $\mathcal{T}_L(\mathbf{k},\omega)$ that reaches its maximum value 1 at the resonances of the corrugated cavity. Our system is periodic so that the mode structure, distributed over the whole range of wave vectors in the absence of corrugations, now shows many branches folded in the first Brillouin zone. More precisely, there are $2(2N + 1)$ branches where the factor 2 is due to the two polarizations and the factor $2N + 1$ is the number of orders (or branches) used when taking into account mode coupling by diffraction on the gratings.

We represent in Fig. 3 the sum of transmission factors $\mathcal{T}_L(\mathbf{k},\omega)$ over all polarizations and all branches. It is shown as a function of the frequency ω and the depth of the corrugations a for a fixed value of the transverse wave vector $\mathbf{k} = (\frac{\pi}{2d},0)$, here chosen to be in the middle of the positive-k_x first Brillouin zone. The plot corresponds to the period $d = 2.5$ μm, which was shown as the solid curve in Fig. 2. The vertical red line represents the light line $\omega = ck_x \approx 1.88 \times 10^{14}$ rad s^{-1}.

It clearly appears in Fig. 3 that the transmission factor takes significant values only on resonances which correspond to the mode structure of the corrugated cavity. The transmission factor $\mathcal{T}_L(\mathbf{k},\omega)$ goes to a maximum value of 1 for each nondegenerate mode $(\mathbf{k},\omega)$; it can be 2 if two modes cross each other and we see one of these occurrences in the figure. The general trend is clear on the diagram: As the depth a of the corrugations is increased, new modes appear, with frequencies decreasing as a increases. When these modes enter into the thermal window $\omega \lesssim \omega_T$ they contribute more and more to the heat transfer. This explains the enhancement of the heat flux, due to the presence of additional modes in the thermal window for a deeply corrugated structure.

We now examine in more detail the nature of the modes. While varying the corrugation depth a from 0 to 3 μm we can follow the evolution of each mode. Note that, for $k_y = 0$, the polarizations $\sigma = s$ and $\sigma = p$ are not mixed (however, the computation of h takes into account all modes for which polarization mixing is important).

We show in Fig. 4 the modes calculated for a particular corrugation depth $a = 1.5$ μm indicated by the red horizontal line on Fig. 3. The position of the peaks have been confirmed through a direct mode calculation[21] of the eigenfrequencies of the structure modes obtained for p (black arrows) and s (red arrows) polarizations. In addition to the excellent agreement between the peaks of the transmission factor and the directly calculated modes (arrows on Fig. 4), direct mode calculations show the fields and, therefore, allow us to identify the first few modes. For the second p polarization and the first s polarization modes appearing at $\omega \approx 2.4 \times 10^{14}$ rad s^{-1} and $\omega \approx 6.5 \times 10^{14}$ rad s^{-1} in particular, the frequencies are largely independent upon the value of k_x, which is usually the signature of guided modes. By looking at the fields corresponding to those two modes, we indeed confirmed that the electric field is to some extent confined in the waveguides formed by the corrugations.

It is also worth discussing the shape of the resonance curve drawn by the variation of the transmission factor in the vicinity of a mode. In Fig. 5, we focus on the modes which lie inside the thermal window. In the case considered here of sharp, isolated modes, the resonance of the transmission factor shows a Lorentzian profile. We have checked that the two parameters of this profile are identified respectively to the real and imaginary parts of the complex frequency, with mode calculation of the dissipative structure defined with complex frequencies and real wave vectors.[3] This proves that the variation of the transmission factor contains all the relevant information about the mode structure. Not only the frequencies but also their finite lifetime are well described in the case considered here of lossy materials.

This discussion allows one to predict the effect of a change of the dissipation parameter γ. As this parameter is the only one to determine the widths of the peaks in the transmission factor $\mathcal{T}_L(\mathbf{k},\omega)$, one deduces that these widths vary linearly with γ. As a direct consequence of Eq. (1) and as long as

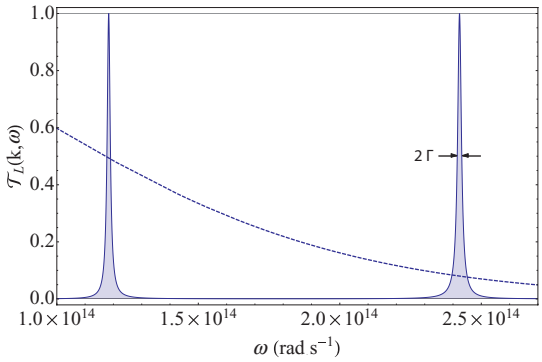

FIG. 5. (Color online) Same as Fig. 4 for the first two modes which are in the thermal window. Each peak can be fitted by a Lorentzian of resonance frequency ω_0 and half width at half maximum Γ. The dashed curve is the function $\frac{e^{T_1}-e^{T_2}}{k_B(T_1-T_2)}$.

the modes remain sharp and isolated, it follows that the heat fluxes vary in proportion of γ, so that the enhancement factor Ω, defined in Eq. (3) and drawn on Fig. 2, is independent of the dissipation parameter γ.

We have theoretically demonstrated the enhancement of the heat transfer between two nanocorrugated gold plates in comparison with flat plates with the same distance of closest approach. This enhancement is due to the presence of additional modes in the thermal frequency window contributing to the heat transfer. We have described all the relevant information about the mode structure in terms of the transmission factor $\mathcal{T}_L(\mathbf{k},\omega)$ which appears in the scattering formula for the heat flux. We have discussed the enhancement of the heat transfer in a regime where the three characteristic lengths of the problem (the distance L between the gratings, the period d of the gratings, and the height a of the corrugations) are of the same order. We stress that neither the proximity nor the effective medium approximations can work in this regime. We have in fact shown that the proximity approximation predicts a decrease of the heat transfer, in complete contradiction with the striking enhancement of the heat flux observed in the exact results.

The authors thank the ESF Research Networking Programme CASIMIR (www.casimir-network.com) for providing excellent possibilities for discussions and exchange. The research described here has been supported by Triangle de la Physique Contract No. EIEM 2010-037T. This work was carried out under the auspices of the National Nuclear Security Administration of the US Department of Energy at Los Alamos National Laboratory under Contract No. DE-AC52-06NA25396. R.G. and D.A.R.D. thank LANL and ENS, respectively, for funding their stay at these institutions, where part of this work was done.

[1] D. Polder and M. V. Hove, Phys. Rev. B **4**, 3303 (1971).
[2] A. I. Volokitin and B. N. J. Persson, Rev. Mod. Phys. **79**, 1291 (2007).
[3] K. Joulain, J.-P. Mulet, F. Marquier, R. Carminati, and J.-J. Greffet, Surf. Sci. Rep. **57**, 59 (2005).
[4] J.-P. Mulet, K. Joulain, R. Carminati, and J.-J. Greffet, Appl. Phys. Lett. **78**, 2931 (2011).
[5] S. Shen, A. Narayanaswamy, and G. Chen, Nano Lett. **9**, 2909 (2009).
[6] S.-A. Biehs, P. Ben-Abdallah, F. S. S. Rosa, K. Joulain, and J.-J. Greffet, Opt. Express **19**, A1088 (2011).
[7] S.-A. Biehs, F. S. S. Rosa, and P. Ben-Abdallah, Appl. Phys. Lett. **98**, 243102 (2011).
[8] A. W. Rodriguez, O. Ilic, P. Bermel, I. Celanovic, J. D. Joannopoulos, M. Soljačić, and S. G. Johnson, Phys. Rev. Lett. **107**, 114302 (2011).
[9] F. Marquier, C. Arnold, M. Laroche, J.-J. Greffet, and Y. Chen, Opt. Express **16**, 5305 (2008).
[10] A. Lambrecht, A. Canaguier-Durand, R. Guérout, and S. Reynaud, in *Casimir Physics*, edited by D. A. R. Dalvit *et al.*, Lecture Notes in Physics, Vol. 834 (Springer, Berlin, 2011), Chap. 4.
[11] S. J. Rahi, T. Emig, and R. L. Jaffe, in Ref. 10, Chap. 5.
[12] G. Bimonte, Phys. Rev. A **80**, 042102 (2009).
[13] R. Messina and M. Antezza, Europhys. Lett. **95**, 61002 (2011).
[14] M. Krüger, T. Emig, and M. Kardar, Phys. Rev. Lett. **106**, 210404 (2011).
[15] P. Ben-Abdallah, S.-A. Biehs, and K. Joulain, Phys. Rev. Lett. **107**, 114301 (2011).
[16] A. Lambrecht and V. N. Marachevsky, Phys. Rev. Lett. **101**, 160403 (2008).
[17] S.-A. Biehs, E. Rousseau, and J.-J. Greffet, Phys. Rev. Lett. **105**, 234301 (2010).
[18] J. B. Pendry, J. Phys. A **16**, 2161 (1983).
[19] M. G. Moharam, E. B. Grann, D. A. Pommet, and T. K. Gaylord, J. Opt. Soc. Am. A **12**, 1068 (1995).
[20] P. Lalanne and G. M. Morris, J. Opt. Soc. Am. A **13**, 779 (1996).
[21] Q. Cao, P. Lalanne, and J.-P. Hugonin, J. Opt. Soc. Am. A **19**, 335 (2002).

Radiative heat transfer between two dielectric nanogratings in the scattering approach

J. Lussange,[1] R. Guérout,[1] F. S. S. Rosa,[2] J.-J. Greffet,[2] A. Lambrecht,[1] and S. Reynaud[1]
[1]*Laboratoire Kastler-Brossel, CNRS, ENS, UPMC, Case 74, F-75252 Paris, France*
[2]*Laboratoire Charles Fabry, Institut d'Optique, CNRS, Université Paris-Sud, Campus Polytechnique, RD128, F-91127 Palaiseau Cedex, France*
(Received 13 April 2012; published 20 August 2012)

We present a theoretical study of radiative heat transfer between dielectric nanogratings in the scattering approach. As a comparison with these exact results, we also evaluate the domain of validity of Derjaguin's proximity approximation (PA). We consider a system of two corrugated silica plates with various grating geometries, separation distances, and lateral displacement of the plates with respect to one another. Numerical computations show that while the PA is a good approximation for aligned gratings, it cannot be used when the gratings are laterally displaced. We illustrate this by a thermal modulator device for nanosystems based on such a displacement.

DOI: 10.1103/PhysRevB.86.085432 PACS number(s): 73.20.Mf, 44.40.+a, 41.20.Jb

I. INTRODUCTION

Recent experiments and theoretical work have given promising perspectives in the field of radiative heat transfer in the micrometer range.[1,2] It has been shown that radiative heat transfer greatly exceeds the black body limit for distances shorter than the average thermal wavelength, which is understood as an effect arising from the contribution of the evanescent waves. The studies of near-field heat transfer are of great interest to the design of both NEMS and MEMS which are naturally affected by possible side effects of heat exchange at the nanoscale. Other potential applications lie in the fields of nanotechnology, photonic crystals,[3] metamaterials,[4,5] thermalphotovoltaics,[6,7] multilayered structures,[8] improved resolution in nanostructure imaging, and new nanofabrication techniques.

While radiative heat transfer beyond Stefan-Boltzmann's law was observed experimentally[9] and described theoretically[10] over the last forty years, radiative heat transfer between two parallel flat plates at the nanoscale has been considered experimentally only recently.[11–13] The most interesting features of this field are the possible side effects of nontrivial geometries on the thermal emission of nanoobjects. Thus an in-depth study of heat transfer for different configurations has been performed over the years, ranging from the case of a particle facing a surface,[14–17] to particles or nanospheres facing each other,[18–22] or more recently to the sphere-plane geometry.[23,24] One should also note that for nearly flat surfaces where roughness is considered as a perturbation factor, certain perturbative approaches can be used.[25,26] But for larger geometrical irregularities, more accurate methods become necessary.[27] These more complex geometries are best described through a scattering approach.[24,28–30] Another exciting perspective is the study of the variation in heat transfer brought forth by surface polaritons in certain materials.[17] In this paper we focus on the interplay between the surface waves excitation and the surface profile, as shown in Fig. 1.

The fact that the radiative heat transfer in near-field considerably changes with variation of the separation distance between plane surfaces has already been shown.[1,23,31] When introducing a profile for the interfaces, the flux is expected to depend on the relative lateral displacement of the two surfaces denoted δ, as seen in Fig. 1.

This is all the more interesting as a simple argument based on the proximity approximation suggests a strong modulation of the flux. Indeed, by assuming that one can use locally the plane-plane heat transfer coefficient, it is seen that the flux is maximum for $\delta = 0$. The validity of the proximity approximation has been discussed in the context of a plane sphere[23] and between two spheres.[18,19] This validity in the context of lamellar gratings with subwavelength periods remains an open question. Here, we investigate this issue by using the exact formalism of scattering theory. Furthermore, we discuss the physical phenomena involved and show that the nature of the material needs to be taken into account when discussing the validity of the proximity approximation.

II. HEAT TRANSFER IN THE SCATTERING APPROACH

Based on the scattering formalism developed in Ref. 28, we consider two corrugated profiles at temperatures T_1 and T_2, as shown in Fig. 1. The heat transfer is constructed from the statistical average of the (x,y) sum over the z component of the Poynting vector S_z and is thus related to a flux. We define the wave vector $\mathbf{k} = (\mathbf{k}_\perp, k_z)$ with $k_z = \sqrt{\omega^2/c^2 - \mathbf{k}_\perp^2}$ defined with $-\pi/2 < \arg k_z \leqslant \pi/2$.

Following,[32] we then introduce the reflection operators $\mathbf{R_1}(\omega)$ and $\mathbf{R_2}(\omega)$ of the two gratings separated by a distance L, by which we understand the distance of closest approach, equal to zero at contact. We then set our scattering operators such that $\mathbf{S_1} = \mathbf{R_1}(\omega)$ and $\mathbf{S_2} = e^{\imath k_z L}\mathbf{R_2}(\omega)e^{\imath k_z L}$. According to the scattering formalism for gratings developed in Refs. 32 and 33, the scattering matrices are of dimensions $2(2N+1)$, where N is the order of diffraction.

We now define the operators $\Sigma_n^{p\omega/e\omega} = \frac{1}{2}k_z^n \Pi^{p\omega/e\omega}$ as constructed from the projectors on the propagative and evanescent sectors, respectively:

$$\Pi^{p\omega}_{\alpha\alpha'} = \delta_{\alpha\alpha'}[1 + \mathrm{sgn}(\omega^2/c^2 - \mathbf{k}_\perp^2)] \quad (1)$$

$$\Pi^{e\omega}_{\alpha\alpha'} = \delta_{\alpha\alpha'}[1 - \mathrm{sgn}(\omega^2/c^2 - \mathbf{k}_\perp^2)], \quad (2)$$

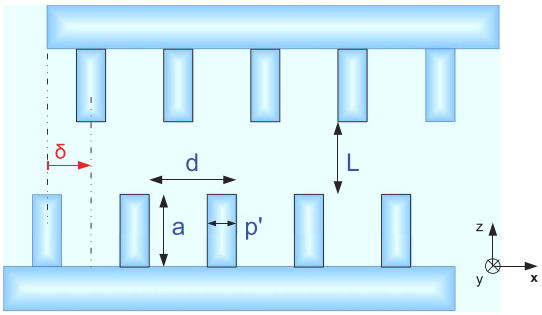

FIG. 1. (Color online) Two identical gratings facing each other at a distance L and relatively shifted by a lateral displacement δ. The corrugations have a period d, height a, and thickness p'. The filling factor $p = p'/d$ is given as a percentage of the period d.

where $\alpha = s, p$ represents the transverse electric and transverse magnetic polarizations, respectively. The thermal energy density per field mode at temperature T writes $e_T(\omega) = \hbar\omega/(e^{\hbar\omega/k_BT} - 1)$. We can now express the heat transfer coefficient between two gratings of the same corrugation depth a as

$$h = \frac{1}{|T_1 - T_2|}\int \frac{d\omega}{2\pi}[e_{T_1}(\omega) - e_{T_2}(\omega)]H_{12} \tag{3}$$

with

$$H_{12} = \int_{k_x=-\pi/d}^{+\pi/d}\int_{k_y\in\mathbb{R}} \frac{dk_x dk_y}{4\pi^2}\mathrm{tr}(\mathbf{D}\mathbf{W_1}\mathbf{D}^\dagger\mathbf{W_2}) \tag{4}$$

$$\mathbf{D} = (1 - \mathbf{S_1}\mathbf{S_2})^{-1} \tag{5}$$

$$\mathbf{W_1} = \Sigma_{-1}^{p\omega} - \mathbf{S_1}\Sigma_{-1}^{p\omega}\mathbf{S_1}^\dagger + \mathbf{S_1}\Sigma_{-1}^{e\omega} - \Sigma_{-1}^{e\omega}\mathbf{S_1}^\dagger \tag{6}$$

$$\mathbf{W_2} = \Sigma_{1}^{p\omega} - \mathbf{S_2}^\dagger\Sigma_{1}^{p\omega}\mathbf{S_2} + \mathbf{S_2}^\dagger\Sigma_{1}^{e\omega} - \Sigma_{1}^{e\omega}\mathbf{S_2}. \tag{7}$$

It is noteworthy that the heat transfer depends on the shape and material properties of the gratings only through their scattering matrices $\mathbf{S_1}$ and $\mathbf{S_2}$. Furthermore, the factor $e_{T_1}(\omega) - e_{T_2}(\omega)$ introduces a cutoff for all frequencies larger than $k_BT/\hbar$. It is hence H_{12} in equation (4), which corresponds to the sum of the transmission factors of the modes, that gives rise to the interesting modes pertaining to the near-field contribution.

Note also that the first perpendicular wave vector component k_x belongs to the first Brillouin zone between $-\pi/d$ and $+\pi/d$, whereas $k_y \in \mathbb{R}$ is not restricted. A practical challenge of the numerical integration of h lays in the choice of the boundaries of ω and k_y through a careful study of the integrand of equation (4) plotted over the whole range of frequencies to determine the modes.

III. NUMERICAL RESULTS FOR GRATINGS

We will from now on consider two gratings of silica glass SiO_2, the dielectric properties of which are given in Ref. 34. This material is chosen as it supports surface phonon-polaritons, which are known to enhance the flux. The gratings temperatures are supposed to be $T_1 = 310$ K and $T_2 = 290$ K. Two sets of data are systematically computed: The first one corresponds to zero lateral displacement of the two plates along the x axis ($\delta = 0$) so that the corrugation maxima directly face those from the opposite profile. The second one corresponds to a lateral displacement of half the grating period ($\delta = d/2$), so that the corrugation peaks face the corrugation trenches of the opposite profile. In near-field, the two structured plates expose a larger surface to each other at $\delta = 0$ than at $\delta = d/2$, so that we expect a strong modulation of the heat transfer coefficient which will be discussed later. This is based on the assumption that the plane-plane heat transfer coefficient is locally valid.

The results of the scattering approach can be compared with the PA, which consists of the weighted sum of the planar normal contributions $h_0(L)$ depending on the local separation distances L within each period. Assuming that $p < 50\%$, we have for $\delta \leqslant p'$:

$$h_\delta^{\mathrm{PA}}(L) = \frac{p' - \delta}{d}h_0(L) + \frac{2\delta}{d}h_0(L + a) + \left(1 - \frac{p' + \delta}{d}\right)h_0(L + 2a). \tag{8}$$

For $\delta > p$, we find the following saturation value of

$$h_{p'}^{\mathrm{PA}}(L) = \frac{2p'}{d}h_0(L + a) + \left(1 - \frac{2p'}{d}\right)h_0(L + 2a). \tag{9}$$

In what follows, we study in detail the interplay between surface waves and corrugations. The results are systematically compared with those obtained within the PA. Figure 2 shows the heat transfer coefficient for $\delta = 0$ and $\delta = d/2$, as a function of the separation distance L, for two gratings of period $d = 1500$ nm, filling factor $p = 20\%$, and groove depth $a = 500$ nm. Regardless of the distance, we can see that the PA is a good approximation of the heat transfer coefficient at $\delta = 0$, but not at $\delta = d/2$. At $L = 25$ nm, the error of the PA is of ∼3% for $\delta = 0$, and of ∼35% for $\delta = d/2$.

The reason for this is illustrated in Fig. 3, which shows the field modulus map for a given source dipole that is placed in the middle of a corrugation right under the surface, and which is

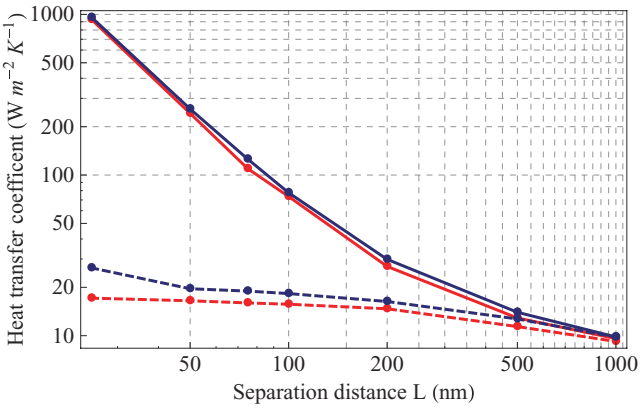

FIG. 2. (Color online) Heat transfer coefficients as a function of separation distance L, when the gratings are not laterally displaced (blue solid line) and when they are by half a period (blue dashed line). This is compared with the proximity approximation in red. The gratings have a period $d = 1500$ nm, filling factor $p = 20\%$, and groove depth $a = 500$ nm.

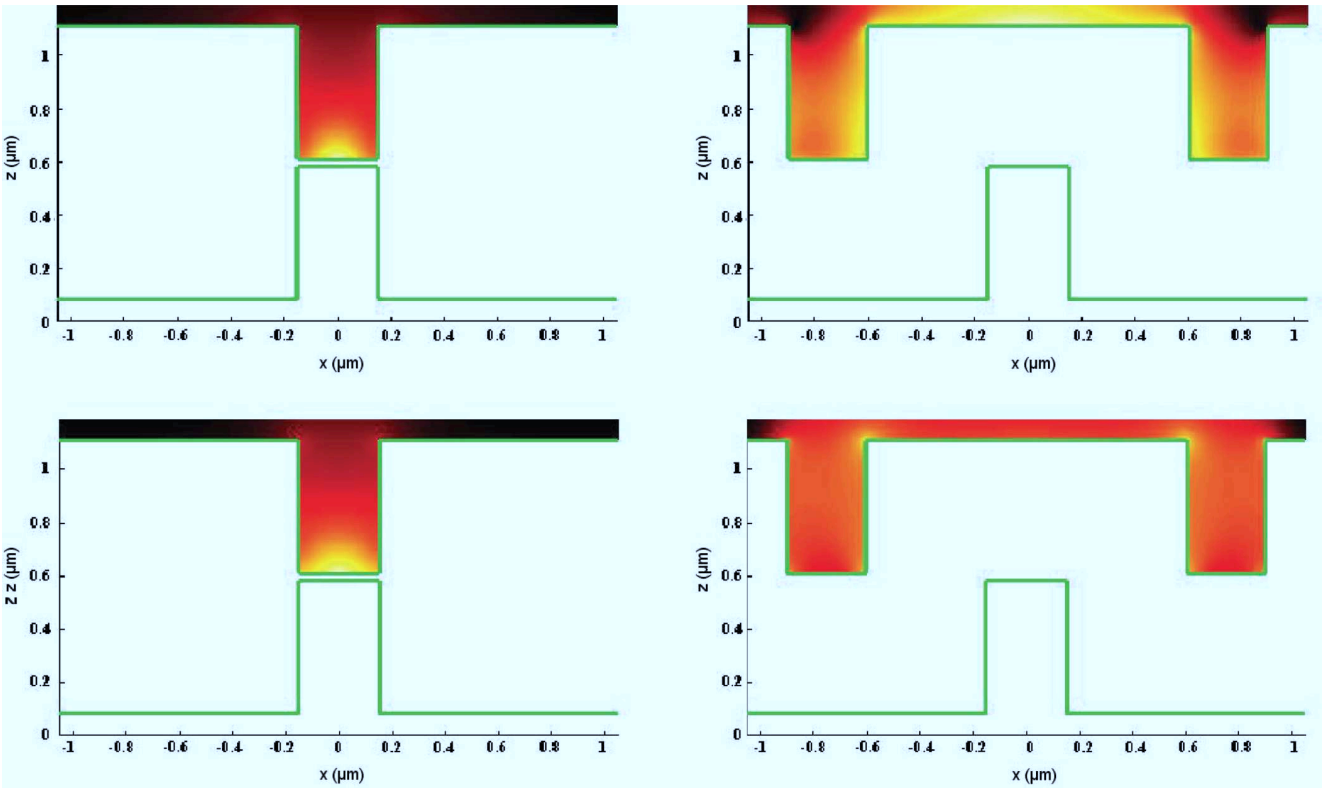

FIG. 3. (Color online) Field modulus map of a given source dipole placed in the middle of a corrugation and right under the surface. The field is here represented only in the upper grating, so as to highlight where the absorption takes place. This is for gratings at a separation distance $L = 25$ nm. The two figures on the left display the profiles in the xz plane (in green) when they are aligned ($\delta = 0$), and the two figures on the right when they are laterally displaced by half a period ($\delta = d/2$), both for two different wavelengths $\lambda = 8.75$ μm (top) and 9.15 μm (down).

oriented perpendicular to it. The color scale is logarithmic. The intensity or square modulus of the electric field is represented only in the upper grating so as to highlight the place of absorption. The gratings have a separation distance $L = 25$ nm, corrugation depth $a = 500$ nm, period $d = 1500$ nm, and filling factor $p = 20\%$. Two different wavelengths $\lambda = 8.75$ μm and $\lambda = 9.15$ μm are considered, knowing that SiO_2 has two resonance frequencies at $\lambda = 8.75$ μm and $\lambda = 21$ μm. In the case where $\delta = 0$ and $\lambda = 8.75$ μm, we see that the field is clearly both intense and confined. As 8.75 μm corresponds to the horizontal asymptote of the surface phonon dispersion relation, a large number of modes with different values of the wave vector are excited. This leads to a highly localized subwavelength hot spot. At 9.15 μm, the spot is broader than expected: This is similar to the loss of resolution of superlens away from the resonance. On the right column of the figure, we show the intensity for $\delta = d/2$. It is seen that the heated region is delocalized so that PA is clearly not valid. In this regime, the heat transfer is no longer due to a dipole-dipole interaction through the gap. Instead, a dipole excites modes of the structures. In turn, these spatially extended modes produce dissipation in the walls. This discussion indicates that PA is valid if the gap width does not vary significantly on a length scale given by the spatial extension of the modes. Furthermore, we have already seen in Fig. 2 the difference between the proximity approximation and the scattering results. This difference can be interpreted as an indicator of the contribution of the lateral modes, since the proximity approximation considers normal modes only.

To further illustrate this qualitative dependence of the radiative heat transfer on separation distance, we show in Fig. 4

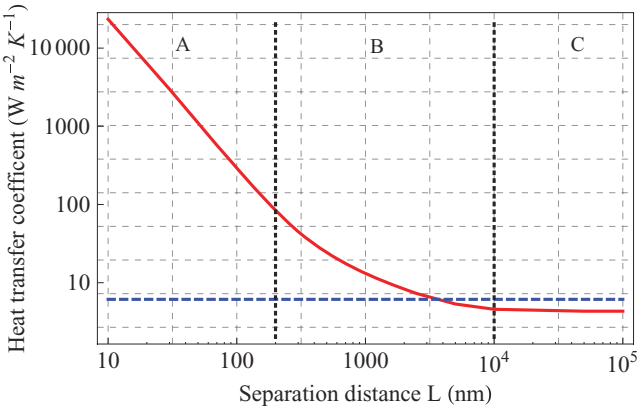

FIG. 4. (Color online) Heat transfer coefficients as a function of the separation distance L between two plane mirrors of SiO_2 (red solid curve), compared with the black body limit (blue dashed line). One can divide the separation distance in three domains A, B, and C, respectively corresponding to the extreme near-field below 200 nm, to the near-field from 200 nm to 10 μm, and to the domain of Stefan-Boltzmann's law beyond 10 μm. This can be seen by the change of the slope of the curve along these three ranges.

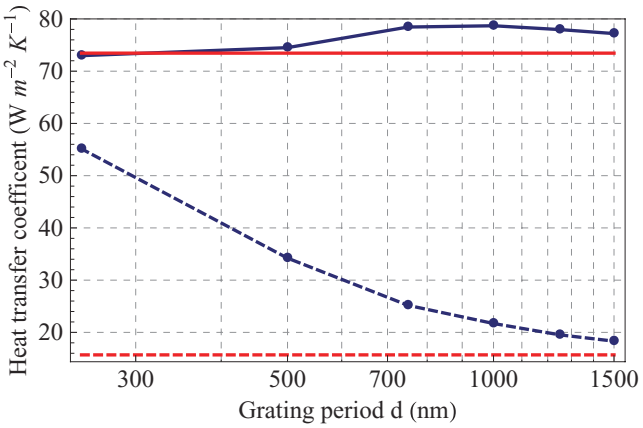

FIG. 5. (Color online) Heat transfer coefficients as a function of grating period d, when the gratings are not laterally displaced (solid blue line) and when they are displaced by half a period (dashed blue line). This is compared with the PA in red. The gratings have a groove depth $a = 500$ nm, filling factor $p = 20\%$, and are at a separation distance $L = 100$ nm.

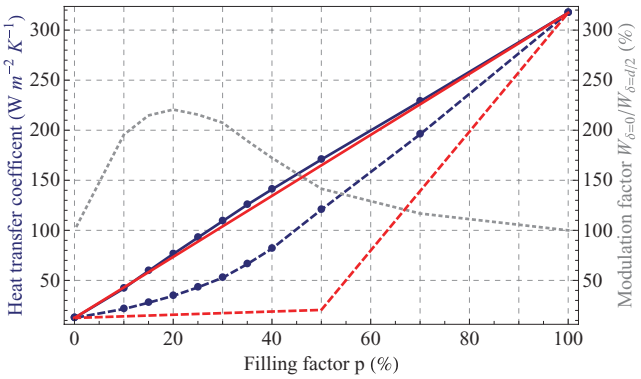

FIG. 6. (Color online) Heat transfer coefficients as a function of filling factor p, when the gratings are not laterally displaced (solid blue line) and when they are displaced by half a period (dashed blue line). Respective PA predictions are in red. The dotted gray line is the percentage of the modulation factor $h_{\delta=0}/h_{\delta=d/2}$. Gratings have a period and groove depth of 500 nm, and are separated by a distance $L = 100$ nm.

the heat transfer coefficients as a function of the separation distance L between two plates of SiO_2. One can distinguish three domains A, B, and C, corresponding respectively to the extreme near-field below 200 nm, to the near-field from 200 nm to 10 μm, and to the domain of Stefan-Boltzmann's law beyond 10 μm. The heat transfer coefficient changes in slope along these three ranges: The strongest contributions come respectively from the dipole-dipole interaction, from surface phonon-polaritons, and from the classical radiative heat transfer. The contribution in the first domain corresponds to the localized heat transfer seen in the upper-left-hand map of Fig. 3, whereas the main contribution in the second domain corresponds to the delocalized heat transfer mediated by the surface wave seen on the right-hand maps of Fig. 3.

It is also instructive to study the heat transfer modulation as a function of the corrugation period d, as shown in Fig. 5. We have selected six types of gratings with corrugation periods ranging from $d = 250$ to 1500 nm, each with a groove depth $a = 500$ nm and filling factor still fixed at $p = 20\%$. The separation distance is $L = 100$ nm. The fact that the heat transfer coefficients at $\delta = 0$ do not vary much with a change of period is further confirmation of the validity of the PA in this configuration. At $\delta = d/2$, however, the scattering and PA results radically differ for small periods, but tend to agree for large periods. The reason for this is that when $d \to \infty$, the ratio a/d tends to zero, and we expect the heat transfer to be well approximated by the plane-plane case, and hence the PA.

Let us finally turn to the discussion of the modulation effect. Figure 2 shows that the heat transfer depends dramatically on the lateral displacement of the two surfaces, opening the possibility of a strong modulation via only lateral displacement of one of the two plates at a fixed distance. To assess the possible performance of such a system as a thermal modulator we investigate the modulation factor $h_{\delta=0}/h_{\delta=d/2}$ for different filling factors. The results are illustrated in Fig. 6 for gratings with a period and groove depth $a = 500$ nm, and a separation distance $L = 100$ nm. For these large separations, the modulation factor $h_{\delta=0}/h_{\delta=d/2}$ still reaches a maximum of about 2.2, at a filling factor corresponding to 20% of the total grating period. At short distances ($L \sim 25$ nm) it can reach up to 35 (c.f. Fig. 2).

IV. CONCLUSION

We have studied radiative heat transfer between laterally shifted corrugated dielectric plates by using the scattering method. When comparing the exact results thus obtained with the commonly used Proximity Approximation, we have clarified the origin of the success and failure of the latter approximation by analyzing the interplay between surface wave resonances and corrugations. We have shown for various nanograting geometries and separation distances that the proximity approximation has a better precision for $\delta = 0$ than for $\delta = d/2$. The key to the understanding of the system is the comparison of the lateral length scale of the surface corrugation with the lateral extension of surface waves involved in the heat transfer. Finally, we have narrowed down the optimum geometrical parameters of a thermal modulator device for nanosystems based on a lateral displacement of two corrugated plates facing each other at fixed distance. We found in general a stronger modulation for small filling factors and separation distances, and for large grating periods. In certain regimes it is possible to reach a modulation factor of more than 35. An in-depth study of the modes accounting for the most important part of the heat transfer would be an interesting prospect as well as to further enhance the modulation by using a broader range of materials[35] such as different alloys combining the polaritons of certain dielectrics and the near-field properties of metals. The issue of heat transfer in near-field in the case of coatings,[8] phase change materials,[31,35] metamaterials,[5,36] or graphene-covered dielectrics[2] in this regard should also be explored.

ACKNOWLEDGMENTS

The authors thank the ESF Research Networking Programme CASIMIR (www.casimir-network.com) for providing excellent possibilities for discussions and exchange. The research described here has been supported by Triangle de la Physique Contract No. EIEM 2010-037T.

[1] S.-A. Biehs and J.-J. Greffet, Phys. Rev. B **82**, 245410 (2010).
[2] V. B. Svetovoy, P. J. van Zwol, and J. Chevrier, arXiv:1201.1824v1.
[3] P. Ben-Abdallah, K. Joulain, and A. Pryamikov, Appl. Phys. Lett. **96**, 143117 (2010).
[4] K. Joulain, P. Ben-Abdallah, and J. Drevillon, Phys. Rev. B **81**, 165119 (2010).
[5] M. Francoeur, S. Basu, and S. Petersen, Opt. Express **19**, 18774 (2011).
[6] K. Park, S. Basu, W. P. King, and Z. M. Zhang, J. Quant. Spectrosc. Radiat. Transfer **109**, 305 (2008).
[7] M. Laroche, R. Carminati, and J. Greffet, J. Quant. Spectrosc. Radiat. Transfer **100**, 063704 (2006).
[8] S.-A. Biehs, Eur. Phys. J. B **58**, 423 (2007).
[9] C. M. Hargreaves, Phys. Lett. A **30**, 491 (1969).
[10] D. Polder and M. V. Hove, Phys. Rev. B **4**, 3303 (1971).
[11] A. I. Volokitin and B. N. J. Persson, Phys. Rev. B **78**, 155437 (2008).
[12] E. Rousseau, A. Siria, G. Jourdan, S. Volz, F. Comin, J. Chevrier, and J.-J. Greffet, Nat. Photonics **3**, 514 (2009).
[13] S. Shen, A. Narayanaswamy, and G. C. Nano, Nano Lett. **9**, 2909 (2009).
[14] S. Y. Buhmann and S. Scheel, Phys. Rev. Lett. **100**, 253201 (2008).
[15] O. Huth, F. Rüting, S.-A. Biehs, and M. Holthaus, Eur. Phys. J. Appl. Phys. **50**, 10603 (2010).
[16] M. Antezza, L. Pitaevskii, S. Stringari, and V. Svetovoy, Phys. Rev. A **77**, 022901 (2008).
[17] J.-P. Mulet, K. Joulain, R. Carminati, and J.-J. Greffet, Appl. Phys. Lett. **78**, 2931 (2001).
[18] A. Narayanaswamy and G. Chen, Phys. Rev. B **77**, 075125 (2008).
[19] K. Sasihithlu and A. Narayanaswamy, Phys. Rev. B **83**, 161406(R) (2011).
[20] G. Domingues, S. Volz, K. Joulain, and J.-J. Greffet, Phys. Rev. Lett. **94**, 085901 (2005).
[21] Y. Sherkunov, Phys. Rev. A **79**, 032101 (2009).
[22] P.-O. Chapuis, M. Laroche, S. Volz, and J.-J. Greffet, Phys. Rev. B **77**, 125402 (2008).
[23] C. Otey and S. Fan, Phys. Rev. B **84**, 245431 (2011).
[24] M. Krüger, T. Emig, and M. Kardar, Phys. Rev. Lett. **106**, 210404 (2011).
[25] B. V. Derjaguin, Kolloid-Z **69**, 155 (1934).
[26] J. Błocki, J. Randrup, W. J. Świątecki, and C. F. Tsang, Ann. Phys. **105**, 427 (1977).
[27] A. McCauley, M. Reid, M. Krüger, and S. Johnson, arXiv:1107.2111.
[28] G. Bimonte, Phys. Rev. A **80**, 042102 (2009).
[29] R. Messina and M. Antezza, Phys. Rev. A **84**, 042102 (2011).
[30] R. Guérout, J. Lussange, F. S. S. Rosa, J.-P. Hugonin, D. A. R. Dalvit, J.-J. Greffet, A. Lambrecht, and S. Reynaud, Phys. Rev. B **85**, 180301 (2012).
[31] P. J. van Zwol, K. Joulain, P. B. Abdallah, J. J. Greffet, and J. Chevrier, Phys. Rev. B **83**, 201404(R) (2011).
[32] A. Lambrecht and V. Marachevsky, Phys. Rev. Lett. **101**, 160403 (2008).
[33] Y. Bao, R. Guérout, J. Lussange, A. Lambrecht, R. A. Cirelli, F. Klemens, W. M. Mansfield, C. S. Pai, and H. B. Chan, Phys. Rev. Lett. **105**, 250402 (2010).
[34] E. Palik, *Handbook of optical constants of solids* (Elsevier, New York, 1998).
[35] P. J. van Zwol, K. Joulain, P. Ben-Abdallah, and J. Chevrier, Phys. Rev. B **84**, 161413(R) (2011).
[36] S. Basu, Z. Zhang, and C. Fu, Int. J. Energy Res. **33**, 1203 (2009).

The Casimir energy for profiles with arbitrary periodic corrugations

J. Lussange,[1] R. Guérout,[1] and A. Lambrecht[1]

[1]*Laboratoire Kastler-Brossel, CNRS, ENS, UPMC, Case 74, F-75252 Paris, France*

We study the dependence of the Casimir energy for different corrugated gratings of arbitrary periodic profiles. We model to this end these profiles as stacks of horizontal rectangular slices following the profiles' shape. The way we study the Casimir energy dependency over these arbitrary gratings is through a lateral displacement of the two corrugated plates before one another. We use a numerical approach based on the scattering formalism for basic rectangular corrugations and apply it individually to these slices, so that the greater the number of slices, the greater the accuracy of this model. We also compare these results with the PFA. At comparable separation distance and periodicity parameters, we find a strong dependency of the Casimir energy on the shape of these profiles.

PACS numbers: PACS numbers: 03.70.+k, 12.20.Ds, 42.50.Lc

The Casimir force, which significantly arises between nano-objects at the sub-micrometer range, is an extension of the van der Waals interaction where the finite speed of light accounts for a manifestation of the relativistic retardation of the electromagnetic waves. The dynamics of any electromagnetic field strongly depends on its external boundary conditions, and in the case of a Fabry-Pérot cavity formed by two flat mirrors separated by vacuum such as first considered in 1948 by H. Casimir [1], the variation in spectral density of the zero-point fluctuations leads to a radiation pressure outside of the cavity being greater than inside, so that the two mirrors are pushed towards one another.

Recent progress have allowed accurate determination and measurements of this force for different configurations of micro-mirrors, ranging from the simplest case of two flat mirrors for different materials [2], to more complicated geometries such as the plane-sphere configuration [3], or corrugated mirrors [4, 5]. This has been done in the past decade through an extensive research into the Casimir effect's theoretical formalism with both numerical computations [6–9] and experimental setups [10–14]. The Casimir force, being proportional with an inverse fourth power law with the separation distance between the mirrors, is also highly dependent on their geometry. The study of non-trivial gratings is therefore an important field for future applications in the design of NEMS and MEMS in nanotechnology, as it is for instance related to the problems of stiction impairing these nanodevices.

We will here consider arbitrary periodic corrugations for dielectric gratings in the case where each corrugation, as taken independently, is symmetric before the y-axis. This is shown in Fig. 1, where a grating having periodic corrugations with arbitrary profiles can be divided into a number of K horizontal slices of depth a vertically stacked on each other. For a corrugation depth a, each slice is treated as a lamellar rectangular grating whose height along the $y-$axis is fixed at a/K and whose length along the $x-$axis is given by the arbitrary profile's length at the level of that slice.

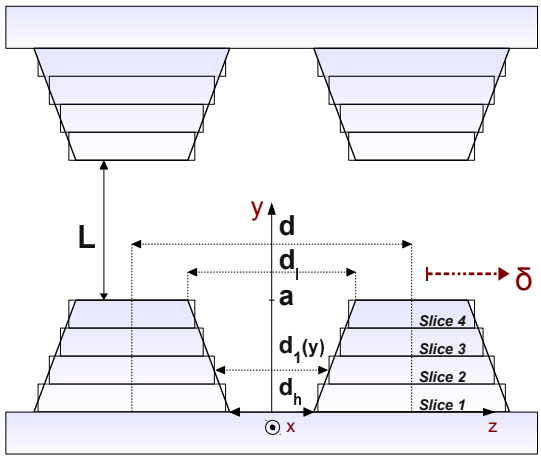

FIG. 1: Arbitrary gratings geometry and parameters in the approximation of vertical stacks of rectangular slices (here for $K = 4$).

Therefore profiles of arbitrary corrugations modeled as such can be treated through an approach derived from the formalism for rectangular corrugations. Such a formalism has already been well established in literature within the scope of scattering formalism [4]. Let's first consider two such dielectric gratings made of rectangular periodic corrugations, separated by a vacuum slit. Because of time and z-invariance, we can write the electric and magnetic fields for $i = (x, y, z)$ such as :

$$E_i(x, y, z, t) = E_i(x, y) \exp(ik_z z - i\omega t) \tag{1}$$

$$H_i(x, y, z, t) = H_i(x, y) \exp(ik_z z - i\omega t). \tag{2}$$

From now on, we take $\mu_0 = \mu = 1$, and $c = 1$ in vacuum. So all we need is to find the longitudinal components outside the corrugated region ($y > a$) and within the transmitted region ($y \leqslant 0$).

In the case of two planar interfaces, we can write the $z-$components of the fields in the vacuum region as an

incident and reflected one :

$$E_z(x,y) = I_e e^{ik_x x - ik_y y} + r_e e^{ik_x x + ik_y y} \tag{3}$$

$$H_z(x,y) = I_h e^{ik_x x - ik_y y} + r_h e^{ik_x x + ik_y y} \tag{4}$$

and in the material region, we can write the $z-$components of the fields as a transmitted one :

$$E_z(x,y) = t_e e^{ik_x x - ik'_y y} \tag{5}$$

$$H_z(x,y) = t_h e^{ik_x x - ik'_y y} \tag{6}$$

for $k_y^2 = \omega^2 - k_x^2 - k_z^2$ and $k_y'^2 = \epsilon\omega^2 - k_x^2 - k_z^2$, and where $r_{e,h}$, $t_{e,h}$ are the Fresnel-Stokes amplitudes. Then we can generalize this for gratings, with a Rayleigh expansion for an incident monochromatic wave for the field outside the corrugated region, such that we consider p incident waves and a diffraction order $n \in [-N, \ldots, +N]$:

$$E_z(x,y)_{y>a} = I_p^e \exp(i\alpha_p x - i\beta_p^{(1)} y) + \sum_{n\in\mathbb{Z}} R_{np}^e \exp(i\alpha_n x + i\beta_n^{(1)} y) \tag{7}$$

$$H_z(x,y)_{y>a} = I_p^h \exp(i\alpha_p x - i\beta_p^{(1)} y) + \sum_{n\in\mathbb{Z}} R_{np}^h \exp(i\alpha_n x + i\beta_n^{(1)} y) \tag{8}$$

and within the transmitted region ($y \leqslant 0$) :

$$E_z(x,y)_{y\leqslant 0} = \sum_{n\in\mathbb{Z}} T_{np}^e \exp(i\alpha_n x - i\beta_n^{(2)} y) \tag{9}$$

$$H_z(x,y)_{y\leqslant 0} = \sum_{n\in\mathbb{Z}} T_{np}^h \exp(i\alpha_n x - i\beta_n^{(2)} y). \tag{10}$$

where I_p, R_{np}, and T_{np} are now the incidence, reflection, and transmission *matrix elements* respectively. Also, we used :

$$\alpha_p = k_x + 2\pi p/d \tag{11}$$
$$\alpha_n = k_x + 2\pi n/d \tag{12}$$
$$\beta_p^{(1)2} = \omega^2 - k_z^2 - \alpha_p^2 \tag{13}$$
$$\beta_n^{(1)2} = \omega^2 - k_z^2 - \alpha_n^2 \tag{14}$$
$$\beta_n^{(2)2} = \epsilon\omega^2 - k_z^2 - \alpha_n^2. \tag{15}$$

where for $n = 0$ we have a specular reflection. By symmetry, the other field components of the electric and magnetic fields can each be expressed through the z-components of *both* fields, following Maxwell's equations. For example, if we define $\kappa^2 = \frac{\epsilon\omega^2}{c^2} - k_z^2$, we have :

$$E_x = \frac{ik_z}{\kappa^2}\partial_x E_z + \frac{i\omega}{\kappa^2}\partial_y H_z. \tag{16}$$

$$H_x = \frac{ik_z}{\kappa^2}\partial_x H_z + \frac{i\omega\epsilon}{\kappa^2}\partial_y E_z. \tag{17}$$

Now what we need are the reflection coefficients R_{np} of these rectangular corrugated gratings. First, we must rewrite the Maxwell equations inside the corrugated region $0 < y < a$ through the set of first-order differential equations $\partial_y \mathbf{F} = \mathbf{M}\mathbf{F}$, for $\mathbf{F}^\top = (E_x, E_z, H_x, H_z)$ and $\mathbf{M}$ a constant square matrix of dimension $8N + 4$. The solution of the fields is then of the form :

$$\mathbf{F}(y) = e^{\mathbf{M}y}\mathbf{F}(0) \tag{18}$$

with :

$$\mathbf{M} = \begin{pmatrix} 0 & 0 & \frac{-ik_z\alpha_n}{\epsilon\omega} & -i\frac{\epsilon\omega^2-\alpha_n^2}{\epsilon\omega} \\ 0 & 0 & i\frac{\epsilon\omega^2-k_z^2}{\epsilon\omega} & \frac{ik_z\alpha_n}{\epsilon\omega} \\ \frac{ik_z\alpha_n}{\omega} & i\frac{\epsilon\omega^2-\alpha_n^2}{\omega} & 0 & 0 \\ -i\frac{\epsilon\omega^2-k_z^2}{\omega} & \frac{-ik_z\alpha_n}{\omega} & 0 & 0 \end{pmatrix} \tag{19}$$

where the elements appearing in matrix $\mathbf{M}$ are in fact block matrices of dimension $2N + 1$. We can then write the fields inside the corrugation region and match them in continuity relations for each E_x, E_z, H_x, H_z, with equation (18), at boundary $y = a$ for $y > a$, and at boundary $y = 0$ for $y \leqslant 0$. Eventually we can find the vectors $\mathbf{F}(a)$ and $\mathbf{F}(0)$, which can be written as a product of a matrix and the vector of variables X :

$$\mathbf{F}(a) = TX + Y \quad \text{and} \quad \mathbf{F}(0) = SX \tag{20}$$

with $X^T = (R_{np}^e, R_{np}^h, T_{np}^e, T_{np}^h, \ldots)$, and Y being the variable-independent term including the polarization of the incident waves, since must take into account the two polarizations independently : we take for example $I_p^{(e)} = 1$ and $I_p^{(h)} = 0$ for electric waves ($H_z = 0$), and $I_p^{(e)} = 0$ and $I_p^{(h)} = 1$ for magnetic waves ($E_z = 0$). Y hence characterizes the two separate solutions for e-waves and h-waves. Here we wrote two superscript labels, the first referring to the polarization of the reflected field, and the second referring to the incident field. Note that in the presence of gratings, the polarization of the reflected field can be either e or h for a given incident field e. The solution is then given by :

$$X = (e^{\mathbf{M}a}S - T)Y \tag{21}$$

we have :

$$X\left(I_p^{(e)} = 1, I_p^{(h)} = 0\right) = \begin{pmatrix} R_{np}^{(e,e)} \\ R_{np}^{(h,e)} \\ \vdots \end{pmatrix} \tag{22}$$

$$X\left(I_p^{(e)} = 0, I_p^{(h)} = 1\right) = \begin{pmatrix} R_{np}^{(e,h)} \\ R_{np}^{(h,h)} \\ \vdots \end{pmatrix} \tag{23}$$

so that we obtain the reflection matrix for each grating :

$$R(\omega) = \begin{pmatrix} R_{np}^{(e,e)} & R_{np}^{(e,h)} \\ R_{np}^{(h,e)} & R_{np}^{(h,h)} \end{pmatrix} \tag{24}$$

After making use of Cauchy's argument principle, we arrive to the exact expression of the Casimir energy as the usual sum over the modes issuing from these reflection matrices $R_1(i\omega)$ and $R_2(i\omega)$ associated with each grating :

$$E = \frac{\hbar d}{8\pi^3} \int_{\mathbb{R}^{+*}} d\omega \int_{\mathbb{R}} dk_z \int_{-\pi/d}^{\pi/d} dk_x$$

$$\times \ln \det[I - R_1(i\omega)P(i\omega)R_2(i\omega)P(i\omega)] \tag{25}$$

for :

$$P(i\omega) = \begin{pmatrix} G & 0 \\ 0 & G \end{pmatrix} \tag{26}$$

with $G = \mathrm{diag}\left(e^{-L\sqrt{\omega^2+k_y^2+[k_x+(2m\pi/d)]^2}}\right)$ and $m = -N, \ldots, +N$. The matrices P thus act as propagation matrices within the cavity.

Now for our case of arbitrary profiles modeled as stacks of K horizontal rectangular slices, the difference appears in the parameter d_1, which will now depend on y. Arbitrary profiles defined by $d_1(y)$ can be divided into K slices, each being seen as a rectangular corrugation, as described in Fig. 1. For each slice (i), the spacing between the corrugations ridges is $d_1^{(i)}$, and the former scattering formalism for rectangular corrugations can be applied. More specifically, a differential equation akin to equation (18) $\partial_y \mathbf{F} = \mathbf{M}^{(i)}\mathbf{F}$ can be solved within each slice (i) to relate the fields at boundary $y = i\frac{a}{K}$ and $y = (i+1)\frac{a}{K}$.

In a similar way that for the case $K = 1$ above, the field at $y = a$ is thus related to the field at $y = 0$ via the relation :

$$\mathbf{F}(a) = \left[\prod_{i=K}^{1} e^{\mathbf{M}^{(i)}\frac{a}{K}}\right]\mathbf{F}(0) \tag{27}$$

where the product $\prod$ runs from $i = K$ to $i = 1$, in that order.

The greater the number of slices K, the greater the fitting of the gratings' shape will be, and thus the accuracy of the overall model. This convergence in K is shown in Fig. 4 for given profiles shaped as *sawteeth*, with a separation distance $L = 100$ nm, grating period $d = 400$ nm, corrugation depth $a = 50$ nm, and distance between ridges $d_1(y) = 4y{+}200$. Hence a correct parametrization of the quantity d_1 as a function of y allows one to generate arbitrary symmetric profiles for the corrugations. The arbitrary profiles that we will study are shown on Fig. 2 and Fig. 3. For instance, *sawtooth* profiles where $d_l = d$ (as seen on Fig. 2a and Fig. 3a) are generated by the function $d_1(y) = \frac{d}{a}y$, and *sinusoidal* profiles by $d_1(y) = (d/\pi)\arccos[1 - (2y/a)]$. *Barbed wire* profiles, where $d_h > d_l$ (as seen on Fig. 2b) are generated by the function $d_1(y) = (d_l - d_h)y/a + d_h$. *Ellipsoid* profiles along the $x-$axis are generated by $d_1(y) = d - \frac{2R}{r}\sqrt{r^2-(y-Y)^2}$ (as seen on Fig. 2c), and those along the $y-$axis are generated by $d_1(y) = d - \frac{2r}{R}\sqrt{R^2-(y-Y)^2}$, for R and r being the major and minor axes of the ellipse respectively, and Y being the value in y of the ellipse center. *Circular* periodic profiles are also generated by these expressions (as seen on Fig. 2c and Fig. 3c), with $R = r$ being the radius of these 2D circles in the xy-plane. Notice that what we call for example "circular" periodic profiles in two dimensions, look more in fact like periodic "tubes" in the actual three-dimensional gratings, as shown on Fig. 3.

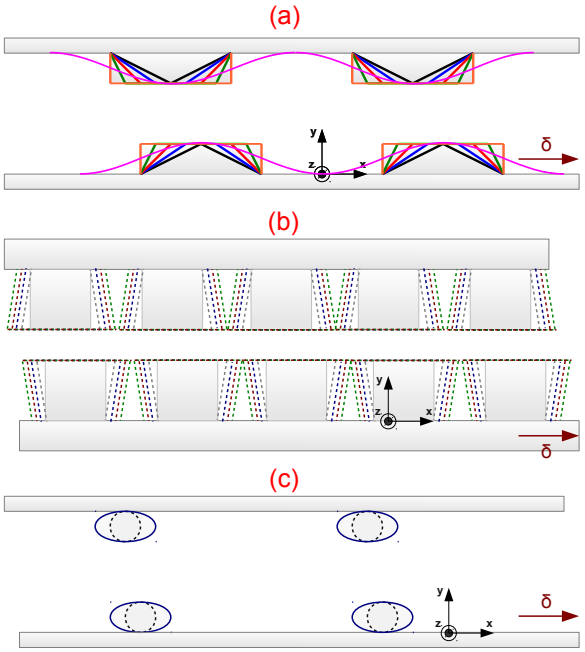

FIG. 2: Two-dimensional perspective on the different considered periodic gratings. (a) and (c) are at the same scale, but the scale of (b) has been increased by a factor two.

We can also compare the results of the scattering theory presented here with Derjaguin's Proximity Force Approximation (PFA) [15]. The PFA comes from the weighted sum of the planar normal contributions $E_{\mathrm{PP}}(L)$ depending on the local separation distances L within each period, and hence on the lateral displacement δ between the gratings. If we express the shapes of the arbitrary periodic gratings in an analytical form such as $y = f(x,\delta)$ for the lower grating and $y = L + 2a - f(x, \delta = 0)$ for the upper grating in the xy-plane shown on Fig. 1, we can then define the function $h(x,\delta) = L + 2a - f(x,\delta = 0) - f(x,\delta)$ expressing the local distance of separation be-

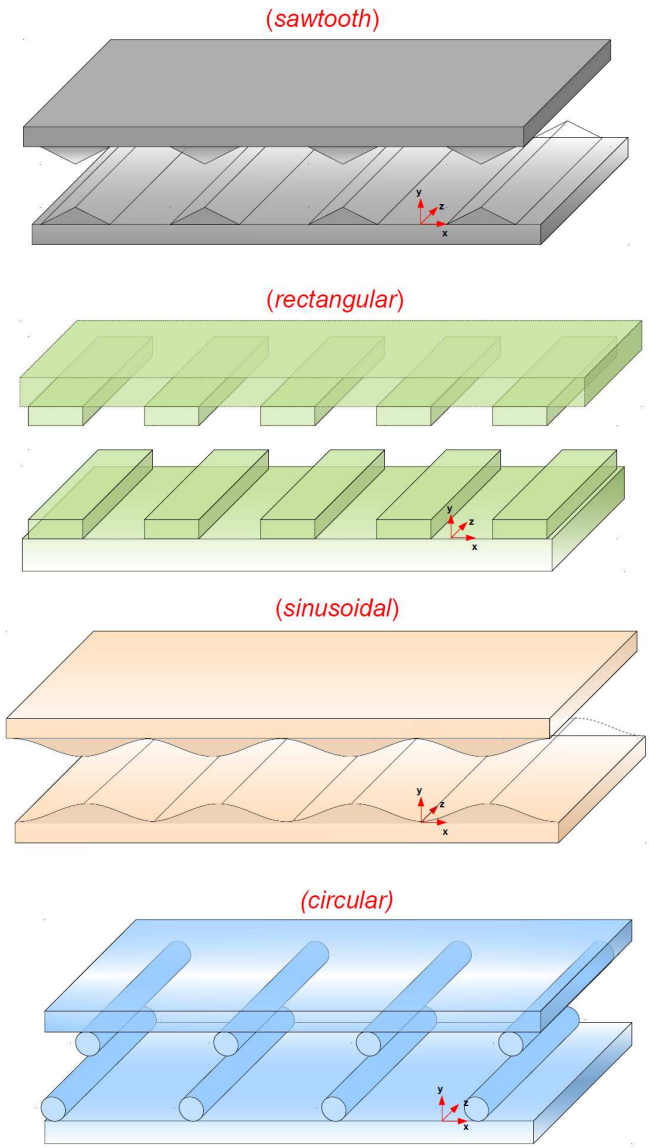

FIG. 3: Three-dimensional perspective on the *sawtooth*, rectangular, *sinusoidal*, and *circular* periodic gratings shown in Fig. 2. The profiles are here represented at the same scale.

tween the two profiles, as a function of x and δ. Dividing the period d in a number $\eta \to \infty$ of intervals of individual widths $d/\eta \to 0$, we then obtain a general expression of the Casimir energy in the PFA for arbitrary gratings as a function of lateral displacement δ :

$$E^{\mathrm{PFA}}(L,\delta) = \frac{1}{d}\int_0^d E_{\mathrm{PP}}\left(h(x,\delta)\right)dx \qquad (28)$$
$$= \frac{1}{\eta}\sum_{i=1}^{\eta} E_{\mathrm{PP}}\left(L = h\left(x = i\frac{d}{\eta},\delta\right)\right)$$

We now consider several types of arbitrary profiles and review the dependence of the Casimir energy as a function of the two mirrors' lateral displacement δ with respect to one another. As for the rest of this text, the material chosen for these profiles is intrinsic silicon, such as modeled by a Drude model from [5, 16].

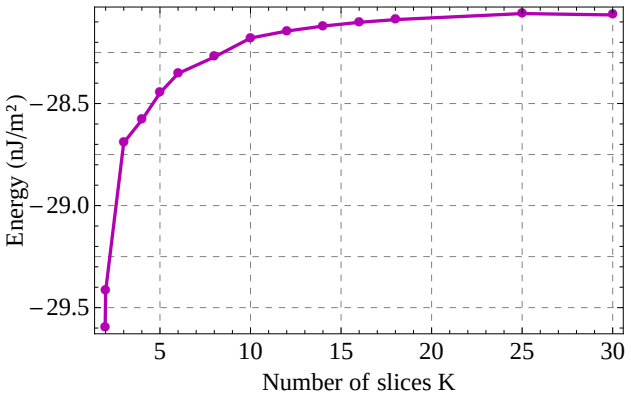

FIG. 4: Dependence of the Casimir energy to the number of slices K for the case of *sawtooth* gratings, with $L = 100$ nm, $d = 400$ nm, $a = 50$ nm, and $d_1(y) = 4y + 200$.

To begin with, let's take $L = 100$ nm, $d = 400$ nm, $a = 50$ nm, and a number of slices $K = 20$. We consider five corrugated periodic profiles parametrized by $d_1(y) = 4y + 200$, $d_1(y) = 3y + 200$, $d_1(y) = 2y + 200$, $d_1(y) = y + 200$, and $d_1(y) = 200$ nm respectively, as shown in Fig. 5. With these parameters, we can study the dependence of the Casimir energy for gratings ranging from *sawtooth* (in black) all the way to rectangular corrugations (in orange) so that d_l ranges from $d = 400$ nm to $d_h = 200$ nm progressively by steps of 50 nm. This is also compared with *sinusoidal* profiles of same sizes for d, a, and L, but parametrized by $d_1(y) = (d/\pi)\arccos[1 - (2y/a)]$.

One can see that the Casimir energy increases as d_l decreases, and that this is especially true at $\delta = d/2$. So we can say that both the Casimir energy and its modulation over lateral displacement are larger for smaller d_l such as rectangular corrugations and smaller for larger d_l such as *sawtooth* profiles. Note also the behavior of the *sinusoidal* profile at $\delta = d/2$, which shows that such profiles are less sensitive to lateral displacement than sawtooth profiles or rectangular gratings.

On Fig. 6 we show a comparison between the scattering results and the PFA for the *sawtooth*, *sinusoidal*, and rectangular profiles seen in Fig. 5. It is clear that regardless of the considered profile, the PFA does not approximate well the case $\delta = 0$. The error ratio $E_{\mathrm{PFA}} - E_{\mathrm{scattering}}/E_{\mathrm{PFA}}$ at $\delta = 0$ is roughly equal to 11% for *sawtooth*, 12% for *sinusoidal*, and 15% for rectangular gratings. Furthermore, as one shifts δ to half-a-period $d/2$, the error becomes much smaller for the *sawtooth* and *sinusoidal* gratings, but for all cases, the PFA is not a good approximation to the rectangular gratings in this configuration.

On Fig. 7 we show the results issuing for different

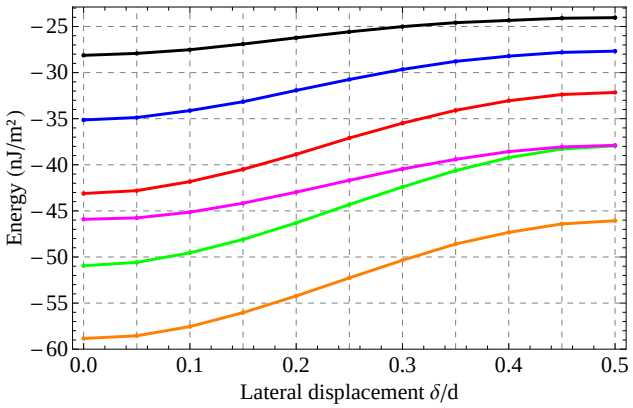

FIG. 5: Dependence of the Casimir energy to the mutual lateral translation of two corrugated periodic profiles of intrinsic silicon. We took here $L = 100$ nm, $K = 20$, $d = 400$ nm, $a = 50$ nm, and $d_1 = 4y + 200$ (*sawtooth* in black), $d_1 = 3y + 200$ (blue), $d_1 = 2y + 200$ (red), $d_1 = y + 200$ (green), $d_1 = 200$ (rectangular corrugations in orange). This is compared with a *sinusoidal* profile (magenta curve) with same parameters, except $d_1 = (d/\pi)\arccos[1 - (2y/a)]$.

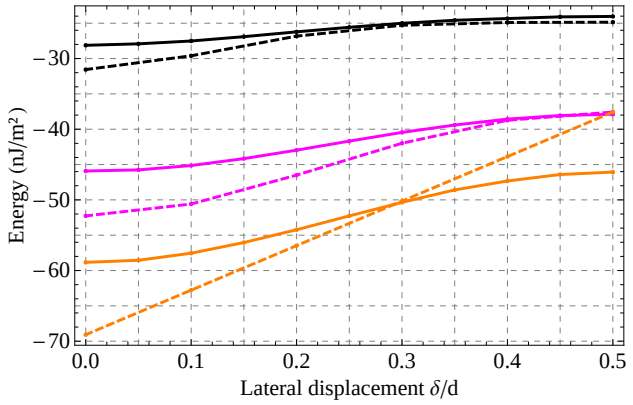

FIG. 6: Comparison between the scattering and PFA results for the *sawtooth*, *sinusoidal*, and rectangular profiles of Fig. 5.

profiles shaped as *barbed wire*, which is for $d_h > d_l$. We take $L = 20$ nm, $d = 100$ nm, $a = 50$ nm, and a number of slices $K = 20$. By carefully choosing $d_h = 85$ nm and $d_l = 60$ nm, we get a filling factor $d_1 = (d_l - d_h)y/a + d_h = d_1 = 85 - y/2$. Now we compare the case with $d_1(y) = 85 - y/2$ with two different corrugated rectangular gratings : the first one with $d_1 = d_h = 85$ nm so that the corrugations are as wide as the top of the *barbed wires*, and the second one with $d_1 = d_l = 60$ nm so that the corrugations are as wide as the base of the *barbed wires*. One can see that the Casimir energy of these profiles in *barbed wire* are much closer to the latter rectangular gratings than the former.

Finally we consider two different gratings as shown in Fig. 8, each with $L = 100$ nm, $d = 400$ nm, $a = 50$ nm, and a number of slices $K = 15$. The first one has

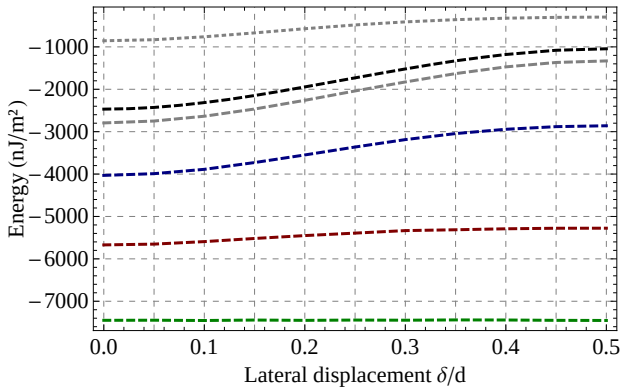

FIG. 7: Dependence of the Casimir energy to the mutual lateral translation of two *barbed wire* periodic profiles of intrinsic silicon. We took here $L = 20$ nm, $K = 20$, $d = 100$ nm, $a = 50$ nm, and $d_1 = -0.5y + 85$ (dashed black line), $d_1 = -0.5y + 65$ (dashed blue line), $d_1 = -0.5y + 45$ (dashed red line), $d_1 = -0.5y + 25$ (dashed green line). This is compared with two rectangular corrugated profiles of different value $d_1 = d_h = 85$ nm (dotted gray line), and $d_1 = d_l = 60$ nm (dashed gray line).Notice that while we varied the spacing between the corrugations d_1, the grating period d was kept constant.

the shape of periodic horizontal *ellipses*, with major axis $R = 50$ nm along x, minor axis $r = 25$ nm, and origin at $y = Y = 25$ nm, so that $d_1(y) = 400 - 4\sqrt{50y - y^2}$. The second grating has the shape of periodic *circles* with radii $R = 25$ nm and center at $y = Y = 25$ nm, such that $d_1 = 400 - 2\sqrt{50y - y^2}$. One can see that the Casimir energy increases with the ratio R/r. This is again especially true at $\delta = d/2$.

One should note that compared to the profiles studied in Fig. 5, the energy variation over δ for these *ellipsoid* and *circular* gratings varies very slowly except around $\delta = d/4$, where a sudden increase in energy is found. This could be a probable consequence of the concave nature of these shapes for $y < Y$.

As a conclusion, we have studied the dependence of the Casimir energy over different arbitrary periodic gratings, ranging from the case of *sawtooth* and *sinusoidal* profiles, to *barbed wires*, *circular* and *ellipsoid* shapes. These all have practical applications; the *circular* profiles describe the geometries of carbon nanotubes, for example. It seems that in general, at same separation distance L, period d, and corrugation depth a, periodic gratings presenting concave shapes (such as those considered in Fig. 7 and Fig. 8) have a tendency to maximize the Casimir energy compared to those of convex shape (such as those considered in Fig. 5). This is a probable consequence of the fact that for a given mirror, the greater the exposed surface in near field to the other mirror, the greater the Casimir energy [17]. An interesting topic to further investigate would be to parametrize the profiles in such a way that the lateral displacement δ also de-

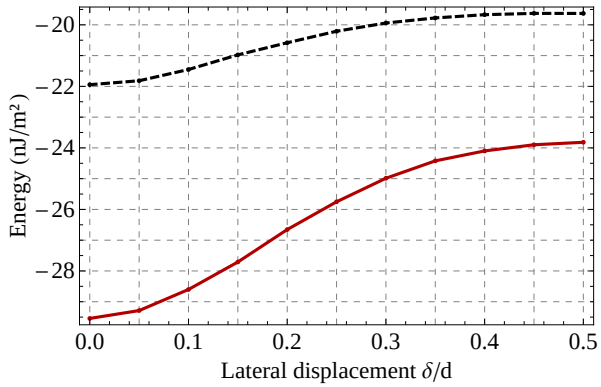

FIG. 8: Dependence of the Casimir energy to the mutual lateral translation of two corrugated periodic profiles shaped as *circular* (black dashed line) and *ellipsoid* (red solid line). We took here $L = 100$ nm, $K = 15$, $d = 400$ nm, $a = 50$ nm, and $d_1 = 400 - 2\sqrt{50y - y^2}$ for *circles* in black (with $R = r = Y = 25$ nm), and $d_1 = 400 - 4\sqrt{50y - y^2}$ for *ellipses* in red (with $r = Y = 25$ nm and $R = 50$ nm).

pends on y, thus generating asymmetric profiles. This, as well as our previous results, should also be put in relation with the recent results and measurements of the Casimir lateral force and Casimir torque effect.

We thank for support the European Science Foundation (ESF) within the activity *New Trends and Applications of the Casimir Effect* (www.casimir-network.com).

[1] H. Casimir, Proc. K. Ned. Akad. Wet. **51**, 793 (1948).

[2] A. Lambrecht and S. Reynaud, Eur. Phys. J. D. **8**, 309 (2000).

[3] A. Canaguier-Durand, A. Gérardin, R. Guérout, P. M. Neto, V. Nesvizhevsky, A. Voronin, A. Lambrecht, and S. Reynaud, Phys. Rev. A **83**, 032508 (2011).

[4] A. Lambrecht and V. Marachevsky, Phys. Rev. Lett. **101**, 160403 (2008).

[5] Y. Bao, R. Guérout, J. Lussange, A. Lambrecht, R. A. Cirelli, F. Klemens, W. M. Mansfield, C. S. Pai, and H. B. Chan, Appl. Phys. Lett. **105**, 250402 (2010).

[6] C. Henkel and K. Joulain, Europhys. Lett. **72**, 929 (2005).

[7] F. S. S. Rosa, D. A. R. Dalvit, and P. W. Milonni, Phys. Rev. Lett. **100**, 183602 (2008).

[8] R. B. Rodrigues, P. A. M. Neto, A. Lambrecht, and S. Reynaud, Phys. Rev. A **75**, 062108 (2007).

[9] M. Levin, A. P. McCauley, A. W. Rodriguez, M. T. H. Reid, and S. G. Johnson, Phys. Rev. Lett. **105**, 090403 (2010).

[10] F. Chen, G. L. Klimchitskaya, V. M. Mostepanenko, and U. Mohideen, Opt. Express **15**, 4823 (2007).

[11] G. Torricelli, P. J. van Zwol, O. Shpak, C. Binns, G. Palasantzas, B. J. Kooi, V. B. Svetovoy, and M. Wuttig, Phys. Rev. A **82**, 010101 (2010).

[12] M. Brown-Hayes, D. A. R. Dalvit, F. D. Mazzitelli, W. J. Kim, and R. Onofrio, Phys. Rev. A **72**, 052102 (2005).

[13] H. B. Chan, Y. Bao, J. Zou, R. A. Cirelli, F. Klemens, W. M. Mansfield, and C. S. Pai, Phys. Rev. Lett. **101**, 030401 (2008).

[14] J. N. Munday, F. Capasso, and V. A. Parsegian, Nature (London) **457**, 170 (2009).

[15] B. V. Derjaguin, Kolloid-Z **69**, 155 (1934).

[16] A. Lambrecht, I. Pirozhenko, L. Duraffourg, and P. Andreucci, Europhys. Lett. **77**, 44006 (2007).

[17] R. Guérout, A. Lambrecht, and S. Reynaud, *The Casimir effect : error made by the pairwise summation method* (in preparation, 2009).

PHYSICAL REVIEW A **87**, 052514 (2013)

Thermal Casimir force between nanostructured surfaces

R. Guérout,[1] J. Lussange,[1] H. B. Chan,[2] A. Lambrecht,[1] and S. Reynaud[1]
[1]*Laboratoire Kastler-Brossel, CNRS, ENS, UPMC, Case 74, F-75252 Paris, France*
[2]*Department of Physics, the Hong Kong University of Science and Technology, Hong Kong, China*
(Received 18 December 2012; published 24 May 2013)

We present detailed calculations for the Casimir force between a plane and a nanostructured surface at finite temperature in the framework of the scattering theory. We then study numerically the effect of finite temperature as a function of the grating parameters and the separation distance. We also infer nontrivial geometrical effects on the Casimir interaction via a comparison with the proximity force approximation. Finally, we compare our calculations with data from experiments performed with nanostructured surfaces.

DOI: 10.1103/PhysRevA.87.052514 PACS number(s): 31.30.jh, 12.20.Ds, 03.70.+k, 42.50.Lc

I. INTRODUCTION

The Casimir interaction at finite temperature consists of two parts: a purely quantum one which subsists as $T \to 0$ K involving the zero-point energy of the electromagnetic vacuum [1] and a thermal one [2] which takes into account the real thermal photons emitted by the bodies. For the thermal part to become noticeable, frequencies relevant to the Casimir interaction must fall in the range of relevant thermal frequencies. For this reason, at room temperature the thermal part of the Casimir interaction becomes important for separation distances of the order of micrometers or tens of micrometers. At those separation distances, the absolute value of the Casimir force is small as it decreases as the inverse third power of the separation distance. Experimentally, there is thus a tradeoff when one wants to measure the thermal component of the Casimir interaction: at small separation distance where the Casimir force is comparably large, the thermal part is small, whereas at large separation distance where the thermal part is large, the total Casimir force is small. A solution is to use "large" interacting bodies to maximize the Casimir force at large distances [3].

The above reasoning is well adapted to the parallel-plates geometry (or a plate-sphere situation when the radius of the sphere is large) where the only characteristic length is the separation distance. In the case of a plate-grating situation, additional characteristic lengths such as the grating period or the corrugation depth are to be taken into account. The importance played by the thermal part of the Casimir interaction is highly nontrivial in the case of the plate-grating geometry and full calculations become necessary. First calculations for this geometry for perfect reflectors at zero temperature have used a path integral approach [4]. A first exact solution for the Casimir force between two periodic dielectric gratings was given in [5]. On the basis of this method a scattering approach to the Casimir force in the gratings geometry at zero temperature has been presented in [6]. In this paper we use the scattering approach to Casimir forces [7–9] to calculate the Casimir interaction between a plate and a grating at arbitrary temperature. Alternatively, the Casimir force in such geometries can also be calculated using a modal approach [10], which is in principle identical to the method presented in [6] and in this paper. There are, however, a few differences that will lead to slightly different results which we will detail later. In the following we study the contribution of the thermal part as a function of the grating parameters and assess the validity of the proximity force approximation (PFA). We finally compare our results with experimental data presented elsewhere [6,11]. The most important result is that in the grating geometry the thermal contribution to the Casimir interaction is overall enhanced and occurs at shorter separation distance, which opens interesting perspectives for new experiments.

II. THEORY: THERMAL CASIMIR FORCE BETWEEN GRATINGS

We study the Casimir interaction within the scattering approach between a plate and a 1D lamellar grating as depicted in Fig. 1. Above the grating $z > 0$, we have a homogeneous region labeled I characterized by a permittivity ϵ_i. Below the grating $z < -a$, a homogeneous region labeled III characterized by a permittivity ϵ_t. The plate is characterized by a permittivity ϵ_p for $z > L$. In the grating region $-a \leqslant z \leqslant 0$, the permittivity is a periodic function of x, $\epsilon(x)$.

In the following we will use $c = 1$ for convenience and work with a generalized complex frequency $\Omega = \omega + i\xi$ having real and imaginary parts ω and ξ, respectively. The Casimir force per unit area between two parallel plates is given by the Lifshitz formula [12] with specular reflection on the plates described by Fresnel coefficients. The scattering theory generalizes this formula by treating nonspecular reflections from a grating through the use of reflection operators coupling different plane-wave modes [8]. The Casimir force per unit area $F_{p,g}(L)$ between a plane and a grating at finite temperature T, separated by a distance L, is

$$F_{p,g}(L;T) = 2\pi k_B T \sum_{n=0}^{\infty}{}' \iint \mathrm{tr}[(\mathbf{1} - \boldsymbol{\mathcal{M}}_n)^{-1}\partial_L \boldsymbol{\mathcal{M}}_n]dk_x dk_y, \quad (1)$$

where the prime on the sum means that the term with $n = 0$ is to be multiplied by a factor $1/2$. The discrete sum in the above equation runs over the Matsubara frequencies $i\xi_n = i\frac{2\pi n k_B T}{\hbar}$, which are the poles of the function $\coth(\frac{\hbar\Omega}{2k_B T}) = 1 + 2(e^{\hbar\Omega/k_B T} - 1)^{-1}$ and take into account zero-point energy fluctuations as well as thermal fluctuations. It originates from a contour integration in the complex frequency plane.

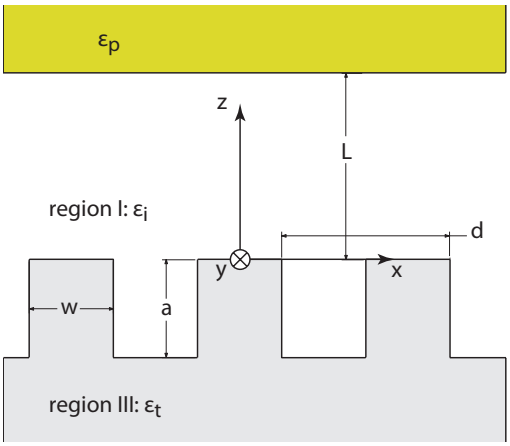

FIG. 1. (Color online) A 1D lamellar grating and its associated reference frame.

The operator $\mathcal{M}_n$ is evaluated at the Matsubara frequencies and reads $\mathcal{M}(i\xi_n) = \mathbf{R}_p(i\xi_n)e^{-\kappa L}\mathbf{R}_g(i\xi_n)e^{-\kappa L}$. It describes a full round-trip of the field between the two scatterers, that is, a reflection on the plate via the operator $\mathbf{R}_p$, the free propagation from the plate to the grating corresponding to the translational operator $e^{-\kappa L}$ with the imaginary wave vector $\boldsymbol{\kappa} = -i\mathbf{k}_z = (\epsilon_i\xi_n^2 + \mathbf{k}_x^2 + k_y^2)^{1/2}$, the scattering on the grating via the reflection operator $\mathbf{R}_g$ and a free propagation back to the plate. The vector $\mathbf{k}_x$ of dimension $2N+1$ collects the diffracted wave vectors $\mathbf{k}_x = (k_x - N\frac{2\pi}{d}, \ldots, k_x, \ldots, k_x + N\frac{2\pi}{d})$, where N is the highest diffraction order retained in the calculation. The integration in Eq. (1) is restricted to the first Brillouin zone, i.e., $-\frac{\pi}{d} \leqslant k_x \leqslant \frac{\pi}{d}$.

The plate's reflection operator $\mathbf{R}_p$ is diagonal and collects the appropriate Fresnel reflection coefficients $\mathbf{R}_p = \mathrm{diag}(\frac{\boldsymbol{\kappa}-\boldsymbol{\kappa}_p}{\boldsymbol{\kappa}+\boldsymbol{\kappa}_p}, \frac{\epsilon_p\boldsymbol{\kappa}-\epsilon_i\boldsymbol{\kappa}_p}{\epsilon_p\boldsymbol{\kappa}+\epsilon_i\boldsymbol{\kappa}_p})$ with $\boldsymbol{\kappa}_p = (\epsilon_p\xi_n^2 + \mathbf{k}_x^2 + k_y^2)^{1/2}$. We calculate the grating reflection operator $\mathbf{R}_g$ in the framework of the rigorous coupled wave analysis (RCWA) or Fourier modal method. We use a method of resolution inspired by the formalism presented, e.g., in [13], which we will briefly outline below.

The physical problem is time and y invariant. A global dependence in $e^{i(k_y y-\omega t)}$ can be factored out of all the fields.

For an incident wave characterized by a wave vector $\mathbf{k}_i^{(p)} = (\alpha_p, k_y, -\gamma_p^{(i)})$, a grating structure with period d will generate an infinite number of reflected waves with wave vectors $\mathbf{k}_r^{(n)} = (\alpha_n, k_y, \gamma_n^{(i)})$ and transmitted waves with wave vectors $\mathbf{k}_t^{(n)} = (\alpha_n, k_y, -\gamma_n^{(t)})$. $\alpha_n = k_x + n\frac{2\pi}{d}$ and $\gamma_n^{(i/t)} = (\epsilon_{i/t}\omega^2 - \alpha_n^2 - k_y^2)^{1/2}$.

In region I, the y components of the fields are written as a Rayleigh expansion involving incident and reflected fields of order p and n, respectively:

$$E_y(x,z) = \sum_{n=-\infty}^{+\infty} \delta_{np} I_p^{(e)} e^{i(\alpha_p x - \gamma_p^{(i)} z)} + R_{np}^{(e)} e^{i(\alpha_n x + \gamma_n^{(i)} z)}, \quad (2a)$$

$$H_y(x,z) = \sum_{n=-\infty}^{+\infty} \delta_{np} I_p^{(h)} e^{i(\alpha_p x - \gamma_p^{(i)} z)} + R_{np}^{(h)} e^{i(\alpha_n x + \gamma_n^{(i)} z)}, \quad (2b)$$

whereas in region III, the Rayleigh expansion involves the transmitted fields

$$E_y(x,z) = \sum_{n=-\infty}^{+\infty} T_{np}^{(e)} e^{i[\alpha_n x - \gamma_n^{(t)}(z+a)]}, \quad (3a)$$

$$H_y(x,z) = \sum_{n=-\infty}^{+\infty} T_{np}^{(h)} e^{i[\alpha_n x - \gamma_n^{(t)}(z+a)]}. \quad (3b)$$

Whether in region I or III, the x components of the fields are obtained from the y components thanks to the Maxwell's curl equations:

$$E_x(x,z) = \frac{ik_y}{\epsilon_{i/t}\omega^2 - k_y^2}\partial_x E_y(x,z) + \frac{i\omega}{\epsilon_{i/t}\omega^2 - k_y^2}\partial_z H_y(x,z), \quad (4a)$$

$$H_x(x,z) = \frac{ik_y}{\epsilon_{i/t}\omega^2 - k_y^2}\partial_x H_y(x,z) - \frac{i\omega\epsilon_{i/t}}{\epsilon_{i/t}\omega^2 - k_y^2}\partial_z E_y(x,z). \quad (4b)$$

In the grating region $-a \leqslant z \leqslant 0$, owing to the periodicity along the x direction the fields as well as the permittivity $\epsilon(x)$ and its reciprocal $1/\epsilon(x)$ can be expanded in Fourier series. We have

$$E_x(x,z) = \sum_n e_x^{(n)}(z) e^{ik_x x} e^{2in\pi x/d}, \quad (5a)$$

$$E_y(x,z) = \sum_n e_y^{(n)}(z) e^{ik_x x} e^{2in\pi x/d}, \quad (5b)$$

$$H_x(x,z) = \sum_n h_x^{(n)}(z) e^{ik_x x} e^{2in\pi x/d}, \quad (5c)$$

$$H_y(x,z) = \sum_n h_y^{(n)}(z) e^{ik_x x} e^{2in\pi x/d}, \quad (5d)$$

$$\epsilon(x) = \sum_n \epsilon_n e^{2in\pi x/d}, \quad (5e)$$

$$1/\epsilon(x) = \sum_n \mathfrak{d}_n e^{2in\pi x/d}. \quad (5f)$$

With those notations, we are able to express the Maxwell's curl equations in a compact matrix form. Let $\mathbf{F}$ be a column vector collecting the Fourier components of the fields $\mathbf{F} = (\mathbf{e}_x, \mathbf{e}_y, \mathbf{h}_x, \mathbf{h}_y)^{\mathsf{T}}$, we then may write

$$\partial_z \mathbf{F} = \mathbf{M}\mathbf{F} \quad (6a)$$

$$\mathbf{M} = \begin{pmatrix} \mathbf{0} & \mathbf{0} & -\frac{ik_y}{\omega}\boldsymbol{\alpha}\boldsymbol{\epsilon}^{-1} & -i\omega\mathbf{1} + \frac{i}{\omega}\boldsymbol{\alpha}\boldsymbol{\epsilon}^{-1}\boldsymbol{\alpha} \\ \mathbf{0} & \mathbf{0} & i\omega\mathbf{1} - \frac{ik_y^2}{\omega}\boldsymbol{\epsilon}^{-1} & \frac{ik_y}{\omega}\boldsymbol{\epsilon}^{-1}\boldsymbol{\alpha} \\ \frac{ik_y}{\omega}\boldsymbol{\alpha} & i\omega\boldsymbol{\epsilon} - \frac{i}{\omega}\boldsymbol{\alpha}\boldsymbol{\alpha} & \mathbf{0} & \mathbf{0} \\ -i\omega\,\boldsymbol{\mathfrak{d}}^{-1} + \frac{ik_y^2}{\omega}\mathbf{1} & -\frac{ik_y}{\omega}\boldsymbol{\alpha} & \mathbf{0} & \mathbf{0} \end{pmatrix} \equiv \begin{pmatrix} \mathbf{0} & \mathbf{M}_1 \\ \mathbf{M}_2 & \mathbf{0} \end{pmatrix}. \quad (6b)$$

In the above equation, $\boldsymbol{\alpha} = \mathrm{diag}(\alpha_n)$, $\mathbf{1}$ is the identity and $\boldsymbol{\epsilon}$, resp. $\boldsymbol{\mathfrak{z}}$, are Toeplitz matrices whose structure is defined as having elements $\{\epsilon_n, n \geqslant 0\}$ on the first line and elements $\{\epsilon_n, n \leqslant 0\}$ on the first column. Note that in accordance with Ref. [14], we have replaced the matrix $\boldsymbol{\epsilon}$ by $\boldsymbol{\mathfrak{z}}^{-1}$ in the lower-left block of the matrix $\mathbf{M}$. This constitutes an improvement with respect to Ref. [5], where this replacement had not been done. Note that our operator $\mathbf{M}$ in Eq. (6b) bears resemblance with Eq. (22) of Ref. [10], but these two operators are slightly different. They coincide only when an infinite number of diffraction orders are retained but they differ upon truncation. The matrix $\mathbf{F}$ has dimension 4×1 in units of $2N + 1$. A particular column of $\mathbf{F}$ corresponds to a particular incident order p. In the following, bold quantities are matrices whose dimensions will be given in units of $2N + 1$ if not trivial. As an example, in Eq. (6b), $\boldsymbol{\alpha}$, $\boldsymbol{\epsilon}$, $\boldsymbol{\mathfrak{z}}$, and $\mathbf{1}$ are matrices of dimension 1×1, whereas $\mathbf{M}_1$ and $\mathbf{M}_2$ are of dimension 2×2.

In [5] Eq. (6a) had been numerically solved. Here we follow a different path, which has proven to lead to more stable numerical calculations. Because of the block antidiagonal structure of matrix $\mathbf{M}$, Eq. (6a) can be recast as a Helmholtz-like equation for the electric fields provided that $\mathbf{M}$ is independent of z, which is the case for the lamellar gratings we consider here:

$$\partial_{z^2}^2 \begin{pmatrix} \mathbf{e}_x \\ \mathbf{e}_y \end{pmatrix} = \mathbf{M}_1 \mathbf{M}_2 \begin{pmatrix} \mathbf{e}_x \\ \mathbf{e}_y \end{pmatrix} \equiv \mathbf{M}^{(e)} \begin{pmatrix} \mathbf{e}_x \\ \mathbf{e}_y \end{pmatrix}. \tag{7}$$

This equation is solved as $\left(\begin{smallmatrix} \mathbf{e}_x \\ \mathbf{e}_y \end{smallmatrix}\right)(z) = e^{\sqrt{\mathbf{M}^{(e)}} z} \mathbf{C}^+ + e^{-\sqrt{\mathbf{M}^{(e)}} z} \mathbf{C}^-$, where $\mathbf{C}^+$ and $\mathbf{C}^-$ are unknown coefficients to be determined. Let $\boldsymbol{\phi}$, $\boldsymbol{\lambda}$ be, respectively, the eigenvectors and eigenvalues of the matrix $\mathbf{M}^{(e)}$ such that $\mathbf{M}^{(e)} = \boldsymbol{\phi}\, \mathrm{diag}(\boldsymbol{\lambda})\, \boldsymbol{\phi}^{-1}$. Writing explicitly the expression for $e^{\pm\sqrt{\mathbf{M}^{(e)}} z}$, we can include the matrix $\boldsymbol{\phi}^{-1}$ in the unknown coefficients $\mathbf{C}^+$ and $\mathbf{C}^-$; furthermore, we want to avoid exponentially growing solutions at $z = -a$. Following the prescriptions in [13] we finally arrive at

$$\begin{pmatrix} \mathbf{e}_x \\ \mathbf{e}_y \end{pmatrix}(z) = \boldsymbol{\phi} e^{\sqrt{\boldsymbol{\lambda}} z} \mathbf{C}^+ + \boldsymbol{\phi} e^{-\sqrt{\boldsymbol{\lambda}}(z+a)} \mathbf{C}^-, \tag{8a}$$

$$\begin{pmatrix} \mathbf{h}_x \\ \mathbf{h}_y \end{pmatrix}(z) = \mathbf{M}_1^{-1} \boldsymbol{\phi} \sqrt{\boldsymbol{\lambda}} e^{\sqrt{\boldsymbol{\lambda}} z} \mathbf{C}^+ - \mathbf{M}_1^{-1} \boldsymbol{\phi} \sqrt{\boldsymbol{\lambda}} e^{-\sqrt{\boldsymbol{\lambda}}(z+a)} \mathbf{C}^-, \tag{8b}$$

where Eq. (8b) has been obtained by injecting Eq. (8a) into $\left(\begin{smallmatrix} \mathbf{h}_x \\ \mathbf{h}_y \end{smallmatrix}\right) = \mathbf{M}_1^{-1} \partial_z \left(\begin{smallmatrix} \mathbf{e}_x \\ \mathbf{e}_y \end{smallmatrix}\right)$ from Eq. (6b).

We can use Eqs. (2) and (4) to write the fields at $z = 0$, and Eqs. (3) to write the fields at $z = -a$. In compact matrix form, this leads to

$$\mathbf{F}(-a) = \begin{pmatrix} -\frac{k_y \boldsymbol{\alpha}}{\epsilon_t \omega^2 - k_y^2} & \frac{\omega \boldsymbol{\gamma}^{(t)}}{\epsilon_t \omega^2 - k_y^2} \\ \mathbf{1} & \mathbf{0} \\ -\frac{\omega \epsilon_t \boldsymbol{\gamma}^{(t)}}{\epsilon_t \omega^2 - k_y^2} & -\frac{k_y \boldsymbol{\alpha}}{\epsilon_t \omega^2 - k_y^2} \\ \mathbf{0} & \mathbf{1} \end{pmatrix} \begin{pmatrix} \mathbf{T}^{(e)} \\ \mathbf{T}^{(h)} \end{pmatrix} \equiv \begin{pmatrix} \mathbf{t}_e \\ \mathbf{t}_h \end{pmatrix} \begin{pmatrix} \mathbf{T}^{(e)} \\ \mathbf{T}^{(h)} \end{pmatrix} \tag{9}$$

and

$$\begin{aligned} \mathbf{F}(0) &= \begin{pmatrix} -\frac{k_y \boldsymbol{\alpha}}{\epsilon_i \omega^2 - k_y^2} & \frac{\omega \boldsymbol{\gamma}^{(i)}}{\epsilon_i \omega^2 - k_y^2} \\ \mathbf{1} & \mathbf{0} \\ -\frac{\omega \epsilon_i \boldsymbol{\gamma}^{(i)}}{\epsilon_i \omega^2 - k_y^2} & -\frac{k_y \boldsymbol{\alpha}}{\epsilon_i \omega^2 - k_y^2} \\ \mathbf{0} & \mathbf{1} \end{pmatrix} \begin{pmatrix} \mathbf{I}^{\sigma=e} \\ \mathbf{I}^{\sigma=h} \end{pmatrix} \\ &+ \begin{pmatrix} -\frac{k_y \boldsymbol{\alpha}}{\epsilon_i \omega^2 - k_y^2} & -\frac{\omega \boldsymbol{\gamma}^{(i)}}{\epsilon_i \omega^2 - k_y^2} \\ \mathbf{1} & \mathbf{0} \\ \frac{\omega \epsilon_i \boldsymbol{\gamma}^{(i)}}{\epsilon_i \omega^2 - k_y^2} & -\frac{k_y \boldsymbol{\alpha}}{\epsilon_i \omega^2 - k_y^2} \\ \mathbf{0} & \mathbf{1} \end{pmatrix} \begin{pmatrix} \mathbf{R}^{(e)} \\ \mathbf{R}^{(h)} \end{pmatrix} \\ &\equiv \begin{pmatrix} \mathbf{i}_{ee} & \mathbf{i}_{eh} \\ \mathbf{i}_{he} & \mathbf{i}_{hh} \end{pmatrix} \begin{pmatrix} \mathbf{I}^{\sigma=e} \\ \mathbf{I}^{\sigma=h} \end{pmatrix} + \begin{pmatrix} \mathbf{r}_e \\ \mathbf{r}_h \end{pmatrix} \begin{pmatrix} \mathbf{R}^{(e)} \\ \mathbf{R}^{(h)} \end{pmatrix}, \end{aligned} \tag{10}$$

where $\boldsymbol{\gamma}^{(i/t)} = \mathrm{diag}(\gamma_n^{(i/t)})$, and we have introduced the basis of polarizations σ that we use, denoted e and h. The polarizations $\sigma = e,h$ are defined by imposing $H_y = 0$ and $E_y = 0$, respectively. Hence, in the above equation for incident $\sigma = e$ waves, we impose $\mathbf{I}^{\sigma=e} = \mathbf{1}$ and $\mathbf{I}^{\sigma=h} = \mathbf{0}$ and vice versa for incident $\sigma = h$ waves. Note that $\mathbf{t}_e$, $\mathbf{t}_h$, $\mathbf{r}_e$, and $\mathbf{r}_h$ are of dimension 2×2, whereas $\mathbf{i}_{ee}$, $\mathbf{i}_{eh}$, $\mathbf{i}_{he}$, and $\mathbf{i}_{hh}$ are of dimension 2×1. Other dimensions are deduced so as to be consistent with those of $\mathbf{F}$.

Evaluating Eqs. (8) at $z = -a$ and $z = 0$ and identifying with Eqs. (9) and (10) leads to a linear system of equations of dimension $8(2N + 1)$ for the $8(2N + 1)$ unknowns $\mathbf{C}^+$, $\mathbf{C}^-$, $\mathbf{R}^{(e)}$, $\mathbf{R}^{(h)}$, $\mathbf{T}^{(e)}$, and $\mathbf{T}^{(h)}$. Nevertheless, it is numerically more stable to eliminate the reflection and transmission unknowns from this system and to solve instead a reduced system of dimension $4(2N + 1)$ for solely $\mathbf{C}^+$ and $\mathbf{C}^-$. All done, this system reads as follows:

$$\begin{aligned} &\begin{pmatrix} \left(\boldsymbol{\phi} - \mathbf{t}_e \mathbf{t}_h^{-1} \mathbf{V}\right) e^{-\sqrt{\boldsymbol{\lambda}} a} & \boldsymbol{\phi} + \mathbf{t}_e \mathbf{t}_h^{-1} \mathbf{V} \\ \boldsymbol{\phi} - \mathbf{r}_e \mathbf{r}_h^{-1} \mathbf{V} & \left(\boldsymbol{\phi} + \mathbf{r}_e \mathbf{r}_h^{-1} \mathbf{V}\right) e^{-\sqrt{\boldsymbol{\lambda}} a} \end{pmatrix} \begin{pmatrix} \mathbf{C}^+ \\ \mathbf{C}^- \end{pmatrix} \\ &= \begin{pmatrix} \mathbf{0} \\ \left(\mathbf{i}_{ee} - \mathbf{r}_e \mathbf{r}_h^{-1} \mathbf{i}_{he} \quad \mathbf{i}_{eh} - \mathbf{r}_e \mathbf{r}_h^{-1} \mathbf{i}_{hh}\right) \begin{pmatrix} \mathbf{I}^{\sigma=e} \\ \mathbf{I}^{\sigma=h} \end{pmatrix} \end{pmatrix}, \end{aligned} \tag{11}$$

where we have defined $\mathbf{V} = \mathbf{M}_1^{-1} \boldsymbol{\phi} \sqrt{\boldsymbol{\lambda}}$. Once the unknown coefficients $\mathbf{C}^+$ and $\mathbf{C}^-$ are determined by solving Eq. (11), the reflection and transmission coefficients are

$$\begin{pmatrix} \mathbf{R}^{(e)} \\ \mathbf{R}^{(h)} \end{pmatrix} = \mathbf{r}_h^{-1} \left[\mathbf{V}(\mathbf{C}^+ - e^{-\sqrt{\boldsymbol{\lambda}} a} \mathbf{C}^-) - (\mathbf{i}_{he} \ \mathbf{i}_{hh}) \begin{pmatrix} \mathbf{I}^{\sigma=e} \\ \mathbf{I}^{\sigma=h} \end{pmatrix} \right], \tag{12a}$$

$$\begin{pmatrix} \mathbf{T}^{(e)} \\ \mathbf{T}^{(h)} \end{pmatrix} = \mathbf{t}_h^{-1} [\mathbf{V}(e^{-\sqrt{\boldsymbol{\lambda}} a} \mathbf{C}^+ - \mathbf{C}^-)]. \tag{12b}$$

Resolution of Eqs. (11) and (12) first for incident $\sigma = e$ waves and then for incident $\sigma = h$ waves leads to the complete reflection and transmission matrices $\mathbf{R}_g$ and $\mathbf{T}_g$:

$$\mathbf{R}_g = \begin{pmatrix} \mathbf{R}^{(e)}(\sigma = e) & \mathbf{R}^{(e)}(\sigma = h) \\ \mathbf{R}^{(h)}(\sigma = e) & \mathbf{R}^{(h)}(\sigma = h) \end{pmatrix}, \tag{13a}$$

$$\mathbf{T}_g = \begin{pmatrix} \mathbf{T}^{(e)}(\sigma = e) & \mathbf{T}^{(e)}(\sigma = h) \\ \mathbf{T}^{(h)}(\sigma = e) & \mathbf{T}^{(h)}(\sigma = h) \end{pmatrix}. \tag{13b}$$

The force at $T = 0$ K is recovered by the substitution

$$2\pi k_B T \sum_{n=0}^{\infty}{}' \to \hbar \int_0^\infty d\xi. \tag{14}$$

We define two quantities, $\vartheta_F(L)$ and $\eta_F(L)$, to assess, respectively, the effect of the finite temperature and the deviation from PFA:

$$\vartheta_F(L) = \frac{F_{p,g}(L; T = 300\ \text{K})}{F_{p,g}(L; T = 0\ \text{K})}, \tag{15}$$

$$\eta_F(L;T) = \frac{F_{p,g}(L;T)}{F_{p,g}^{PFA}(L;T)}, \tag{16}$$

where $F_{p,g}^{PFA}(L;T) = \frac{1}{d}\int_0^d F_{p,p}[L(x);T]dx$, and $F_{p,p}(L;T)$, the force between two plane-parallel plates, is given by the Lifshitz formula [12].

III. NUMERICAL EVALUATIONS

We now study the thermal Casimir interaction between a gold plate and a doped silicon grating. Therefore, $\epsilon_t \equiv \epsilon_{Si}(\omega)$ and $\epsilon_p \equiv \epsilon_{Au}(\omega)$. The plate and the grating are separated by vacuum $\epsilon_i \equiv \epsilon_0 = 1\ \forall\omega$. As described in [11], the permittivity of gold is taken from experimental data extrapolated to low frequencies by the Drude model. The permittivity of doped silicon is modeled by a two-oscillator model: one describing the intrinsic part of silicon and the other one describing its metallic behavior at low frequencies [15]. The metallic part of doped silicon is determined by a doping level of 2×10^{18} cm^{-3}. In the calculations, we choose to truncate our reflection operator at $N = 10$, which is sufficient to show convergence at all separation distances studied. This is another difference with respect to Ref. [10] where $N = 5$ has been used. The situation is characterized by four length scales: the separation distance L, the corrugation height a, the grating period d, and the corrugation width w. (For this last quantity, we will prefer to work with the filling factor $f = w/d$). A complete analysis would in principle involve full Casimir force calculations in a four-dimensional parameters space. Instead we explore here the parameter space at fixed filling factor and grating period d corresponding to the experimental setup in [11].

In Fig. 2 we illustrate the effect of the temperature in the plate-grating geometry by plotting the ratio $\vartheta_F(L,a)$ as a function of both the separation distance L and the trench depth a. The grating period d and the filling factor f are fixed, respectively, at $d = 400$ nm and $f = 0.5$. For this choice of materials, we find over the whole range of parameters $\vartheta_F(L,a) > 1$ so that the thermal photons always lead to an increase in the Casimir force. For $a = 0$ we recover the two-plate configuration and we have necessarily $\lim_{L\to 0}\vartheta_F(L,a = 0) = 1$. The total temperature effect $\vartheta_F(L,a = \infty) - \vartheta_F(L,a = 0)$ increases with larger separation distances L. The limiting value $\vartheta_F(L,a = \infty)$ is reached for larger a as the separation distance L increases, since this limiting value rather means $a \gg L$.

Interestingly, for a fixed separation distance L, there is a steep increase of ϑ_F as a function of the corrugation depth a towards saturation, as shown in detail in Fig. 3. At a distance of 1.2 μm the temperature corrections increase the zero temperature force by ∼5% between two flat plates.

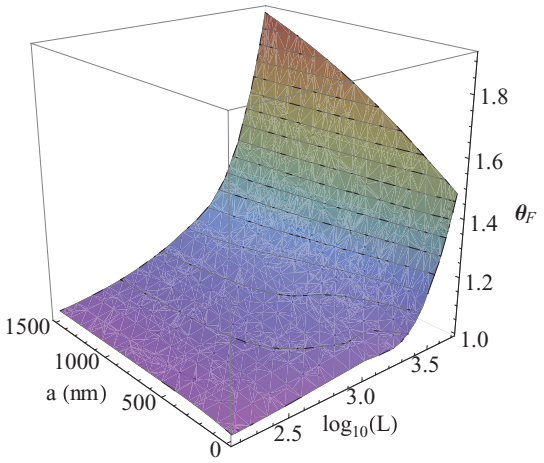

FIG. 2. (Color online) Effect of temperature on the Casimir force given by the ratio ϑ_F as a function of the separation distance L and corrugation depth a.

Remarkably, this increase becomes ∼20% if the doped Si plate contains deep trenches ($a \sim 1.4$ μm). For $L = 600$ nm the effect is less pronounced but still amounts to an increase from 3 to about 10. Clearly the use of a structured surface increases the thermal Casimir force and makes the effect easier to be observed at shorter distances. A possible explanation is that the nanostructures change the spectral mode density, especially in the infrared frequency domain, so that thermal effects become enhanced, as it has already been pointed out in heat-transfer phenomena between gratings [16,17].

Next, we turn to assess the validity of PFA. Figure 4 shows the deviation from PFA η_F as a function of the separation distance L and the corrugation depth a. By definition, $\eta_F(L,a = 0) = 1$. For a fixed separation distance L, the error made by PFA increases with deeper trench depth a. We have $\eta_F(L,a;T = 300\ \text{K}) > \eta_F(L,a;T = 0\ \text{K})$ for all values of separation distance L and trench depth a so that a finite temperature is seen to always increase the deviation from PFA. At large separation distances, we expect PFA to be valid so that $\lim_{L\to\infty}\eta_F(L,a;T) = 1$. In particular, for a fixed corrugation depth a, the functions η_F show a maximum for a particular distance $L = L_{\text{max}}$, as illustrated in Fig. 5. *Qualitatively*, we

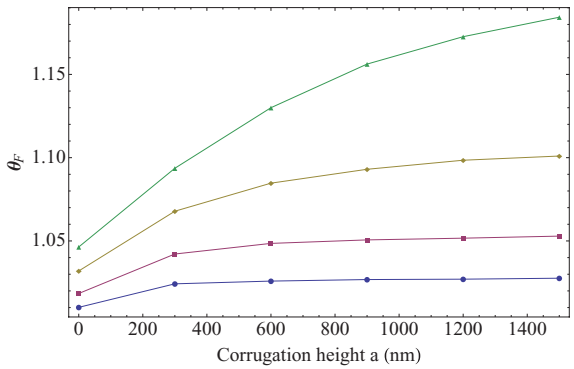

FIG. 3. (Color online) Effect of the temperature ϑ_F on the Casimir force for $L = 150$, 300, 600, and 1200 nm (from bottom to top) as a function of the trench depth a.

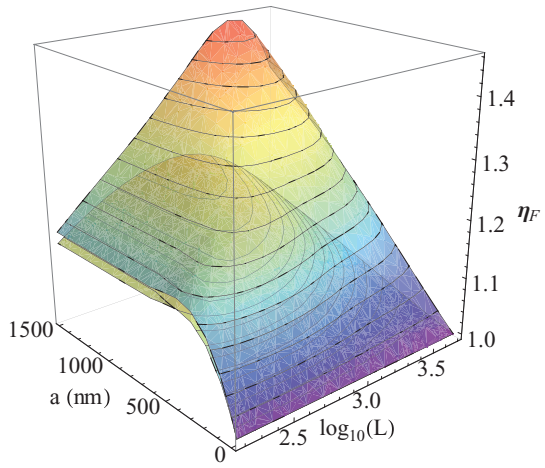

FIG. 4. (Color online) Deviation from PFA η_F as a function of the separation distance L and trench depth a. The lower surface is for $T = 0$ K, the upper one for $T = 300$ K.

can say that this value $L_{\max} \approx a$. More precisely, we find $L_{\max} \lessapprox a$ for $T = 0$ K and $L_{\max} \gtrapprox a$ for $T = 300$ K. Thus the deviation from PFA increases with increasing distances for $L \leqslant a$ and decreases with increasing distances for $L \geqslant a$. The deviation from PFA for $T \neq 0$ K shows the same qualitative behavior as for $T = 0$ K.

IV. COMPARISON WITH EXPERIMENTAL DATA

We are now in the position to compare our calculations with experimental data from [6,11]. In these experiments the interaction between a nanostructured silicon surface and a gold-coated sphere with a radius of 50 μm was measured. The force was detected at ambient temperature using a silicon micromechanical resonator onto which the gold sphere was attached. As the distance between the nanostructured surface and the sphere was varied, the change in the resonant frequency of the resonator was recorded. This quantity is proportional to the Casimir force gradient $\partial_L F_{s,g}(L)$ between the gold sphere and the silicon grating. Since the separation distance between the sphere and the grating is small compared to the radius of the sphere, we can relate this Casimir force gradient to the Casimir pressure $F_{p,g}(L)$ between a plate and the grating

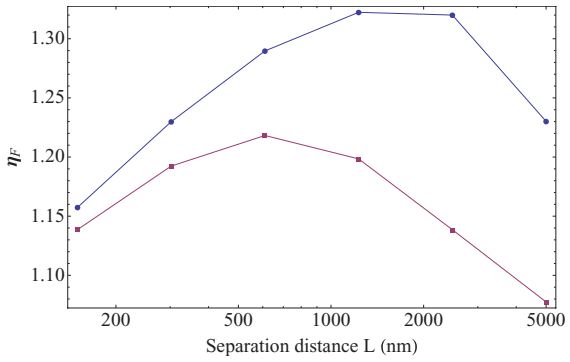

FIG. 5. (Color online) Deviation from PFA η_F at fixed trench depth $a = 900$ nm as a function of the separation distance L for $T = 0$ K (bottom) and $T = 300$ K (top).

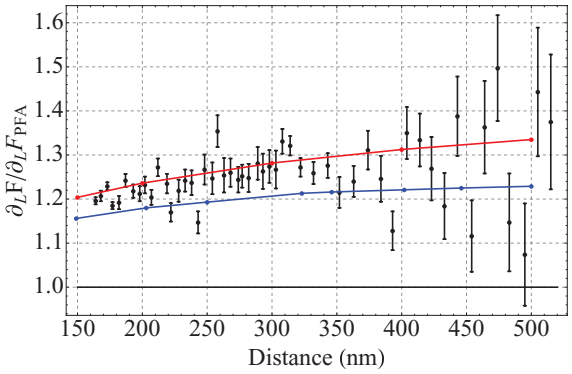

FIG. 6. (Color online) Experimental data for the Casimir force gradient between a gold sphere and a silicon grating with deep trenches (black dots with error bars). The data are normalized to their PFA expression. This is compared with our calculations both for $T = 0$ K (blue, lower line) and $T = 300$ K (red).

as $\partial_L F_{s,g}(L) = 2\pi R F_{p,g}(L)$. Under these assumptions, the measured quantity $\partial_L F_{s,g}(L)$ when normalized by its PFA value is identical to η_F, i.e., $\partial_L F(L)/\partial_L F^{PFA}(L) = \eta_F(L)$, where we have omitted for simplicity the indices indicating the sphere grating geometry.

In Fig. 6 we plot $\eta_F(L)$ for a silicon structure with deep trenches (sample B in Ref. [6]). This sample has a period $d = 400$ nm, trench depth $a = 980$ nm, and filling factor $f = 0.478$. The experimental data are plotted as circles with error bars. Our calculations for $T = 0$ K and $T = 300$ K are plotted as the blue and red curves, respectively. As first reported in [6], the measured values of $\eta_F(L)$ between gold and silicon surfaces were found to be smaller than predictions using perfect reflectors at zero temperature [4]. The inclusion of the material properties at zero temperature leads to better agreement [5]. Our zero-temperature results presented here are larger than those in Refs. [5] and [10] by about $\partial_L F/\partial_L F^{PFA} \approx 0.05$. We attribute these differences to the replacement of the matrix $\boldsymbol{\epsilon}$ by $\mathfrak{z}^{-1}$ in the lower-left block of the matrix $\mathbf{M}$ in Eq. (6b) and to solving the differential equations (7) instead of (6a) compared to results in [5] and to a higher truncation at $N = 10$ here, compared to $N = 5$ in [10].

Let us now discuss the thermal effects. The red line in Fig. 6 plots the calculated results for $T = 300$ K, at separation L from ≈ 150 nm to $L \approx 500$ nm. Following our previous discussion of Fig. 5, since the experiment was conducted in a regime where $L < a$, both η_F and $\partial_L F/\partial_L F^{PFA}$ increase with separation distance. In Fig. 6, the difference between the red line for $T = 300$ K and the blue line for $T = 0$ K is clearly visible. When compared to the experimental data measured at ambient temperature, the theory curve calculated for $T = 300$ K gives better agreement than the one at $T = 0$ K. Unambiguous demonstration of the thermal contributions of the Casimir force in this sample, however, would require experimental improvements to further reduce the measurement uncertainty.

So far, the thermal contributions to the Casimir force have only been observed at distances larger than 1 μm between smooth surfaces [3]. At smaller distances, the thermal effects decrease significantly. As shown in Fig. 3, the thermal

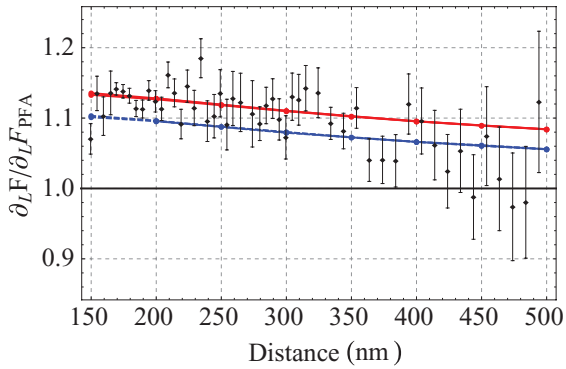

FIG. 7. (Color online) Experimental data for the Casimir force gradient between a gold sphere and a silicon grating with shallow trenches (black dots with error bars). The data are normalized to their PFA expression. This is compared with our calculations both for $T = 0$ K (blue) and $T = 300$ K (red).

contributions to the Casimir force between flat surfaces are expected to be only about 3% at ∼500 nm. By replacing one of the surfaces with a grating with deep trenches, the thermal contributions increase by a factor of 3. Nanostructured surfaces therefore hold promise for precise measurements of the thermal Casimir force.

Next we focus on gratings with shallow trenches that were used in Ref. [11]. The period was again $d = 400$ nm, but the trench depth was only $a = 98$ nm. The filling factor was approximately $f = 0.48$. Figure 7 shows the measured data points from this experiment together with the results of our calculations for this sample both at $T = 300$ K (red curve) and $T = 0$ K (blue curve). In the calculation we take into account the exact trapezoidal shape of the corrugation profile via a generalization of the formalism presented above [18]. As the range of separation distances is the same as in the experiment with deep trenches, the situation now corresponds to a regime where $L > a$. Therefore η_F and thus $\partial_L F/\partial_L F^{PFA}$ both decrease with increasing distance to reach its asymptotic value of 1. Again the theoretical prediction at 300 K is in good agreement with the measured data. The overall temperature effect is less pronounced here than for the deep trenches, as the trench depth is about a factor of 10 smaller.

V. CONCLUSIONS

We have calculated the Casimir interaction between a plate and a grating at finite temperature. We find good agreement between our calculations for $T = 300$ K and experimental data taken at ambient temperature. Even though the experiments are performed at relatively small separation distances $L < 500$ nm, the use of gratings enhances the thermal contributions of the Casimir force. Our findings provide an alternative approach to study thermal Casimir forces without having to reach separation distances of the order of micrometers.

ACKNOWLEDGMENTS

H.B.C. is supported by HKUST 600511 from the Research Grants Council of Hong Kong SAR, Shun Hing Solid State Clusters Lab, and US Department of Energy Grant No. DE-FG02-05ER46247. We thank the European Science Foundation (ESF) within the activity *New Trends and Applications of the Casimir Effect* for support.

[1] H. Casimir, Proc. K. Ned. Akad. Wet. **51**, 793 (1948).
[2] J. Mehra, Physica **37**, 145 (1967).
[3] A. Sushkov, W. Kim, D. Dalvit, and S. Lamoreaux, Nat. Phys. **7**, 230 (2011).
[4] R. Büscher and T. Emig, Phys. Rev. A **69**, 062101 (2004).
[5] A. Lambrecht and V. N. Marachevsky, Phys. Rev. Lett. **101**, 160403 (2008).
[6] H. B. Chan, Y. Bao, J. Zou, R. A. Cirelli, F. Klemens, W. M. Mansfield, and C. S. Pai, Phys. Rev. Lett. **101**, 030401 (2008).
[7] M. T. Jaekel and S. Reynaud, J. Phys. I (France) **1**, 1395 (1991).
[8] A. Lambrecht, P. A. M. Neto, and S. Reynaud, New J. Phys. **8**, 243 (2006).
[9] T. Emig, N. Graham, R. L. Jaffe, and M. Kardar, Phys. Rev. Lett. **99**, 170403 (2007).
[10] P. S. Davids, F. Intravaia, F. S. S. Rosa, and D. A. R. Dalvit, Phys. Rev. A **82**, 062111 (2010).
[11] Y. Bao, R. Guérout, J. Lussange, A. Lambrecht, R. A. Cirelli, F. Klemens, W. M. Mansfield, C. S. Pai, and H. B. Chan, Phys. Rev. Lett. **105**, 250402 (2010).
[12] E. Lifshitz, Sov. Phys. JETP **2**, 73 (1956).
[13] M. G. Moharam, D. A. Pommet, E. B. Grann, and T. K. Gaylord, J. Opt. Soc. Am. A **12**, 1077 (1995).
[14] P. Lalanne and G. M. Morris, J. Opt. Soc. Am. A **13**, 779 (1996).
[15] A. Lambrecht, I. Pirozhenko, L. Duraffourg, and P. Andreucci, Eur. Phys. Lett. **77**, 44006 (2007).
[16] R. Guérout, J. Lussange, F. S. S. Rosa, J.-P. Hugonin, D. A. R. Dalvit, J.-J. Greffet, A. Lambrecht, and S. Reynaud, Phys. Rev. B **85**, 180301(R) (2012).
[17] J. Lussange, R. Guérout, F. S. S. Rosa, J. J. Greffet, A. Lambrecht, and S. Reynaud, Phys. Rev. B **86**, 085432 (2012).
[18] J. Lussange, R. Guérout, and A. Lambrecht, Phys. Rev. A **86**, 062502 (2012).